(12) INTERNATIONAL APPLICATION PUBLISHED UNDER THE PATENT COOPERATION TREATY (PCT)

(19) World Intellectual Property Organization
International Bureau

(43) International Publication Date
29 April 2021 (29.04.2021)

WIPO | PCT

(10) International Publication Number
WO 2021/080694 A2

(51) International Patent Classification:
H01M 10/24 (2006.01)

(21) International Application Number:
PCT/US2020/049142

(22) International Filing Date:
03 September 2020 (03.09.2020)

(25) Filing Language: English

(26) Publication Language: English

(30) Priority Data:
62/895,455 03 September 2019 (03.09.2019) US

(71) Applicant: **GEORGIA TECH RESEARCH CORPORATION** [US/US]; 926 Dalney Street NW, Atlanta, Georgia 30318 (US).

(72) Inventors: **LIU, Nian**; c/o Georgia Tech Research Corporation, 926 Dalney Street NW, Atlanta, Georgia 30318 (US). **WU, Yutong**; c/o Georgia Tech Research Corporation, 926 Dalney Street NW, Atlanta, Georgia 30318 (US). **ZHANG, Yamin**; c/o Georgia Tech Research Corporation, 926 Dalney Street NW, Atlanta, Georgia 30318 (US).

(74) Agent: **SCHNEIDER, Ryan A.** et al.; Troutman Pepper Hamilton Sanders LLP, 600 Peachtree Street NE, Suite 3000, Atlanta, Georgia 30318 (US).

(81) Designated States *(unless otherwise indicated, for every kind of national protection available)*: AE, AG, AL, AM, AO, AT, AU, AZ, BA, BB, BG, BH, BN, BR, BW, BY, BZ, CA, CH, CL, CN, CO, CR, CU, CZ, DE, DJ, DK, DM, DO, DZ, EC, EE, EG, ES, FI, GB, GD, GE, GH, GM, GT, HN, HR, HU, ID, IL, IN, IR, IS, IT, JO, JP, KE, KG, KH, KN, KP, KR, KW, KZ, LA, LC, LK, LR, LS, LU, LY, MA, MD, ME, MG, MK, MN, MW, MX, MY, MZ, NA, NG, NI, NO, NZ, OM, PA, PE, PG, PH, PL, PT, QA, RO, RS, RU, RW, SA, SC, SD, SE, SG, SK, SL, ST, SV, SY, TH, TJ, TM, TN, TR, TT, TZ, UA, UG, US, UZ, VC, VN, WS, ZA, ZM, ZW.

(84) Designated States *(unless otherwise indicated, for every kind of regional protection available)*: ARIPO (BW, GH, GM, KE, LR, LS, MW, MZ, NA, RW, SD, SL, ST, SZ, TZ, UG, ZM, ZW), Eurasian (AM, AZ, BY, KG, KZ, RU, TJ, TM), European (AL, AT, BE, BG, CH, CY, CZ, DE, DK, EE, ES, FI, FR, GB, GR, HR, HU, IE, IS, IT, LT, LU, LV, MC, MK, MT, NL, NO, PL, PT, RO, RS, SE, SI, SK, SM, TR), OAPI (BF, BJ, CF, CG, CI, CM, GA, GN, GQ, GW, KM, ML, MR, NE, SN, TD, TG).

Published:
— *without international search report and to be republished upon receipt of that report (Rule 48.2(g))*

(54) Title: DEEPLY RECHARGEABLE BATTERY SYSTEMS AND METHODS

(57) Abstract: Deeply rechargeable battery systems and methods, where a core/shell nanoscale structure provides deeply rechargeable anodes that overcome intrinsic limitations of conventional battery materials that involve soluble intermediates or insulating discharge products. The deeply rechargeable battery systems and methods simultaneously overcome the dilemmas of passivation and dissolution. An ion-sieving concept is applied to a Zn anode that confines larger zincate ions and allows smaller hydroxide ions to permeate, can limit/prevent ZnO dissolution and electrode shape change.

WO 2021/080694 A2

DEEPLY RECHARGEABLE BATTERY SYSTEMS AND METHODS

CROSS-REFERENCE TO RELATED APPLICATIONS

[001] This application claims the benefit of US Provisional Patent Application No. 62/895,455 filed 3 September 2019, the entire contents and substance of which are hereby incorporated by reference as if fully set forth below.

STATEMENT REGARDING FEDERALLY SPONSORED RESEARCH OR DEVELOPMENT

[002] Not Applicable

THE NAMES OF THE PARTIES TO A JOINT RESEARCH AGREEMENT

[003] Not Applicable

SEQUENCE LISTING

[004] Not Applicable

STATEMENT REGARDING PRIOR DISCLOSURES BY THE INVENTOR OR A JOINT INVENTOR

[005] Not Applicable

BACKGROUND OF THE DISCLOSURE

1. Field of the Disclosure

[006] The various exemplary embodiments of the disclosure relate generally to processes, methods, and systems energy carrying. It is particularly related to deeply rechargeable battery systems and methods.

2. Background

[007] Alternative energy carriers have been sought after due to fossil fuels' slow regeneration and environmental concerns such as climate change, air and water pollution. Indeed, the depletion of fossil fuel resources is leading to steadily increasing energy demands.

[008] Sustainable electrochemical energy storage (EES) systems are being sought that are low-cost, reliable, and eco-friendly. Extensive research into EES in recent years has prompted the emergence of technologies for applications in portable devices, electric vehicles (EVs) and grid-scale energy-storage systems.

[009] When carrying clean electricity from solar or wind, batteries are promising to alleviate the current energy and environmental problems. A wide variety of electrochemical cells, or "batteries," are known, and in general are devices that convert chemical energy into electrical energy by means of an electrochemical oxidation-reduction reaction.

[0010] Batteries can be generally described as comprising three components: an anode that contains a material that is oxidized (yields electrons) during discharge of the battery (i.e., while it is providing power), a cathode that contains a material that is reduced (accepts electrons) during discharge of the battery, and an electrolyte that provides for transfer of ions between the cathode and anode. During discharge, the anode is the negative pole of the battery, and the cathode is the positive pole.

[0011] Batteries can also be generally categorized as being "primary," where the electrochemical reaction is essentially irreversible, so that the battery becomes unusable once discharged, and "secondary," where the electrochemical reaction is, at least in part, reversible so that the battery can be "recharged" and used more than once. Secondary batteries are increasingly used in many applications because of their convenience (particularly in applications where replacing batteries can be difficult), reduced cost (by reducing the need for replacement), and environmental benefits (by reducing the waste from battery disposal).

[0012] Secondary batteries utilizing faradaic energy storage mechanisms are the most prominent systems among the EES technologies. Undoubtedly, lithium-ion batteries (LIBs) have been an enormous success in the realms of portable devices and EVs due to their high energy density, light weight, and low self-discharge rate. For these reasons, LIBs are still receiving significant attention.

[0013] However, LIBs continue to face challenges related to safety (with their use of flammable organic electrolytes), energy density, longevity, and concerns around material availability (such as Li and Co metals). Particularly, battery safety is an increasingly vital concern in electric vehicle applications. These issues seriously limit the popularization of EVs and the development of grid-energy storage.

[0014] One approach to these limitations includes research into fluorinated organic electrolytes and solid-state electrolytes as alternatives to flammable organic solvents. Another approach

towards ultra-safe batteries is to develop battery chemistries that are compatible with aqueous electrolytes. Batteries that use aqueous electrolytes have enhanced safety, ion conductivity, and cost-effectiveness. Yet, a main obstacle to successful aqueous batteries includes their narrow stable voltage window and evolution of hydrogen and oxygen gases that occurs upon the electrolysis of water.

[0015] Neutral and alkaline electrolytes are two major classes of aqueous electrolytes for zinc anodes. Rechargeable zinc anodes in neutral electrolytes such as "water-in-salt" electrolytes and molten hydrate electrolytes have been investigated. Nonetheless, cycling zinc anodes deeply in alkaline electrolytes remains challenging due to the dramatic change of the chemical and physical forms of zinc species and the severe hydrogen evolution side reaction during cycling. Despite the challenges, it is important to enable highly rechargeable zinc anodes in alkaline electrolytes to propel the development of rechargeable Zn-air batteries, as air cathodes kinetically favor alkaline electrolytes over neutral ones.

[0016] Although non-alkaline electrolytes have been investigated for Zn-air batteries, their oxygen reduction reaction (ORR) and their oxygen evolution reaction (OER) kinetics at the air cathode are slow. In alkaline electrolytes, there are two consecutive zinc conversion reactions (Complexation, **Equation (1)** and Anode, **Equation (2)**). This solid-solute-solid mechanism inherently causes passivation and dissolution issues on zinc anodes.

$$ZnO + H_2O + 2OH^- \rightleftharpoons Zn(OH)_4^{2-} \quad \textbf{(1)}$$

$$Zn(OH)_4^{2-} + 2e^- \rightleftharpoons Zn + 4OH^- \quad \textbf{(2)}$$

[0017] These issues are due to the following processes: (i) the insulating discharge product ZnO passivates the surface of zinc anodes, preventing the latter from further discharging or recharging back to metallic zinc, and (ii) the intermediate zincate $Zn(OH)_4^{2-}$ is soluble in alkaline electrolytes, which leads to active material loss, random ZnO precipitation on the electrode, and morphology change of the electrode over cycling.

[0018] In addition, the hydrogen evolution reaction (HER) **Equation (3)** is a side reaction on the zinc anode. In an alkaline electrolyte with pH 14, the Zn/ZnO standard reduction potential (-1.26 V vs the standard hydrogen electrode (SHE)) is lower than that of the HER (-0.83 V vs SHE). Thus, HER is thermodynamically favored during charging, which causes low Coulombic efficiency, electrolyte drying, bubble accumulation, and eventually cell failure.

$$2H_2O + 2e^- \rightleftharpoons H_2 + 2OH^- \quad \textbf{(3)}$$

[0019] A battery-gas chromatography (GC) quantitative analysis method is used herein to identify the influence of HER on the capacity loss of zinc anodes. The cathode and overall reactions are, respectively:

$$2ZiOOH + 2H_2O + 2e^- \rightleftharpoons 2Ni(OH)_2 + 2OH^- \quad \textbf{(4)}$$

$$2ZiOOH + Zn + H_2O \rightleftharpoons 2Ni(OH)_2 + Zn \quad \textbf{(5)}$$

[0020] In consideration of Zn anodes, HER suppressing Zn anodes should possess high Coulombic efficiency (discharge capacity/charge capacity). Thus, the need for ultra-safe, high-energy, and low-cost EES devices has prompted a search for new energy-storage technologies.

[0021] Within the stability window of water, zinc is an attractive anode material because it is the most active metal that is stable with water. Rechargeable Zn-based aqueous batteries have immense potential in large-scale energy storage systems due to their high gravimetric capacity (specific capacity) of 820 milliampere hours per gram (mA•h/g; hereinafter "mAh/g" or similar units) and high volumetric capacity of 5854 milliampere hours per cubic centimeter (mA•h/cm^3; hereinafter "mAh/cm^3", "mAh/mL" or similar units), cost effectiveness, and high chemical stability in air and aqueous solution. Thus, as an anode, Zn has roughly three times the volumetric capacity compared to Li (2062 mAh/cm^3). Without the necessity of flammable organic electrolyte, aqueous Zn-based batteries do not require the comparably complex subsystems required for lithium-based batteries including thermal management, sophisticated electronic controls, and structural protection to manage any catastrophic events.

[0022] By using aqueous electrolyte, zinc-based batteries not only are safer, but also can be manufactured in ambient air rather than dry room, and have much higher tolerance to moisture and air during operation. Having two valence electrons and high density, zinc metal has three times the volumetric capacity of lithium metal. Among various zinc-based batteries, Zn-air has a theoretical volumetric energy density (energy density) of 4400 watt-hour per liter (W•h/L; hereinafter "Wh/L" or similar units), that is more than three times of conventional Li-ion batteries (1400 Wh/L), and approaching Li-S batteries (5200 Wh/L). Primary Zn-air batteries have already been the battery of choice for hearing aids, which require extremely high energy density and safety. Finally, zinc is abundant, low-cost, and environmentally benign, rendering them suitable for large scale applications.

[0023] In contrast to a LIB graphite host anode, which undergoes intercalation and de-intercalation, the zinc anode undergoes dissolution/precipitation, complexation, and

reduction/oxidation repetitive processes during the charge/discharge process in aqueous electrolytes. The overall reactions on the zinc anode are:

[0024] As a result of this dissolution/precipitation cycle, the longstanding constraint that has prevented the implementation of Zn in next-generation batteries for large-scale application is its poor rechargeability due to, among other things, dendrite growth, shape change, and passivation.

[0025] Major challenges for a rechargeable Zn anode for aqueous batteries as a result of the solid-solute-solid mechanism, the insulating nature of discharge product (ZnO), and the water stability window include: (1) ZnO (the soluble and insulating discharge product) passivates the surface of unreacted Zn, which leads to low utilization of active material and a poor rechargeability; (2) ZnO dissolution causes Zn deposition to happen in random locations, which leads to electrode morphology change and dendrite growth after continuous cycling. In a lean electrolyte configuration, the Zn dendrite can penetrate the separator to short-circuit the battery; and (3) H_2 evolution on the Zn anode compromises Coulombic efficiency. Especially in a sealed cell with a limited amount of electrolyte (rather than the often-used beaker cell with saturated ZnO), H_2 evolution dries out the electrolyte, enhances internal pressure of the battery, and gas bubbles block the ionic pathway, which leads to a low Coulombic efficiency ($\approx$ 60%) and even sudden battery failure.

[0026] Zn dendrites are formed during the charging process (i.e., electrodeposition of Zn metal) when $Zn(OH)_4^{2-}$ and/or Zn^{2+} ions are deposited unevenly, with faster growth occurring along energetically favorable crystallographic directions, resulting in internal short circuit. Furthermore, incomplete reduction of zincate ions coupled with non-uniform redistribution of Zn electrode material during the charging process leads to densification of the electrode at specific regions over many charge/discharge cycles, causing loss of usable capacity.

[0027] Aside from dendrite formation and shape change of the Zn electrode, the passivation layer on the bulk zinc anode shortens the cycle life because active Zn is transformed into relatively insulating ZnO, which increases the internal resistance of the Zn electrode. This passivation inhibits the discharge process as the insulating ZnO film on the Zn surface blocks the migration of the discharge products and/or hydroxide ions, causing significant loss of energy efficiency for the charge/discharge cycles. While the passivation mechanism of the Zn anode in alkali electrolytes has been investigated, effective methods for resolving this problem have yet to be proposed.

[0028] Attempts have been made in the past to overcome one or two of the challenges of passivation, dissolution, and HER. For example, a recent attempt has been made to mitigate dendrite formation and shape change of the Zn electrode by altering the Zn electrode design. In one, a 3D-zinc sponge anode was prepared to improve the rechargeability of Zn-based batteries. Although the performance of the zinc battery improved with this design, problems persist: (1) passivation is still present in the 3D-zinc anodes, especially with a high depth of discharge (DOD); (2) the larger electrode-electrolyte contact area accelerates the dissolution of zinc, leading to shape change and capacity fading; and (3) the volume capacity decreases because of the porosity of the zinc sponge and the low depth-of-discharge.

[0029] In another investigation, Zn anodes with a carbon coating were utilized to improve anti-corrosion performance. However, most of these studies could not overcome the dissolution and passivation problems simultaneously. In these studies, although nanoscale, carbon-coated zinc oxide particles were used as anode materials in rechargeable zinc cells, there is considerable room for improvement to mitigate the dissolution problem. An anode composed of micron-sized ZnO spheres was synthesized by a complicated co-precipitation process or ball milling approach, which increased the tap density of the electrode, but the passivation problem still needs to be resolved.

[0030] Also, some zinc battery systems using mild electrolytes, such as $ZnSO_4$-MSO_4 (M = Mn, Co), $Zn(CF_3SO_3)_2$-$Mn(CF_3SO_3)$, and $Zn(TFSI)_2$-LiTFSI, in which expensive TFSI salts should be replaced with salts having lower costs, were developed to mitigate the zinc dendritic growth effectively. Nevertheless, the reversibility of a zinc anode in alkaline electrolyte is a great concern to exploit some highly rechargeable Zn-air batteries with high specific energy density (5200 Wh/kg).

[0031] In terms of battery testing protocols, most previous results of Zn anode performance were obtained using beaker cells rather than closed cells (cylindrical cells or coin cells). In these beaker cells, abundant electrolyte significantly decreased the overall specific capacity of batteries. Also, since electrolyte saturated with ZnO was used in these beaker cells, it is difficult to ascribe the contribution of active material and calculate the performance of batteries due to the inevitable reduction of zin-cate from outsourcing of ZnO in the electrolyte. The performance of these cells cannot reflect real conditions in practical commercial batteries in which the reasonable electrolyte content is a pivotal factor for high volumetric and gravimetric capacity.

[0032] These problematic conventional battery testing protocols raise several problems: (1) the amount of electrolyte exceeds the amount of electrode materials by ≈ 1000 times, which lowers the overall energy density and covers the problem of electrolyte side reactions; (2) the open cell

configuration covers the problem of gas evolution and cell swelling; (3) the electrolyte is usually saturated with ZnO to extend the cycle life. Yet, the capacity from the ZnO dissolved in the electrolyte is 250-fold the active material used (for example, assuming 10 mL of electrolyte and ZnO solubility of approximately 0.256 mol/L measured by inductively coupled plasma), and the mass of dissolved ZnO is not counted when calculating the specific capacity. The true performance of the active material was not evaluated; (4) the utilization of Zn is usually low (< approximately 50%), which extends the cycle life, but lowers the overall energy density.

[0033] As noted, advantages of the Zn-air cell compared to the Li-S cell are that Zn is much more economical than Li and the battery is safer due to absence of flammable organic liquid, making Zn-based batteries attractive candidates for electric vehicles and large-scale energy storage. There has been recent progress on rechargeable Zn anode materials in neutral or mildly acidic conditions that eliminate concerns of ZnO passivating the Zn surface.

[0034] In order for Zn-based aqueous batteries to have higher specific energy than state-of-the-art LIBs, however, an oxygen cathode must be used, which favors alkaline electrolytes (e.g., KOH) to facilitate the ORR and the OER. Although developing efficient ORR and OER electrocatalysts could lower the polarization and improve the round trip energy efficiency of Zn-air batteries, their reversibility is mainly limited by the Zn anode, which has received far less attention.

[0035] From the above, it is evident that improvements in battery technologies are needed. Batteries can be characterized by the specific materials that make up each of the three main components of the anode, cathode and electrolyte. Selection of these components can yield batteries having specific voltage and discharge characteristics that can be optimized for particular applications.

[0036] Although stable cycling of Zn anodes in mild acidic electrolyte has been demonstrated, an alkaline electrolyte is ideal for zinc-air batteries because an oxygen cathode has minimum overpotential in alkaline electrolyte. However, a deeply rechargeable (> 50% DOD) Zn anode in lean alkaline electrolyte (mass ratio of electrolyte to electrode < 100:1) is still lacking due to multiple challenges.

[0037] A particularly rich avenue for increased benefits relates to improvements in rechargeability and specific capacities by limiting passivation and dissolution issues related to the choices of anode, cathode and electrolyte. While Zn vs. Li is discussed above, various chemistries can provide the improvements being sought. An exemplary electrode would include anodic core elements comprising core material, the core material having a passivation interface size and an

intrinsic dissolution rate, and a conformal shell coating on an outer surface of the anodic core elements forming core/shell structures, wherein the anodic core elements comprise a feature size smaller than the core material passivation interface size, and wherein a dissolution rate of the core material from the core/shell structures is less than the intrinsic dissolution rate. Further, the shell should be made of material that has low activity towards the HER of reduction of water to hydrogen as a side reaction.

BRIEF SUMMARY OF THE DISCLOSURE

[0038] In exemplary embodiments of the present invention, core/shell nanoscale structures provide deeply rechargeable anodes, and can overcome intrinsic limitations of other battery materials that involve soluble intermediates or insulating discharge products.

[0039] Starting with a nanomaterial with high-surface area could avoid the passivation layer problem. However, the dissolution problem is more severe. On the other hand, a nonporous coating could prevent ZnO dissolution, but would also block the OH^- transport necessary for the zinc redox reaction to occur. Therefore, simultaneously solving the dilemmas of passivation and dissolution are an answer.

[0040] While specific exemplary embodiments disclose particular metals, coatings, thicknesses, the present invention encompasses a myriad of core material/coatings that with optimization of the core and shell materials, from aspects of pore size, porosity, and surface charge, leads to various improvements of anode performance and stability. Many materials with controlled ion-sieving and HER suppressing properties are contemplated herein. The design principles can be applied to other morphologies (e.g. particles) of starting materials for large scale production. The mechanistic understanding and design principles cover many types of rechargeable high-energy aqueous batteries.

[0041] The concept of separating ions and molecules by size using selective membranes is known. A variety of materials such as graphene, graphene oxide, polymer, and metal carbide membranes with a controllable pore size and permeability have been demonstrated to have ion-sieving capabilities in various applications. Applying the ion-sieving concept to Zn anode, to confine larger zincate ions and allow smaller hydroxide ions to permeate, can limit/prevent ZnO dissolution and electrode shape change.

[0042] In an exemplary embodiment of the present invention, an electrode comprises anodic core elements comprising a core material of zinc, the core material having a core material passivation

interface size of approximately 2 μm, a core material intrinsic dissolution rate, and a core material hydrogen evolution reaction (HER) rate.

[0043] The electrode further comprises a conformal shell coating of TiO_2 on an outer surface of the anodic core elements, thus forming ZnO@TiO_2 core/shell structures. The electrode can be a sub-micron zinc anode sealed with an ion-sieving coating that suppresses hydrogen evolution reaction. ZnO nanorods are coated with TiO_2, which overcomes passivation, dissolution, and hydrogen evolution issues simultaneously. It achieves superior reversible deep cycling performance with a high discharge capacity of approximately 616 mAh/g and Coulombic efficiency of approximately 93.5% when cycled with 100% depth of discharge at lean electrolyte. It can also deeply cycle ~ 350 times in a beaker cell.

[0044] In an exemplary embodiment, the electrode further comprises a conformal shell coating of TiN_xO_y on an outer surface of the anodic core elements, thus forming ZnO@TiN_xO_y core/shell structures. The anodic core elements are nanoscale, so as to comprise a feature size smaller than the zinc passivation interface size. The anodic core elements can be nanorods with a diameter of less than approximately 2 μm, and more preferably less than approximately 500 nm.

[0045] The dissolution rate of zinc from the core/shell structures is less than the Zn intrinsic dissolution rate, as the relatively thin (having a thickness of less than approximately 10 nm) and conformal TiN_xO_y coating mitigates Zn dissolution in an alkaline electrolyte.

[0046] The ZnO@TiN_xO_y core/shell nanorod structures provide a deeply rechargeable Zn anode. The small diameter of ZnO limits to fully prevents passivation, and allows near to full utilization of active materials, while the relatively thin and conformal TiN_xO_y coating not only mitigates the Zn dissolution, but also mechanically maintains the morphology of the nanostructures, and delivers electrons to the nanorods. As a result, the ZnO@TiN_xO_y core/shell nanorod anode achieves superior specific capacity and cycle life compared with bulk Zn foil and uncoated ZnO nanorod anodes.

[0047] The discharge capacity of the ZnO@TiN_xO_y core/shell nanorod anode is approximately twice as large as that of an uncoated ZnO nanorod anode. It was surprisingly found that the ZnO@TiN_xO_y nanorod anode achieves a much higher specific discharge capacity of approximately 508 mAh/g than that of conventional zinc anodes. Further, it can deeply cycle greater than approximately 640 times (over 64 days) in a beaker cell, and can deliver excellent long-term electrochemical performance (more than approximately 7500 cycles) when cycled under start-stop conditions.

[0048] In another exemplary embodiment of the present invention, an electrode comprises anodic core primary elements comprising a core material of zinc, the core material having a core material passivation interface size of approximately 2 μm, a core material intrinsic dissolution rate, and a core material HER rate.

[0049] The electrode further comprises a conformal shell coating of carbon on an outer surface of the anodic core primary elements, thus forming ZnO@C core/shell structures. The anodic core primary elements are nanoscale, so as to comprise a feature size smaller than the zinc passivation interface size. The anodic core primary elements can be particles with a diameter of less than approximately 2 μm, and more preferably are nanoparticles (NPs) with a diameter of less than approximately 100 nm.

[0050] The dissolution rate of zinc from the core/shell structures is less than the Zn intrinsic dissolution rate, as the relatively thin (having a thickness of less than approximately 15 nm) and conformal amorphous, microporous, and conductive carbon coating mitigates Zn dissolution in an alkaline electrolyte.

[0051] An assembly (secondary cluster) of these core/shell structures form Zn-pome microspheres (pomegranate-like nanoporous carbon-coated ZnO clusters). Each secondary cluster/Zn-pome microsphere can be approximately 6 mm in size and comprise on the order of approximately 10^5 ZnO NPs individually encapsulated by an amorphous, microporous, and conductive carbon shell that slows down the dissolution of zincate intermediate species during cycling. The shell further suppresses zinc dissolution by decreasing the electrode-electrolyte contact area.

[0052] The nanoscale, pomegranate-structured Zn anode can be fabricated via a bottom-up microemulsion approach. As disclosed, the in the Zn-pome, primary ZnO NPs assemble into secondary clusters after which they are individually encapsulated by a conductive, microporous carbon framework. The small size of ZnO NPs overcomes the problematic issue of passivation, whereas the secondary structure and ion-sieving carbon shell mitigates the dissolution problem.

[0053] Inductively coupled plasma (ICP) analysis confirms that Zn dissolution from the Zn-pome anode is effectively suppressed, leading to a considerably prolonged cycle life compared to that of a conventional ZnO anode in an alkaline aqueous electrolyte. The Zn-pome anode maintains its capacity after long resting. This performance is achieved in harsh yet practical conditions: a limited amount of electrolyte, sealed coin cells, and approximately 100% DOD.

[0054] In another exemplary embodiment of the present invention, an electrode comprises anodic core primary elements comprising a core material of zinc, the core material having a core material

passivation interface size of approximately 2 μm, a core material intrinsic dissolution rate, and a core material HER rate.

[0055] The electrode further comprises a conformal shell coating of an ion-sieving carbon on an outer surface of the anodic core elements, thus forming ZnO@C core/shell structures. The anodic core primary elements are nanoscale, so as to comprise a feature size smaller than the zinc passivation interface size. The anodic core primary elements can be particles with a diameter of less than approximately 2 μm, and more preferably are nanoparticles (NPs) with a diameter of less than approximately 100 nm.

[0056] The dissolution rate of zinc from the core/shell structures is less than the Zn intrinsic dissolution rate, as the relatively thin (having a thickness of less than approximately 30 nm) and conformal ion-sieving carbon coating mitigates Zn dissolution in an alkaline electrolyte.

[0057] The ion-sieving carbon nanoshell coated ZnO nanoparticle anode can be synthesized in a scalable way with controllable shell thickness. The nanosized ZnO prevents passivation, while the microporous carbon shell slows down Zn species dissolution. Under extremely harsh testing conditions (closed cell, lean electrolyte, no ZnO saturation), this Zn anode shows significantly improved performance compared to Zn foil and bare ZnO nanoparticles. The ion-sieving nanoshell can be beneficial to other electrodes such as sulfur cathode for Li-S batteries.

[0058] In another exemplary embodiment of the present invention, an electrode comprises anodic core elements comprising core material, the core material having a core material passivation interface size, a core material intrinsic dissolution rate, and a core material hydrogen evolution reaction (HER) rate, a conformal shell coating on an outer surface of the anodic core elements forming core/shell structures, wherein the anodic core elements comprise a feature size smaller than the core material passivation interface size, wherein a dissolution rate of the core material from the core/shell structures is less than the core material intrinsic dissolution rate; and wherein the HER rate of the shell is less than the core material HER rate.

[0059] The electrode can be deeply rechargeable.

[0060] The electrode can have a DOD of greater than 50%.

[0061] The core material can be selected from the group comprising a metal, metal oxide, metal sulfide, and combinations thereof.

[0062] The core material can be selected from the group comprising Zn, Li, Na, Mg, Ca, ZnO, Li_2O, Na_2O, MgO, CaO, ZnS, Li_2S, Na_2S, MgS, CaS, and combinations thereof.

[0063] The conformal shell coating can comprise a cermet. The conformal shell coating can comprise carbon.

[0064] The core/shell structures can have a specific discharge capacity of at least 70% of the theoretical limit of the specific discharge capacity of the core material.

[0065] The electrode can have a coulombic efficiency greater than about 93.5%.

[0066] The anodic core/shell structures can be formed by a deposition technique of layers of the conformal shell coating over a deposition cycling series, and wherein a morphology of the anodic core elements prior to the deposition cycling series is substantially the same as a morphology of the core/shell structures after the deposition cycling series.

[0067] The anodic core/shell structures can be formed by an atomic layer deposition (ALD) technique of layers of the conformal shell coating over an ALD cycling series, and wherein a morphology of the anodic core elements prior to the ALD cycling series is substantially the same as a morphology of the core/shell structures after the ALD cycling series.

[0068] In another exemplary embodiment of the present invention, the anodic core elements are nanorod structures, the core material comprises ZnO, and the conformal shell coating comprises TiN_xO_y.

[0069] The diameter of the nanorods can be less than approximately 2 μm. The diameter of the nanorods can be less than approximately 500 nm.

[0070] The conformal shell coating can have a thickness of less than 10 nm. The conformal shell coating can have a thickness of less than approximately 6 nm.

[0071] In another exemplary embodiment of the present invention, the anodic core elements are nanoparticles, the core material comprises ZnO, and the conformal shell coating comprises carbon.

[0072] The conformal shell coating can comprise an amorphous, microporous, and conductive carbon.

[0073] An assembly of core/shell structures can form Zn-pome microspheres (pomegranate-like nanoporous carbon-coated ZnO clusters). Each Zn-pome microsphere can have a diameter of

approximately 6 μm. Each Zn-pome microsphere can comprise on the order of approximately 10^5 core/shell structures.

[0074] The diameter of the nanoparticles can be less than approximately 2 μm. The diameter of the nanoparticles can be less than approximately 100 nm.

[0075] The conformal shell coating can have a thickness of less than 15 nm. The conformal shell coating can have a thickness of less than approximately 10 nm.

[0076] In another exemplary embodiment of the present invention, the anodic core elements are nanoparticles, the core material comprises ZnO, and the conformal shell coating comprises an ion-sieving carbon shell.

[0077] In another exemplary embodiment of the present invention, a rechargeable battery system comprises anodic core/shell structures comprising a ZnO core coated with a shell layer of TiN_xO_y, an aqueous electrolyte, and a cathode.

[0078] In another exemplary embodiment of the present invention, a rechargeable battery system comprises anodic Zn-pome microspheres each comprising a pomegranate-like assembly of individual ZnO nanoparticles coated with a shell layer of carbon, an aqueous electrolyte, and a cathode.

[0079] In another exemplary embodiment of the present invention, a rechargeable battery system comprises anodic core/shell nanoparticles comprising a ZnO core coated with a shell layer of ion-sieving carbon, an aqueous electrolyte, and a cathode.

[0080] In each of the rechargeable battery systems, the rechargeable battery system can be deeply rechargeable.

[0081] In each of the rechargeable battery systems, the rechargeable battery system can have a DOD of greater than 50%.

[0082] In each of the rechargeable battery systems, the cathode can comprise $Ni(OH)_2$.

[0083] In each of the rechargeable battery systems, the anodic core/shell structures can be formed by a deposition technique of the conformal shell on the core over a deposition cycling series, and wherein a morphology of the core prior to the deposition cycling series can remain substantially the same as the morphology of the core/shell structures after the deposition cycling series.

[0084] These and other objects, features and advantages of the present disclosure will become more apparent upon reading the following specification in conjunction with the accompanying description, claims and drawings.

BRIEF DESCRIPTION OF THE DRAWINGS

[0085] The accompanying Figures, which are incorporated in and constitute a part of this specification, illustrate several aspects described below.

[0086] FIG. 1 is illustrative of typical issues of Zn anode in alkaline electrolyte and design of a high-performance Zn anode by overcoming the issues, and includes schematic diagrams of passivation (**FIG. 1A**) and dissolution (**FIG. 1B**) issues of zinc anodes. **FIG. 1C** is a schematic diagram of the battery-GC quantitative analysis method developed to quantitatively identify the influence of HER on Coulombic efficiency of zinc anodes by measuring the H_2 evolved in the reactor after charging/discharging the zinc anode for 1 cycle. **FIG. 1D** illustrates the distribution of the charged capacity on the zinc anode in a Zn-Ni battery. The capacity loss on the Zn anode is almost fully caused by HER. Thus, HER suppressing zinc anodes should possess high Coulombic efficiency.

[0087] FIGS. 2A-C present a schematic diagram (**FIG. 2A**), experiment setup (**FIG. 2B**), and reactor design (**FIG. 2C**) of the battery-GC quantitative analysis method used to quantitatively identify the influence of HER on Coulombic efficiency of zinc anodes. PRR: pressure reducing regulator; MFC: mass flow controller; and GC: gas chromatography.

[0088] FIGS. 3A-B include a graph (**FIG. 3A**) and schematic diagram (**FIG. 3B**) of electrode reactions happening during charging for the Zn-Ni battery system of **FIGS. 1C** and **2A-C**.

[0089] FIG. 4 is a schematic illustration of the presently inventive HER suppressing sealed nanorod (HSSN) zinc anode design principle: sealed sub-micron-sized anodes with an HER suppressing ion-sieving coating to overcome passivation, dissolution, and hydrogen evolution issues simultaneously in alkaline electrolytes.

[0090] FIGS. 5A-C illustrate the fabrication of an HSSN anode. Schematic diagrams and scanning electron microscopy (SEM) images of carbon paper (**FIG. 5A**), ZnO nanorod anode (**FIG. 5B**), and HSSN anode (**FIG. 5C**).

[0091] FIGS. 6A-C are SEM images of an uncoated ZnO nanorod anode with a mass loading of ZnO nanorods ranging from 0.5 mg/cm^2 to 5.5 mg/cm^2.

[0092] FIG. 7A is a schematic diagram of TiO_2 coating process. **FIGS. 7B-C** are SEM images of ZnO nanorods before (**FIG. 7B**) and after TiO_2 coating (**FIG. 7C**). **FIG. 7D** is a SEM image and elemental mappings of the present HSSN anode.

[0093] FIGS. 8-11 are a characterization of a single ZnO@TiO_2 nanorod collected from the present HSSN anode. **FIGS. 8A-8C** include a scanning transmission electron microscopy (STEM) image and elemental mappings of a ZnO@TiO_2 nanorod.

[0094] FIGS. 9A-B shows spatial distributions of Zn and Ti elements and energy-dispersive X-ray (EDX) spectroscopies in the core and shell regions.

[0095] FIG. 10 is a transmission electron microscopy (TEM) diffraction image of a ZnO@TiO_2 nanorod, showing the diffraction pattern of hexagonal ZnO. A [002]; B [110]; C [112].

[0096] FIG. 11 is a TEM image of a ZnO@TiO_2 nanorod, showing the thickness (~ 30 nm) of a TiO_2 coating.

[0097] FIGS. 12A-C are varying magnitude SEM images of the present HSSN anode after etching ZnO away.

[0098] FIG. 13 presents ICP results showing dissolved Zn concentration after soaking the present HSSN and uncoated ZnO anodes in 4M KOH solution. 90% ZnO dissolution is suppressed in the HSSN anode, which means that the TiO_2 coating effectively blocks zincate ions.

[0099] FIGS. 14A-B are varying magnitude SEM images and elemental mappings of the uncoated ZnO (**FIG. 14A**) and HSSN (**FIG. 14B**) anodes after soaking in 4M KOH solution. The reservation of Zn in the HSSN anode supports the assumption that a TiO_2 coating can effectively block zincate ions.

[00100] FIG. 15 is a graph of X-ray diffraction (XRD) patterns of uncoated ZnO and HSSN anodes before and after charging. The weak ZnO peaks of the HSSN anode after charging is from residual unreacted ZnO.

[00101] FIGS. 16-17 are SEM images before and after charging of an uncoated ZnO anode (**FIG. 16**) and HSSN anode (**FIG. 17**).

[00102] FIGS. 18-19 are SEM images of an uncoated ZnO nanorod anode (**FIG. 18**) and HSSN anode (**FIG. 19**) after five galvanostatic cycles with 25 μL electrolyte. They were cycled

at ~ 0.25 mA/cm^2 for 2 hours of charge and ~ 0.25 mA/cm^2 discharge to 1.5V. The mass loadings of ZnO nanorods on both anodes are ~ 3.3 mg/cm^2.

[00103] **FIG. 20** is a STEM image of a ZnO@TiO_2 nanorod after charging.

[00104] **FIG. 21** is a STEM image and elemental mappings of a ZnO@TiO_2 nanorod after charging. The same anode sample was used in **FIGS. 17** and **20-21**.

[00105] **FIG. 22** is a SEM image and elemental mappings of the present HSSN anode after charge.

[00106] **FIGS. 23A-B** are graphs illustrating the Brunauer-Emmett-Teller (BET) pore width distribution (**FIG. 23A**) and surface areas (**FIG. 23B**) of uncoated ZnO and HSSN anodes. After TiO_2 coating, nanopores are measured which indicates that TiO_2 coating is nanoporous.

[00107] **FIG. 24** is an X-ray photoelectron spectroscopy (XPS) survey of the ZnO@TiN_xO_y anode. The atomic ratio of O to N is ~ 6.66 in the TiN_xO_y coating.

[00108] **FIG. 25** is a schematic diagram of a three-electrode cell in 4M KOH electrolyte with a TiO_2 or TiN_xO_y electrode as the working electrode, an Hg/HgO electrode as the reference electrode, and Pt foil as the counter electrode.

[00109] **FIG. 26** is a schematic of TiN ALD recipe.

[00110] **FIG. 27** shows IR-corrected polarization curves of TiN_xO_y and TiO_2 electrodes. At any fixed potential, the hydrogen evolution on TiN_xO_y electrode is severer than TiO_2 electrode. Scan rate: 2 mV/s.

[00111] **FIG. 28** shows IR-corrected polarization curves of a CP substrate, and TiN_xO_y and TiO_2 electrodes. HER can be suppressed with the existence of TiO_2. CP: carbon paper. Scan rate: 2 mV/s.

[00112] **FIG. 29A** is an XPS survey spectra of the TiO_2 coating. **FIG. 29B** is an XPS survey spectra of the TiN_xO_y coating. **FIG. 29C** is a table that shows sheet resistance and resistivity of TiN_xO_y and TiO_2 coatings measured using a four-point probe system.

[00113] **FIG. 30A** shows basic models of TiO_2, TiN_xO_y-1 and TiN_xO_y-2 clusters, and **FIG. 30B** an adsorption free energy diagram of each cluster.

[00114] **FIG. 31A** shows basic models of TiO_2, TiN_xO_y-3 and TiN_xO_y-4 clusters, and **FIG. 31B** an adsorption free energy diagram of each cluster.

[00115] **FIG. 32** is a table of a summary of simulated energy of clusters (M) and H-adsorbed clusters (M-H), binding energy, and free energy. Atoms in clusters: smallest "atom", N; larger, H; larger still, Ti; and largest, O.

[00116] **FIG. 33** illustrates ICP results showing dissolved Zn concentration after soaking the uncoated ZnO, HSSN and ZnO@TiN_xO_y anodes in 4M KOH solution. 90% ZnO dissolution is suppressed in the HSSN and ZnO@TiN_xO_y anodes. This shows HSSN and ZnO@TiN_xO_y anodes have very similar ion-sieving capability.

[00117] **FIG. 34** contains SEM images and elemental mappings of the ZnO@TiN_xO_y anode after soaking in 4M KOH solution. The reservation of Zn in the ZnO@TiN_xO_y anode supports that TiN_xO_y coating can effectively block zincate ions.

[00118] **FIG. 35A** shows cell components of a pouch cell, and **FIG. 35B** the assembled pouch cell. The separator has a 1.5 cm diameter. The anode has a 1 cm diameter.

[00119] **FIG. 36** illustrates voltage profiles of Zn-Ni batteries with HSSN and ZnO@TiN_xO_y as anodes. The Coulombic efficiency of the present HSSN anode is higher with better HER suppressing capability.

[00120] **FIG. 37A** shows cycling performance of the ZnO@TiN_xO_y and HSSN anodes in lean electrolyte at 100% DOD. **FIG. 37B** shows cycling performance of the HSSN and ZnO@TiN_xO_y anodes at various C rates. State of charge: 20%.

[00121] **FIGS. 38A-B** are graphs illustrating BET pore width distribution (**FIG. 38A**) and surface areas (**FIG. 38B**) of HSSN and ZnO@TiN_xO_y anodes.

[00122] **FIG. 39** is a table showing a comparison of Coulombic efficiency of the present HSSN anode with conventional zinc-based anodes (100% DOD) in alkaline electrolytes.

[00123] **FIG. 40** shows cycling performance of the present HSSN anode in a lean electrolyte at 40% DOD

[00124] **FIG. 41** illustrates charge-discharge profiles of the present HSSN anode in a lean electrolyte at 40% DOD.

[00125] **FIG. 42** are CV curves of CP-TiO_2 and HSSN electrodes. There is no capacity contribution from TiO_2 during the electrochemical reaction. Scan rate: 10 mV/s.

[00126] **FIG. 43** are optic microscope images of the HSSN anode before and after battery failure.

[00127] **FIG. 44** shows cycling performance of the present HSSN anode in a beaker cell with a large amount of electrolyte at 100% DOD.

[00128] **FIGS. 45A-B** are voltage profiles (from cycle 50^{th} to 70^{th}) of the HSSN anode cycled in a lean electrolyte at 40% DOD (**FIG. 45A**) and a beaker cell with a large amount of electrolyte at 100% DOD (**FIG. 45B**).

[00129] **FIG. 46** is a table comparing the present HSSN anode with conventional zinc-based anodes in aspects of electrolyte-to-discharge-capacity (E/DC) ratio and Coulombic efficiency in alkaline electrolyte. The DOD of Anode No. 0 is 40%. The DOD of the remaining Anode Nos. 1-22 are 100%.

[00130] **FIG. 47** illustrates via graph a comparison of the HSSN anode and conventional anodes (with 100% DOD) in aspects of E/DC ratio and Coulombic efficiency.

[00131] **FIG. 48** is another schematic similar to **FIG. 1A** of morphological changes of zinc electrode during electrochemical cycling, where Zn foil of the prior art shows very low utilization (< 1%) because of the ZnO passivation layer. The critical passivation size is ~ 2 μm, as shown above the foil.

[00132] **FIG. 49** is a graph of 1 cycle discharge and charge test for Zn foil under 10 mA, showing that Zn foil can only deliver ~ 1.7 mAh capacity (1% utilization) and charge capacity is only $1/5^{th}$ of discharge capacity.

[00133] **FIG. 50** is an SEM image of ZnO passivation layer on Zn mesh (Dexmet), formed by discharging Zn mesh under 1 mA with a 10 μL electrolyte. The separator used was Celgard 3501.

[00134] **FIG. 51** is a schematic of morphological changes of zinc electrode during electrochemical cycling, where the feature size of an uncoated ZnO nanorod of the prior art is smaller than the critical passivation size, however, the large electrode-electrolyte surface area accelerates anode dissolution and promotes electrode shape change.

[00135] **FIG. 52** is a schematic of morphological changes of zinc electrode during electrochemical cycling, where the shape of the present ZnO@TiN_xO_y nanorod anode retains during cycling with the inventive sealed nanorod structure.

[00136] **FIG. 53** is a schematic of a TiN ALD recipe.

[00137] **FIGS. 54A-54C** are pictures of a beaker cell (**FIG. 54A**), a coin cell (**FIG. 54B**) and scalability of Zn-Ni single coin cell (**FIG. 54C**). Top and bottom cases have an approximate 2 cm diameter. The separator has an approximate 1.5 cm diameter. The working electrode (WE) has an approximate 1 cm diameter.

[00138] **FIG. 55** is an optical picture of a pouch cell.

[00139] **FIG. 56** is a schematic of the fabrication process for the present ZnO@TiN_xO_y core/shell nanorod anode.

[00140] **FIG. 57** is a low magnification SEM image of a ZnO nanorod anode.

[00141] **FIGS. 58A-58C** are high magnification SEM images of three ZnO nanorod anodes with different mass loadings.

[00142] **FIG. 59** is an SEM image of a ZnO@TiN_xO_y nanorod anode.

[00143] **FIG. 60** is a TEM image of a ZnO@TiN_xO_y nanorod.

[00144] **FIG. 61** is a high resolution transmission electron microscopy (HRTEM) image of a ZnO@100TiN_xO_y nanorod, showing the thickness (~ 6.1 nm) of the TiN_xO_y coating.

[00145] **FIG. 62** is an HRTEM image of a ZnO@TiN_xO_y nanorod, showing the lattice of ZnO, [002], d ≈ 0.26 nm.

[00146] **FIG. 63** is an electron diffraction pattern of a ZnO@TiN_xO_y nanorod, showing the diffraction pattern of ZnO. A [002]; B [200]; C [202].

[00147] **FIG. 64** is an SEM image and elemental mapping of ZnO@TiN_xO_y nanorods.

[00148] **FIGS. 65-67** are graphs of an XPS survey of ZnO nanorod and ZnO@TiN_xO_y nanorod anodes (**FIG. 65**); a high-resolution XPS spectra of Zn 2p peaks (**FIG. 66**); and a high-resolution XPS spectra of Ti 2p peaks (**FIG. 67**). The samples shown in **FIGS. 59-67** are all deposited by ALD for 100 cycles.

[00149] **FIGS. 68-69** are XPS survey spectra (**FIG. 68**) and high-resolution Zn 2p and Ti 2p spectra (**FIG. 69**) of a ZnO@TiN_xO_y nanorod anode with 200 cycles ALD.

[00150] **FIG. 70** illustrates ICP results and an image (inset) showing dissolved Zn concentration after soaking the ZnO@TiN_xO_y and uncoated ZnO anodes in 4M KOH solution.

[00151] **FIGS. 71-72** are SEM images of an uncoated ZnO nanorod anode (**FIG. 71**) and a ZnO@TiN_xO_y nanorod anode (**FIG. 72**) before and after a 2 hour charge with a 25 μL electrolyte.

[00152] **FIG. 74** are SEM images of approximately 0.5 mg/cm^2 ZnO@TiN_xO_y nanorod anode with 200 cycles ALD after a 1 hour constant current charge at 1C rate with a 25 μL electrolyte. Tin was used as anode current collector.

[00153] **FIG. 74** is an SEM image and elemental mapping of a ZnO@TiN_xO_y nanorod anode after a 2 hour charge.

[00154] **FIG. 75** is an TEM image of a ZnO@TiN_xO_y nanorod anode after 2 hour charge. **FIGS. 72** and **74-75** are from the same anode sample with 100 cycles ALD.

[00155] **FIG. 76** are XRD results of a ZnO nanorod and a ZnO@TiN_xO_y nanorod anode before and after charge. The weak ZnO peaks of ZnO@TiN_xO_y nanorod anode with 200 cycles ALD after charge is from residual unreacted ZnO. Tin foils were used as anode current collectors.

[00156] **FIG. 77** is an electrochemical impedance spectroscopy (EIS) result and equivalent circuit of an uncoated ZnO anode and a ZnO@TiN_xO_y nanorod anode. Z_w: Warburg impedance; R_{ct}: charge-transfer resistance; CPE: double layer capacity; R_c: total ohmic resistance.

[00157] **FIGS. 78-80** are SEM images of a pristine ZnO@TiN_xO_y nanorod anode with 200 cycles ALD (**FIG. 78**), after a 3 hour constant current charge at 0.33C with a 25 μL electrolyte (**FIG. 79**), and after further constant current discharge at 0.33C (0.7 hours) to 1.5 V with a 25 μL electrolyte (**FIG. 80**). All SEM images are from same sample with a mass density of ~ 1.7 mg/cm^2. This result indicates that there is almost no shape change during the charge and discharge step.

[00158] **FIGS. 81-82** are SEM images of a pristine uncoated ZnO nanorod anode (**FIG. 81**), and after a 3 hour constant current charge at 0.33C with a 25 μL electrolyte (**FIG. 82**). All SEM images are from same sample with a mass density of ~ 1.7 mg/cm^2. Some nanorods were detached from the beginning as shown in **FIG. 81**, due to external mechanical force during transfer. After charge, most ZnO nanorods grown on the top layer of carbon fibers detached. Because of the small

amount of electrolyte, the ZnO nanorods grown on the inner carbon fibers were not in contact with electrolyte in the first charge, and remained.

[00159] **FIG. 83** is a schematic diagram of beaker cell and coin cell.

[00160] **FIG. 84** shows cycling performance of pure current collector in the beaker cell and coin cell. Real: count all the zinc in the electrolyte. Pseudo: calculation without counting zinc in the electrolyte. One dot every four data points.

[00161] **FIG. 85** illustrates discharge capacity for the first 32 galvanostatic cycles of an uncoated ZnO nanorod and the ZnO@TiN_xO_y nanorod anodes with ~ 2.1 mg/cm^2 at 0.5C rate in a coin cell with ZnO-free electrolyte. 50 μL electrolyte was dropped onto a separator and 10 μL electrolyte was dropped onto cathode. Inset: optical image of a coin cell.

[00162] **FIG. 86** is a graph of the charge voltage profiles of the ZnO and ZnO@TiN_xO_y anodes.

[00163] **FIG. 86** illustrates discharge capacity retention of uncoated ZnO nanorod and ZnO@TiN_xO_y nanorod anodes with ~ 1.5 mg/cm^2 at 0.25C rate in coin cells. 25 μL electrolyte was dropped onto separator. The cut-off voltages are approximately ~ 1.5/1.9V. The maximum discharge capacity (corresponding to approximately 100%) of uncoated ZnO nanorod and ZnO@TiN_xO_y nanorod anodes are approximately 235.2 mAh/g and approximately 153.5 mAh/g, respectively.

[00164] **FIG. 88** shows cycling performance of ~ 1.1 mg/cm^2 ZnO@TiN_xO_y nanorod anodes in pouch cells with ZnO saturated and ZnO-free electrolytes, respectively. They were cycled at 1C for charge and 5C for discharge with approximately 1.4/2V cut-off voltages.

[00165] **FIG. 89** is a comparison of specific discharge capacity between the present anode and previously reported anodes. Zinc in the electrode and electrolyte are both counted.

[00166] **FIG. 90** shows cycling performance of the ZnO@TiN_xO_y nanorod anode (~ 2 mg/cm^2) with 200 cycles with ALD at 0.5C charge and 2C discharge rates in beaker cell with 10 mL ZnO saturated 4M KOH electrolyte. The cut-off voltages are approximately 1.4/2 V. One dot every five data points.

[00167] **FIG. 91** is a cyclic voltammogram (CV) for ZnO@TiN_xO_y anode in a coin cell at approximately 0.1 mV/s scan rate. The CV was done using two electrodes with ZnO@TiN_xO_y anode and $Ni(OH)_2$ cathode in ZnO free electrolyte.

[00168] **FIGS. 92-93** are CVs for $ZnO@TiN_xO_y$ anodes in a pouch cell (**FIG. 92**) and beaker cell (**FIG. 93**) at an approximately 0.1 mV/s scan rate. The CV for the anode in pouch cell was done using two electrodes with $ZnO@TiN_xO_y$ anode and $Ni(OH)_2$ cathode in ZnO saturated electrolyte. The CV for the anode in beaker cell was done using three electrodes with $ZnO@TiN_xO_y$ anode, Hg/HgO reference electrode and graphite counter electrode in ZnO saturated 4M KOH electrolyte.

[00169] **FIG. 94** is a current density profile as cycled under start-stop conditions in coin cells.

[00170] **FIG. 95** shows long-term discharge capacity retention of Zn foil and a $ZnO@TiN_xO_y$ nanorod anode as cycled under start-stop conditions with 100 μL electrolyte. The Zn foil with approximately 0.02% DOD and the $ZnO@TiN_xO_y$ nanorod anode with approximately 1% DOD were cycled at the same current density, which is shown in **FIG. 94**. Tin foils were used as anode current collectors. Cells were cycled between approximately 0 and 2 V.

[00171] **FIG. 96** are voltage profiles of a $ZnO@TiN_xO_y$ nanorod anode of the 2000^{th} and 4000^{th} cycles under start-stop conditions.

[00172] **FIGS. 97-98** are photos of cells, with a $ZnO@TiN_xO_y$ nanorod anode (**FIG. 97**) and Zn foil (**FIG. 98**) as anode respectively, after long-term start-stop conditions at the same current density (shown in **FIG. 94**).

[00173] **FIG. 99** shows the discharge capacity of a $ZnO@TiN_xO_y$ nanorod anode under rate test conditions, showing electrochemical stability at different rate after several activation cycles.

[00174] **FIG. 100A** illustrates ZnO NPs with fast dissolution rate in alkaline aqueous solution; (**FIG 100B**) illustrates ZnO NPs coated with carbon; (**FIG. 100C**) illustrates the present Zn-pomegranate in which carbon filled into the free space of ZnO clusters plays an important role in ion sieving, conductivity, and structure stabilization of the electrode; and (**FIG. 100D**) shows the calculated surface area in contact with electrolyte and the number of primary nanoparticles in one Zn pomegranate cluster versus its diameter. The smaller the surface contact with the electrolyte, the lower the capacity fading.

[00175] **FIG. 101** is a cross-sectional SEM image of Zn mesh with a ZnO passivation layer formed on it after discharging the Zn mesh under 1 mA with a 100 μL electrolyte comprising 2M KF, 2M K_2CO_3 and 4M KOH. The passivation layer is approximately 2 μm.

[00176] **FIG. 102** illustrates the synthesis of a Zn-pome. **FIG. 102A** shows the Zn-pome were prepared by a bottom-up microemulsion approach. **FIG. 102B** is a picture of ZnO NPs. **FIG. 102C** is a picture and **FIG. 102F** is a SEM image of ZnO clusters collected from centrifugation at approximately 1500 rpm for 5 minutes. The size is not uniform. **FIG. 102D** is a picture and **FIG. 102G** is a SEM image of ZnO clusters obtained by first centrifuging at 400 rpm for 1 minute to remove large clusters, and then centrifuging at approximately 1500 rpm for 5 minutes. **FIG. 102E** is a picture and **FIG. 102H** is a SEM image of Zn-pome synthesized using Zn clusters shown in **FIGS. 102D** and **102G**.

[00177] **FIGS. 103A-C** are SEM images of clusters of ZnO nanoparticles assembled via a microemulsion approach. **FIGS. 103D-F** are SEM images of Zn-pome (nano-porous carbon-coated ZnO cluster). **FIG. 103G** is a TEM image of Zn-pome. **FIG. 103H** is a TEM image of the carbon framework of Zn-pome after etching away ZnO in 1M HCl for 24 hours. **FIG. 103I** is a cross-sectional SEM image of one Zn-pome microparticle obtained by focused ion beam (FIB) analysis.

[00178] **FIG. 104A** is a TEM image of a Zn-pome. **FIG. 104B** is a schematic of etching ZnO. **FIGS. 104C-F** are TEM images of the Zn-pome after etching away ZnO in 1M HCl.

[00179] **FIGS. 105-106** are FIB milling of Zn-pome. **FIG. 105** is a top-view image of Zn-pome after FIB milling. **FIG. 106** is a cross-section image of Zn-pome after FIB milling.

[00180] **FIG. 107A** illustrates XRD patterns and **FIG. 107B** XPS spectra of ZnO NPs, ZnO@C NPs and Zn-pome. **FIG. 107C** is a high-resolution XPS spectra of ZnO NPs and Zn-pome. **FIG. 107D** is a TGA weight loss curve and **FIG. 107E** is a BET pore size distribution of Zn-pome. **FIG. 107F** shows dissolved and undissolved portions of zinc in 4M KOH electrolyte for ZnO NPs, ZnO@C NPs and Zn-pome; embedded pictures show the electron microscopy images of ZnO NPs, ZnO@C NPs and Zn-pome.

[00181] **FIG. 108** includes a picture of CR2032 coin cell cases (left) and a schematic of coin cell components and their arrangement used (right).

[00182] **FIG. 109A** is a graph of specific capacity of ZnO NPs and Zn-pome. **FIG. 109B** is voltage profiles of Zn-pome/$Ni(OH)_2$. **FIG. 109C** is a graph of specific capacity of ZnO NPs/$Ni(OH)_2$ and Zn-pome/$Ni(OH)_2$ at a 5C discharge rate. **FIG. 109D** illustrates testing of self-discharge of Zn-pome cell cycling at 0.5C for one cycle, resting for 24 hours, then cycling at 1C. **FIG. 109E** is a SEM image of Zn-pome anode before cycling (**FIGS. 109F** and **G**) and after two cycles.

[00183] **FIG. 110A** is a graph of specific capacity of Zn-pome, ZnO NPs@C and ZnO NPs. **FIG. 110B** shows additional battery cycling data of bare ZnO and Zn-pome anodes (1C rate).

[00184] **FIG. 111** illustrates the performance of bare ZnO and Zn-pome anodes at 5C discharge rate.

[00185] **FIG. 112** presents the cycle performance of bare ZnO and Zn-pome anodes (charged at 1C, discharged at 5C), after resting for 24 hours followed by the first cycle at 0.5C.

[00186] **FIGS. 113A-F** are SEM images of Zn-pome anode after cycling at 1C. **FIGS. 113A-D** after cycling 10 cycles. **FIGS. 113E-L** after cycling 20 cycles.

[00187] **FIG. 114A** is a SEM image of commercial ZnO nanoparticles with a short rod-like shape. **FIG. 114B** is a TEM image of a ZnO@C nanoparticle. **FIG. 114C** are TGA results used to determine the carbon content in ZnO@C nanoparticles. **FIG. 114D** is SEM image of carbon-coated ZnO nanoparticles (ZnO@C). **FIG. 114E** is a TEM image of HCl etched ZnO@C particles, resulting in a uniform hollow carbon nanoshell. **FIG. 114F** are XRD results for bare ZnO and ZnO@C nanoparticles.

[00188] **FIG. 115** is a SEM image of nanoparticles ZnO@C at 5.0 kV. The ZnO@C core-shell structure is visible.

[00189] **FIG. 116** contains SEM images of ZnO@C particles with different carbon shell thickness, synthesized using different mass of dopamine hydrochloride. The mass of dopamine hydrochloride is 100 mg (1:1), 200 mg (2:1), and 300 mg (3:1).

[00190] **FIG. 117** shows TGA data of ZnO@polydopamine nanoparticles under an Ar environment. Above about 680 °C, there is a dramatic sample weight loss, suggesting that ZnO gets reduced by carbon and escapes from the carbon shell.

[00191] **FIG. 118A** illustrates the structure and size of hydroxide ion and zincate ion calculated by DFT. **FIG. 118B** is XPS spectra for bare ZnO and ZnO@C nanoparticles. **FIG. 118C** is XPS high-resolution Zn spectra for bare ZnO and ZnO@C nanoparticles. **FIG. 118D** is a graph of N_2 adsorption/desorption isotherms of ZnO and ZnO@C nanoparticles. **FIG. 118E** is a graph of BET pore width distribution of ZnO and ZnO@C nanoparticles. **FIG. 118F** is a graph of ICP-AES quantification of ZnO dissolution in KOH electrolyte from bare ZnO and ZnO@C nanoparticles for 5 minutes, 1 day, and 10 days. Bare ZnO dissolves much faster than ZnO@C.

[00192] **FIG. 119** illustrates specific capacity and Coulombic efficiency of bare ZnO (1.03 mg), ZnO@C (0.94 mg), and bulk Zn foil anodes during discharge process, the inset shows a typical 2032 coin cell fabricated during the experiment.

[00193] **FIG. 120** is a second set of cycling data of bare ZnO and ZnO@C anodes. The mass loading of the bare ZnO and ZnO@C is ~ 0.941 mg and ~ 0.98 mg. The cycling performance is similar to the data presented in **FIG. 119**.

[00194] **FIG. 121** is a comparison of voltage profile between bare ZnO and ZnO@C for the first charging process, ZnO@C particles show a lower overpotential.

[00195] **FIG. 122** is a comparison of voltage profile between bare ZnO and ZnO@C for all the cycles, ZnO@C particles show a lower overpotential for every cycle.

[00196] **FIG. 123** shows voltage profiles of the cell with ZnO@C anode at 1^{st}, 10^{th}, 20^{th}, 30^{th}, 40^{th} cycles.

[00197] **FIG. 124A** is a SEM image of bare ZnO anode before cycling. **FIG. 124B** is a SEM image of bare ZnO anode after three cycles, showing a dramatic shape change. Pores are indicated by yellow arrows. **FIG. 124C** is a SEM image of ZnO@C anode before cycling. **FIG. 124D** is a SEM image of ZnO@C anode after three cycles, the nanoparticles maintained a spherical shape as before cycling.

[00198] **FIG. 125** is a TEM image of a ZnO@C particle after charging, the active material is still well confined inside the nanoshell.

[00199] **FIG. 126** illustrates the performance of ZnO@C batteries with different thickness of nanoshell coating. The mass of active material is ~ 1mg and the batteries are tested at 1C rate and 100% DOD. ZnO@C 2:1 shown in the main text demonstrates superior performance.

[00200] **FIG. 127** presents the Coulombic efficiency in a ZnO@C pouch cell with ZnO saturated electrolyte at 1C and 100% DOD.

[00201] **FIG. 128** presents the Coulombic efficiency of a ZnO@C pouch cell with >95% Coulombic efficiency and ~ 100% retention for 500 cycles, with an actual rate of 12C.

DETAILED DESCRIPTION OF THE DISCLOSURE

[00202] Although preferred exemplary embodiments of the disclosure are explained in detail, it is to be understood that other exemplary embodiments are contemplated. Accordingly, it

is not intended that the disclosure is limited in its scope to the details of construction and arrangement of components set forth in the following description or illustrated in the drawings. The disclosure is capable of other exemplary embodiments and of being practiced or carried out in various ways. Also, in describing the preferred exemplary embodiments, specific terminology will be resorted to for the sake of clarity.

[00203] As used in the specification and the appended claims, the singular forms "a," "an" and "the" include plural referents unless the context clearly dictates otherwise.

[00204] Also, in describing the preferred exemplary embodiments, terminology will be resorted to for the sake of clarity. It is intended that each term contemplates its broadest meaning as understood by those skilled in the art and includes all technical equivalents which operate in a similar manner to accomplish a similar purpose.

[00205] Ranges can be expressed herein as from "about" or "approximately" one particular value and/or to "about" or "approximately" another particular value. When such a range is expressed, another exemplary embodiment includes from the one particular value and/or to the other particular value.

[00206] Using "comprising" or "including" or like terms means that at least the named compound, element, particle, or method step is present in the composition or article or method, but does not exclude the presence of other compounds, materials, particles, method steps, even if the other such compounds, material, particles, method steps have the same function as what is named.

[00207] Mention of one or more method steps does not preclude the presence of additional method steps or intervening method steps between those steps expressly identified. Similarly, it is also to be understood that the mention of one or more components in a device or system does not preclude the presence of additional components or intervening components between those components expressly identified.

[00208] Exemplary embodiments of the present invention comprise innovative components of a deeply rechargeable battery system, and an innovative system and method of rechargeable batteries. A core/shell nanoscale structure provides deeply rechargeable anodes that overcome intrinsic limitations of conventional battery materials that involve soluble intermediates or insulating discharge products. The present invention simultaneously overcomes the dilemmas of passivation and dissolution. An ion-sieving concept is applied to a Zn anode that confines larger zincate ions and allows smaller hydroxide ions to permeate, can limit/prevent ZnO dissolution and electrode shape change.

[00209] Examples of the present invention include sealing ZnO nanorods for deeply rechargeable high-energy aqueous battery anodes, a deeply rechargeable zinc anode with pomegranate-inspired nanostructure for high-energy aqueous batteries, ion-sieving carbon nanoshells for deeply rechargeable Zn-based aqueous batteries, and a deeply rechargeable and hydrogen-evolution-suppressing zinc anode in alkaline aqueous electrolyte.

[00210] **A Deeply Rechargeable And Hydrogen-Evolution-Suppressing Zinc Anode In Alkaline Aqueous Electrolyte**

[00211] **FIG. 1A** is illustrative of the passivation issue, where **FIG. 1B** is illustrative of the dissolution issue. As discussed above, these issues are due to the following processes: (i) the insulating discharge product ZnO passivates the surface of zinc anodes, preventing the latter from further discharging or recharging back to metallic zinc, and (ii) the intermediate zincate $Zn(OH)_4^{2-}$ is soluble in alkaline electrolytes, which leads to active material loss, random ZnO precipitation on the electrode, and morphology change of the electrode over cycling.

[00212] A GC quantitative analysis method (**FIGS. 1C** and **2A-C**) is used herein to identify the influence of HER on the capacity loss of zinc anodes. This is achieved by measuring the evolved H_2 using GC after charging/discharging the zinc anode in alkaline electrolyte (ZnO-saturated 4M KOH) for one cycle (**FIGS. 3A-B**).

[00213] The amount of NiOOH was in excess, which could guarantee the full depletion of Zn in the discharge step. In other words, the capacity loss (charge capacity-discharge capacity) on Zn anodes is attributed to side reactions on Zn anodes. As shown in **FIG. 2D**, the capacity loss on the Zn anode is almost fully caused by HER (~ 99.47% ≈ 87.34%/87.81%). The other ~ 0.46% of capacity loss might be caused by the oxidation of Zn through reacting with O_2. In consideration of Zn anodes, HER suppressing Zn anodes should possess high Coulombic efficiency (discharge capacity/charge capacity).

[00214] In an exemplary embodiment, the present invention comprises sealed sub-micron-sized anodes, coated with a HER suppressing ion-sieving layer to simultaneously tackle passivation, dissolution, and HER issues (**FIG. 4**). Such a design features at least the following advantages: (i) sub-micron-sized ZnO avoids passivation and allows complete utilization of the active materials; (ii) the ion-sieving coating layer confines zincate inside and mitigates shape changes of the electrode; and (iii) the coating layer is made of a HER suppressing material, which represses side reactions. The results demonstrate that HER suppressing sealed nanorod (HSSN)

zinc anodes exhibit long cycle life, high Coulombic efficiency, and high specific discharge capacity.

[00215] The critical thickness of ZnO passivation layer has previously been quantified to be ~ 2 μm when a zinc metal anode is completely passivated. Thus, sub-micron-sized zinc anodes are believed to be able to overcome the passivation problem. However, decreasing the feature size to be nanoscale will intensify the dissolution and HER problems, due to increased electrode-electrolyte contact area. Therefore, sealing sub-micron-sized anodes by uniformly coating a HER suppressing ion-sieving layer is developed, which can suppress HER and selectively block larger zincate ions inside the coating while enabling OH^-/H_2O transport (**FIG. 4**).

[00216] Coat technology is important, as conventional attempts with non-uniform coatings creates structures that still suffer dissolution and HER issues, which might be a reason these prior results had short cycle life (< 20 cycles) and low specific discharge capacity. In this embodiment of the present invention, a TiO_2 coating material is investigated to demonstrate it is stable with alkaline electrolytes and has a low HER activity.

[00217] The present HSSN anode was successfully fabricated as shown in **FIGS. 5A-C**. ZnO nanorods were first grown on the carbon paper hydrothermally. The mass loading of ZnO nanorods on carbon paper can be tuned from 0.5 mg/cm^2 to 5.5 mg/cm^2.

[00218] **Synthesis Of The Uncoated ZnO Nanorod Anode**

[00219] ZnO nanorods were grown on carbon papers (~ 8.4 mg/cm^2) by a hydrothermal method. Carbon paper (Fuel Cell Store) was first heated in air at 500 °C for 1 hour to increase its wettability. Then, the carbon paper was soaked in 0.1M $KMnO_4$ (Sigma Aldrich) aqueous solution for 1 hour to form a seed layer. The ZnO precursor solution was prepared by mixing 50 mL zinc nitrate hexahydrate (30 mM, Alfa Aesar), 50 mL hexamethylenetetramine (30 mM, Sigma Aldrich), and ammonia (28.0-30.0% NH3 basis, Sigma Aldrich).

[00220] The seeded carbon paper was placed in the solution, followed by heating in an oven at 90 °C. After DI-H_2O washing and drying at 80 °C for 3 hours, the white-colored product on carbon paper was obtained. Different mass loadings (0.5 ~ 5.5 mg/cm^2) of ZnO nanorods on carbon paper were achieved by adjusting reaction conditions, as summarized in **TABLE 1** and shown in **FIGS. 6A-C**. Specifically, the "Repeat" column means that the ZnO nanorods-loaded carbon paper from the first reaction was put into a new precursor solution to repeat the reaction.

Mass Loading	Carbon Paper Area Per Batch	NH_3 Quantity	Total Hydrothermal Time	Repeat
0.5 mg/cm^2	2×(2.1*6) cm^2	2 mL	13 h	No
0.9 mg/cm^2	1×(2.1*6) cm^2	4 mL	22 h	No
5.5 mg/cm^2	1×(2.1*6) cm^2	4 mL	2*20 = 40 h	Once

[00221] TABLE 1 - Experiment Conditions For Different Mass Loadings Of ZnO Nanorods

[00222] Synthesis of the HER Suppressing Sealed Nanosized (HSSN) Zinc Anode

[00223] The HSSN zinc anode (a ZnO core/TiO_2 shell structure) was synthesized using a solution method. The carbon paper with grown ZnO nanorods was immersed into a solution of 0.075M $(NH_4)_2TiF_6$ and 0.2M H_3BO_3 for 10 minutes at room temperature. A layer of ~ 30 nm thick TiO_2 was deposited.

[00224] Synthesis of the ZnO@TiN_xO_y Anode

[00225] To achieve the ZnO@TiN_xO_y anode, TiN was deposited onto the uncoated ZnO nanorod anode through ALD. ALD was conducted in Cambridge FIJI Plasma ALD system. The detailed ALD recipe is shown in **Fig. 26**. The precursors of TiN were TDMAT and N_2. During the TiN ALD process, the recipe was run 200 cycles (1 Å per cycle) at 250 °C. Then, when ZnO@TiN nanorods were exposed to air, the TiN was partially oxidized to TiN_xO_y (**FIG. 24**).

[00226] Sheet Resistance Measurement Of TiN_xO_y And TiO_2 Coatings Using A Four-Point Probe System

[00227] To measure the sheet resistance of TiN_xO_y and TiO_2 coatings, TiN_xO_y and TiO_2 are deposited onto glass slides, respectively. The glass slides were cleaned by sonication in acetone/ethanol, followed by ultraviolet-ozone (UVO) treatment. TiN_xO_y was obtained through an ALD of TiN on the glass slides followed by an oxidation step in air.

[00228] The precursors of TiN were TDMAT and N_2. The detailed ALD recipe is shown in **Fig. 26**. During ALD process, the recipe was run 400 cycles (1 Å per cycle) at 250 °C. A layer of ~ 1 μm thick TiO_2 was deposited on the glass slides by immersing the glass slides in a solution of 0.1M $(NH_4)_2TiF_6$ +0.2M H_3BO_3 for 11 hours at 25 °C. The sheet resistance was measured using a four-point probe measurement system (2000 multimeter, Keithley).

[00229] Material Characterization and Measurements

[00230] The morphological and compositional analyses were carried out using SEM (Hitachi SU 8230), TEM (Hitachi HT7700, FEI Tecnai F30, and JEOL 100 CX-II), and STEM (Hitachi HD-2700). The XRD patterns (Panalytical XPert PRO Alpha-1) were carried out with Cu K-Alpha radiation. The XPS was measured with Thermo Scientific K-Alpha system. The specific BET surface areas and pore size distribution were determined by physisorption (BELSORP-max, MicrotracBEL Corp.). The dissolved Zn concentration of samples in 4M KOH electrolyte was measured with an ICP measurement. Cyclic voltammetry, linear sweep voltammetry, and electrochemical impedance spectroscopy were conducted using a VSP system (BioLogic). Battery cycling tests were carried out using LANHE operating in galvanostatic mode.

[00231] In the battery-gas chromatography quantitative analysis measurement, the airtight battery system (**FIGS. 2A-C)** was connected to a gas chromatography (MG#5, SRI Instruments). The system was purged with Ar before the measurement. The stainless-steel rod was used as the anode. ZnO-saturated 4M KOH (Sigma Aldrich) was used as the electrolyte. A 4 cm^2 cathode from a commercial Ni-Zn AA battery (PowerGenix), which is a mixture of NiOOH (~ 8 mAh/cm^2)/$Ni(OH)_2$ (~ 32 mAh/cm^2), was harvested to pair with the anode.

[00232] The battery was charged at 20 mA for 15 minutes and then fully discharged (20 mA) to 0.8 V for 1 cycle. Then H_2 measurements were conducted using the thermal conductivity detector. Ar was the carrier gas for gas chromatography. The capacity loss on the Zn anode is almost fully caused by HER (99.47%).

$$Capacity\ loss = Charge\ capacity\text{-}Discharge\ capacity = Capacity\ (HER) + Capacity\ (Other) \quad \textbf{(6)}$$

[00233] Electrochemistry

[00234] The zinc anodes were cut to round disks with a diameter of 1 cm. Cathodes from commercial Ni-Zn AA batteries (PowerGenix), which is a mixture of NiOOH (~ 8 mAh/cm^2)/$Ni(OH)_2$ (~ 32 mAh/cm^2), were harvested to pair with the anodes.

[00235] Coin Cell

[00236] CR2032 cases (MTI Corporation) were used to make coin cells. The aqueous electrolyte consists of 4M KOH (Sigma Aldrich, 99.99%), 2M KF (Alfa Aesar, 99.99%) and 2M K_2CO_3 (Alfa Aesar, 99.997%). 25 μL electrolyte was used. Glass fiber (GE Healthcare, WhatmanTM10370003) was used as the separator.

[00237] **Pouch cell**

[00238] Pouch-type batteries (**FIGS. 35A-B**) were assembled using Ampac's SealPAK. The mass loading of active material (ZnO) on the anode is 1.5 mg/cm^2. The aqueous electrolyte comprises 4M KOH (Sigma Aldrich, 99.99%), 2M KF (Alfa Aesar, 99.99%) and 2M K_2CO_3 (Alfa Aesar, 99.997%) with saturated ZnO. 100 μL electrolyte was used. Glass fiber (GE Healthcare, WhatmanTM10370003) was used as the separator. Ti wires were used as electrode terminals.

[00239] Cells are galvanostatically cycled at a charge rate of 1C and a discharge rate of 5C between 1.4 and 1.9 V. For anodes cycled at 100% DOD, the anodes were activated by being pre-cycled in pouch cells for 6 cycles. The charge capacity limit cut-off is 658 mAh/g (theoretical specific capacity of ZnO). For anodes cycled at 40% DOD, the anodes were activated by being pre-cycled with 100% active material utilization for 1 cycle and then being fully charged.

[00240] **Beaker cell**

[00241] In beaker-type batteries, the mass loading of active material (ZnO) on the anode is 1.6 mg/cm^2. 10 mL ZnO-saturated 4M KOH (Sigma Aldrich) was used as the electrolyte. Cells are galvanostatically cycled at 100% DOD at a charge rate of 1C and a discharge rate of 5C between 1.4 and 1.9 V. The anodes were activated by being pre-cycled in beaker cells for 50 cycles. The charge capacity limit cut-off is 658 mAh/g. Ag wire was used as the anode terminal. Stainless steel wire was used as the cathode terminal.

[00242] As discussed, the charge capacity was limited to the theoretical capacity of ZnO (approximately 658 mAh/g). The theoretical specific capacity (charge capacity) was calculated by:

$$C_T(mAh/g) = \frac{1}{MW} * \frac{nF}{3.6} \quad (7)$$

[00243] where MW is the molar weight of active material, n is the number of electrons transferred in the relevant reaction, and F is the Faraday's constant. In this work, MW of ZnO = 81.38 g/mol; n = 2; F = 96485 C/mol.

[00244] The specific discharge capacity of the electrode was calculated by:

$$C = It/m \quad (8)$$

[00245] where I is the discharge current, t is the discharge time per cycle, and m is active materials' mass (ZnO).

[00246] A rate of mC corresponds to a full charge/discharge in $1/m$ hour(s). The electrolyte-to-discharge-capacity (E/DC) ratio is:

$$E/C\ ratio\ =\ Volume\ of\ electrolyte\ /\ measured\ discharge\ capacity \quad \textbf{(9)}$$

[00247] Thus, the theoretical gravimetric capacity of Zn metal is:

$$C_g(mAh/g)\ =\ \frac{1}{MW_{Zn}} * \frac{nF}{3.6}\ =\ \frac{1}{65.38} * \frac{2*96485}{3.6}\ =\ 820 \quad \textbf{(10)}$$

[00248] The theoretical volumetric capacity of Zn metal is:

$$C_v(mAh/cm^3)\ =\ C_g * \rho_{Zn}\ =\ 5854 \quad \textbf{(11)}$$

[00249] where ρ_{Zn} is the density of Zn:

$$\rho_{Zn}\ =\ 7.14\ g/cm^3 \quad \textbf{(12)}$$

[00250] The theoretical gravimetric energy density of Zn-air batteries (calculated based on the discharged state, ZnO) is:

$$E_g(Wh/kg)\ =\ \frac{1}{MW_{ZnO}} * \frac{nF}{3.6} * V\ =\ \frac{1}{81.38} * \frac{2*96485}{3.6}\ =\ 1093 \quad \textbf{(13)}$$

[00251] where V is the battery volatge. V = 1.66 V.

[00252] The theoretical volumetric energy density of Zn-air batteries is:

$$E_v(Wh/L)\ =\ E_g * \rho_{ZnO}\ =\ 6134 \quad \textbf{(14)}$$

[00253] where ρ_{ZnO} is the density of ZnO.

$$\rho_{ZnO}\ =\ 5.61\ g/cm^3 \quad \textbf{(15)}$$

[00254] The TiO_2 layer was coated on the ZnO nanorods via a mild solution method at room temperature. The ZnO nanorods were immersed in an aqueous solution comprising 0.075M $(NH_4)_2TiF_6$ and 0.2M H_3BO_3. After the TiO_2 coating, the ZnO nanorod structure was well maintained (**FIGS. 7A-D**).

[00255] STEM image and elemental mappings (**FIGS. 8A-C**) of the present HSSN anode confirm that the TiO_2 coating is uniform. Spatial distributions of Zn and Ti were obtained by taking EDX spectroscopies in the core and shell regions (**FIGS. 9A-B**). The core region shows a much

higher Zn intensity than that of the shell region, which further affirms the ZnO core/TiO_2 shell structure.

[00256] During synthesis, $(NH_4)_2TiF_6$ hydrolyzed to TiO_2 on the surface of ZnO while the surface of ZnO slightly dissolved in the solution with acids produced by $(NH_4)_2TiF_6$ hydrolysis. Thus, it appears some Zn species went into the TiO_2 coating during the synthesis, which may explain for the Zn signal on the TiO_2 shell.

[00257] As evidenced by **FIG. 10**, the ZnO in the core has a hexagonal close packed crystal structure and the TiO_2 coating is amorphous. The TiO_2 layer has a thickness of ~ 31.7 nm (**FIG. 11**). The mass loading of TiO_2 is ~ 0.35 mg/cm^2, which is only ~ 10.4 wt% of the present HSSN anode (with approximately 3 mg/cm^2 ZnO nanorods). After etching the ZnO away, the hollow nanoarrays stayed in place (**FIGS. 12A-C**), displaying that the TiO_2 coating, although only ~ 30 nm thick, is mechanically strong and firmly supports the ZnO nanorods.

[00258] To evaluate the capability of the TiO_2 shell to suppress zincate dissolution, both the HSSN and the uncoated ZnO anodes were soaked in a ZnO-free 4M KOH solution for 15 minutes. The ratio of ZnO active material mass and solution volume was 0.02 mg/μL. The dissolved Zn concentration was then measured in both solutions using inductively coupled plasma atomic emission spectroscopy (ICP-AES). As shown in **FIG. 13**, the dissolved Zn of the HSSN anode (1.9%) was much lower than that of the uncoated ZnO anode (~ 16.9%). ~ 90% ZnO dissolution is suppressed in the HSSN anode, which displays that the TiO_2 shell effectively blocks zincate ions. Both anodes were imaged after soaking in 4M KOH solution (**FIGS. 14A-B**), which also supports that TiO_2 coating can effectively confine zincates inside the shell.

[00259] The zinc-based anodes were also characterized before and after a single charge in coin cells. As shown in **FIG. 15**, XRD patterns confirmed the existence of the charging product, metallic Zn. After being charged at 0.25 mA/cm^2 for 1.5 hours, the uncoated ZnO nanorod anode showed severe structural degradation. The nanorods detach from carbon paper (**FIG. 16**). In contrast, the HSSN anode has no obvious shape change (**FIG. 17**). Additionally, the HSSN anode kept nearly unchanged after five cycles (**FIGS. 18-19**).

[00260] STEM images and elemental mappings of the present HSSN anode after charging are presented in **FIGS. 20-22**. These results indicate that the TiO_2 shell confines zinc active materials inside during cycling, which can be attributed to the ion-sieving effect of the TiO_2 shell. As shown in the N_2 absorption spectrum (**FIG. 23**), TiO_2 layer has nanosized pores, which block

larger zincate ion inside the shell and enable OH^-/H_2O transport through the shell. The porosity of TiO_2 can likely be further engineered to optimize its ion-sieving performance.

[00261] As discussed above, an ion-sieving coating layer is important for nanostructured Zn anodes to effectively suppress active material dissolution. In consideration of HER, such an ion-sieving coating layer should be HER suppressing. To evaluate the HER suppressing capability of the TiO_2 shell and its effect on the Coulombic efficiency, HER activities of TiO_2 and TiN_xO_y were investigated.

[00262] TiN_xO_y (**Fig. 24**) was chosen to be the control material because its uniform coating and ion-sieving property have been achieved. To best represent the anodes, ZnO was etched away from the HSSN and ZnO@TiN_xO_y anodes to get TiO_2 and TiN_xO_y hollow nanorod coatings on carbon paper substrates, respectively (**FIG. 24**). Three-electrode cells were then assembled in 4M KOH electrolyte with TiO_2 or TiN_xO_y electrode as the working electrode, Hg/HgO electrode as the reference electrode, and Pt foil as the counter electrode (**FIGS. 25-26**).

[00263] As shown in IR-corrected polarization curves (**FIG. 27**), the HER on the TiN_xO_y electrode was more severe (higher current density at a fixed HER potential) than on TiO_2. These experimental results reveal that the TiO_2 is more hydrogen suppressive than TiN_xO_y. In addition, the HER activities of the TiO_2 electrode were also compared with the carbon paper substrate, which experimentally indicates that the existence of TiO_2 coating can suppress HER (**FIG. 28**). To understand the hydrogen suppressing property of TiO_2, the sheet resistance of TiO_2 and TiN_xO_y was measured using a four-point probe system (**FIGS. 29A-C**).

[00264] TiO_2 has lower electrical conductivity, which may be part of the reason for its lower HER activity and better HER suppressing capability. Simulations based on the force field model were also conducted to confirm the hydrogen suppressing property of TiO_2. Cluster rather than the slab model was chosen because of its applicability in representing amorphous materials (**FIG. 30A**). In a three-state diagram (**FIG. 30B**), ΔG_H^* represents the free energy for H adsorption. The material with higher $|\Delta G_H^*|$ value possesses lower catalytic activity and better hydrogen suppressing capability. The free energy for TiO_2 is 0.495 eV, which is higher than that of TiN_xO_y clusters (**FIGS. 31A-B** and **32**). This result illustrates that TiO_2 is the most hydrogen suppressive.

[00265] Simulation based on the force field model was conducted to investigate the hydrogen suppressing property of TiO_2 and TiN_xO_y. The Monte Carlo and Least Squares techniques were used to minimize the energy. A Ti_5O_{10} cluster was used to represent amorphous

TiO_2. For TiN_xO_y, the overall atomic ratio of O to N (O/N) was experimentally determined to be ~ 6.66 as evidenced by XPS (**FIG. 24**).

[00266] From many possible structures of amorphous TiN_xO_y, four representative models (denoted as TiN_xO_y-n, n = 1, 2, 3, 4) were chosen and built with O/N atomic ratios of 9 and 4 to simulate the actual shell material. Ti_5O_9N cluster (O/N = 9) for TiN_xO_y-1 and TiN_xO_y-2, and $Ti_5O_8N_2$ cluster (O/N = 4) for TiN_xO_y-3 and TiN_xO_y-4 were built. ΔG_H^* represents the free energy for H adsorption.

[00267] In a three-state diagram, comprising an initial H^+ state, an intermediate H* state, and $1/2H_2$ as the final product, the material with higher $|\Delta G_H^*|$ value possesses lower catalytic activity and thus better hydrogen suppressing capability. ΔG_H^* was obtained by $\Delta G_{H*} = \Delta E_H + \Delta E_{ZPE} - T\Delta S_H$, where ΔE_H is the binding energy of H species, and ΔE_{ZPE} and ΔS_H are the zero point energy change and entropy change of adsorption H, respectively. The contribution of entropies and ZPE for ΔG_{H*} were obtained, where finally $\Delta G_{H*} = \Delta E_H + 0.24\ eV$. ΔE_H was obtained by $\Delta E_H = E_{M-H} - E_M - 1/2 * E_{H_2}$. E_{H_2} was calculated to be -3.040 eV. The summary of these values is listed in the table of **FIG. 32.**

[00268] As shown in **FIGS. 33** and **34**, HSSN and $ZnO@TiN_xO_y$ anodes have very similar ion-sieving capability. With hydrogen suppressing capability, the present HSSN anode shows higher Coulombic efficiency compared to the $ZnO@TiN_xO_y$ counterpart. To specifically focus on Zn anodes, for all the cells shown below, cathodes with excess capacity were harvested to pair with Zn anodes. The calculation of the specific capacity of zinc anodes is based on the mass of ZnO (theoretical capacity: 658 mAh/g) if not otherwise specified. Cells were galvanostatically cycled at a charge rate of 1C and a discharge rate of 5C. The anodes were cycled in pouch cells (**FIGS. 35A-B**) instead of coin cells to avoid the HER on stainless steel coin cell cases. They were cycled at 100% DOD. Thus, the extent of side reactions on them can be directly indicated by the cell Coulombic efficiency. Higher "clean" Coulombic efficiency means fewer side reactions.

[00269] The charge/discharge profiles of HSSN and $ZnO@TiN_xO_y$ anodes cycled in lean electrolyte (100 μL) are plotted in **FIG. 36**. Their cycling performance and rate-capability tests can be found in **FIGS. 37A** and **37B**. The average Coulombic efficiency (~ 93.50%) of the present HSSN anode in the first 12 galvanostatic cycles is much higher than that of the $ZnO@TiN_xO_y$ anode (~ 84.96%). Even though TiO_2 has lower electrical conductivity than TiN_xO_y, the HSSN anode showed slightly better rate capability than the $ZnO@TiN_xO_y$ anode, which may be because there are more pores on the present HSSN anode and thus the faster OH^-/H_2O transport can be achieved through the TiO_2 shell (**FIGS. 38A** and **38B**). The HSSN anode achieves higher Coulombic

efficiency of ~ 93.09% than the ZnO@TiN_xO_y anode (~ 88.07%). In similar alkaline electrolytes with 100% DOD, conventional studies show Coulombic efficiency lower than ~ 90% (**FIG. 39**).

[00270] As shown in **FIGS. 40** and **41**, when cycled at 40% DOD in a lean electrolyte, the present HSSN anode (with 1.05 mg/cm^2 ZnO) demonstrated long-term stable cycling for more than 170 cycles. There was no capacity contribution from the TiO_2 shell during the electrochemical reactions (**FIG. 42**). When cycled at 100% DOD in a lean electrolyte, the present HSSN anode (with ~ 1.5 mg/cm^2 ZnO) achieved an average Coulombic efficiency of 93.5% and average discharge capacity of 616 mAh/g in the first 12 galvanostatic cycles (**FIG. 37A**).

[00271] The capacity fading occurs after 33 cycles. The battery failure can be attributed to (1) the structural collapse of the HSSN anode (**FIG. 43**) due to the shape and volume changes of Zn/ZnO inside the shell, and (2) the limited mass transfer of Zn species caused by electrolyte decomposition and hydrogen accumulation. The anode was also evaluated in a beaker cell with a large amount of ZnO-saturated electrolyte. As shown in **FIG. 44**, the present HSSN anode (with ~ 1.6 mg/cm^2 ZnO) was cycled more than 350 times with Coulombic efficiency of 94.3% and a discharge capacity of 621 mAh/g.

[00272] Voltage profiles for the batteries shown in **FIGS. 40** and **44** can be found in **FIGS. 45A-45B**. From the above cycling results, cycle life of Zn anodes in a lean electrolyte is much shorter than in a large amount of ZnO-saturated electrolyte. This can be explained by the electrochemistry of alkaline Zn anodes. In a large amount of ZnO-saturated electrolyte, the effect of minor electrolyte decomposition can be minimized with excess water. Moreover, there is excess zincate in the electrolyte, which is the active material for Zn anodes. With a large capacity contribution from the zincate supplied from the electrolyte, the long cycle life of Zn anodes can be achieved yet it is inauthentic. In lean electrolyte (100 μL), batteries fail quicker as a result of complicated synergistic effects caused by electrolyte decomposition and limited mass transfer of Zn species. However, it is still necessary to cycle anodes in lean electrolyte to evaluate their true performance which can represent practical situations despite their short cycle life.

[00273] Electrolyte-to-discharge-capacity (E/DC) ratio is also critical for device-level energy density and is crucial for practical applications. The tested Coulombic efficiency of alkaline Zn anodes is highly correlated to the E/DC ratio. Thus, it is necessary to provide E/DC ratios to get a fair comparison on the Coulombic efficiency of different Zn anode materials. However, only a few previous works (summarized in the table of **FIG. 46**) reported this ratio or provided necessary information for its calculation.

[00274] Prior results were summarized, and the anode compared with them in terms of Coulombic efficiency and E/DC ratio in **FIG. 47**. Notably, to get a comparison on "clean" Coulombic efficiency of different Zn anodes, only deeply cycled Zn anodes with 100% DOD are listed. Partially utilized (DOD < 100%) metallic zinc anodes are not included in the comparison because their Coulombic efficiency cannot indicate the extent of side reactions occurring on Zn anodes.

[00275] In comparison, the present anode achieves a superior Coulombic efficiency (93.5%) at a low E/DC ratio (0.14 mL/mAh), which suggests the advance of the designed functionally coated Zn anodes (**FIG. 37A**). With the featured HER suppressing core/shell Zn anode: (1) Zn species are confined inside the shell so there is minimized active material loss; and (2) minimized HER and less electrolyte decomposition can be achieved with the HER suppressing property. These enable the present anode to achieve high Coulombic efficiency in lean electrolyte. The overall real and specific discharge capacities of the present HSSN anode were ~ 0.9 mAh/cm^2 and ~ 91 mAh/g, respectively, after considering the mass of the current collector. Due to its specially featured core/shell nanorod structure, its overall capacity was unable to meet design parameters for practical Zn anodes (11.7 mAh/cm^2), however the present design principals achieves practically high energy-density Zn anodes.

[00276] The present zinc anode design, namely sealing sub-micron-sized ZnO with a HER suppressing and ion-sieving layer, to overcome simultaneously passivation, dissolution, and hydrogen evolution issues in alkaline electrolytes is disclosed. A ZnO nanorod anode and TiO_2 shell were chosen to demonstrate this concept. The fabricated HSSN anode achieves superior reversible deep cycling performance at lean electrolyte. While the Coulombic efficiency of the present HSSN anode is higher than that of most of the previously reported zinc anodes, it will be improved to approach the efficiency of LIBs (99.9%).

[00277] Optimization of the shell material, from aspects of pore size, porosity, and surface charge, leads to improvement of anode performance and stability. Other materials with controlled ion-sieving and HER suppressing properties have the potential to be applied as the shell material. This design principle can potentially be applied to other morphologies (e.g. particles) of starting materials for large scale production. The mechanistic understanding and design principle herein will also guide future design of other rechargeable high-energy aqueous batteries.

[00278] Sealing ZnO Nanorods For Deeply Rechargeable High-Energy Aqueous Battery Anodes

[00279] As noted in the background, in aqueous alkaline electrolyte, a zinc anode undergoes two consecutive reactions: complexation (or dissolution) and electroreduction reactions in charging (shown in **Equation 1**: Complexation/Precipitation), and electrooxidation and precipitation reactions in discharging (shown in **Equation 2**: Electroreduction/Electrooxidation).

[00280] Different from conventional intercalation electrodes in lithium ion batteries, this solid-solute-solid (ZnO-$Zn(OH)_4^{2-}$-Zn) transformation of zinc electrode inherently represents a series of challenges: (i) discharge product ZnO passivates the surface of Zn, preventing Zn from further discharging; (ii) ZnO is insulating, which can be hardly recharged to metallic Zn; and (iii) ZnO precipitation from soluble zincates occurs randomly on the electrode surface, and changes the morphology of electrode over cycling.

[00281] Zn metal foil is the most commonly used Zn anode in aqueous batteries. However, as exemplified in **FIGS. 48-49**, the passivation problem (nonconductive property of ZnO) of Zn foil limits the utilization (< approximately 1%) of Zn foil anode and makes it non-rechargeable. Under approximately 10 mA discharge, one can only get ~ 1.7 mAh capacity of Zn foil with approximately 0.25 mm thickness and approximately 1 cm diameter in a coin cell. As shown in **FIG. 50**, the thickness of the passivation layer (or the critical passivation size) is ~ 2 μm. Microporous Zn sponges are known, and enhance rechargeability, yet the Zn sponge feature size is ~ 10 μm (greater than the critical passivation size of approximately 2 μm), so only approximately 40% DOD of them can be achieved.

[00282] As shown in **FIG. 51**, the feature size of an uncoated ZnO nanorod is smaller than the critical passivation size, however, the large electrode-electrolyte surface area accelerates anode dissolution and promotes electrode shape change. Moreover, due to the relatively insulating property of ZnO, electrons can only be distributed on carbon paper, which leads to fast complexation and electroreduction reactions on the root of nanorods in charging. As a result, the nanorods of **FIG. 51** detach from carbon paper.

[00283] In an exemplary embodiment of the present invention as shown in **FIG. 52**, the conventional Zn anode dilemmas of passivation and dissolution are overcome with a sealed structure (ZnO@TiN_xO_y nanorod anode), with a feature size smaller than the critical passivation size, and a thin and conformal coating to limit/prevent dissolution of the anode.

[00284] A hydro-thermal method was used to grow ZnO nanorods on carbon fiber paper. Then, the ALD technique was used to form a strong and conductive stable TiN_xO_y coating on the ZnO nanorods. This structure has advantages that include: (i) the feature size of each ZnO

nanorod is smaller than the critical passivation size; (ii) a carbon paper framework and TiN_xO_y coating, which encapsulates the ZnO nanorod, function as an electrical pathway so that all ZnO nanorods are electrochemically active; and (iii) the TiN_xO_y coating enables fast hydroxide/water diffusion as well as blocks large zincates from escaping during electrochemical cycling, thus effectively preventing anode structure fracture.

[00285] **Synthesis of ZnO Nanorods**

[00286] Carbon paper (Fuel Cell Store) was first heat-treated at 500 °C for 1 hour in air to increase its wettability. Then, ZnO nanorods were grown on the carbon paper by a wet chemical process. First, carbon paper was soaked in an aqueous solution containing 0.1M $KMnO_4$ (Sigma Aldrich) for 1 hour to form a seed layer. Second, the seeded carbon paper was then dipped into a glass bottle with a precursor solution containing 50 mL zinc nitrate hexahydrate (30 mM, Alfa Aesar), 50 mL hexamethylene-tetramine (30 mM, Sigma Aldrich), and ammonia (28.0 ~ 30.0% NH_3 basis, Sigma Aldrich).

[00287] Third, the sealed bottle was placed into an oven at 90 °C. Next, the white-colored carbon paper ZnO nanorods were obtained by water washing and drying at 80 °C for 3 hours. As shown in **TABLE 2**, different mass loadings of ZnO nanorods on carbon paper ranging from 0.5 mg/cm^2 to 5.5 mg/cm^2 were synthesized by adjusting: the carbon paper area per bottle, the NH_3 concentration, the hydrothermal time, and the hydrothermal times.

Mass Loading	Carbon Paper Area Per Bottle	NH_3 Quantity	Hydrothermal Time	Hydrothermal Times
0.5 mg/cm^2	2×(2.1*6) cm^2	2 mL	13 h	1
0.9 mg/cm^2	1×(2.1*6) cm^2	4 mL	22 h	1
5.5 mg/cm^2	1×(2.1*6) cm^2	4 mL	20 h	2

TABLE 2

[00288] **Synthesis of ZnO@TiN_xO_y Core/Shell Nanorods**

[00289] The synthesis of ZnO@TiN_xO_y core/shell nanorods was conducted in Cambridge FIJI Plasma ALD system. First, the TiN was deposited onto the ZnO nanorods. The precursors of TiN were Tetrakis(dimethylamido)Titanium(IV) (TDMAT, Sigma Aldrich) and N_2. During the TiN ALD process, the recipe was run 100 or 200 cycles at 250 °C. The TiN ALD recipe is shown in **FIG. 53**. Then, when the ZnO@TiN nanorods were exposed to air, the TiN was partially

oxidized to TiN_xO_y (evidenced by XPS spectra in **FIG. 67**). Thus, for accuracy purpose, the anode is termed throughout as $ZnO@TiN_xO_y$.

[00290] Electrochemistry

[00291] To investigate the Zn anode, full batteries were made using $Ni(OH)_2$ as the rechargeable cathode. The $Ni(OH)_2$ cathodes were harvested from commercial Ni-Zn AA batteries from PowerGenix.

[00292] Coin Cell

[00293] Coin-type batteries were assembled using CR2032 cases (MTI Corporation), the present zinc anodes (round disk, approximately 1 cm diameter) and $Ni(OH)_2$ cathodes with excess capacity, as shown in **FIGS. 54A-54C**. The coin cell has a small volume of electrolyte, which is required for practical application. The aqueous electrolyte comprises 4M KOH (Sigma Aldrich, 99.99%), 2M KF (Alfa Aesar, 99.99%) and 2M K_2CO_3 (Alfa Aesar, 99.997%). Glass fiber (GE Healthcare, Whatman™ 10370003) was used as the separator.

[00294] For start-stop operation, the $ZnO@TiN_xO_y$ nanorod anode and Zn foil were pre-activated. The $ZnO@TiN_xO_y$ nanorod anode was pre-cycled three times at 0.5C between approximately 1.4 and 2 V. The Zn foil (approximately 0.02% DOD) was firstly discharged for 2 hours and re-charged for 2 hours at a constant current of approximately 1.35 mA. Then it was discharged twice and charged once at the same time interval of 1 hour at approximately 1.35 mA.

[00295] The Zn foil (approximately 1% DOD) was pre-cycled twice at a constant current of approximately 1 mA. When the Zn foil was used as the anode, the cathode harvested from commercial Ni-Zn AA batteries was electrochemically oxidized to approximately 0.6 V vs an HgO/Hg reference electrode in a beaker cell with 2M KOH as the electrolyte.

[00296] Pouch Cell

[00297] Pouch-type batteries (**FIG. 55**) were assembled using Ampac's SealPAK, the present zinc anodes (round disk, approximately 1 cm diameter) and $Ni(OH)_2$ cathodes with excess capacity. The aqueous electrolyte comprises 4M KOH (Sigma Aldrich, 99.99%), 2M KF (Alfa Aesar, 99.99%) and 2M K_2CO_3 (Alfa Aesar, 99.997%). Celgard 3501 (close to anode) and Freudenberg 700/28K (close to cathode) were used as the separators.

[00298] Beaker Cell

[00299] Beaker-type batteries (**FIG. 54A**) were assembled using beakers, the present zinc anodes (round disk, 1 cm diameter) and $Ni(OH)_2$ cathodes with excess capacity. The electrolyte was 10 mL ZnO saturated 4M KOH (Sigma Aldrich).

[00300] EIS measurements were performed on a Bio-Logic instrument. The frequency range was between 100 KHz and 10 mHz. The amplitude of the AC signal was approximately 10 mV. Coin-type batteries assembled using the present zinc anodes and $Ni(OH)_2$ cathodes were used to measure EIS. 100 μL 4M KOH, 2M KF and 2M K_2CO_3 electrolyte was added to a glass fiber separator.

[00301] **Results and Discussion**

[00302] ZnO nanorods are synthesized on carbon paper with mass loading ranging from approximately 0.5 to approximately 5.5 mg/cm^2 (**FIGS. 56-58C**) by adjusting the area of carbon paper placed in hydrothermal reactor, NH_3 concentration, hydrothermal time, etc. (**TABLE 1**). In the ALD process (**FIG. 53**), the recipe was run 100 or 200 cycles. The TiN_xO_y mass loadings of 100 cycles and 200 cycles are approximately 0.057 mg/cm^2 and approximately 0.19 mg/cm^2, which are only approximately 0.6 wt% and approximately 1.9 wt% of ZnO@TiN_xO_y nanorod anode, respectively (for approximately 3 mg/cm^2 ZnO nanorods).

[00303] The nanorod morphology does not change after TiN_xO_y coating (**FIGS. 59** and **64**). HRTEM images show uniform TiN_xO_y coating with a thickness of approximately 6.1 nm for ZnO@TiN_xO_y nanorod with 100 cycles ALD (**FIGS. 60-61**). ZnO nanorod is hexagonal and TiN_xO_y coating is amorphous, which are evident from TEM (**FIGS. 62-63**) and XRD results (**FIG. 76**).

[00304] In addition to TEM, XPS results also indicate complete coverage of TiN_xO_y on ZnO (**FIGS. 65-66** and **68-69**), which is important for encapsulating zincate during cycling. Besides, nitrogen peak in the XPS survey spectra (**FIG. 65**) and three Ti 2p peaks in the high-resolution XPS spectra (**FIG. 67**), which belong to TiO_2, indicate that ALD TiN is partially oxidized to TiN_xO_y.

[00305] The TiN_xO_y coating, although only a few nanometers thick, firmly supports the ZnO nanorod, blocks zincates, and enables OH^-/H_2O to pass through. As shown in **FIG. 70**, a ZnO@TiN_xO_y anode and an uncoated ZnO anode (1 cm diameter disk) were soaked into two tubes with 2 mL 4M KOH solution, respectively. Then the dissolved Zn concentration was measured in both solutions using ICP atomic emission spectroscopy (ICP-AES). The dissolved Zn of the ZnO@TiN_xO_y anode is much lower than that of the uncoated ZnO anode, which means that

TiN_xO_y coating effectively blocks zincates. Furthermore, coin cells were assembled with these two anodes and $Ni(OH)_2$ cathodes to investigate the influence of the TiN_xO_y coating during electrochemical cycling.

[00306] After 2 hours of charge (1 hour constant current at 1C rate, and 1 hour constant voltage at 1.93 V), the uncoated ZnO nanorod anode shows severely morphological degradation, almost all ZnO nanorods detach from carbon paper because of dissolution (**FIG. 71**). On the other hand, there is no obvious shape change for the ZnO@TiN_xO_y nanorod anode with 100 cycles ALD (**FIG. 72**). ZnO@TiN_xO_y nanorod anode with 200 cycles ALD maintained its morphology after charging as well (**FIG. 73**). Additional SEM images, elemental mapping (**FIG. 74**), TEM image (**FIG. 75**), and Zn peaks in XRD results (**FIG. 76**) all support that the TiN_xO_y coating confined zinc active material inside, while still allowing it to participate in electrochemical reaction. The mass loading of the ZnO nanorods shown in **FIGS. 71-72** and **74-75** is approximately 0.5 mg/cm^2. For longer nanorods with higher mass loading (~ 1.7 mg/cm^2), there is also no apparent shape change of ZnO@TiN_xO_y nanorod anode after the first charge and discharge (**FIGS. 78-80**), while ZnO nanorod anode shows severe structure degradation after the first charge (**FIGS. 81-82**).

[00307] EIS was also employed to investigate the electrochemical influence of conductive TiN_xO_y coating. As shown in the Nyquist plot (**FIG. 77**) and equivalent circuit (Randles-Ershler impedance), the charge-transfer resistance (R_{ct}) of the ZnO@TiN_xO_y nanorod anode is much lower than that of the uncoated ZnO anode. This can be attributed to the good conductivity of TiN_xO_y and the high zincate concentration inside the TiN_xO_y coating.

[00308] Zinc anodes were tested in coin-type cells with lean zinc-free electrolyte here to evaluate their real performance (**FIGS. 54A-C**), which is different from most of previous investigations using beaker cells with a large amount of ZnO saturated electrolyte. When testing the performance of zinc anodes in ZnO saturated electrolyte, all the zincates in the electrolyte could also participate in electrochemical reactions and contribute capacity in addition to the Zn in the anode. However, most previous works reported their specific capacity without counting Zn in the electrolyte, which gives pseudo performance. In an extreme case, even if there is no active material in the anode, only a pure current collector can cycle in ZnO saturated electrolyte. Here two pure carbon fiber paper substrates (1 cm diameter disk) were tested in a beaker cell with 10 mL ZnO saturated 4M KOH electrolyte and a coin cell with 100 μL ZnO saturated 4M KOH electrolyte (**FIG. 83**), respectively. They were both cycled at approximately 1 mA with a limiting charge capacity of approximately 1 mAh and cut-off voltage of approximately 1.4/2 V.

[00309] The theoretical specific capacity of ZnO is approximately 658 mAh/g. As shown in **FIG. 84**, if zinc in the electrolyte is not counted, the pure current collector without any active material in the beaker cell can show excellent cycling performance with a pseudo specific discharge capacity of approximately 600 mAh/g (assuming there is approximately 1.5 mg ZnO on the anode, which has approximately 1 mAh theoretical capacity). However, when zinc in the electrolyte (see **TABLE 3** for equivalent ZnO mass) is counted, the real specific discharge capacity in the beaker cell is only approximately 4 mAh/g, while that in the coin cell is approximately 150 mAh/g. These results show that testing zinc anodes in beaker cells with a large amount of ZnO saturated electrolyte will dramatically decrease the overall specific energy.

[00310] When testing zinc anodes in beaker cells with 10 mL ZnO saturated 4M KOH electrolyte, electrolyte can contribute a large capacity, which is 100 times that of in coin cells with 100 μL electrolyte (**TABLE 3**). With this big contribution, it is hard to evaluate the true performance of zinc anodes with less amount of active materials. Coin-type cells use minimum amount of electrolyte and have a higher volumetric capacity compared with beaker cells, which is a better testing choice even though the testing environment is harsh.

System	**Large Amount Of Electrolyte**	**Lean Electrolyte**
Test equipment	Beaker cell	Coin cell
Volume of electrolyte	10 mL	100 μL
Electrolyte	ZnO saturated 4M KOH	ZnO saturated 4M KOH
Zincate concentration	0.256 mol/L (*)	0.256 mol/L (*)
Amount of zinc	0.00256 mol	0.0000256 mol
Mass of equivalent ZnO	***208 mg (**)***	***2.08 mg (**)***
Capacity contributed by electrolyte	137 mAh	1.37 mAh
Effect of zinc deposition from electrolyte on anode shape change	Big	Small

TABLE 3 - Calculation Of Equivalent ZnO Quantity And Capacity

[00311] (*) ICP Emission Spectroscopy result.

[00312] (**) used to make **FIG. 84**.

[00313] Moreover, it is hard to evaluate the true performance of anodes with a lot of capacity contributed from electrolyte. Coin-type cells use a minimum amount of electrolyte and have a higher volumetric capacity compared with beaker cells, which is closer to practical operating conditions. Thus, even though the coin cell with lean electrolyte is an extremely harsh

testing environment (~ 25 cycles), that was the choice made for this testing. To evaluate the true performance of anodes, ZnO-free electrolytes were used because capacity contributed by electrolytes could cause an unrealistically high capacity of anodes. 4M KOH, 2M KF and 2M K_2CO_3 was selected as the electrolyte if not otherwise stated because it has lower $Zn(OH)_4^{2-}$ solubility and thus less shape change than 4M KOH as evidenced by ICP results shown in **TABLE 4**.

[00314] ICP Emission Spectroscopy results below indicate that an electrolyte comprising 4M KOH, 2M KF and 2M K_2CO_3 has a lower $Zn(OH)_4^{2-}$ solubility than 4M KOH electrolyte.

Electrolyte	Zincate Concentration (mol/L)
ZnO saturated 4M KOH	0.256
ZnO saturated 4M KOH+2M KF+2M K_2CO_3	0.168

TABLE 4 - ICP Results of $Zn(OH)_4^{2-}$ Solubility In Different Electrolytes

[00315] As shown in **FIG. 85**, the ZnO@TiN_xO_y nanorod anode affords remarkable battery performance in a lean electrolyte configuration even with a high mass loading of active materials (~ 2.1 mg/cm^2). The coin cells are galvanostatically deep-cycled to approximately 100% state of charge (SOC) with approximately 1.5 and 1.9 V as cut-off voltages. The gravimetric capacity or the specific capacity was limited to the theoretical capacity of ZnO (approximately 658 mAh/g). The reversible discharge capacity of the ZnO@TiN_xO_y nanorod anode at the tenth galvanostatic cycle is approximately 279 mAh/g, which is twice as large as that of an uncoated ZnO nanorod anode (approximately 148 mAh/g) at a rate of C/2. The discharge capacity of the ZnO@TiN_xO_y nanorod anode decays to below approximately 150 mAh/g after 30 cycles, versus only 9 cycles for uncoated ZnO nanorod anode.

[00316] For the ZnO@TiN_xO_y anode, the TiN_xO_y coating did not change the over-potential of the ZnO anode with almost the same charge profile as the uncoated ZnO (**FIG. 86**). Cycled at a lower rate (C/4) with approximately 50% SOC, the capacity difference between coated and uncoated ZnO nanorod anodes in initial cycles is small, yet the ZnO@TiN_xO_y nanorod anode shows better capacity retention than uncoated ZnO nanorod anode (**FIG. 87**). The discharge capacities of uncoated and sealed ZnO nanorod anodes decay to approximately 50% after 31 and 53 cycles, respectively. To probe the behavior of ZnO over cycling, the electrodes were imaged after three galvanostatic cycles at 0.33C. As can be seen in **FIG. 88**, the ZnO@TiN_xO_y nanorod anode keeps its original morphology after cycling, whereas almost no nanorods can be found on the carbon paper for the uncoated ZnO nanorod anode.

[00317] The superior performance of $ZnO@TiN_xO_y$ nanorod anode can be attributed to the small feature size of ZnO and conformal TiN_xO_y coating. Below the critical passivation thickness, the anode passivation problem is nearly if not fully eliminated. The TiN_xO_y coating serves as an electrical pathway, confines large zincate molecules, yet allows OH^- and water to pass. As a mechanical backbone, the TiN_xO_y coating protects ZnO nanorods from detaching from the carbon paper substrate, and thus provides a short zincate mass transfer path for the reaction.

[00318] Without a TiN_xO_y coating, the ZnO nanorod will detach from substrate upon charging (**FIG. 89**). This on one hand leads to a much slower mass transport for electrically disconnected ZnO to dissolve in electrolyte to form zincate and then diffuse to current collector. On the other hand, detached ZnO or dissolved zincate may migrate far from anode and never participate in further cycling. Both mechanisms will cause capacity decay over cycling. The utilization of Zn could be potentially modeled by quantitative comparison of electroreduction rate and mass transfer rate of $Zn(OH)_4^{2-}$.

[00319] The $ZnO@TiN_xO_y$ nanorod anode was also tested in pouch cell with a ZnO-free electrolyte (**FIG. 88**). It achieves a specific discharge capacity of approximately 408 mAh/g (based on ZnO if not otherwise stated), which is 508 mAh/g(Zn). As shown in **FIG. 89**, the present $ZnO@TiN_xO_y$ nanorod anode demonstrates a much higher specific capacity than that of many previously reported zinc anodes shown in **TABLE 5**.

Anode Material	Cell Structure	Electrolyte	Mass Loading	ZnO wt%	Reported Capacity (mAh/g)	Real Capacity (mAh/g(Zn)) [c]
In doped ZnO (IZO)	- [a]	4.5M KOH, 1.0M NaOH, 0.5M LiOH, saturated with ZnO	10 mg *	0.98	569	32.56
ZnO Nanoplates	- [a]	4M KOH, 1.6M K_2BO_3, 0.9M KF, 0.1M LiOH, saturated with ZnO	10 mg *	1.00	420	24.01
Calcium Zincate	Sandwich cell [b]	4M KOH, saturated with ZnO	10 mg *	0.64	230	95.54
ZnO@RGO	Sandwich cell [b]	6M KOH, saturated with ZnO	10 mg *	0.90	510	211.85

CC-CF@ZnO	Sandwich cell [b]	2M KOH, saturated with ZnO	0.6 mg/cm^{-2}	1	500	207.69
Zn Sponge	3D printed cell	4M KOH, 1M LiOH	-	0.48	328	328.00
Zn-Al-Sb-LDH	- [a]	6M KOH, saturated with ZnO	10 mg *	0.81	328	18.91
Zn-Al-Bi-LDOs/C	- [a]	6M KOH, saturated with ZnO	9 mg	0.73	475	24.83
LDOs	- [a]	6M KOH, saturated with ZnO	10 mg	0.91	540	31.00
Ag-LDH	- [a]	6M KOH, saturated with ZnO	10 mg *	0.85	400	23.02

TABLE 5 - Comparison Of Specific Discharge Capacity Between The Present Invention And Previously Reported Anodes

[00320] a: The cell structure and electrolyte quantity were not reported. It is assumed 10 mL electrolyte was used in beaker cells. Based on ICP result, the equivalent ZnO mass is approximately 208 mg.

[00321] b: Sandwich cell: anode, separator, and cathode were packed. The electrolyte quantity was not reported. It is assumed that the capacity contributed by ZnO saturated electrolyte was 2 times of that contributed by anodes.

[00322] c: Zinc in the electrode and electrolyte are both counted.

[00323] *: The mass loading was not reported. For calculation, it is assumed the mass of materials is 10 mg.

[00324] The ZnO@TiN_xO_y nanorod anode was also tested in a beaker cell (**FIG. 90**) and pouch cell (**FIG. 55** and **88**) with ZnO saturated electrolyte, which achieves a discharge capacity of ~ 550 mAh/g for > 640 cycles (64 days) and 50 cycles, respectively. **FIG. 91** shows the CV of the ZnO@TiN_xO_y nanorod anode in a coin cell with ZnO free electrolyte. The CV of the ZnO@TiN_xO_y nanorod anode in pouch and beaker cells is shown in **FIGS. 92-93**.

[00325] In addition, the $ZnO@TiN_xO_y$ nanorod anode has excellent performance under start-stop operations, demonstrating potential to replace lead acid batteries in micro-hybrid vehicles. Engine restart, rest and pulse discharge are involved in the start-stop operation. The procedure of a test is showed in **FIG. 94**. The capacity of $ZnO@TiN_xO_y$ nanorod anode was kept at approximately 1% DOD per duty cycle. The $ZnO@TiN_xO_y$ nanorod anode maintained 100% discharge capacity for more than 7500 cycles (**FIG. 95**) at approximately 1% DOD. Voltage profile of the $ZnO@TiN_xO_y$ nanorod anode is shown in **FIGS. 96-98**. Under the same current density (**FIG. 95**), the Zn foil died after 3400 cycles, which is less than half of cycle number of $ZnO@TiN_xO_y$ nanorod anode, even though the DOD of Zn foil is only approximately 0.02% ($1/50^{th}$ of that of $ZnO@TiN_xO_y$ nanorod anode). This Zn foil cell died with a sudden voltage drop to < 0 V because Zn is completely passivated by ZnO. And the cell was severely swelled, possibly due to accumulation of hydrogen evolved on the anode (**FIGS. 96-98**). Severe hydrogen evolution occurs after the passivation of Zn anode. The cell with a $ZnO@TiN_xO_y$ nanorod anode only slightly swelled, which indicated less side reaction and higher utilization of zinc. Less swelling further indicates the present $ZnO@TiN_xO_y$ nanorod anode does not passivate and retains its activity over thousands of cycles. Zn foil start stop performance was tested with approximately 1% DOD at the same time interval as shown in **FIG. 94**, which showed dramatically discharge capacity decay (**FIG. 95**). This result indicates the high stability of $ZnO@TiN_xO_y$ nanorod anode. The $ZnO@TiN_xO_y$ nanorod anode also demonstrated stable cycling at different cycling rates from 0.25C to 4C in **FIG. 99**.

[00326] The $ZnO@TiN_xO_y$ nanorod anode achieves very high specific discharge capacity and superior reversibility when testing in a coin cell with lean ZnO-free electrolyte. In commercial PowerGenix AA batteries, which are made of a Zn metal anode and NiOOH cathode, the discharge capacity decayed to approximately 50% of its initial capacity after only 9 cycles (0.5C, 20 °C, charged to approximately 105% theoretical capacity). NiOOH cathodes are very reversible, and the Zn anode is the main cause of the poor reversibility.

[00327] The present $ZnO@TiN_xO_y$ core/shell nanorod anode structure successfully overcomes problems of ZnO passivation and zincate dissolution simultaneously, and significantly improves the cycle life of Zn anode. Because electrolyte consumption and bubble accumulation resulted from hydrogen evolution side reaction, anodes degraded ultimately when cycled in coin cells with lean electrolyte. This can be further improved by coating hydrogen evolution suppressive materials. In addition, the mechanistic understanding and design principles provide guidance to future designs of zinc and other metal anodes (e.g. Li, Na, Mg, Ca), and a path towards rechargeable Zn-air aqueous batteries and other rechargeable, high-energy and safe batteries.

[00328] A Deeply Rechargeable Zinc Anode With Pomegranate-Inspired Nanostructure For High-Energy Aqueous Batteries

[00329] Also, some zinc battery systems using mild electrolytes, such as $ZnSO_4$-MSO_4 (M = Mn, Co), $Zn(CF_3SO_3)_2$-$Mn(CF_3SO_3)$, and $Zn(TFSI)_2$-LiTFSI, in which expensive TFSI salts should be replaced with salts having lower costs, were developed to mitigate the zinc dendritic growth effectively. Nevertheless, the reversibility of a zinc anode in alkaline electrolyte is a great concern to exploit some highly rechargeable Zn-air batteries with high specific energy density (5200 Wh/kg).

[00330] To tackle the long-standing challenges of a completely rechargeable Zn anode in a limited quantity of electrolyte, in another exemplary embodiment of the present invention, the present invention comprises a ZnO pomegranate (Zn-pome) material in which the zinc oxide nanoparticles (ZnO NPs) are analogous to seeds that are individually encapsulated and held in clusters by a carbon shell diaphragm. The carbon shell coating on the nanoparticles was chosen for its porosity, stability in aqueous alkaline media, and electroconductivity.

[00331] **FIG. 100** shows the schematic of zincate motion during battery cycling of ZnO NPs (**FIG. 100A**), ZnO@C NPs (**FIG. 100B**) and Zn-pome (**FIG. 100C**). There are several distinctive advantages of the Zn-pome electrode.

[00332] First, multi-layered carbon acts as a conductor, protector, and ion barrier in Zn-pome to adequately constrain the migration of $Zn(OH)_4^{2-}$ (the discharge product), thus mitigating the dendrite formation and shape change of the Zn electrode. Meanwhile, species with a smaller diameter (*e.g.*, OH and H_2O) than zincate can permeate through the carbon shell.

[00333] Second, the use of nano-scale (< approximately 100 nm) primary ZnO particles avoids passivation. Once ZnO reaches a critical passivation thickness, it can no longer fully convert to Zn. The thickness of the passivation layer on the zinc foil in coin cells after complete discharging was determined by SEM. As shown in **FIGS. 1A**, **48**, and **101**, the thickness of the passivation layer is ~ 2 μm, which indicates that the Zn anode cannot be consumed entirely in the discharge process if the size of the Zn material is larger than ~ 2 μm regardless of the shape (foil, rod, particle, etc.). Thus, controlling the size of Zn material to nanoscale is a practical approach to fully utilize the Zn material in the charge/discharge process. Therefore, the nanoscale ZnO primary material is chosen to build Zn-pome. Besides, the robust carbon shell on ZnO NPs is both electrically and ionically conducting, which not only allows for effective kinetics, but also improves the mechanical strength of the Zn anode.

[00334] Third, the Zn-pome has a smaller solid-electrolyte contact area than ZnO@C NPs (as shown in **FIG. 100D**), which can significantly reduce the dissolution rate during cycling. Hence, the longstanding limitations that have impeded the rechargeability of Zn electrode (i.e., Zn dendrite formation, Zn electrode shape change and ZnO passivation) can be significantly alleviated by the electrode design of the Zn-pome.

[00335] **Microemulsion-Based Assembly Of ZnO Nanoparticles Into Clusters**

[00336] The synthesis of Zn-pome is schematically illustrated in **FIGS. 102A-H**. The nanoparticles of ZnO (ZnONPs, Aldrich, 100 mg) were dispersed in 2 mL distilled water by ultrasonication for 5 minutes, and then the emulsion was mixed with 8 mL1-octadecene (ODE, Aldrich) solution containing 0.5 wt% of emulsion stabilizer (amphiphilic block copolymer, Hypermer 2524, Croda USA) and homogenized at 7000 rpm for 1 minute. The water in the mixture was evaporated at generally between 92 ~ 98 °C until no water vapor was observed. Then the ZnO clusters were collected by centrifugation for 5 minutes at 1500 rpm and washed with cyclohexane twice. The cyclohexane was dried on the hotplate at 80 °C. The final powder was calcined at 400 °C for 2 hours and 600 °C for 1 hour in air to remove the organics and condense the ZnO clusters.

[00337] **Carbon Coating On Clusters**

[00338] The powder of ZnO clusters (approximately 100 mg) was dispersed in 100 mL of water in 200 mL beaker, and 1000 μL Tris buffer pH 8.5 was added into the beaker while it was stirred at 200 rpm/min. The dopamine (200 mg, Aldrich)was added to the mixture, which was then stirred for 24 hours. The Zn-pome was collected by centrifugation at 1500 rpm and washed three times with distilled water. The water was subsequently removed by heating at 80 °C. The final Zn-pome was carbonized at 600 °C for 1 hour with a heating rate of 5 °C/min in argon atmosphere.

[00339] **Characterization**

[00340] The morphology analysis of bare ZnO, ZnO Clusters, and Zn-pome was carried out using SEM (Hitachi SU 8230). The morphology of Zn-pome and the carbon shell after etching the ZnO cluster was determined using TEM (Hitachi HT7700). The cross-sectioned images of clusters after being etched in 1M HCl were generated using FEI Nova Nanolab 200 FIB/SEM that included SEM imaging and FIB milling. The XRD pattern (Panalytical XPert PRO Alpha-1) for bare ZnO, ZnONPs@C, and Zn-pome were carried out with CuK-Alpha radiation.

[00341] The XPS was measured with AlK-Alpha (Thermo K-alpha). XPS survey spectra and high-resolution spectra of Zn2p, O1s, and C1s were measured. The weight percentage of ZnO in

Zn-pome was determined from the weight loss curves measured under air atmosphere on a thermogravimetric analysis (TGA) instrument (TA instrument, Q500) with a heating rate of 5 °C/min to 850 °C. The specific BET surface areas and pore size distribution were determined by physisorption (BELSORP-MAX, Microtrac BEL Japan, Inc.). The dissolved concentration of bare ZnO, ZnONPs@C, Zn-pome in 4M KOH electrolyte was measured with an ICP measurement: three samples with the same amount of active material were immersed into 4M KOH for 5 minutes, and the supernatant after centrifugation was measured. The ICP samples were filtered with 0.2 μm Acrodisc IC PES filters and diluted 100 times in ICP Matrix Solution.

[00342] Electrode preparation

[00343] Approximately 151 mg synthesized Zn-pome was gently ground in a mortar and transferred into a 4 mL vial with 0.5 g N-Methyl-2-pyrrolidone (NMP) (Aldrich), then the 1.2 g NMP solution containing PVDF (MTI, ~ 10 wt% of PVDF) was added to the sample and stirred for 30 minutes. The slurry was then cast onto Sn foil (Alfa) with a Doctor's blade and dried at 80 °C for 30 minutes.

[00344] Electrochemistry

[00345] 2032 coin cells were assembled under ambient environment, with Zn-pome anode, $Ni(OH)_2$ cathode obtained from commercial Zn-Ni batteries (PowerGenix), and a separator (GF 6, Whatman). The aqueous electrolyte contains 4M KOH (Aldrich), 2M K_2CO_3 (Aldrich) and 2M KF (Aldrich). The control cells were assembled using the same process as Zn-pome anode batteries, just with the Zn-pome anode replaced by the bare ZnO anode. The cells were charged and discharged at 1C for comparison between bare ZnO and Zn-pome, and the performances of the 5C rate discharge and self-discharge were investigated, respectively.

[00346] The SEM images of ZnO clusters were investigated under various magnifications (**FIGS. 103A-C**). These clusters with diameters in the range of approximately 1-6 μm primarily contained ZnO NPs. The rounded edge of the Zn-pome (**FIGS. 103D-F**) indicated that the ZnO clusters were adequately coated with a thin layer of carbon framework.

[00347] The detailed structure of the Zn-pome was investigated using HRTEM and FIB analysis. According to TEM images (**FIGS. 103G** and **104A**), the diameter of a typical Zn-pome microparticle was ~ 6 μm. When the Zn-pome was treated with 1M HCl to etch away ZnO, the hollow carbon framework could be clearly observed in TEM images (**FIGS. 103H** and **104C-F**). This indicated that each ZnO NP was individually coated by a thin layer of carbon framework with thickness of ~ 10-15 nm.

[00348] Moreover, the coated carbon framework was stable even without the solid "seeds," i.e., ZnO NPs, which is important for the structural stability of Zn-pome, especially when the active Zn material is mainly oxidized and dissolved after the deep discharge process. **FIG. 103I** exhibits the cross-sectional images of the Zn-pome microparticle obtained by FIB analysis. A secondary Zn-pome microparticle comprises ZnO NP clusters, in which each ZnO NP with a rounded surface was uniformly encapsulated by the carbon framework. More cross-sectional images are illustrated in **FIGS. 105-106**. The abovementioned morphology investigations of Zn-pome reveal that Zn-pome fabricated by bottom-up approach, comprising a robust carbon framework and ZnO nanoparticles, can be used as an anode in zinc-based batteries.

[00349] XRD and XPS were used to characterize the crystal structure and chemical composition of Zn-pome (**FIGS. 107A-C**). The XRD pattern of Zn-pome is similar to that of ZnO NPs and ZnO@C NPs. No characteristic peak of carbon was detected, indicating an amorphous coating of carbon on ZnO NPs. The reduced intensity of ZnO for Zn-pome suggests that ZnO NPs are uniformly covered by the carbon framework; therefore, it shields the diffractive signals of ZnO slightly.

[00350] Similarly, strong C1s signal and relatively weak Zn 2p and O1s signals in the XPS survey spectrum can be observed for Zn-pome in comparison with that for ZnO NPs. Accordingly, Zn-pome is characterized as ZnO NP clusters uniformly coated with an amorphous carbon layer. The content of carbon is found to be approximately 40% in Zn-pome based on TGA in air, as shown in **FIG. 107D**. The BET results reveal that the average pore size of the carbon shell is ~ 10 Å (**FIG. 107E**). This indicates that the carbon framework can properly mitigate the permeation of zincate through the shell structure.

[00351] To verify the ion-sieving ability of the carbon coating, the dissolution rate of ZnO in an aqueous alkaline electrolyte was investigated. Samples of ZnO NPs, ZnO@C NPs and Zn-pome containing equal amounts of zinc were immersed in 1 mL 4M KOH solutions at the same time. After a certain amount of time, the concentrations of Zn species dissolved in the solutions were analyzed by ICP. As shown in **FIG. 107F**, Zn-pome significantly reduced the portion of dissolved Zn in KOH (approximately 1.05%) in comparison with ZnO NPs (approximately 30.8%) and ZnO@C NPs (approximately 11%). This effect is ascribed to the synergistic function of carbon shell and secondary structure in Zn-pome. The diffusion of zincate in alkaline media is confined within the secondary particles, whereas the confined zincate can still be electrochemically reduced. The pomegranate structure is also expected to alleviate Zn dendrite formation and shape change (i.e., localized densification) during the charge/discharge process.

Thus, the long-standing constraints for rechargeability of Zn electrodes can be effectively overcome.

[00352] The electrochemical performances of Zn-pome and ZnO NPs were evaluated by a full cell configuration comprising $Ni(OH)_2$ cathode with excess capacity obtained from commercial zinc-nickel batteries. The cells were cycled at 1C in a voltage window between 1.5 and 2.0 V in 2M KF, 2M K_2CO_3 and 4M KOH. It should be noted that the battery testing protocols used in this study were extremely harsh in three aspects: (1) limited electrolyte: 2032 coin cells were used with a limited amount of electrolyte (**FIG. 108**) rather than beaker cells with excess electrolyte because coin cells better represent real operating conditions; (2) ZnO-free electrolyte: ZnO-saturated KOH electrolyte is commonly used to provide higher specific capacity and longer cycle life, but zinc species initially present in the electrolyte probably contribute to the capacity of the cell and conceal the actual performance of active zinc material on the electrode; and (3) approximately 100% DOD: under 100% DOD, the full energy density can be delivered. However, < approximately 50% DOD is used for Zn anodes because of the passivation problem.

[00353] Under such harsh testing conditions, the cells containing Zn-pome anode (Zn-pome/$Ni(OH)_2$) exhibited remarkable capacity and cycle life, which were superior to those of ZnO NP and ZnO NPs@C anodes with $Ni(OH)_2$ cathode, respectively.

[00354] As shown in **FIG. 109A** and **FIGS. 110A-B**, although the specific capacity of Zn NPs/$Ni(OH)_2$ was higher than that of Zn-pome in the first few cycles, the discharge capacity of Zn NPs/$Ni(OH)_2$ decreased sharply over 20 cycles due to the fading of the anode resulting from the high dissolution rate of ZnO in strong aqueous alkali electrolyte. The problem of abrupt capacity decay of the control sample after 25 cycles can best be ascribed to high dissolution of zinc, which subsequently results in the formation of dendrites and substantial electrode shape change after several cycles from repeated redistribution of the active material.

[00355] Other issues stem from the HER on the surface of zinc, which not only worsens efficient utilization of zinc but also leads to swelling of the cell, causing the cell to crack and the electrolyte to dry out. The loose contact in the cells inflated by hydrogen further causes abrupt capacity fading. In contrast, the capacity of Zn-pome/$Ni(OH)_2$ is stable for 50 cycles and then gradually decreases, showing better cyclability than that of Zn NPs/$Ni(OH)_2$. This improvement can be ascribed to the ion blocking ability of the carbon shell in the Zn-pome anode and the smaller solid-electrolyte contact area. **FIG. 109B** presents the typical charge/discharge profiles of the Zn-pome/$Ni(OH)_2$ battery in the 1^{st}, 10^{th}, 20^{th}, 30^{th} and 40^{th} cycles. The average discharge

voltage of the Zn-pome/$Ni(OH)_2$ cell is maintained at approximately 1.80 V after 40 cycles, indicating excellent cycling stability.

[00356] The improved performance of Zn-pome/$Ni(OH)_2$ cells compared to that of Zn NPs/$Ni(OH)_2$ is due to the ion-sieving ability of the carbon shell and secondary particle structure. The increase in charging voltage in consecutive cycling is possibly due to the accumulation of hydrogen evolved in the reduction of water. Although managing gas generation in sealed cells remains a concern, hydrogen evolution can be effectively suppressed by the adjustments of electrolyte (such as the use of water-in-salt or solid state additives).

[00357] The electrochemical performance of Zn-pome/$Ni(OH)_2$ is also superior to that of Zn NPs/$Ni(OH)_2$ at a higher discharge rate (5C), as shown in **FIGS. 109C** and **111**. The discharge capacity of Zn-pome/$Ni(OH)_2$ is maintained approximately 400 mAh/g for 45 cycles (*e.g.*, 411 mAh/g at the 44^{th} cycle). However, Zn NPs/$Ni(OH)_2$ suffers from a quick decay of discharge capacity after the 3^{rd} cycle (merely approximately 186 mAh/g at the 21^{st} cycle). Accordingly, the superior performances (both specific capacity and cyclability) of Zn-pome in comparison with that of ZnO NPs clearly demonstrate the merits of the nano-design of pomegranate-structure ZnO.

[00358] To further investigate dissolution-resistivity, coin cells were used for one cycle at 0.5C and then rested for 24 hours before resuming cycling at 1C. During the 24 hour resting period, Zn anodes were in the discharged state, and ZnO, the dominant species, rapidly dissolved in the electrolyte if left unprotected (**FIG. 109F**). As shown in **FIGS. 109D** and **112**, Zn NPs/Ni(OH)2 exhibited fast capacity fading. On the other hand, Zn-pome/$Ni(OH)_2$ still exhibited high capacity after resting and maintained approximately 84% of capacity even after 40 cycles (on the basis of the 3rd cycle), indicating that Zn-pome anode is effective in retaining Zn active species due to the carbon framework.

[00359] The morphology evolution of Zn-pome was investigated by SEM (**FIGS. 109E-G**, and **113A-L**). The Zn-pome anode maintained the microspheric morphology after ten charge/discharge cycles, indicating the robust morphology of the pomegranate structure. Therefore, Zn-pome is considered to be a novel Zn anode material that can mitigate the Zn dendrite formation, shape change and passivation issues in alkaline Zn-ion batteries.

[00360] A nanoscale pomegranate-inspired hierarchical Zn anode material (Zn-pome) is fabricated via a bottom-up microemulsion approach. Each Zn-pome microsphere is around 6 μm in size and is composed of on the order of 10^5 ZnO nanoparticles individually encapsulated by an

amorphous, microporous, and conductive carbon shell that slows down the dissolution of zincate intermediate species during cycling. The secondary structure further suppresses the zinc dissolution by decreasing the electrode-electrolyte contact area. ICP analysis confirms that Zn-pome exhibits significantly suppressed dissolution of zinc compared to ZnO NP nano-particles and ZnO@C nanoparticles.

[00361] The Zn-pome anode demonstrates remarkable capacity and cycle stability under extremely harsh testing conditions (limited electrolyte, ZnO-free electrolyte, and 100% DOD); it also retains high capacity after long-term resting in a discharged state, in which ZnO in the electrode has a massive tendency to dissolve. The success of the Zn-pome anode can be ascribed to inventive design principles that manage soluble intermediates during repeated electrochemical cycling; this is important for future designs of Zn aqueous anodes as well as other battery systems involving soluble intermediates (*e.g.*, lithium-sulfur batteries).

[00362] **Ion-Sieving Carbon Nanoshells for Deeply Rechargeable Zn-Based Aqueous Batteries**

[00363] An optimized structure to solve Zn anodes' passivation and dissolution problems simultaneously is fashioned. Specifically, the structure features (1) a sub-micrometer ZnO particle as the core, and (2) an ion-sieving carbon coating as the shell. First, unlike the bulk Zn foil which is several hundreds of micrometers thick, sub-micrometer particles will not have a passivation problem and will remain active in extended cycling. Starting from ≈ 100 nm ZnO nanoparticles (discharged state) rather than Zn nanoparticles (charged state) was selected because on the synthesis and scalability aspect, compared to Zn, ZnO is much easier to make into nanostructures which serves as the starting material.

[00364] On the battery performance aspect, starting from Zn to ZnO will rupture the carbon shell due to volume expansion. It is of note that nanoparticles with even smaller diameter offer no further benefit to reversibility but have much more severe dissolution concerns. The carbon shell is deposited on the ZnO nanoparticles through carbonization of a uniform polydo-pamine coating. The ability of polydopamine coatings to form a uniform shell with controllable thickness has been confirmed before. The present two-step synthesis method is relatively simple and scalable, and the carbon shell thickness is controllable by simply adjusting the dopamine mass during synthesis.

[00365] **ZnO@C Synthesis**

[00366] 100 mg commercial ZnO nanoparticles (< approximately 100 nm, Aldrich) were dispersed into 100 mL DI water followed by 10 minutes of ultrasonication, then 1 mL of Tris-

buffer (pH 8.5, Alfa) and 100 (1:1), 200 (2:1) and 300 (3:1) mg of dopamine hydrochloride (Aldrich) were added and mixed for different nanoshell thickness, and then stirred for 24 hours. The fabricated polydopamine-coated ZnO nanoparticles ZnO@P were collected and washed with DI water two times in the centrifuge and dried overnight. Then the ZnO@P particles were heated in a tube furnace under Ar gas to 400 °C with a rate of 1 °C/min and stayed for two hours, then to 600 °C with a rate of 5 °C/min and stay for one hour.

[00367] Characterization

[00368] The morphology analysis of ZnO@C nanoparticles was carried out using SEM (Hitachi SU 8230) and TEM (Hitachi HT7700). The weight percentage of carbon for the sample was determined from the weight loss curves measured under ambient environment on a TGA (TA instrument, Q500) with a heating rate of 5 °C/min to 850 °C. The threshold ZnO@P calcination temperature was measured with TGA by heating the sample in Ar gas to 900 °C with a heating rate of 5 °C/min.

[00369] The XRD pattern (Panalytical XPert PRO Alpha-1) for both bare ZnO and ZnO@C nanoparticles were carried out with CuK-Alpha radiation. The specific BET surface areas and pore size distribution were determined by physisorption (BELSORP-MAX, Microtrac BEL Japan, Inc.). The XPS was measured with AlK-Alpha (Thermo K-alpha), XPS survey spectra and high-resolution Zn 2p, O1s, C1s spectra were measured.

[00370] The dissolved concentration of both samples in 4M KOH electrolyte was measured with an ICP measurement, the samples with the same among of active material were immersed into 4M KOH for 5 minutes, 1 day and 10 days, and the supernatant after centrifugation was measured. The ICP samples were filtered with 0.2 μm Acrodisc IC PES filters and diluted 100 times in ICP Matrix Solution.

[00371] Electrode Preparation

[00372] Synthesized ZnO@C or as-received ZnO nanoparticles was mixed with carbon black (MTI) and PVDF (MTI) of an 80:10:10 ratio and grinded in a mortar, then NMP (Aldrich) of two times the mass of slurry was added to the sample and stirred in a 4 mL vial for 8 hours to ensure the slurry uniformity. The slurry was then casted onto Sn foil (Alfa) with a Doctor's blade and dried at 90°C for 1 hour then calendared.

[00373] Electrochemistry

[00374] 2032 coin cells were assembled under atmosphere environment with the can at the bottom, followed by the ZnO anode, 100 μL electrolyte immersed separator, then the $Ni(OH)_2$ cathode, spacer, spring and the cap. A commercial $Ni(OH)_2$ electrode (PowerGenix) was used as the cathode. The separator used for battery testing was glass fiber filter (GF 6, Whatman) unless otherwise noted.

[00375] The composition of the electrolyte was KOH (4M, Aldrich) with $_{K2CO3}$ (2M, Aldrich) and KF (2M, Aldrich) added to enhance ionic conductivity. Zn mesh (Dexmet) was discharged with 1 mA in 10 μL with a Celgard 3501 separator. For bulk Zn foil battery testing, Zn foil (0.25 mm, Alfa) was used for the anode while other battery parts remained the same and the GCPL (galvanostatic cycling with potential limitation) test was performed with 2 mAh at 1C.

[00376] The voltage cutoff for GCPL was 2 V and 1.5 V for the charging and discharging processes, the cells were charged and discharged at 1C for comparison between bare ZnO and ZnO@C nanoparticles. The mass loading of bare ZnO and ZnO@C was 1.03 mg and 0.904 mg for the comparison at low mass loading. Another set of experiments were conducted with 0.941 mg of bare ZnO and 0.98 mg of ZnO@C. The capacity for each cell was calculated with **Equation 16**:

$$Capacity = \frac{Active\ mass\ of\ material}{Molar\ mass\ of\ material} * \frac{nF}{\frac{3.6C}{mAh}} \quad \textbf{(16)}$$

[00377] Where n is the number of electrons transferred in the relevant reaction, and F is the Faraday constant.

[00378] **Computation**

[00379] Planewave DFT calculations were performed within the generalized gradient approximation of Perdew, Burke, and Ernzerhof (PBE) using the Vienna ab initio Simulation Package (VASP). Projector augmented wave pseudopotentials were used for all calculations. A planewave basis set cutoff energy of 600 eV, k-point sampling at Γ, and an interionic force requirement of forces < 0.01 eV/Å were used to model molecular species in a cubic box with 20 Å edge length. All ions were allowed to relax freely to convergence, and molecular species size was determined from the ionic coordinates.

[00380] The characterizations and battery performance are for the powders synthesized with a 2:1 dopamine hydrochloride to ZnO nanoparticles ratio except otherwise specified.

[00381] As noted, the pore size of the carbon nanoshell is tailored to allow hydroxide ions to pass through while blocking transport of zincate ions. During charging, the zincate intermediate is trapped inside the carbon shell and reacts with Zn within the shell, preventing deposition of Zn in another location. In contrast, the OH^- by-product can diffuse out freely through the micropores in the shell due to their smaller size. During discharging, the trapped Zn oxidizes to form ZnO with the participation of OH^- coming from outside the shell.

[00382] The uniform polydopamine shell is first coated onto ZnO nanoparticles by stirring the particles with dopamine hydrochloride in Tris buffer (pH 8.5) for 24 hours at room temperature in the presence of air. After carbonization at 600 °C, ZnO@C nanoparticles are obtained.

[00383] The particles are of short rod-like shapes. An SEM image shows a quasi-spherical morphology of ZnO@C (**FIGS. 114B** and **115**), which indicates the coating is successful, and the particles are of slightly larger size than bare ZnO. The TEM image in **FIG. 114B** shows a single ZnO@C nanoparticle with an amorphous carbon shell coated uniformly on the surface and the thickness of the carbon shell is approximately 20-30 nm. Notice that the coating thickness is tunable by simply changing the dopamine hydrochloride mass.

[00384] TEM images of single coated particles with different coating thickness are shown in **FIG. 116**. 600 °C was selected as the carbonization temperature because the ZnO core is reduced to Zn vapor and escapes at above 680 °C, determined from the TGA results above, and **FIG. 117**.

[00385] TEM results confirm partial ZnO loss inside the carbon shell at 700 °C and complete loss at 800 °C. This phenomenon is also confirmed by the fact that 100 mg ZnO@polydopamine becomes ≈ 20 mg after 800 °C carbonization, and ≈ 70 mg after 600 °C treatment, respectively. Complete and self-supporting hollow carbon nanoshells can be obtained after etching away ZnO using HCl (**FIG. 114E**). The carbon mass fraction in the ZnO@C nanoparticles is determined to be 41% by TGA in ambient air (**FIG. 114C**). The XRD patterns in **FIG. 114F** for both the bare ZnO and ZnO@C have the same peak positions, indicating the retention of ZnO hexagonal wurtzite crystalline structure after coating. No signature of crystallinity is observed for the carbon shell.

[00386] To investigate the nature of the zincate and hydroxide anion species, density functional theory (DFT) calculations discussed above were performed to study the structure and size of each species. The sizes of hydroxide ion and zincate ion, without solvation shells, are simulated to be 2.42 and 6.09 Å, respectively (**FIG. 118A**). These "rigid molecule" sizes computed here are substantially smaller than the sizes of these ions under thermal motion, but that the calculations support the much smaller size of the hydroxide anion relative to the zincate anion species. An

effective ion-sieving nanoshell should be uniform and have a pore size between the sizes of hydroxide and zincate ions.

[00387] XPS results confirm the uniformity of the carbon coating. As shown in **FIG. 118B**, bare ZnO has strong Zn and O signals, while ZnO@C only has a C signal. A comparison between both samples' high-resolution Zn spectra further confirms the complete coverage of carbon on ZnO in ZnO@C (**FIG. 118C**). The BET method is used to analyze the pore size of carbon-coated ZnO (**FIG. 118D**). The pore width is calculated from the adsorption/desorption isotherm to be around 5-8 Å (**FIG. 118E**), between the sizes of hydroxide and zincate ions plus the solvation shell.

[00388] Hydroxide species are expected to be more mobile and zincate species to be less mobile when diffusing through the nanoshell. In comparison, uncoated ZnO particles do not have pores in the same range. To directly verify the ability of the sample to prevent ZnO@C from dissolving into the alkaline electrolyte, both ZnO and ZnO@C powders are soaked in KOH (4M) for 5 minutes, 1 day, and 10 days and the dissolved $Zn(OH)_4^{2-}$ are quantified using inductively coupled plasma atomic emission spectroscopy (ICP-AES). As shown in **FIG. 118F**, although Zn still dissolves into the electrolyte, the dissolved $Zn(OH)_4^{2-}$ from bare ZnO is much lower and slower than that from ZnO@C, which confirms that the carbon nanoshell functions as a barrier to slow down the zincate escape.

[00389] To evaluate the electrochemical performance of ZnO@C nanoparticle anodes, they were paired with commercial $Ni(OH)_2$ counter electrodes with largely excess areal capacity. 2032 coin-type batteries are used to limit the amount of electrolyte and mimic practical application conditions. A $Ni(OH)_2$ counter electrode is used rather than an air electrode to evaluate the present anode because $Ni(OH)_2$ has simpler electrochemistry, fewer factors influencing its battery performance, and it is compatible with sealed coin cells.

[00390] The cells are galvanostatically charged to the theoretical capacity (658.5 mAh/g(ZnO)) and fully discharged to 1.5 V at 1C rate and 100% DOD. An upper voltage cutoff of 2 V is set to avoid electrolyte decomposition. **FIG. 119** compares the specific capacity of ZnO@C anode with a bare ZnO anode at similar mass loading. Performance of Zn foil, which degrades quickly in only seven cycles due to severe ZnO passivation is also shown in the same plot. The bare ZnO anode lasts for 20 cycles before severe capacity degradation is evident, indicating the success of decreasing feature size in mitigating passivation. Without nanoshell encapsulation, zincate is able to dissolve and diffuse prior to redeposition, and electrode morphology changes over cycling. The ZnO@C anode outlasts the bare ZnO anode with ≈ 1.6 times longer life in terms of cycles, we attribute the increased performance to reduction in the mobility of zincate.

[00391] Noticeably, bare ZnO quickly decays to half of the initial energy storage capacity, while ZnO@C has a significantly slower decay and longer cycle life. Another set of cycling data shown in **FIG. 120** demonstrates similar battery performance. This supports the hypothesis that the carbon nanoshell has suitable pore sizes to reduce the transport of zincate ions while allowing the hydroxide ions to pass freely. The carbon shell also increases the conductivity of the anode material, which is helpful for preventing the formation of a passivation layer, also with the help of the carbon nanoshell the overpotential for every single cycle of the battery with ZnO@C is lower than that of bare ZnO (**FIGS. 121-122**).

[00392] The nitrogen doping also facilitates the conductivity of the carbon layer and charge transfer at the interface. **FIG. 123** shows the voltage versus specific capacity during the charging and discharging processes. The performances of the charging processes are similar, indicating a stable performance. **FIGS. 124A-D** shows the SEM images of both bare and coated ZnO anodes before cycling and after three cycles. Noticeably, the surface of bare ZnO anode has holes after cycling, labeled with yellow arrows in **FIG. 124B**, which is a result of ZnO dissolution. In contrast, the ZnO@C anode maintained the electrode morphology, which confirms the ability of the carbon shell on ZnO@C to mitigate Zn anode dissolution and passivation. It is also confirmed from the TEM image in **FIG. 125** that after charging the active material is still confined in the nanoshell.

[00393] To compare the battery performance under harsh testing conditions reported in this work to the performance under mild testing conditions in most of the past reports, we test a ZnO@C pouch cell using electrolyte saturated with ZnO (**FIG. 127**), and the battery reaches 100 cycles with >90% efficiency under 100% DOD at 1C.

[00394] Another ZnO@C pouch cell using electrolyte saturated with ZnO shows a performance of ≈ 95% efficiency and 100% retention for 500 cycles (**FIG. 128**), but the battery is cycled at 12C. The comparison is clear evidence that a deeply rechargeable anode in lean electrolyte configuration is in demand and necessary to reflect the true performance of battery active material in Zn-based aqueous batteries while the drastically enhanced battery performance in most of the past reports is attributed to the ZnO saturated in the electrolyte and low utilization of active material.

[00395] In yet another exemplary embodiment of the present invention, the dissolution and passivation problems of Zn anode materials is simultaneously solved by applying an ion-sieving carbon nanoshell coating onto ZnO nanoparticles which are well below the critical passivation thickness. The carbon nanoshell is uniform and complete. The micropores successfully slow down ZnO dissolution and limit zincate ion transport, but allow hydroxide

ions to pass freely, and the nanoshells' rigidity prevents anode shape change and dendrite growth.

[00396] The battery lifetime is greatly enhanced with the ZnO@C anode; the coated anode outperforms bare ZnO and Zn foil with ≈ 1.6 and 6 times longer cycle life in a coin cell with harsh testing conditions, respectively. The synthesis is relatively simple and scalable with a controllable nanoshell thickness.

[00397] It is to be understood that the exemplary embodiments and claims disclosed herein are not limited in their application to the details of construction and arrangement of the components set forth in the description and illustrated in the drawings. Rather, the description and the drawings provide examples of the exemplary embodiments envisioned. The exemplary embodiments and claims disclosed herein are further capable of other exemplary embodiments and of being practiced and carried out in various ways. Also, it is to be understood that the phraseology and terminology employed herein are for the purposes of description and should not be regarded as limiting the claims.

[00398] Accordingly, those skilled in the art will appreciate that the conception upon which the application and claims are based can be readily utilized as a basis for the design of other structures, methods, and systems for carrying out the several purposes of the exemplary embodiments and claims presented in this application. It is important, therefore, that the claims be regarded as including such equivalent constructions.

CLAIMS

We claim:

1. An electrode comprising:

anodic core elements comprising core material, the core material having a core material passivation interface size, a core material intrinsic dissolution rate, and a core material hydrogen evolution reaction (HER) rate; and

a conformal shell coating on an outer surface of the anodic core elements forming core/shell structures;

wherein the anodic core elements comprise a feature size smaller than the core material passivation interface size;

wherein a dissolution rate of the core material from the core/shell structures is less than the core material intrinsic dissolution rate; and

wherein the HER rate of the shell is less than the core material HER rate.

2. The electrode of Claim 1, wherein the electrode is deeply rechargeable.

3. The electrode of Claim 1, wherein the electrode has a depth of discharge (DOD) of greater than 50%.

4. The electrode of Claim 1, wherein the core material is selected from the group comprising a metal, metal oxide, metal sulfide, and combinations thereof.

5. The electrode of Claim 1, wherein the core material is selected from the group comprising Zn, Li, Na, Mg, Ca, ZnO, Li_2O, Na_2O, MgO, CaO, ZnS, Li_2S, Na_2S, MgS, CaS, and combinations thereof.

6. The electrode of Claim 1, wherein the conformal shell coating comprises a cermet.

7. The electrode of Claim 1, wherein the conformal shell coating comprises carbon.

8. The electrode of Claim 1, wherein the core/shell structures have a specific discharge capacity of at least 70% of the theoretical limit of the specific discharge capacity of the core material.

9. The electrode of Claim 1, wherein the electrode has a coulombic efficiency greater than about 93.5%.

10. The electrode of Claim 1, wherein the anodic core/shell structures are formed by a deposition technique of layers of the conformal shell coating over a deposition cycling series; and

wherein a morphology of the anodic core elements prior to the deposition cycling series is substantially the same as a morphology of the core/shell structures after the deposition cycling series.

11. The electrode of Claim 1, wherein the anodic core/shell structures are formed by an atomic layer deposition (ALD) technique of layers of the conformal shell coating over an ALD cycling series; and

wherein a morphology of the anodic core elements prior to the ALD cycling series is substantially the same as a morphology of the core/shell structures after the ALD cycling series.

12. The electrode of Claim 1, wherein:

the anodic core elements are nanorod structures;

the core material comprises ZnO; and

the conformal shell coating comprises TiN_xO_y.

13. The electrode of Claim 12, wherein the feature size is diameter of the nanorod structures; and

wherein the diameter is less than approximately 2 μm.

14. The electrode of Claim 13, wherein the diameter is less than approximately 500 nm.

15. The electrode of Claim 12, wherein the conformal shell coating has a thickness of less than 10 nm.

16. The electrode of Claim 15, wherein the conformal shell coating has a thickness of approximately 6 nm.

17. The electrode of Claim 12, wherein the core/shell structures have a specific discharge capacity of over 500 mAh/g.

18. The electrode of Claim 1, wherein:

the anodic core elements are nanoparticles;

the core material comprises ZnO; and

the conformal shell coating comprises carbon.

19. The electrode of Claim 18, wherein the conformal shell coating comprises an amorphous, microporous, and conductive carbon.

20. The electrode of Claim 19, wherein an assembly of core/shell structures form Zn-pome microspheres (pomegranate-like nanoporous carbon-coated ZnO clusters).

21. The electrode of Claim 20, wherein each Zn-pome microsphere has a diameter of approximately 6 μm.

22. The electrode of Claim 20, wherein each Zn-pome microsphere comprises on the order of approximately 10^5 core/shell structures.

23. The electrode of Claim 18, wherein the feature size is diameter of the nanoparticles; and

wherein the diameter is less than approximately 2 μm.

24. The electrode of Claim 23, wherein the diameter is less than approximately 100 nm.

25. The electrode of Claim 18, wherein the conformal shell coating has a thickness of less than approximately 15 nm.

26. The electrode of Claim 18, wherein the conformal shell coating has a thickness of approximately 10 nm.

27. The electrode of Claim 20, wherein the Zn-pome microspheres have a specific discharge capacity of over 400 mAh/g.

28. The electrode of Claim 1, wherein:

the anodic core elements are nanoparticles;

the core material comprises ZnO; and

the conformal shell coating comprises carbon.

29. The electrode of Claim 28, wherein the conformal shell coating comprises an ion-sieving carbon shell.

30. The electrode of Claim 28, wherein the feature size is diameter of the nanoparticles; and

wherein the diameter is less than 2 μm.

31. The electrode of Claim 30, wherein the diameter is less than approximately 100 nm.

32. The electrode of Claim 28, wherein the conformal shell coating has a thickness of less than 30 nm.

33. The electrode of Claim 28, wherein the conformal shell coating has a thickness of approximately 20 nm.

34. A rechargeable battery system comprising:

anodic core/shell structures comprising a ZnO core coated with a shell layer of TiN_xO_y;

an aqueous electrolyte; and

a cathode.

35. The rechargeable battery system of Claim 34, wherein the rechargeable battery system is deeply rechargeable.

36. The rechargeable battery system of Claim 34, wherein the rechargeable battery system has a depth of discharge (DOD) of greater than 50%.

37. The rechargeable battery system of Claim 34, wherein each of the core/shell structures function as an electrical pathway and is electrochemically active; and

wherein the dissolution rate of Zn from the anodic core/shell structures is less than the intrinsic dissolution rate of ZnO.

38. The rechargeable battery system of Claim 34, wherein the anodic core/shell structures comprise nanorod structures.

39. The rechargeable battery system of Claim 34, wherein the cathode comprises $Ni(OH)_2$.

40. The rechargeable battery system of Claim 34, wherein the anodic core/shell structures are formed by an atomic layer deposition (ALD) technique of the TiN_xO_y on the core over an ALD cycling series; and

wherein a morphology of the core prior to the ALD cycling series remains substantially the same as the morphology of the core/shell structures after the ALD cycling series.

41. The rechargeable battery system of Claim 40, wherein the ALD cycling series comprises at least 100 cycles.

42. The rechargeable battery system of Claim 34, wherein over an electrochemical cycling series of the battery, the morphology of the core/shell structures after the electrochemical cycling series is substantially the same as the morphology of the core/shell structures prior to the electrochemical cycling series.

43. The rechargeable battery system of Claim 34, wherein a mass loading of the anodic core/shell structures is greater than approximately 1.7 mg/cm^2.

44. The rechargeable battery system of Claim 34, wherein the core has a core specific discharge capacity;

wherein the core/shell structures have a core/shell specific discharge capacity;

wherein if the battery has a core electrochemical cycling series defined as the number of cycles until the core specific discharge capacity decays to 50%;

then a core/shell electrochemical cycling series defined as the number of cycles until the core/shell specific discharge capacity decays to 50% is at least 150% longer than the core electrochemical cycling series.

45. A rechargeable battery system comprising:

anodic Zn-pome microspheres each comprising a pomegranate-like assembly of individual ZnO nanoparticles coated with a shell layer of carbon;

an aqueous electrolyte; and

a cathode.

46. The rechargeable battery system of Claim 45, wherein the rechargeable battery system is deeply rechargeable.

47. The rechargeable battery system of Claim 45, wherein the Zn-pome microspheres are configured with ion-sieving ability due both to the shell layer of carbon and the micro-structure of the Zn-pome microsphere; and

wherein the dissolution rate of Zn from the Zn-pome microspheres is less than the intrinsic dissolution rate of ZnO.

48. The rechargeable battery system of Claim 45, wherein the cathode comprises $Ni(OH)_2$.

49. The rechargeable battery system of Claim 45, wherein the Zn-pome microspheres are formed by a bottom-up microemulsion approach.

50. A rechargeable battery system comprising:

anodic core/shell nanoparticles comprising a ZnO core coated with a shell layer of carbon;

an aqueous electrolyte; and

a cathode.

51. The rechargeable battery system of Claim 50, wherein the rechargeable battery system is deeply rechargeable.

52. The rechargeable battery system of Claim 50, wherein the conformal shell coating comprises an ion-sieving carbon shell.

53. The rechargeable battery system of Claim 50, wherein the core/shell nanoparticles have a diameter less than approximately 2 μm.

54. The rechargeable battery system of Claim 50, wherein the core/shell nanoparticles have a diameter less than approximately 100 nm.

55. The rechargeable battery system of Claim 52, wherein the conformal shell coating has a thickness of less than approximately 30 nm.

56. The rechargeable battery system of Claim 52, wherein the conformal shell coating has a thickness of approximately 20 nm.

57. The rechargeable battery system of Claim 50, wherein the cathode comprises $Ni(OH)_2$.

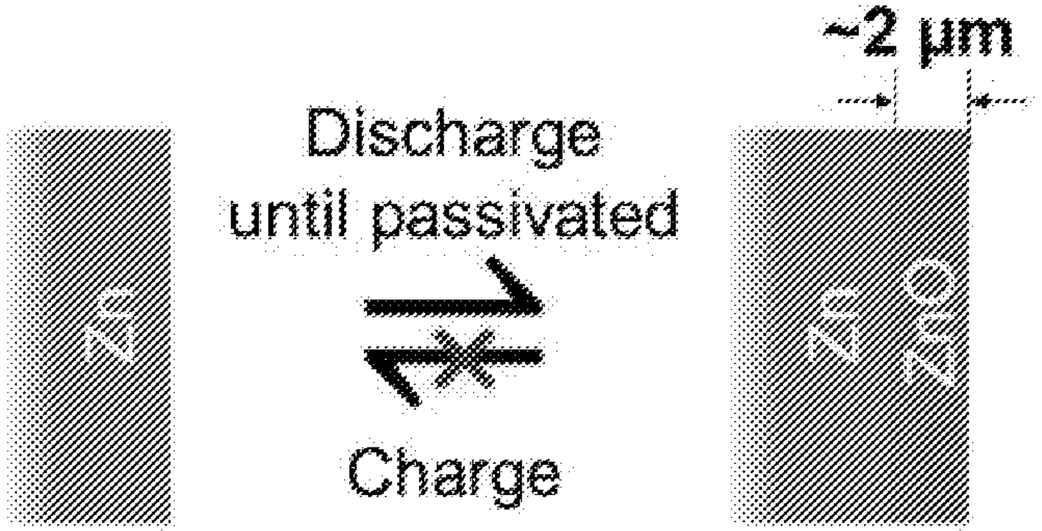


FIG. 1A

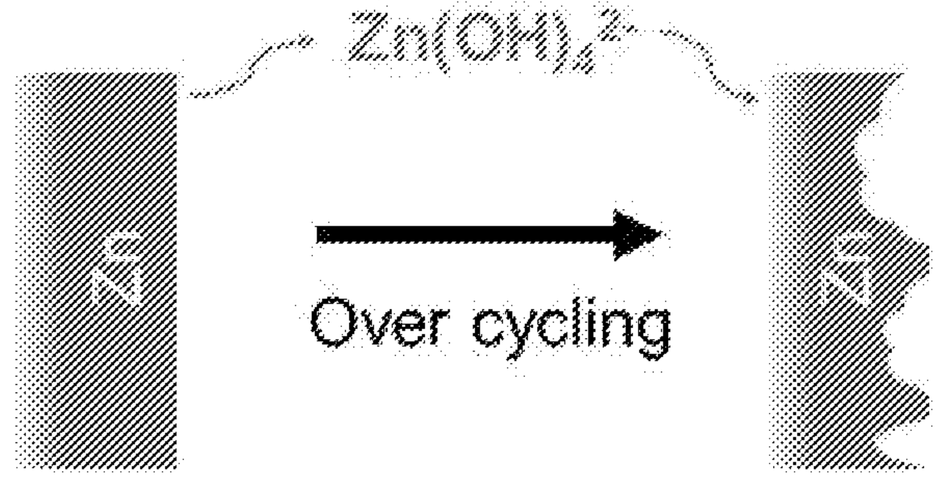


FIG. 1B

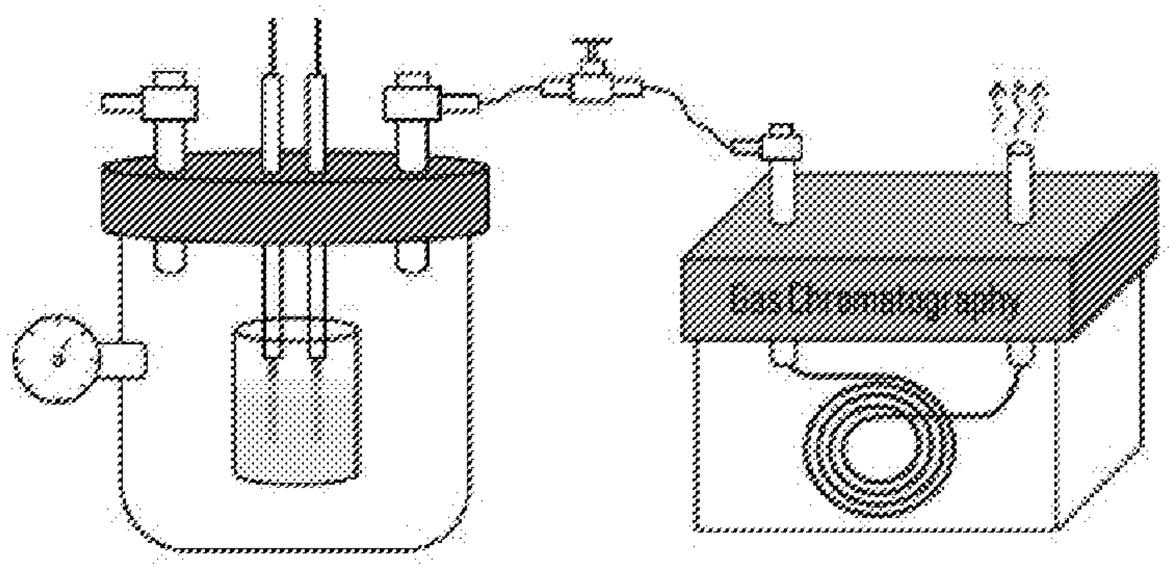


FIG. 1C

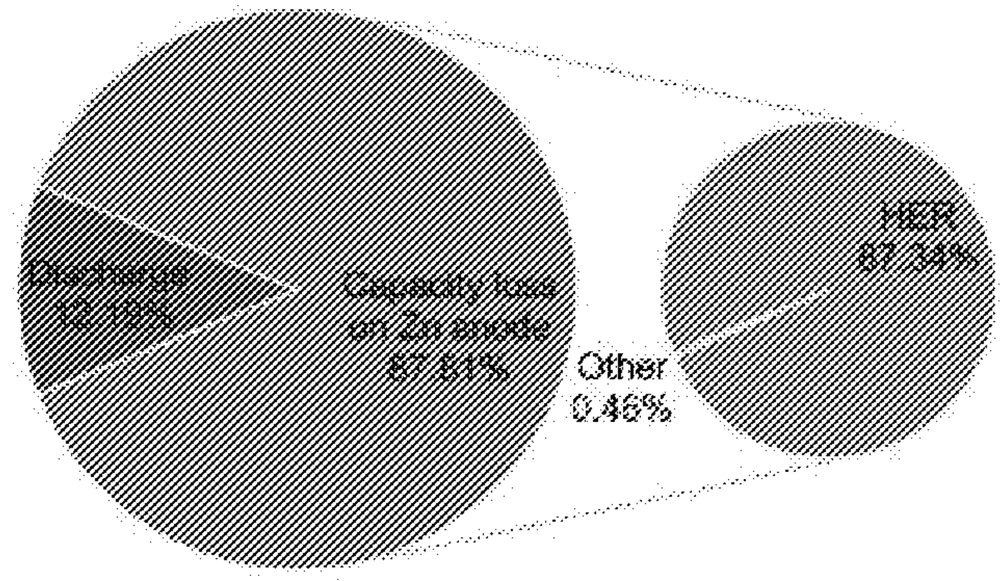


FIG. 1D

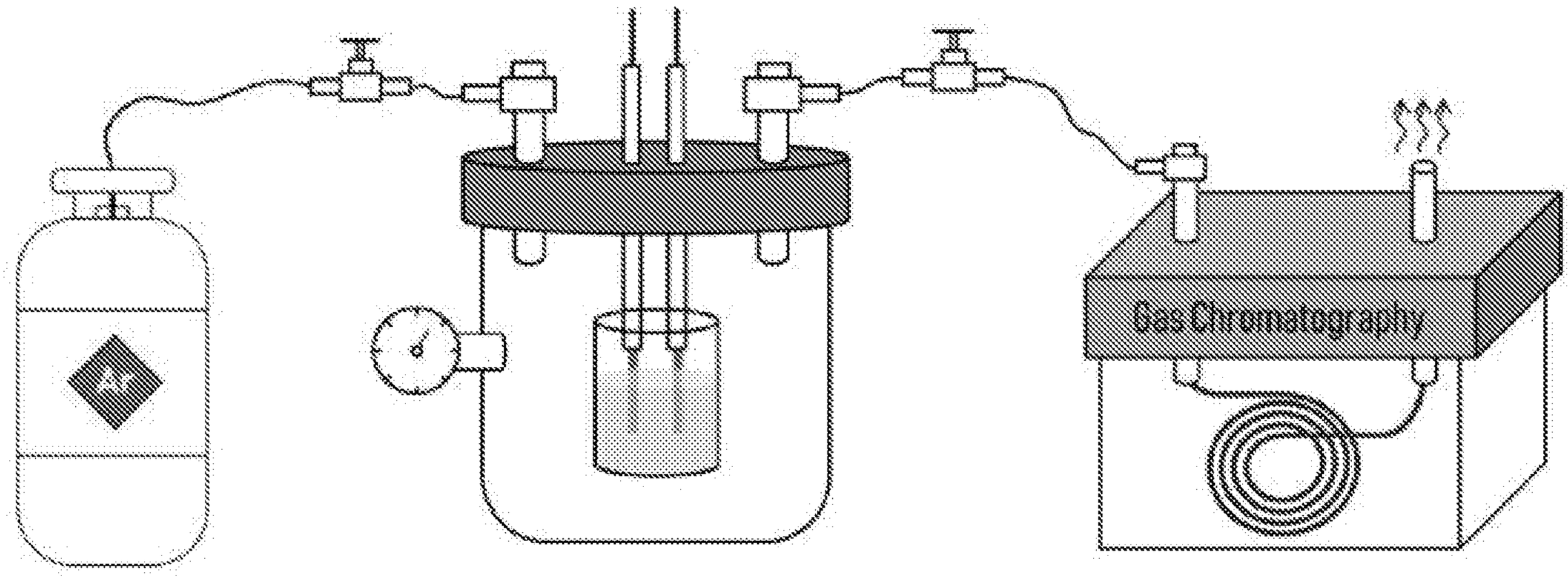


FIG. 2A

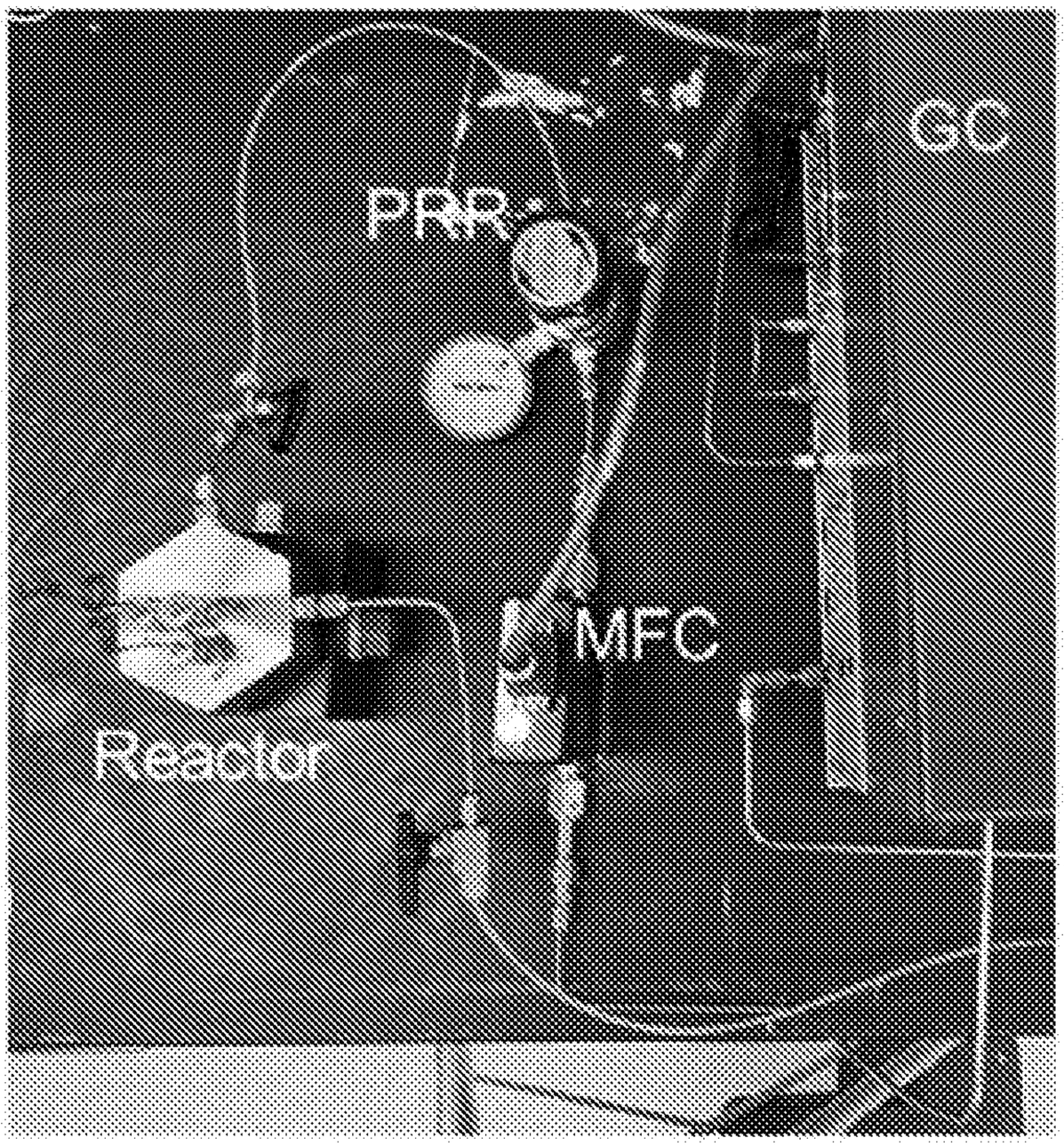


FIG. 2B

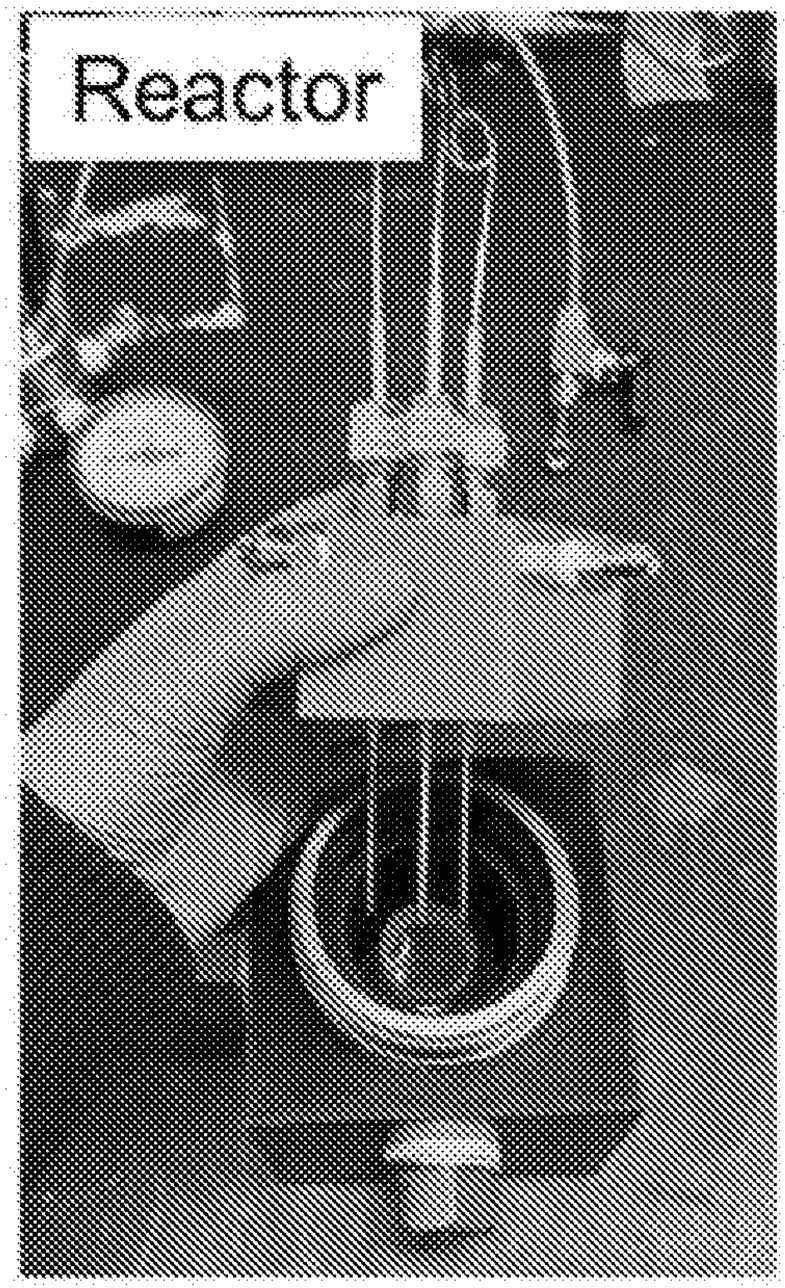


FIG. 2C

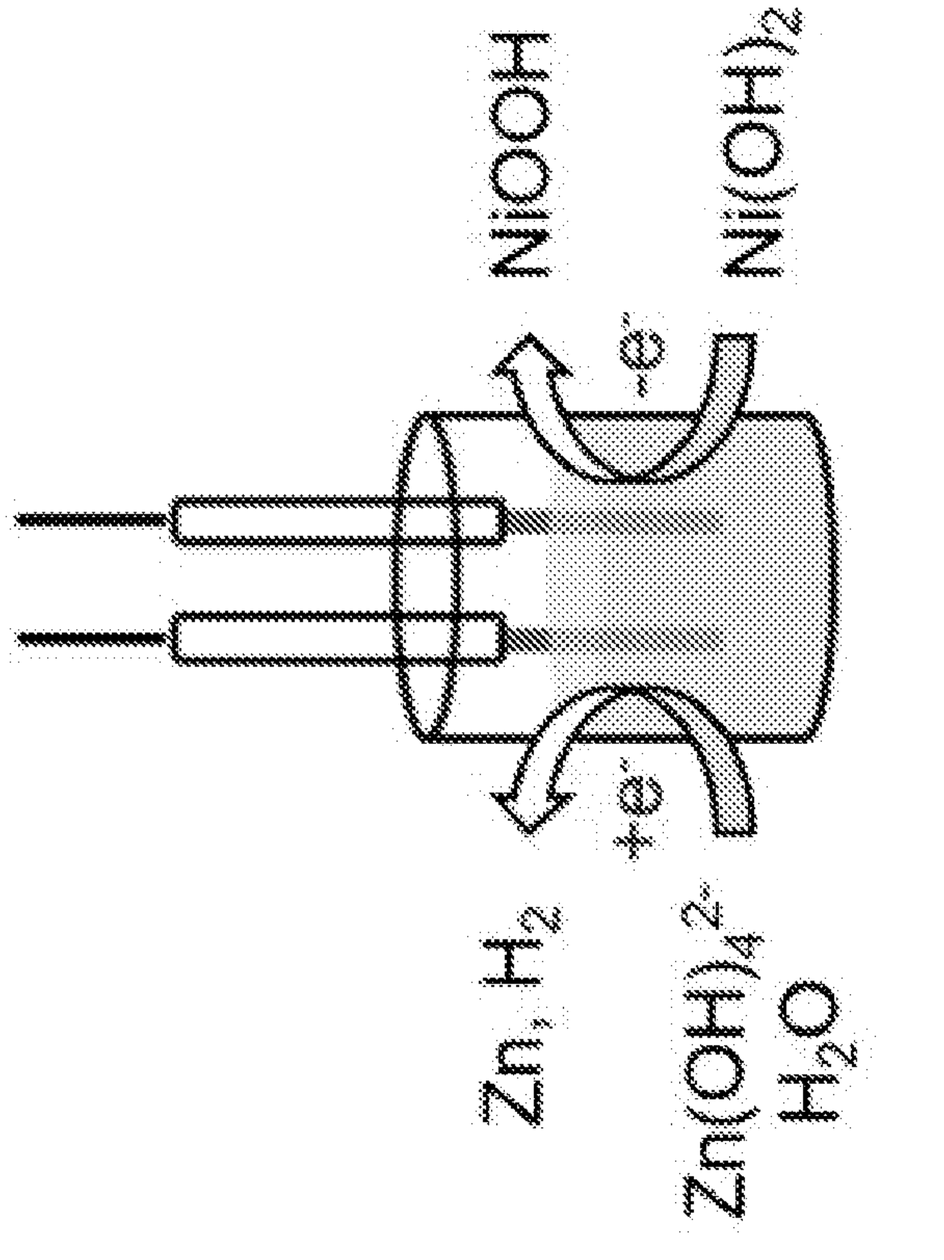

NiOOH
Ni(OH)2
e-
e-
Zn, H2
Zn(OH)4 2-
H2O

FIG. 3B

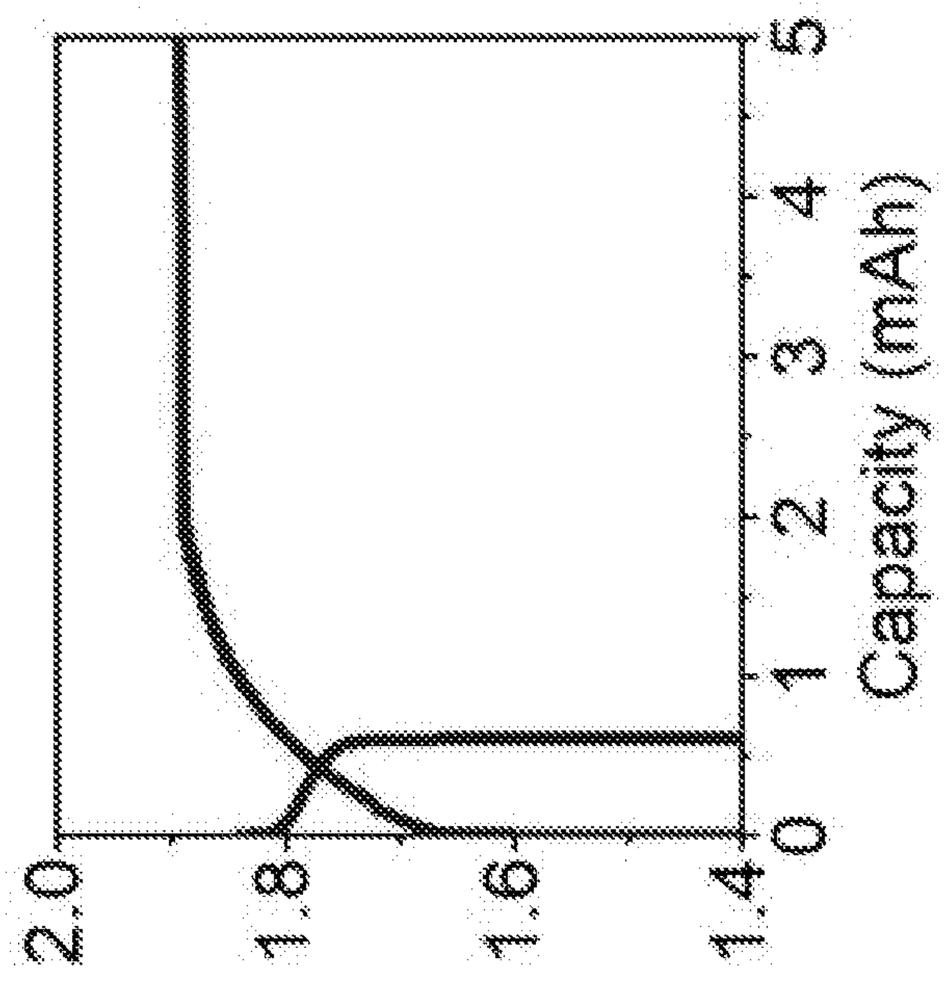

Capacity (mAh)
0
1
2
3
4
5
Voltage (V)
2
1.8
1.6
1.4

FIG. 3A

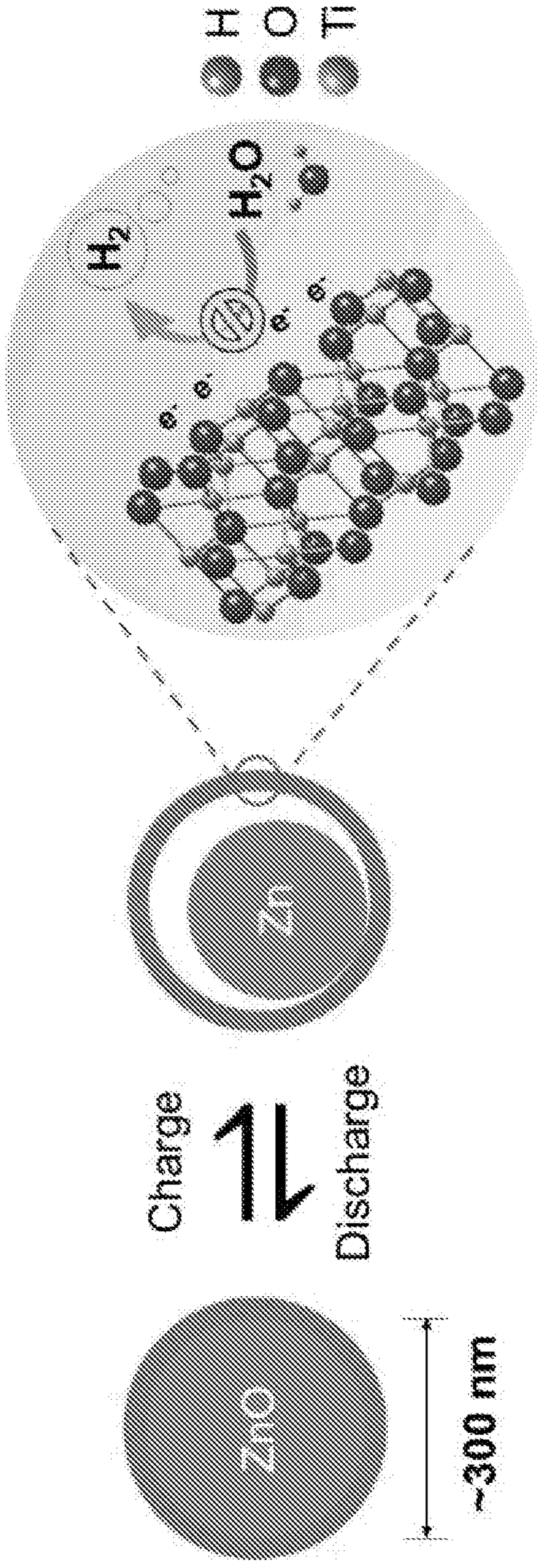


FIG. 4

FIG. 5A

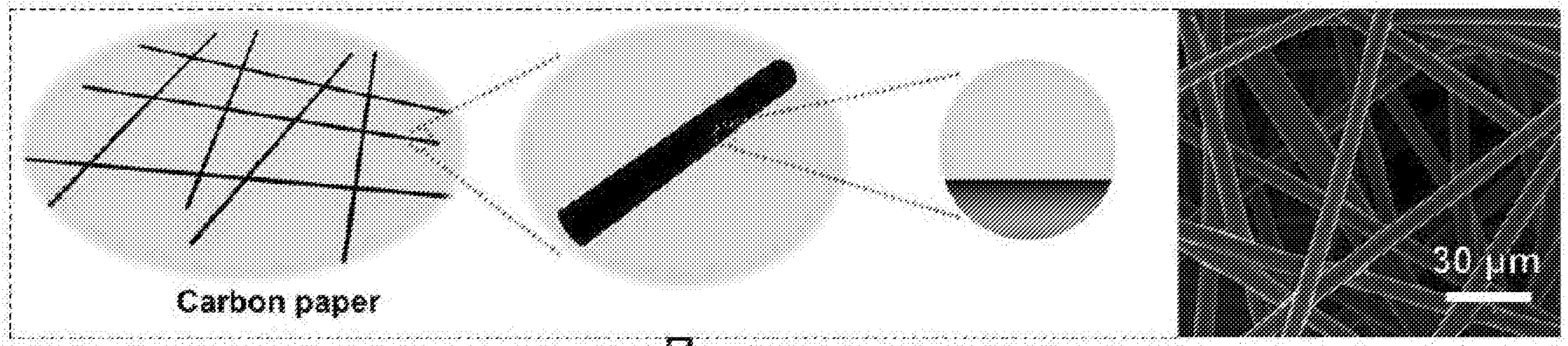


FIG. 5B

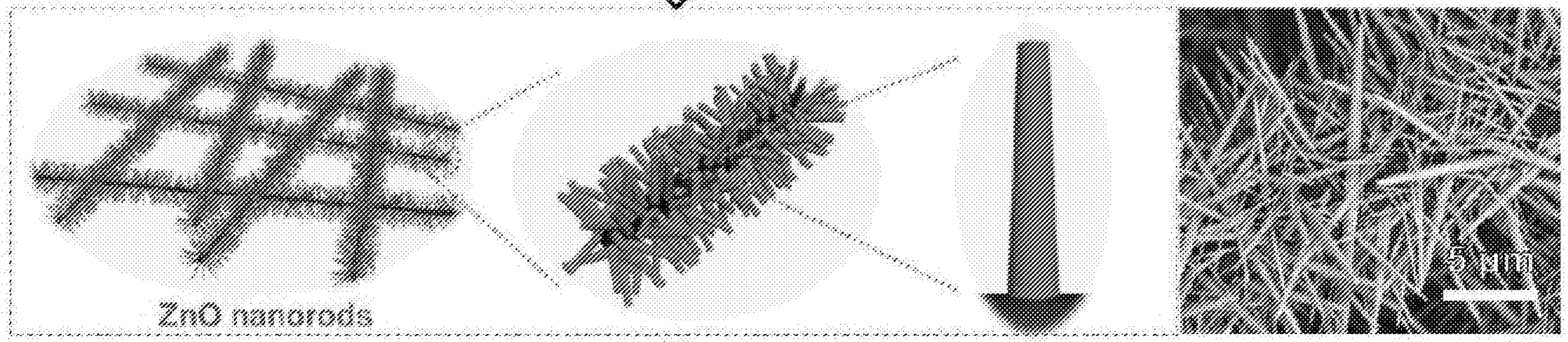
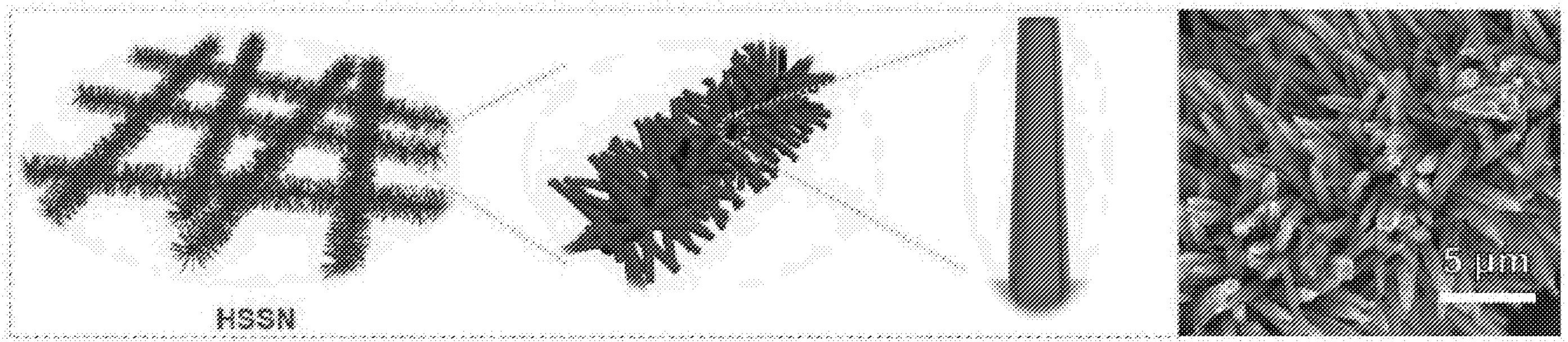


FIG. 5C



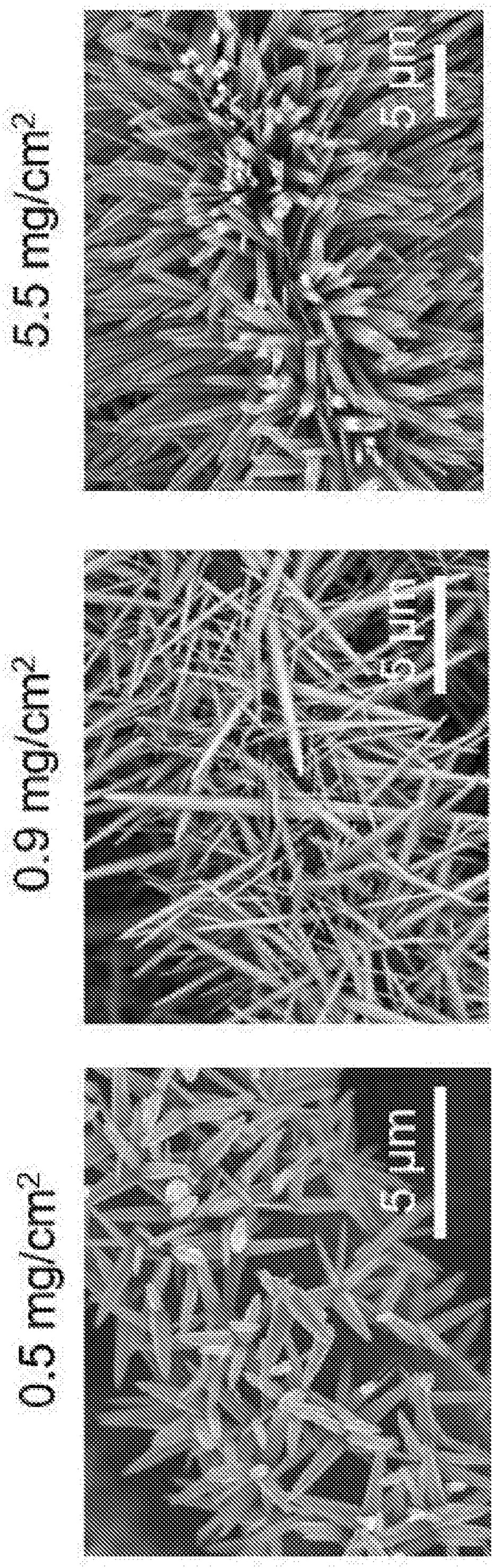


FIG. 6C

FIG. 6B

FIG. 6A

FIG. 7A

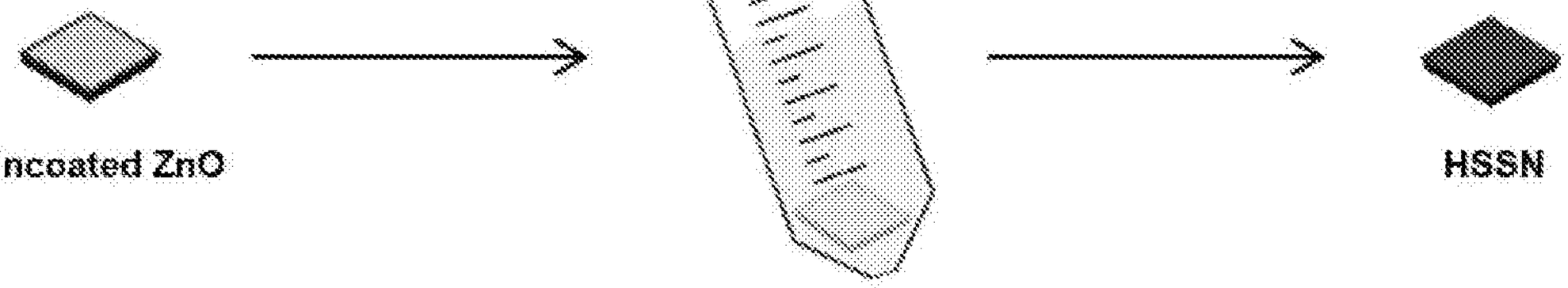


FIG. 7B

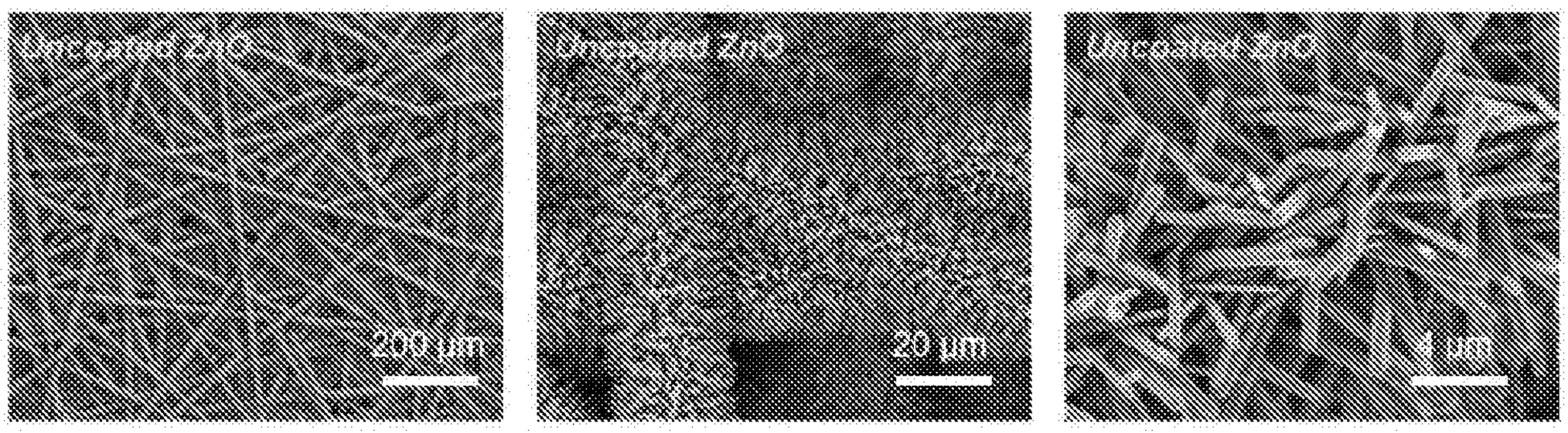


FIG. 7C

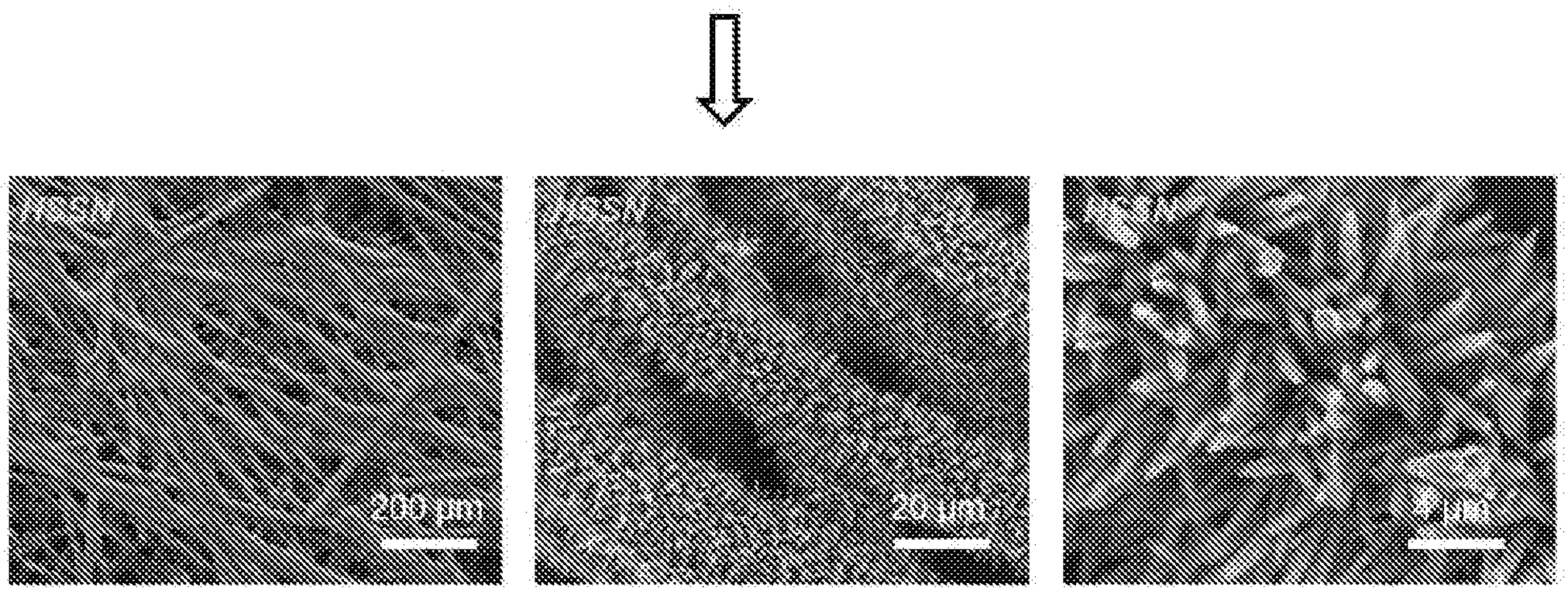


FIG. 7D

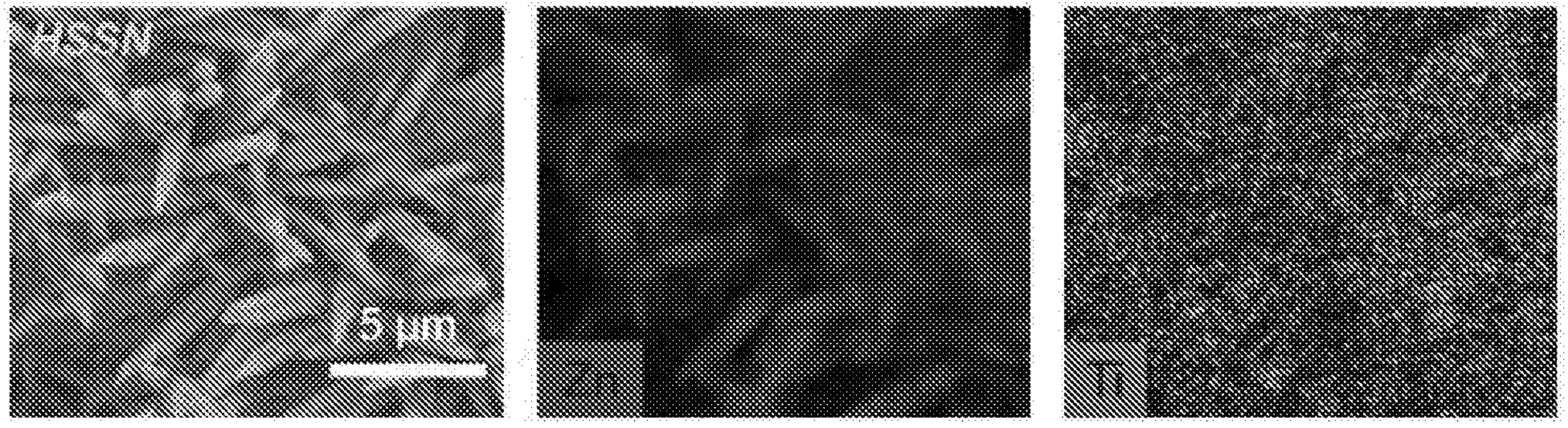


FIG. 8A

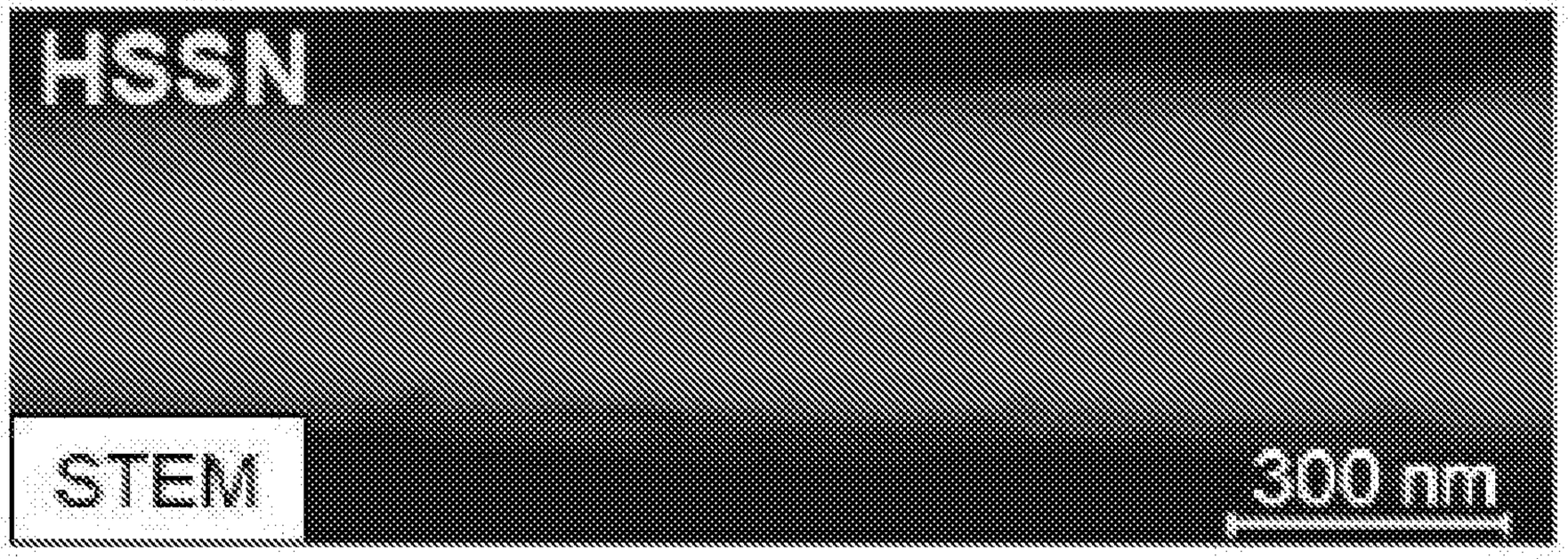


FIG. 8B

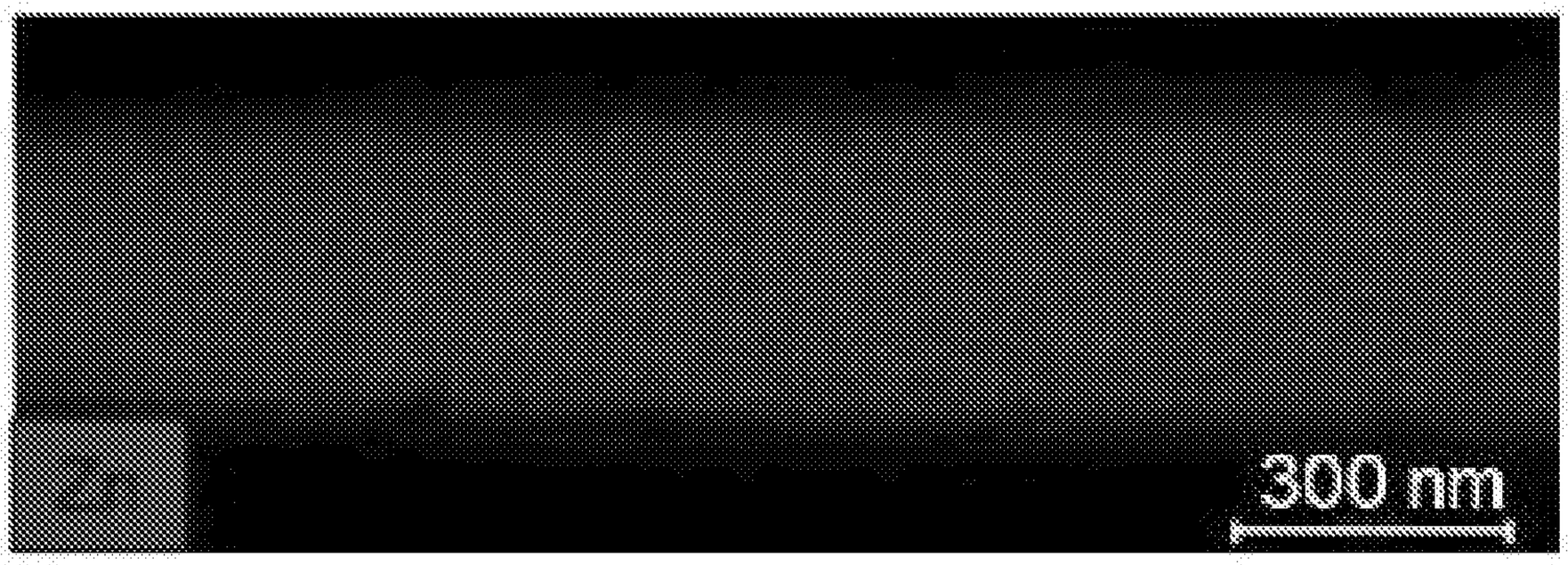
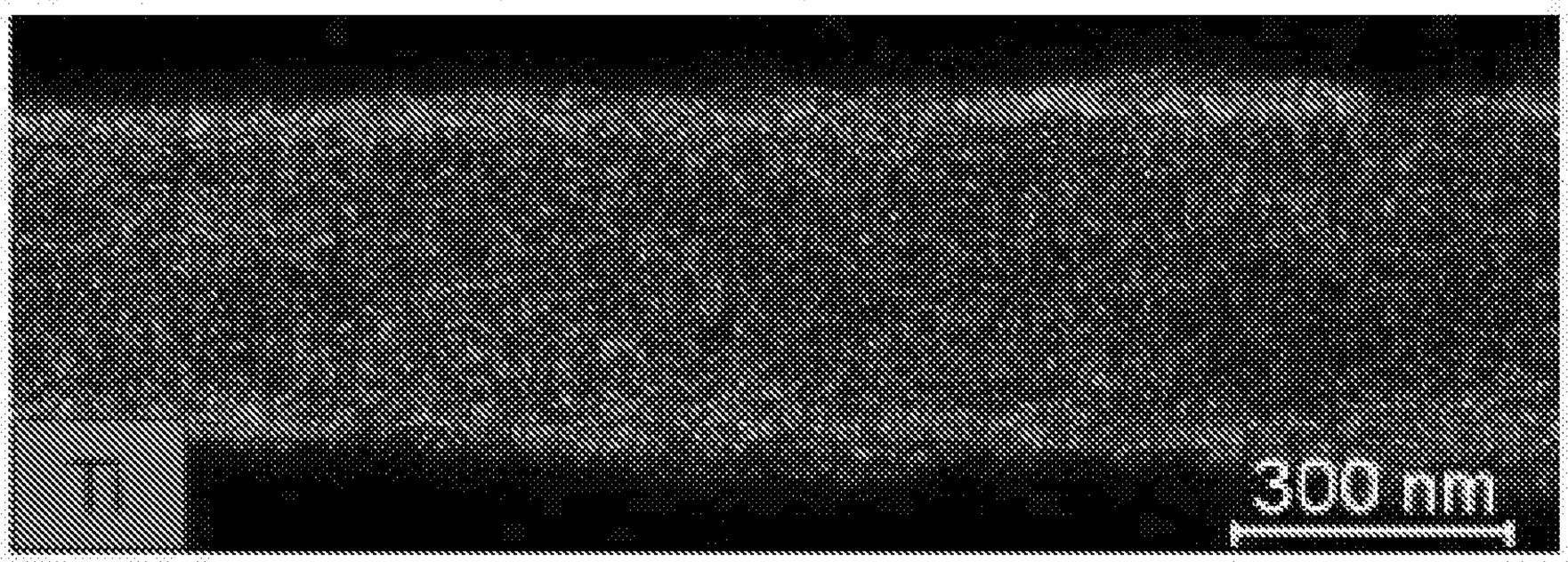


FIG. 8C



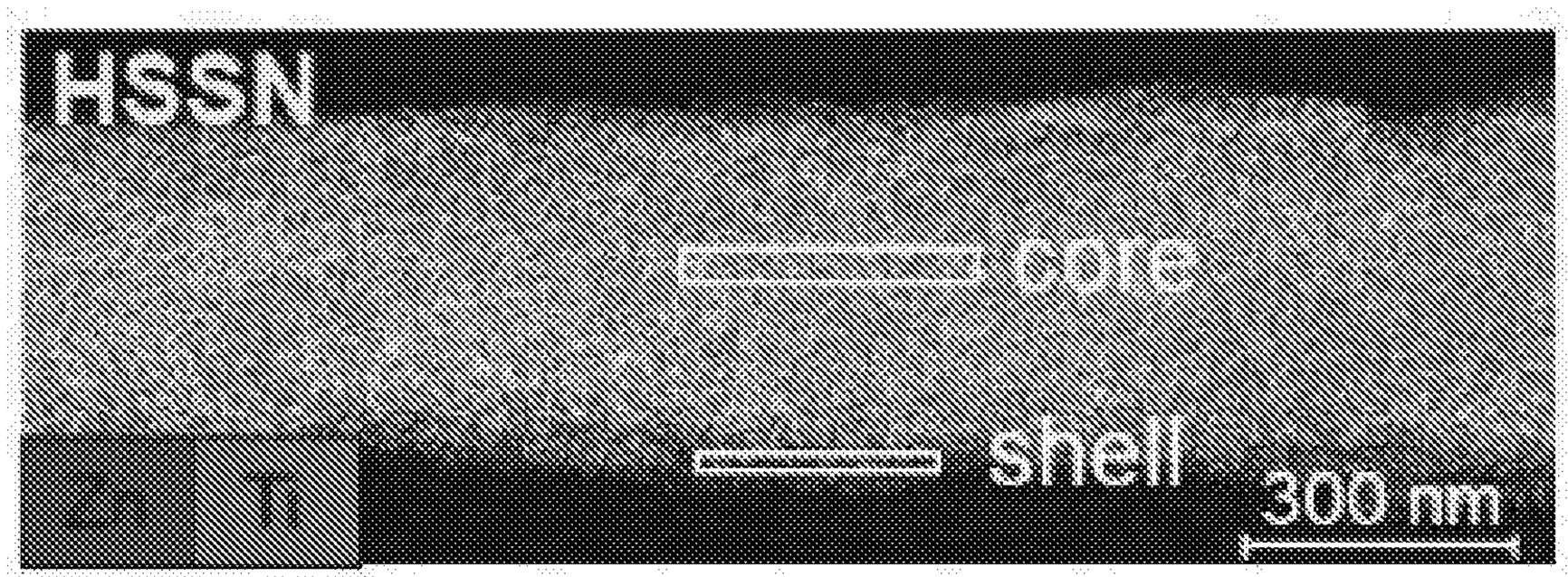

HSSN
core
shell
300 nm

FIG. 9A

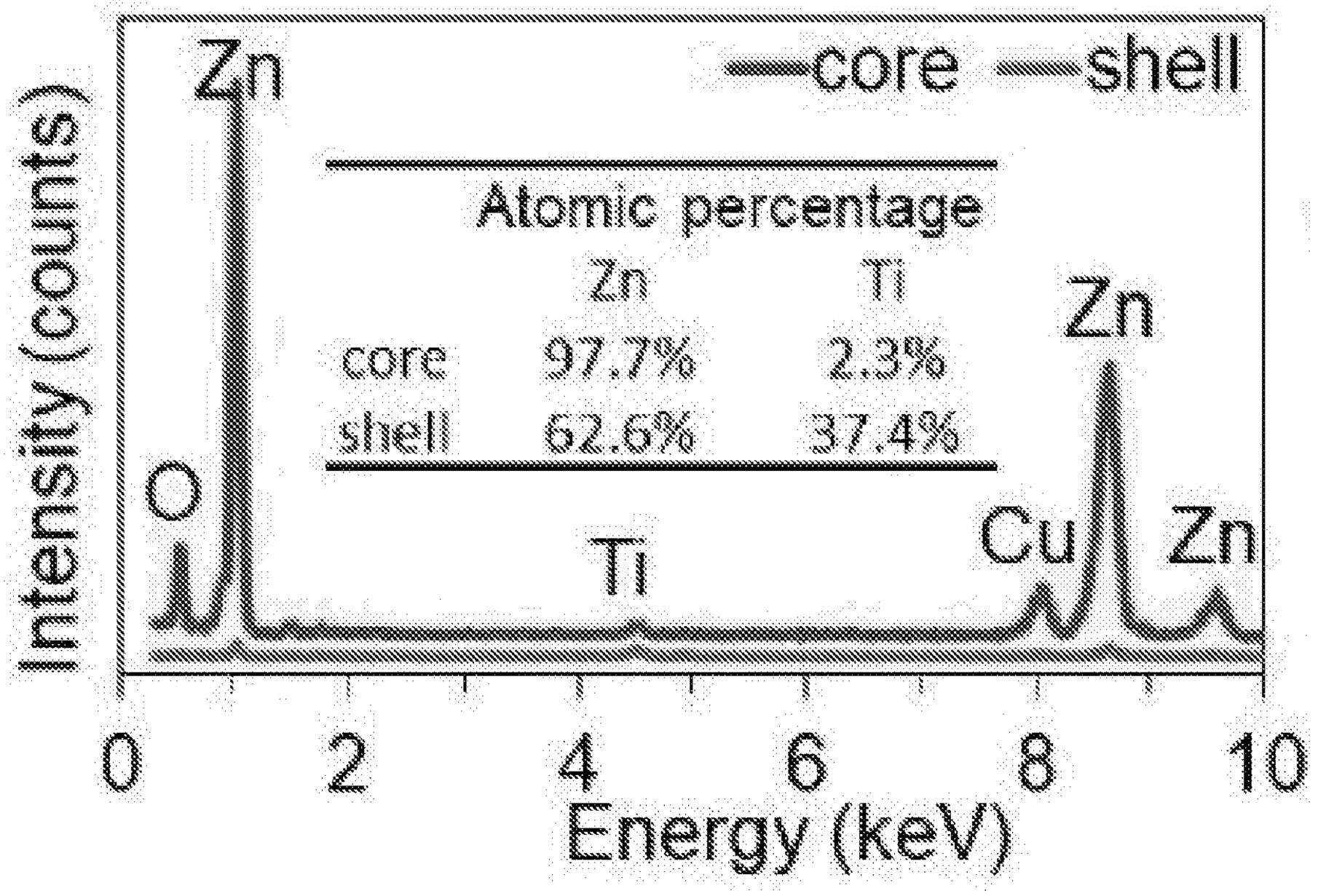

Intensity (counts)
Zn
core
shell
Atomic percentage
Zn
Ti
core
97.7%
2.3%
shell
62.6%
37.4%
O
Ti
Cu
Zn
Zn
0
2
4
6
8
10
Energy (keV)

FIG. 9B

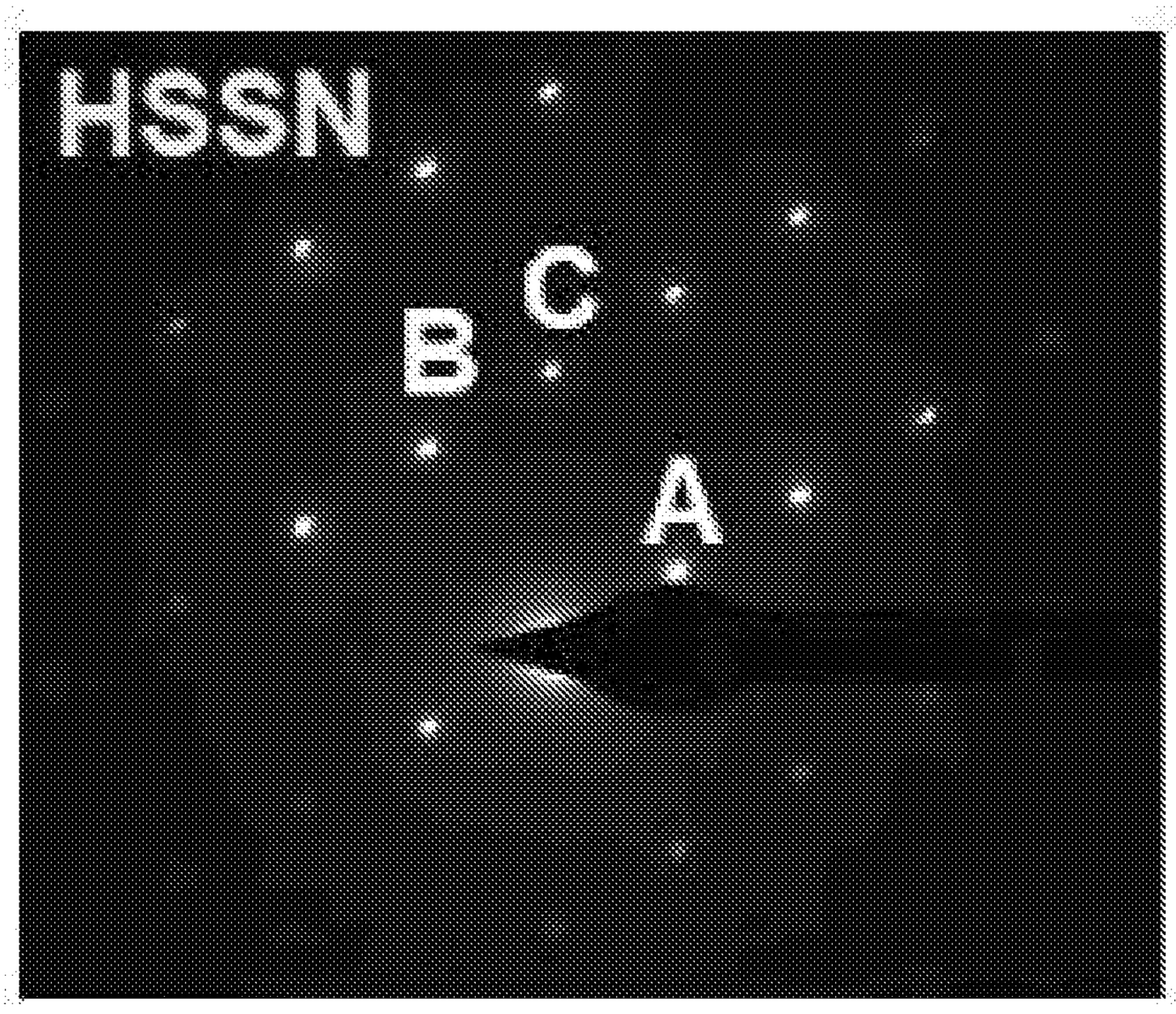
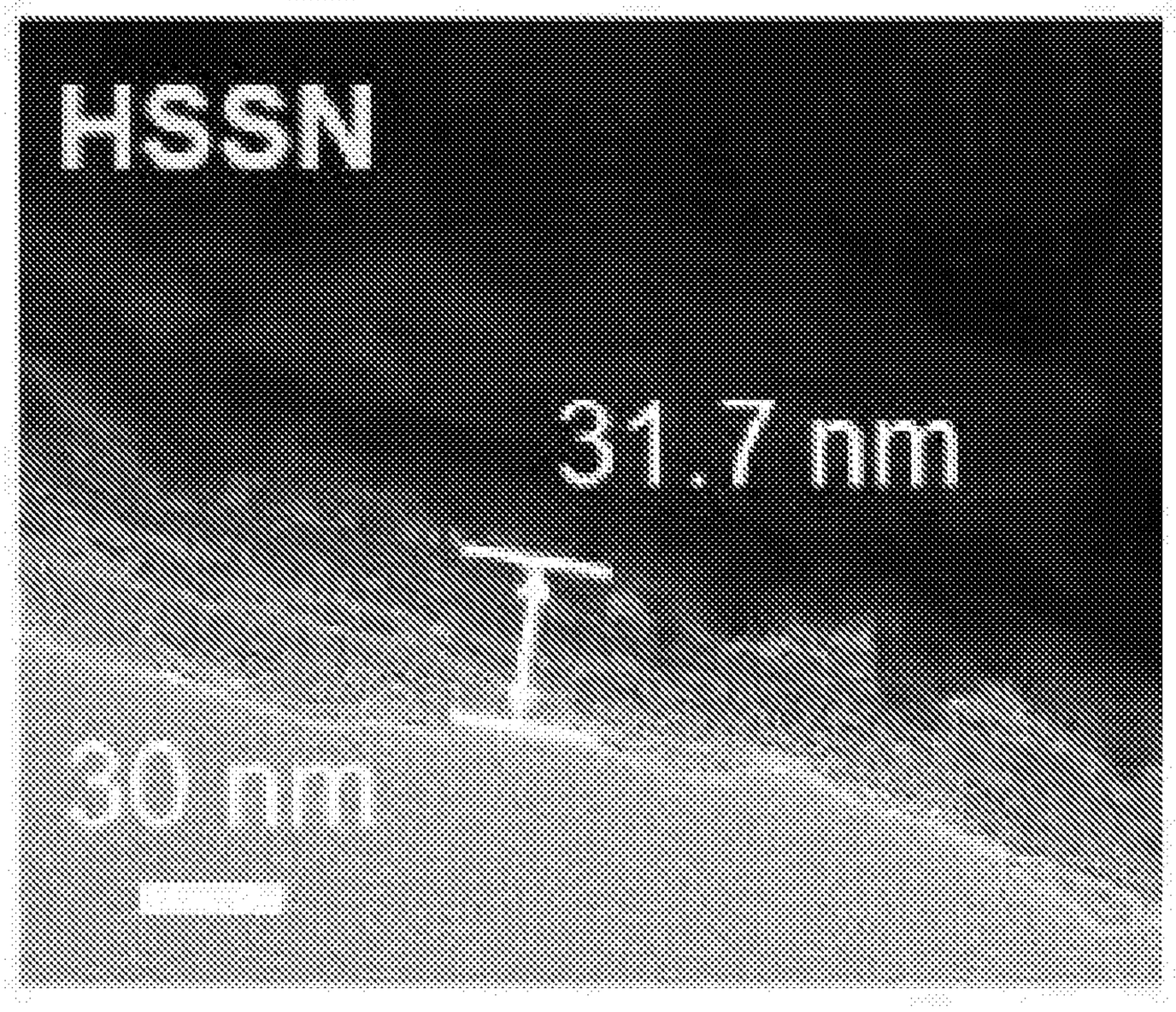


FIG. 10

FIG. 11



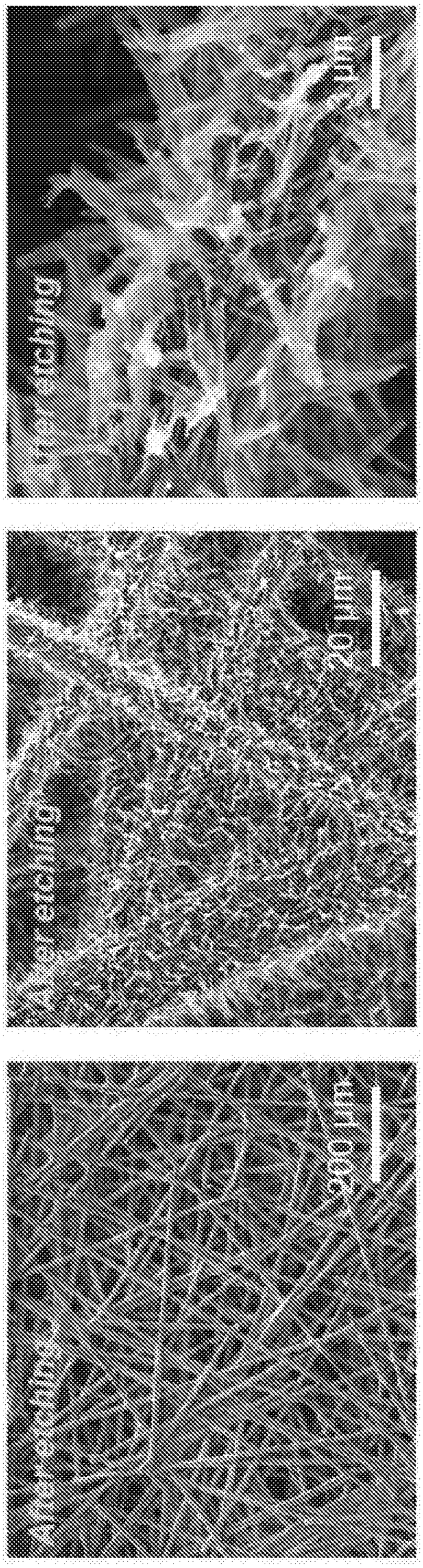


FIG. 12C

FIG. 12B

FIG. 12A

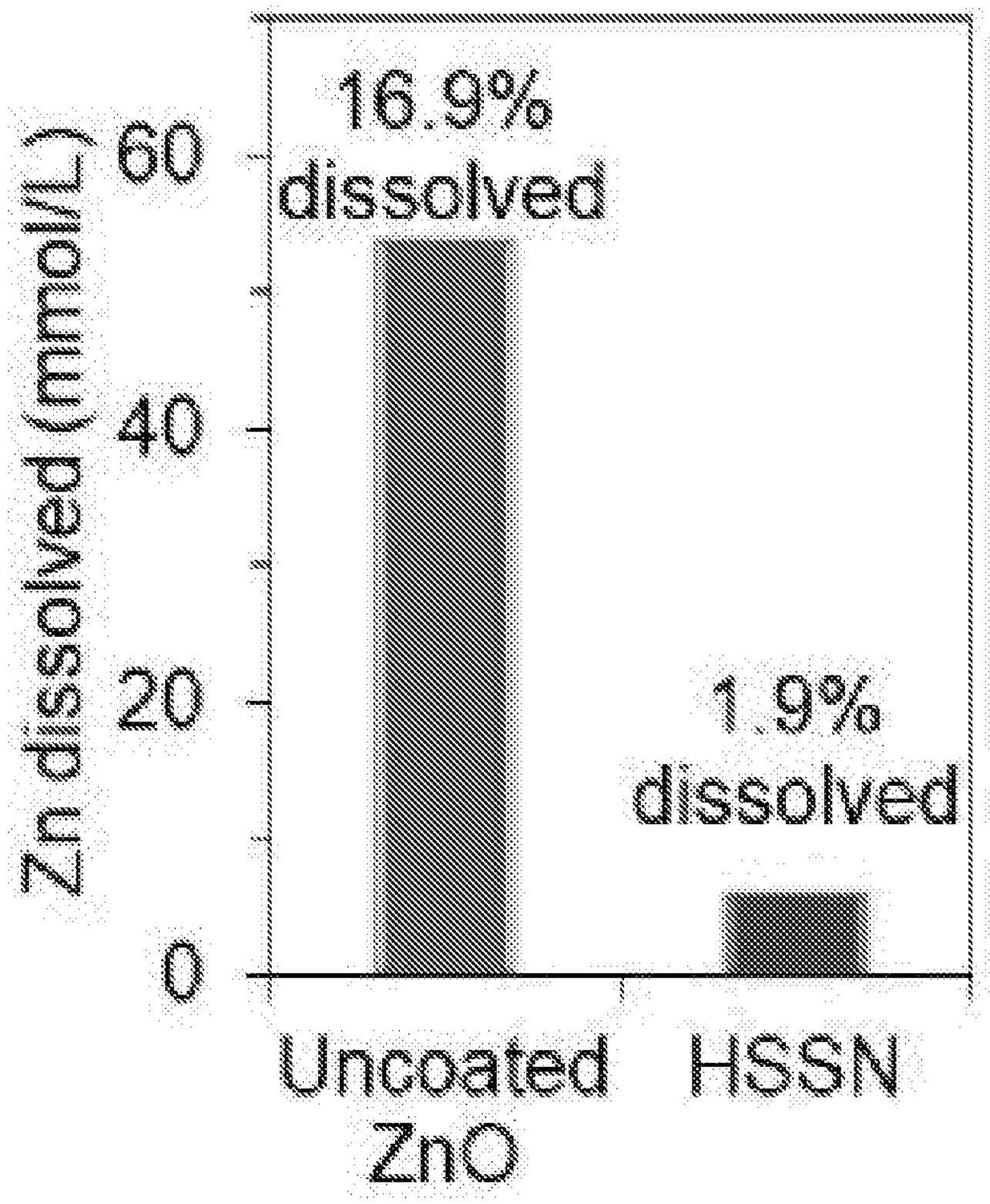

16.9%
dissolved
1.9%
dissolved
Zn dissolved (mol/L)
60
40
20
0
Uncoated ZnO
HSSN

FIG. 13

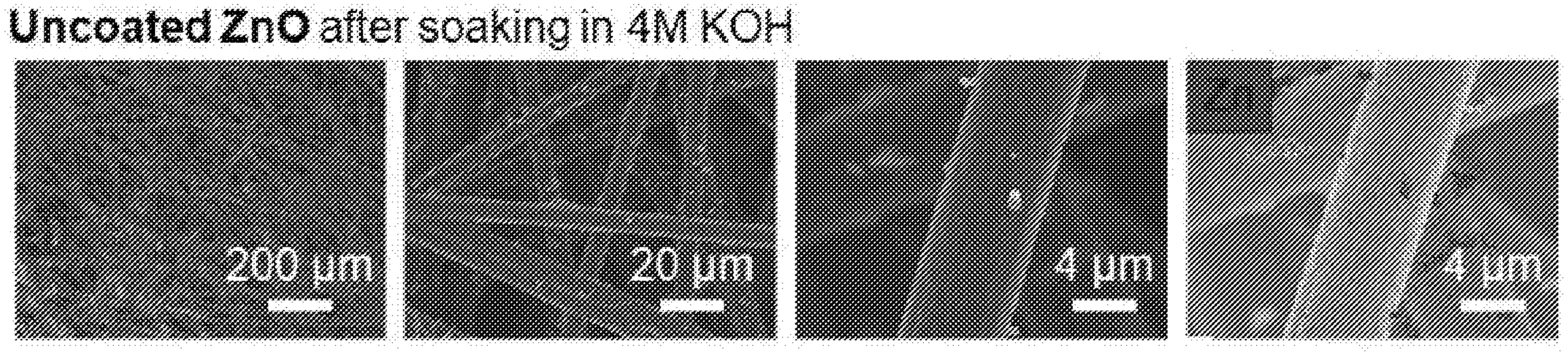


FIG. 14A

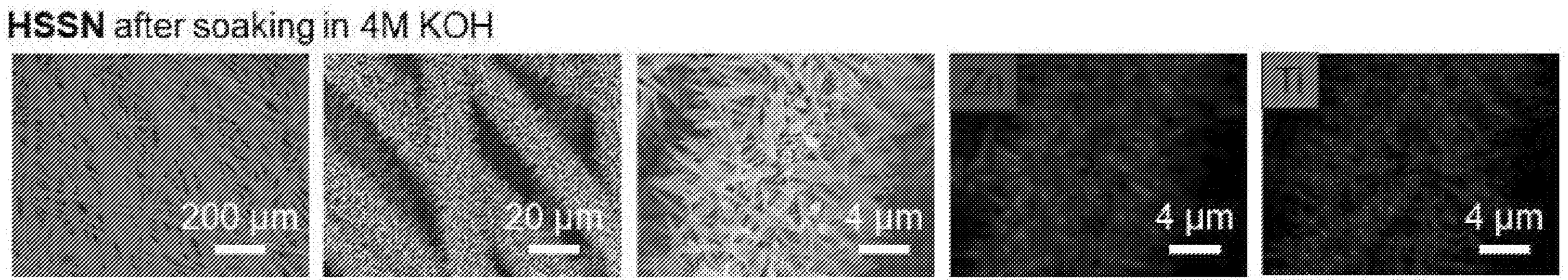


FIG. 14B

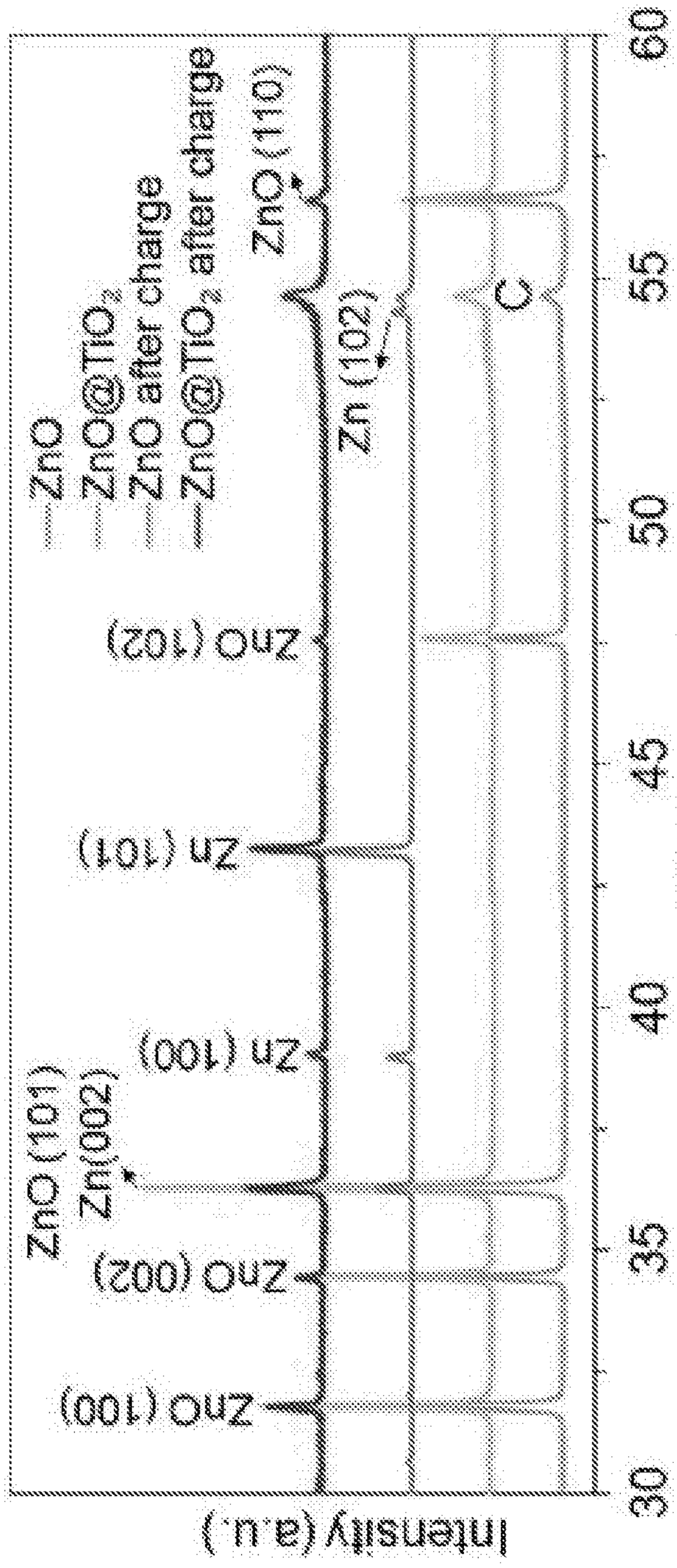

ZnO
ZnO@TiO2
ZnO after charge
ZnO@TiO2 after charge
ZnO (102)
ZnO (110)
Zn (102)
C
Zn (101)
Zn (100)
ZnO (101)
Zn(002)
ZnO (002)
ZnO (100)
Intensity (a.u.)
28 (degrees)
30
35
40
45
50
55
60

FIG. 15

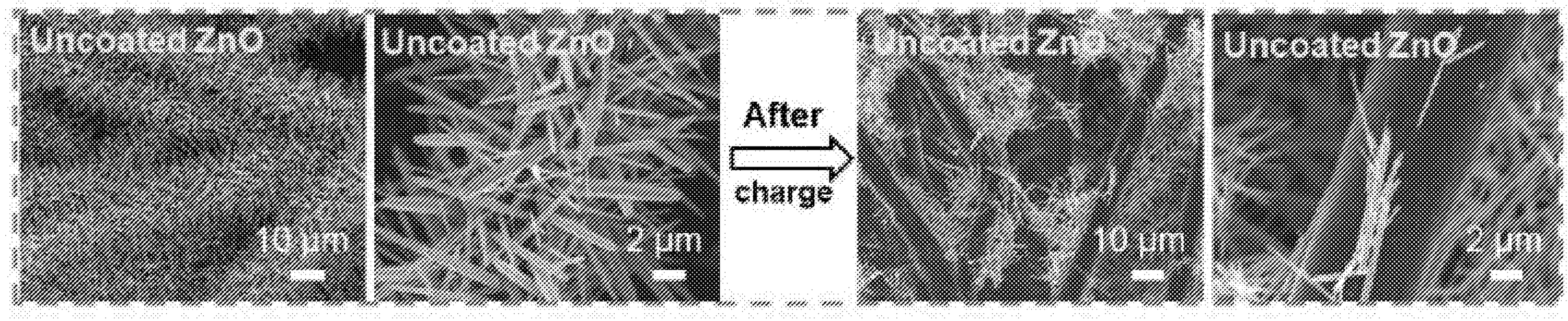

Uncoated ZnO
10 μm
Uncoated ZnO
2 μm
After
charge
Uncoated ZnO
10 μm
Uncoated ZnO
2 μm

FIG. 16

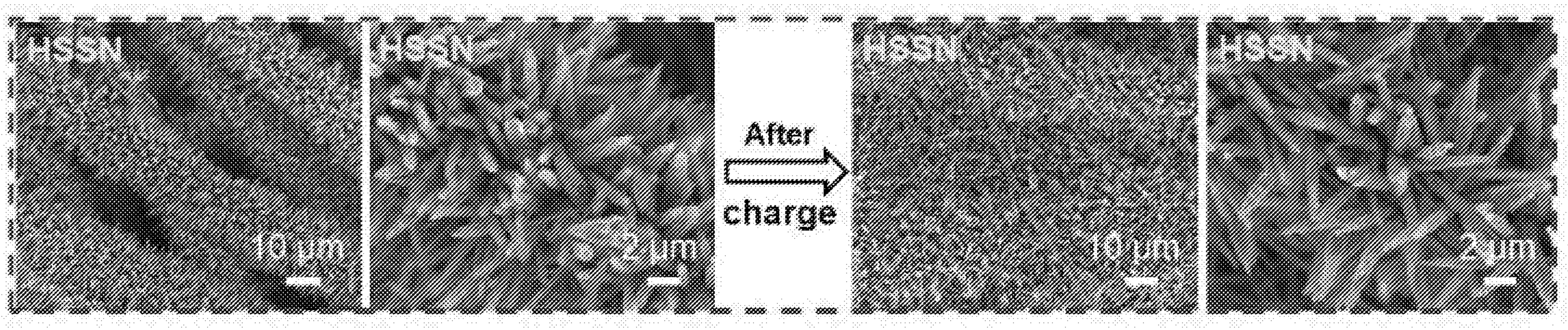

HSSN
10 μm
HSSN
2 μm
After
charge
HSSN
10 μm
HSSN
2 μm

FIG. 17

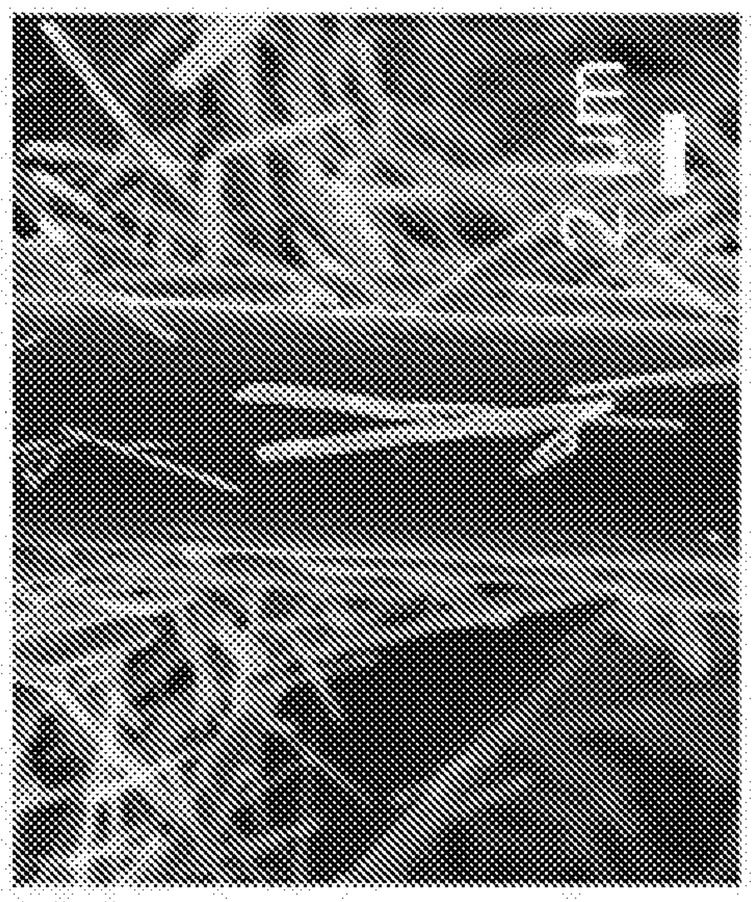


FIG. 18

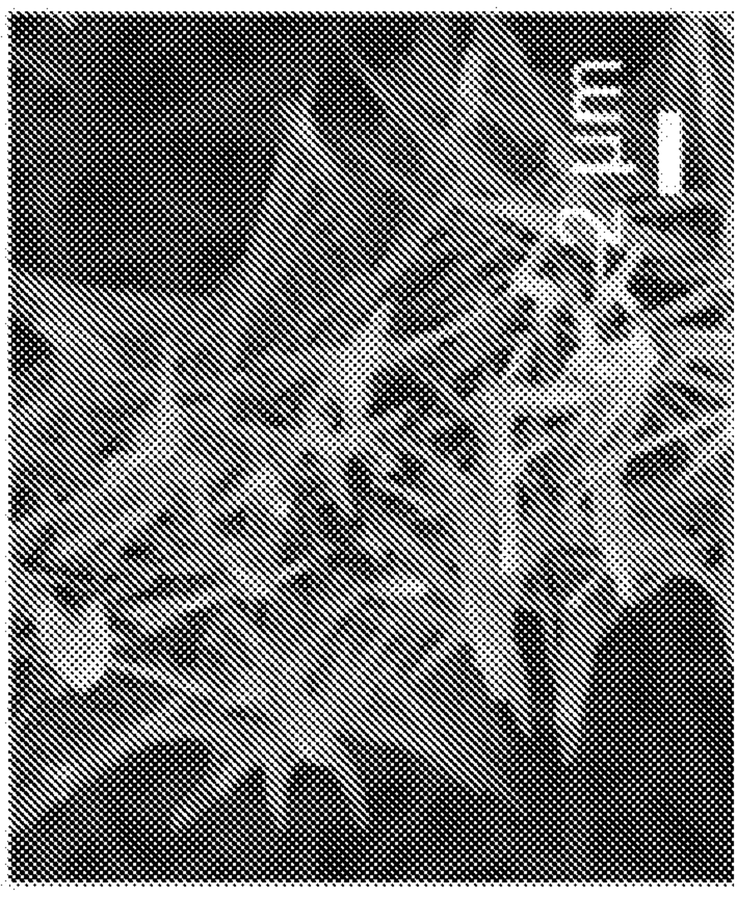


FIG. 19

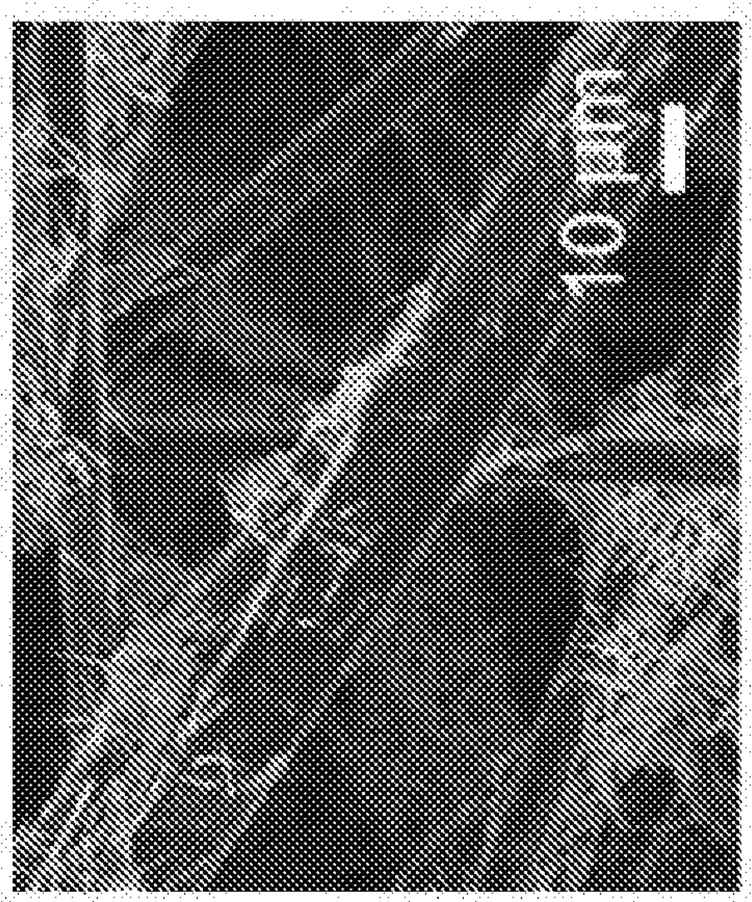


FIG. 20

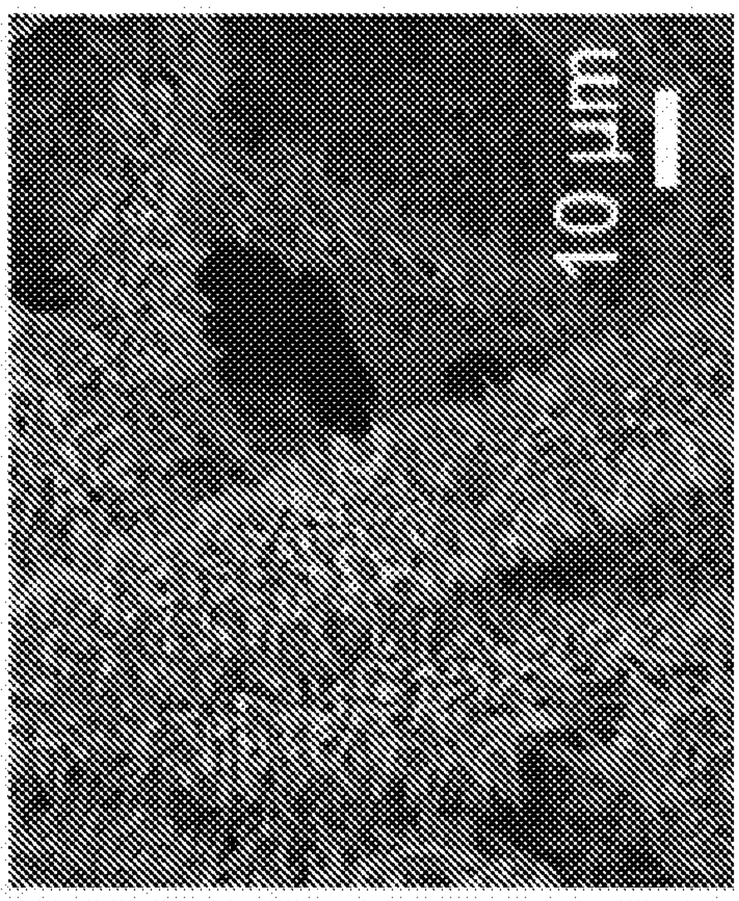
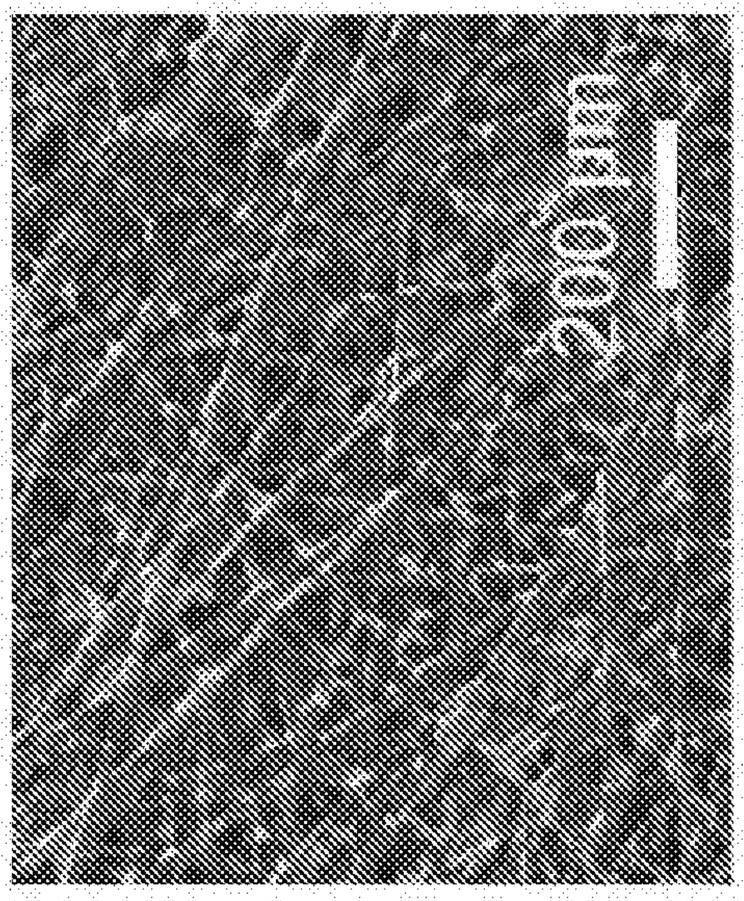
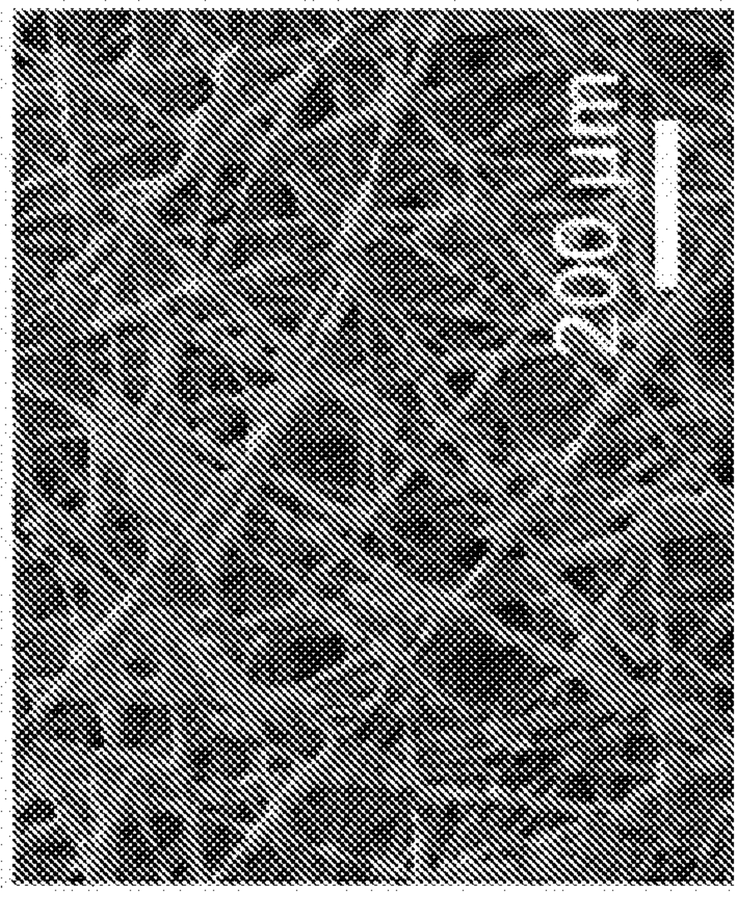


FIG. 21





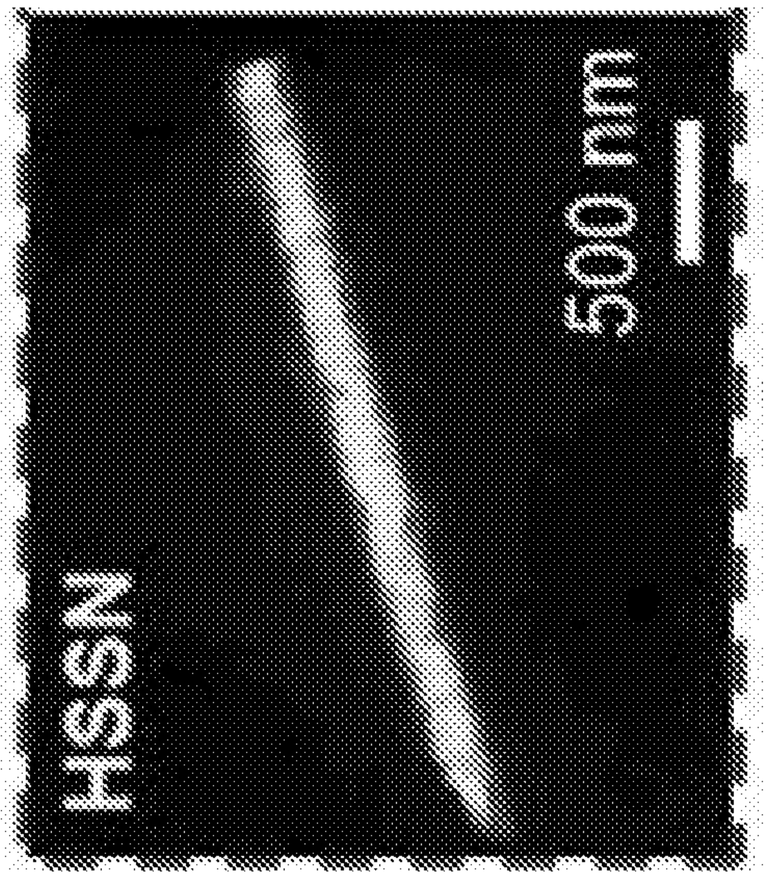


FIG. 20

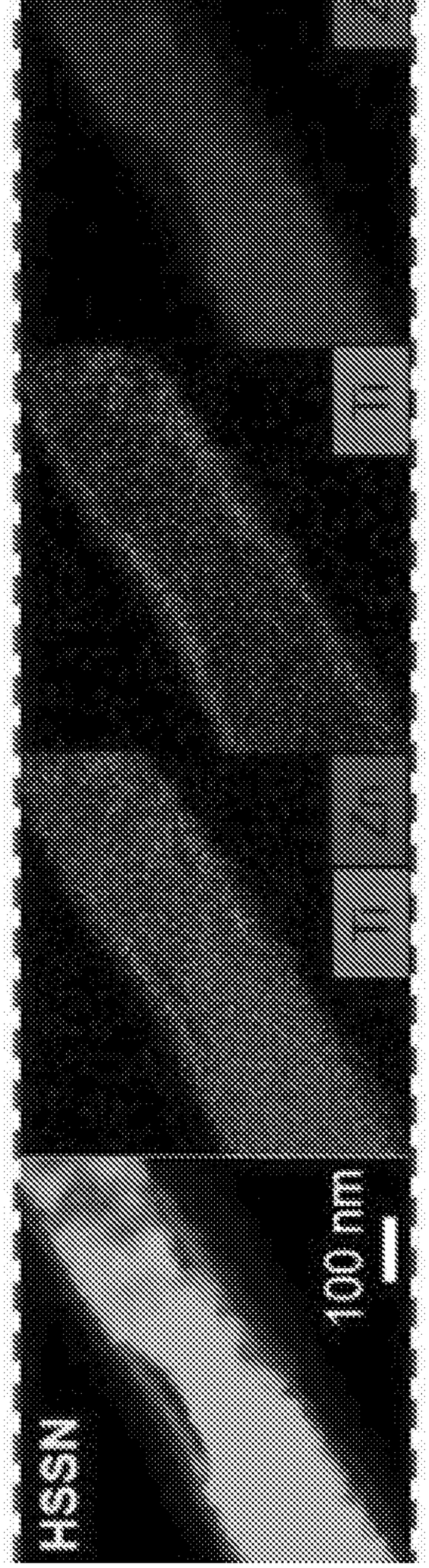


FIG. 21

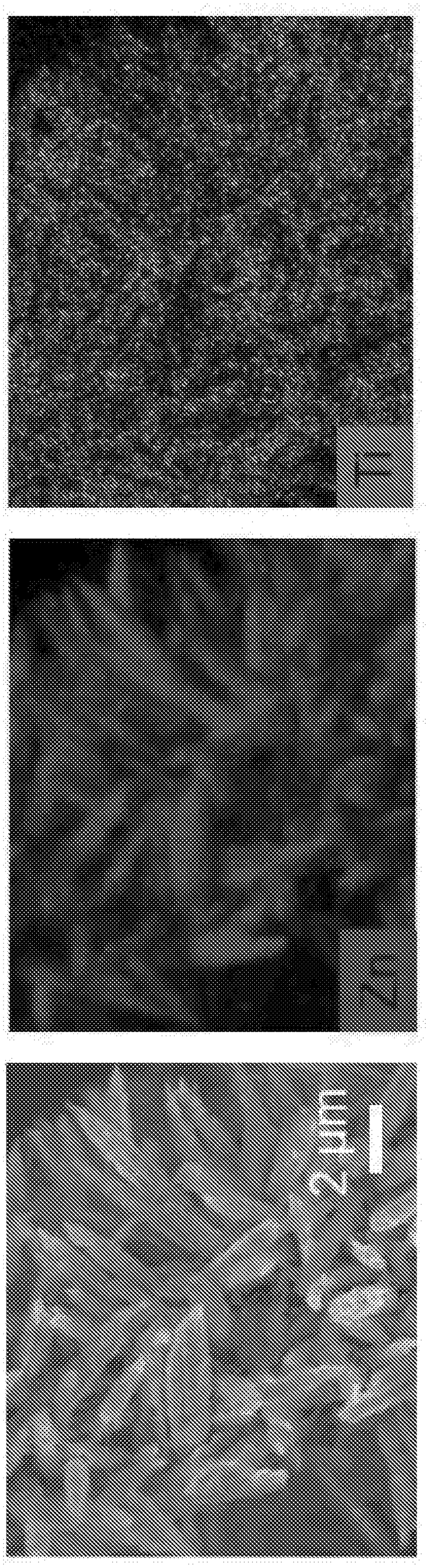


FIG. 22

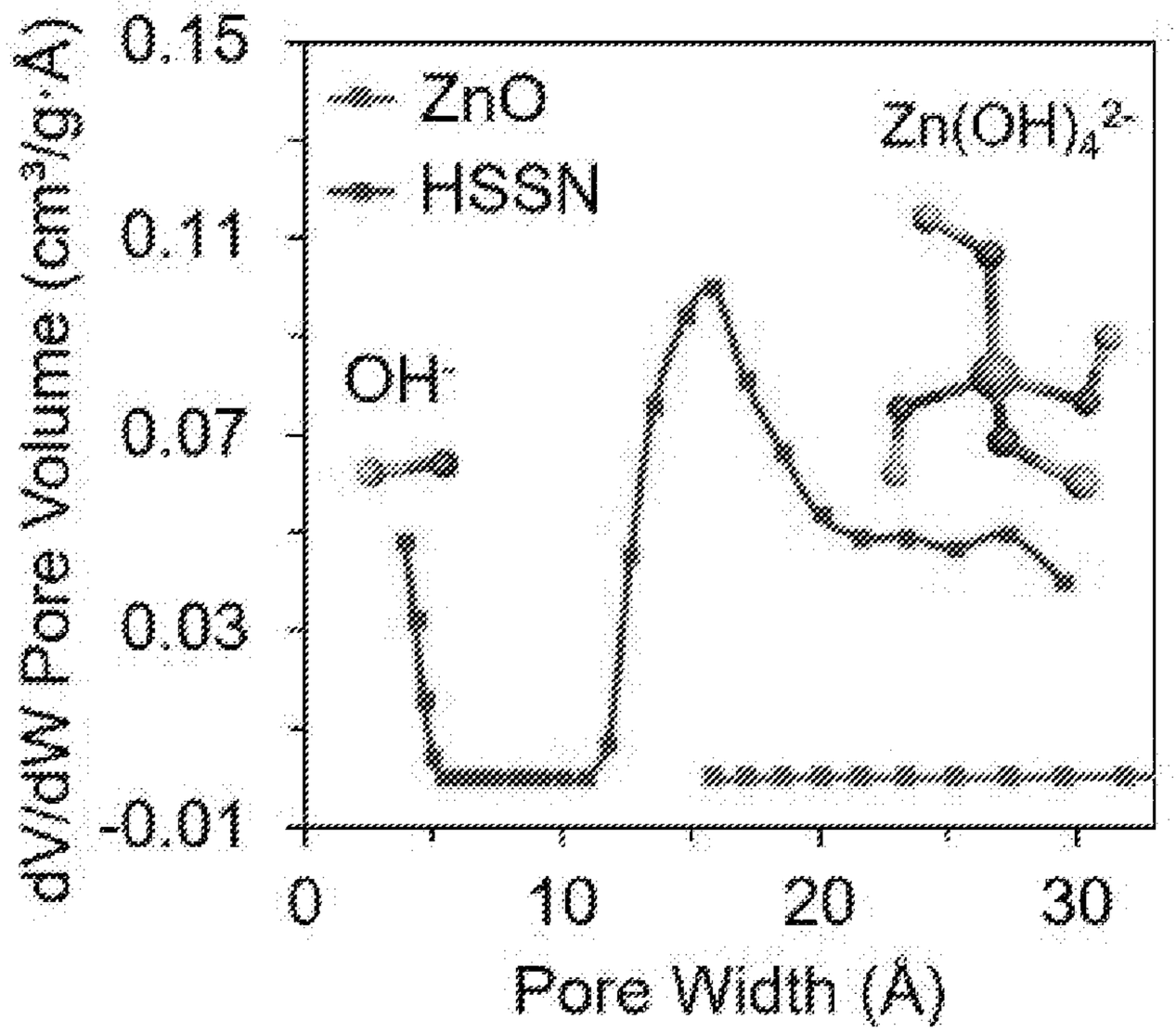


FIG. 23A

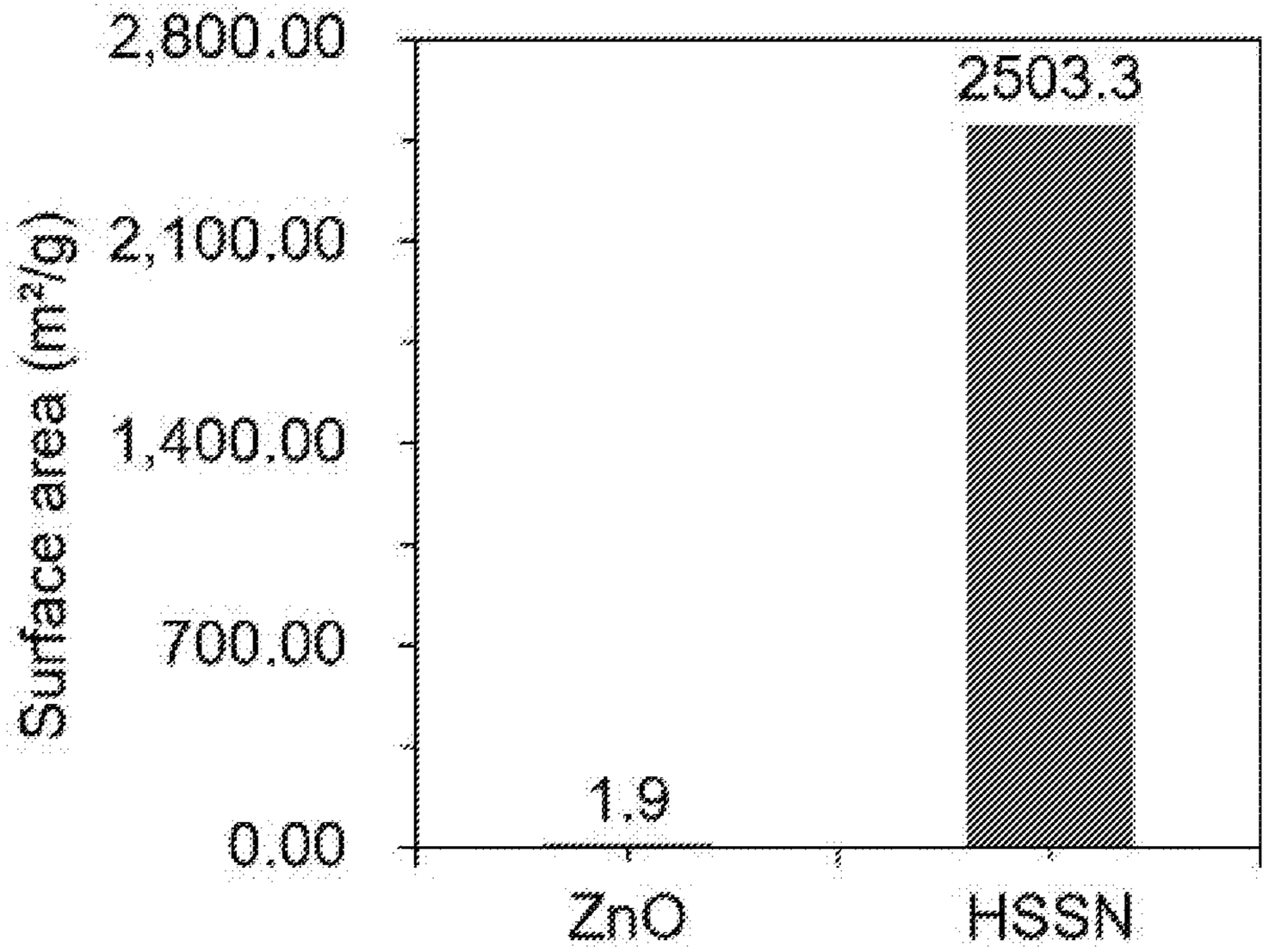


FIG. 23B

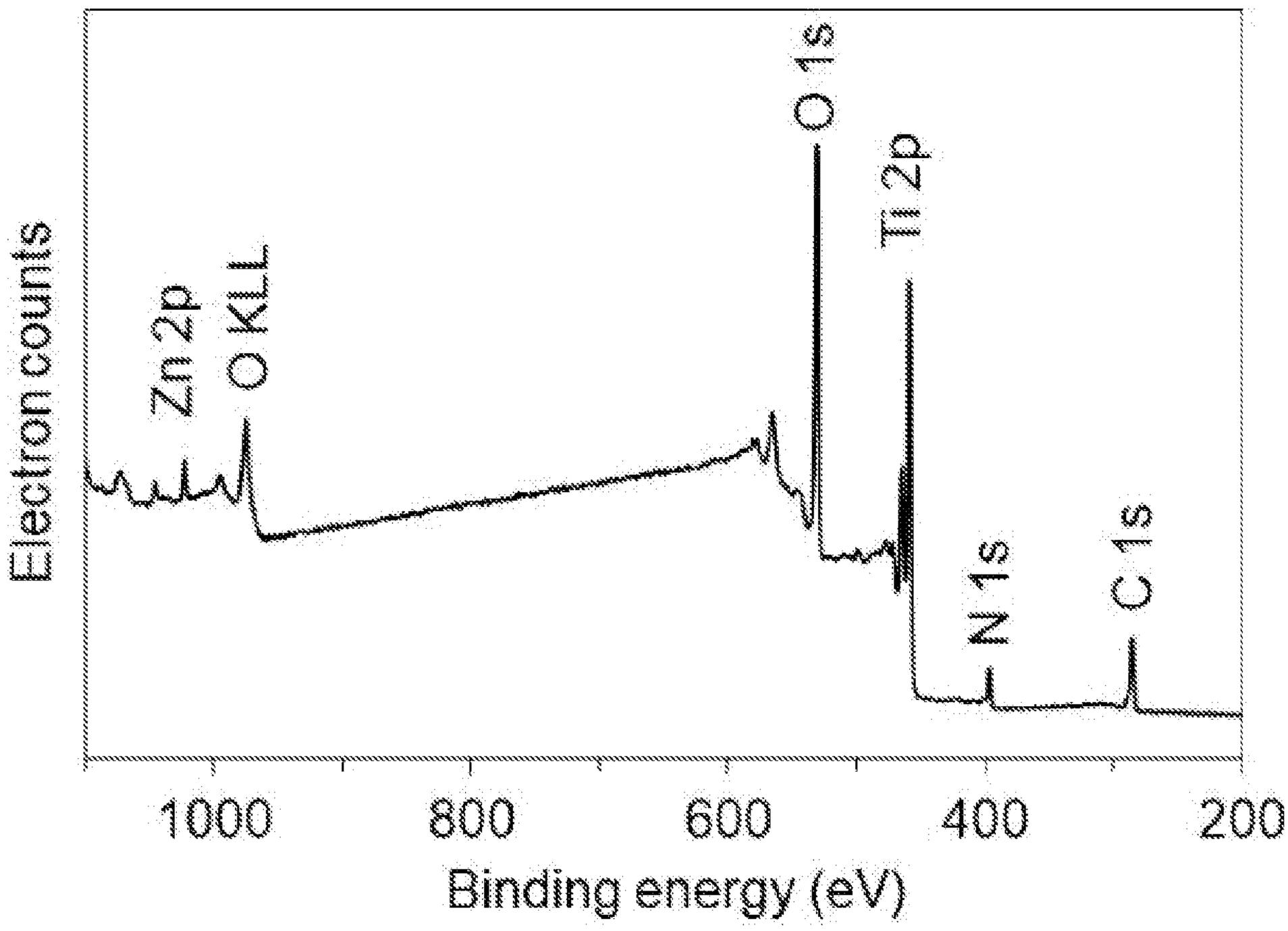

Electron counts
Zn 2p
O KLL
O 1s
Ti 2p
N 1s
C 1s
1000
800
600
400
200
Binding energy (eV)

FIG. 24

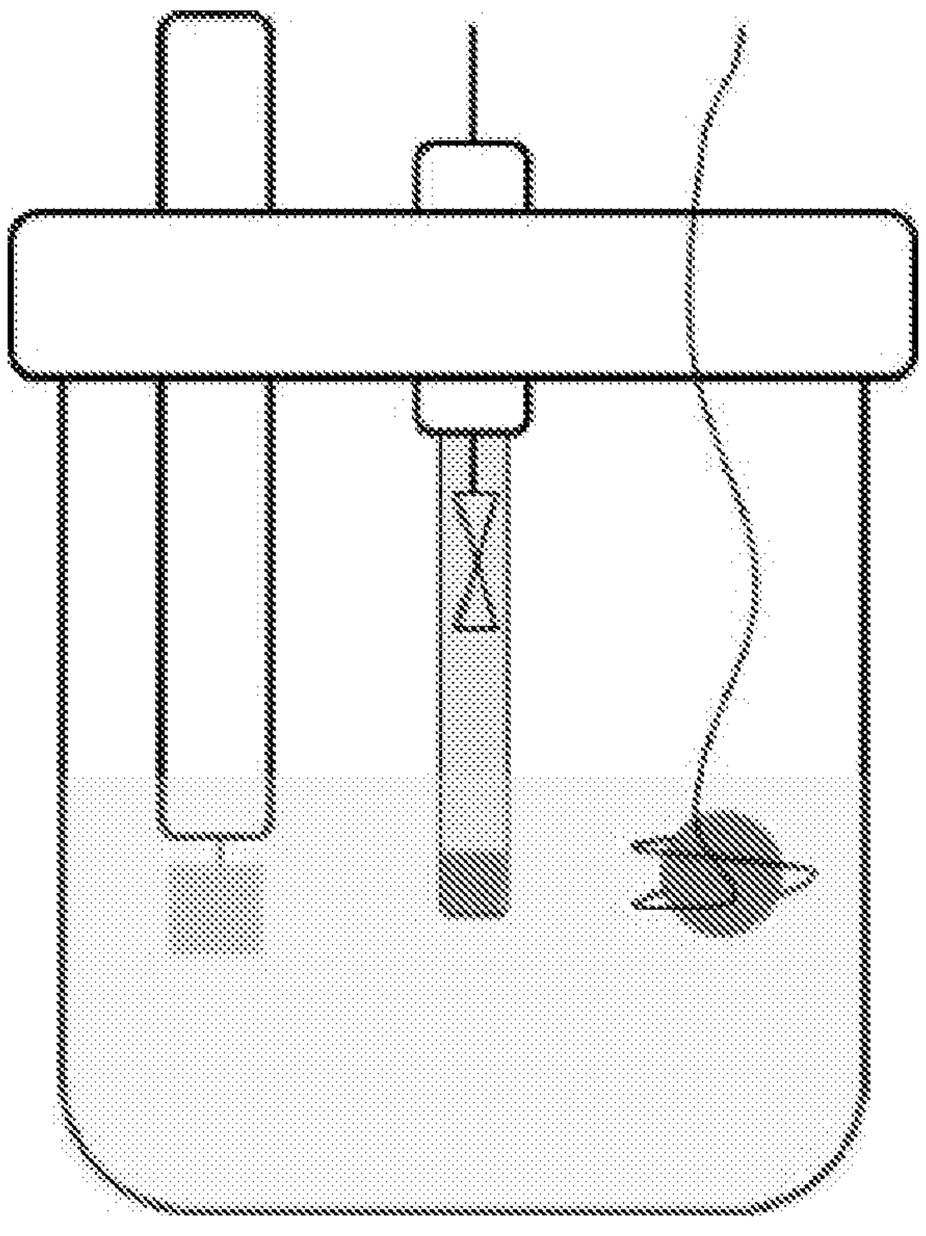
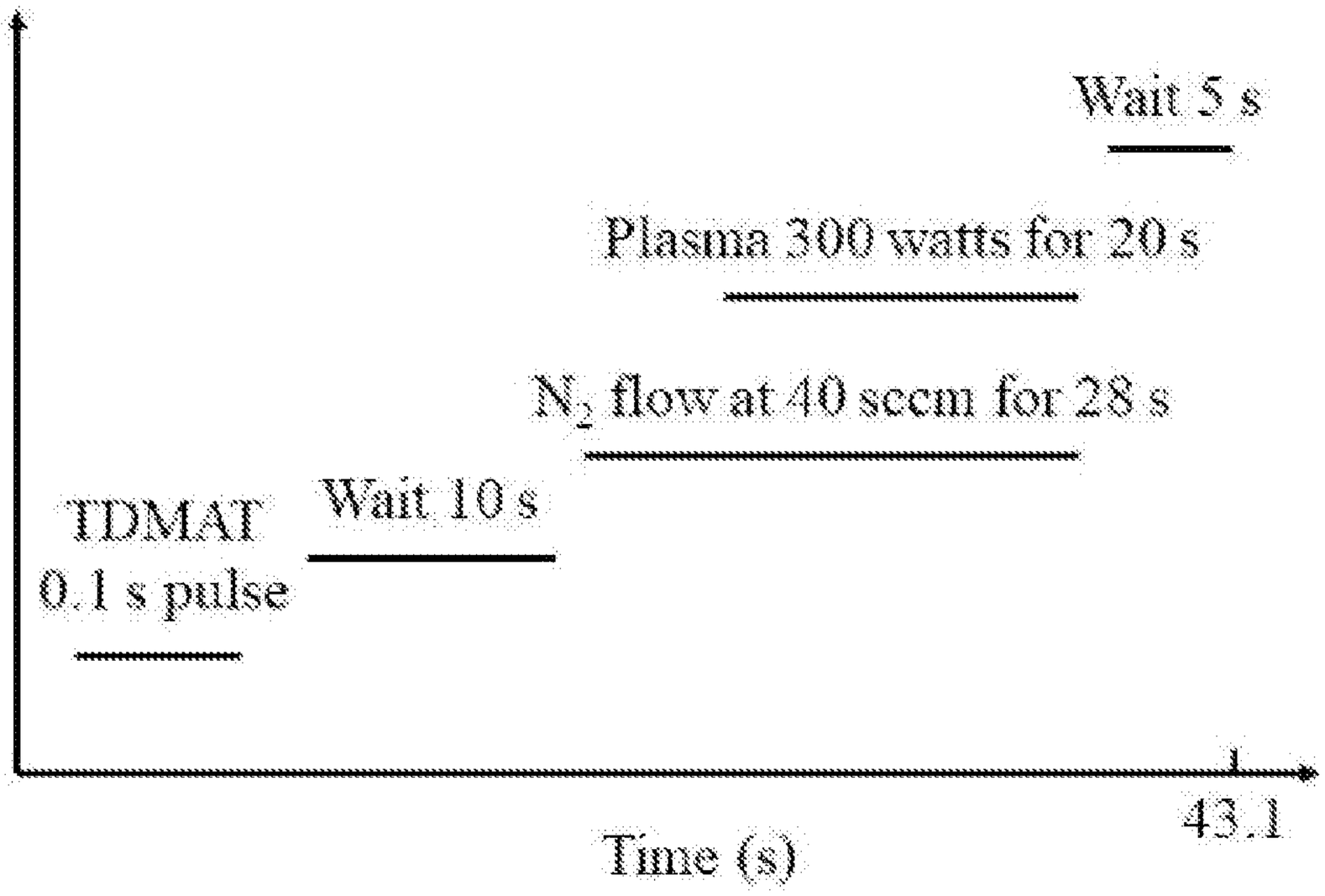


FIG. 25

FIG. 26


Wait 5 s
Plasma 300 watts for 20 s
N_2 flow at 40 sccm for 28 s
Wait 10 s
TDMAT
0.1 s pulse
1
43.1
Time (s)

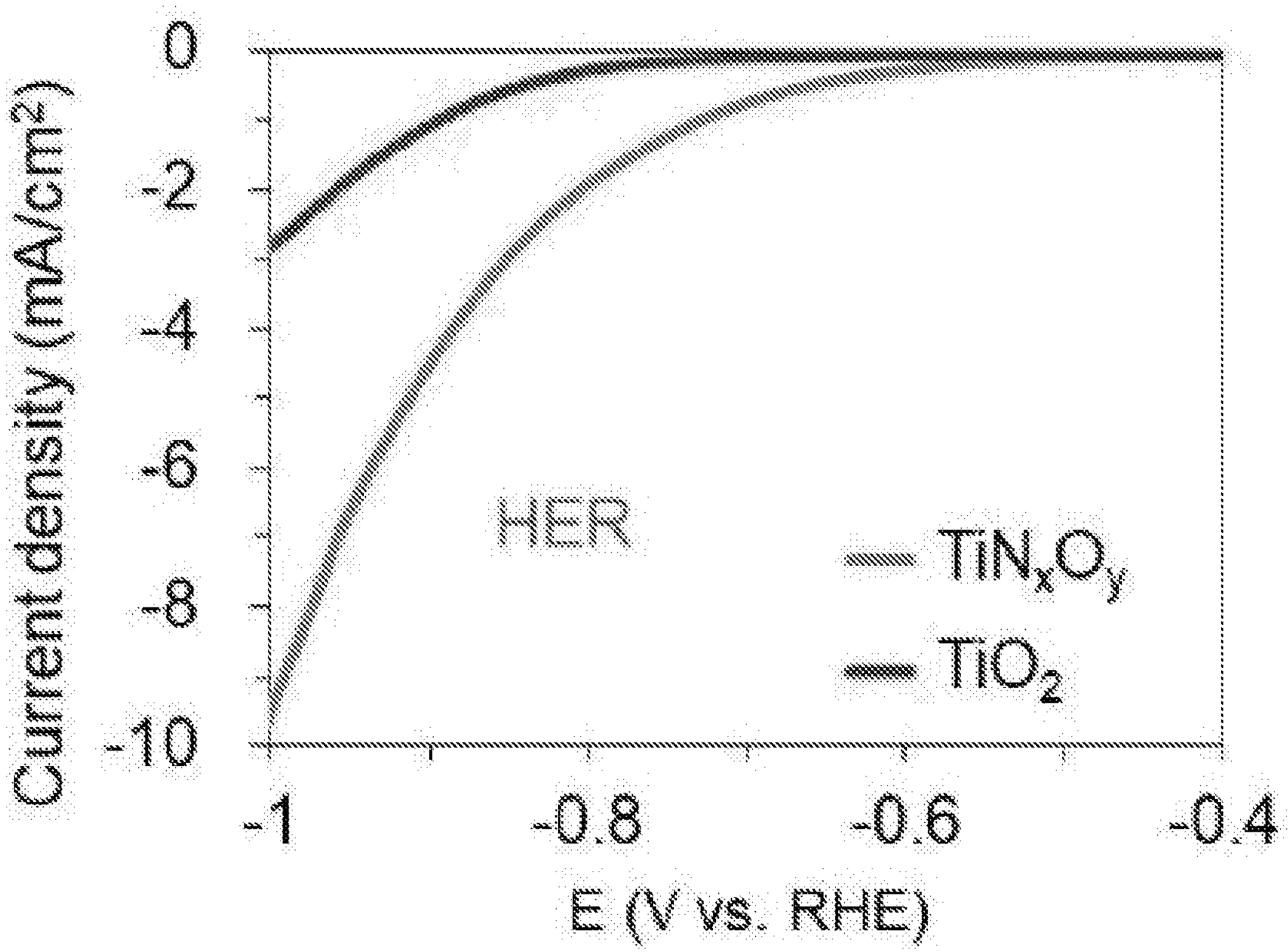

Current density (mA/cm²)
0
-2
-4
-6
-8
-10
-1
-0.8
-0.6
-0.4
E (V vs. RHE)
HER
TiNxOy
TiO2

FIG. 27

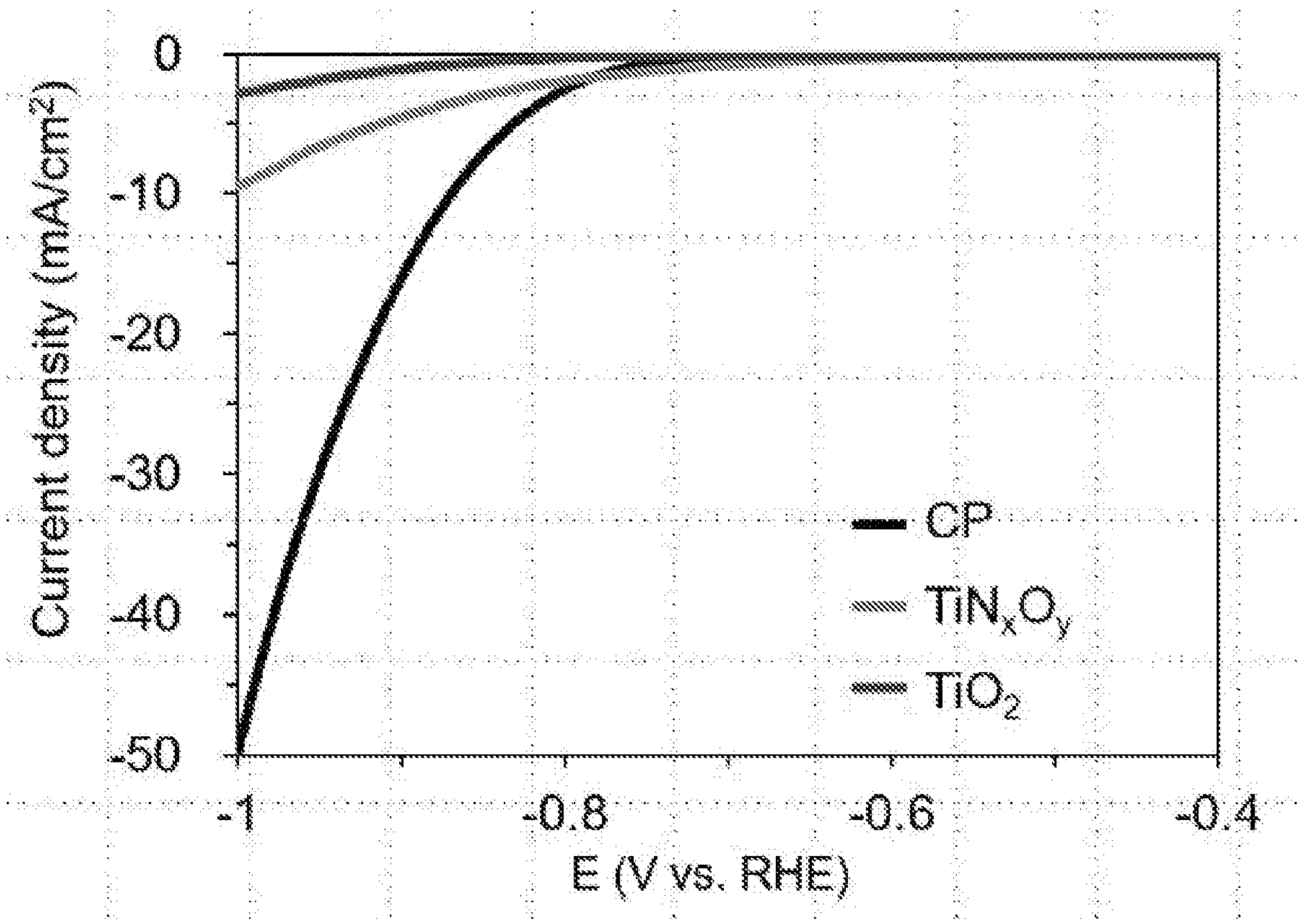

0
-10
-20
-30
-40
-50
Current density (mA/cm²)
-1
-0.8
-0.6
-0.4
E (V vs. RHE)
CP
TiNxOy
TiO2

FIG. 28

FIG. 29A

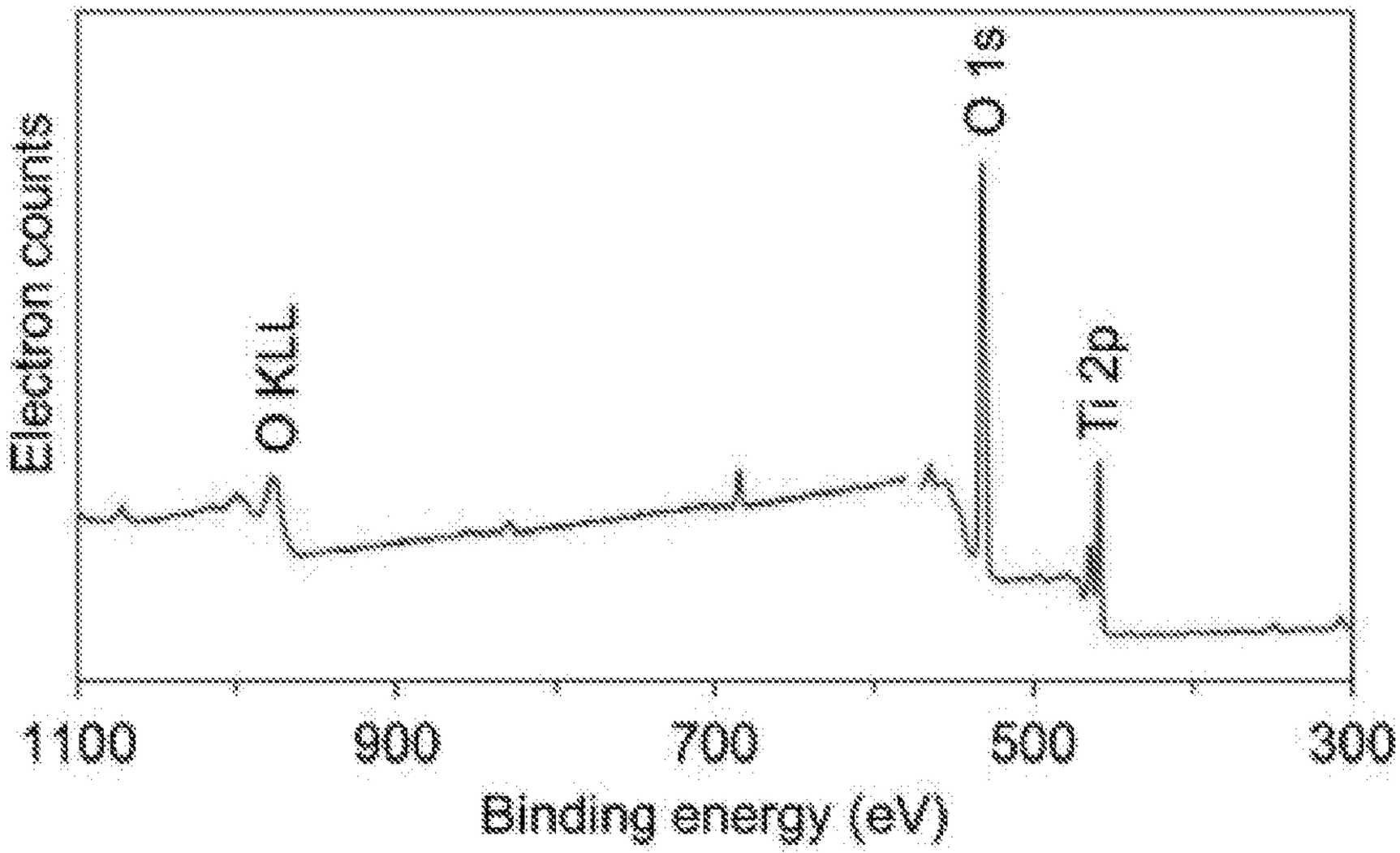


FIG. 29B

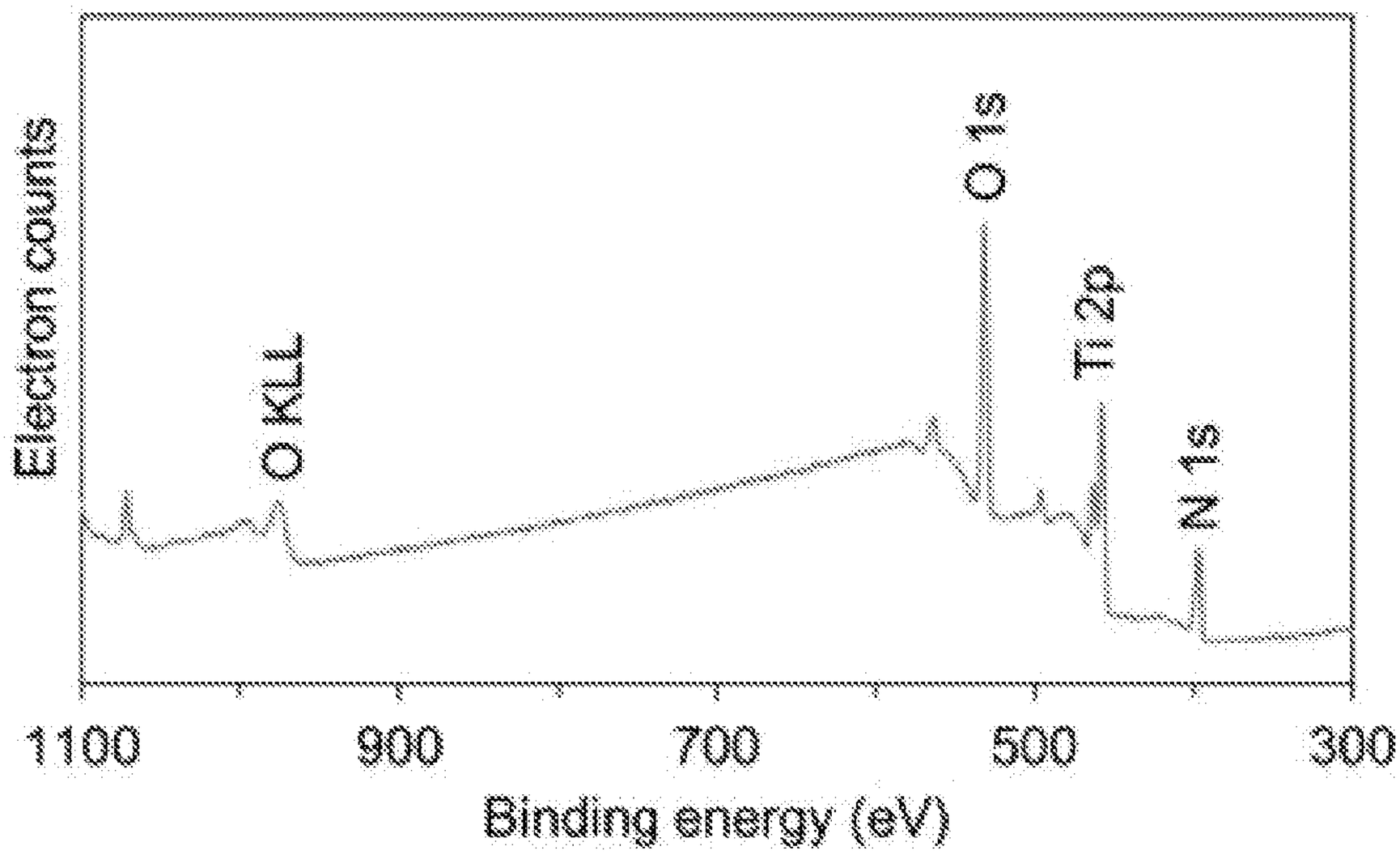


FIG. 29C

	Sheet resistance (Ω/sq.)	Resistivity (μΩ·cm)
TiN_xO_y	466.85	1867
TiO_2	∞	∞

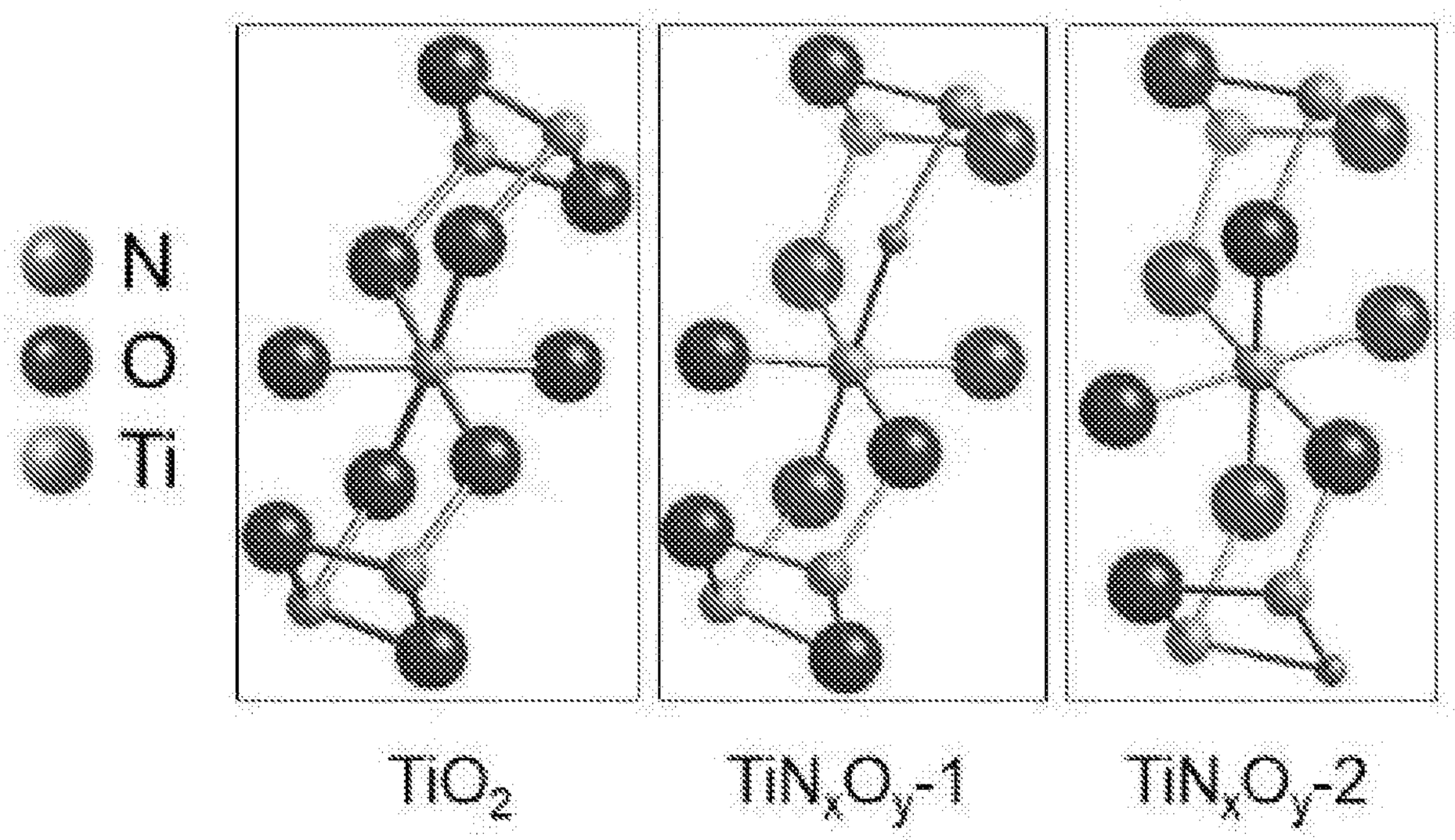


FIG. 30A

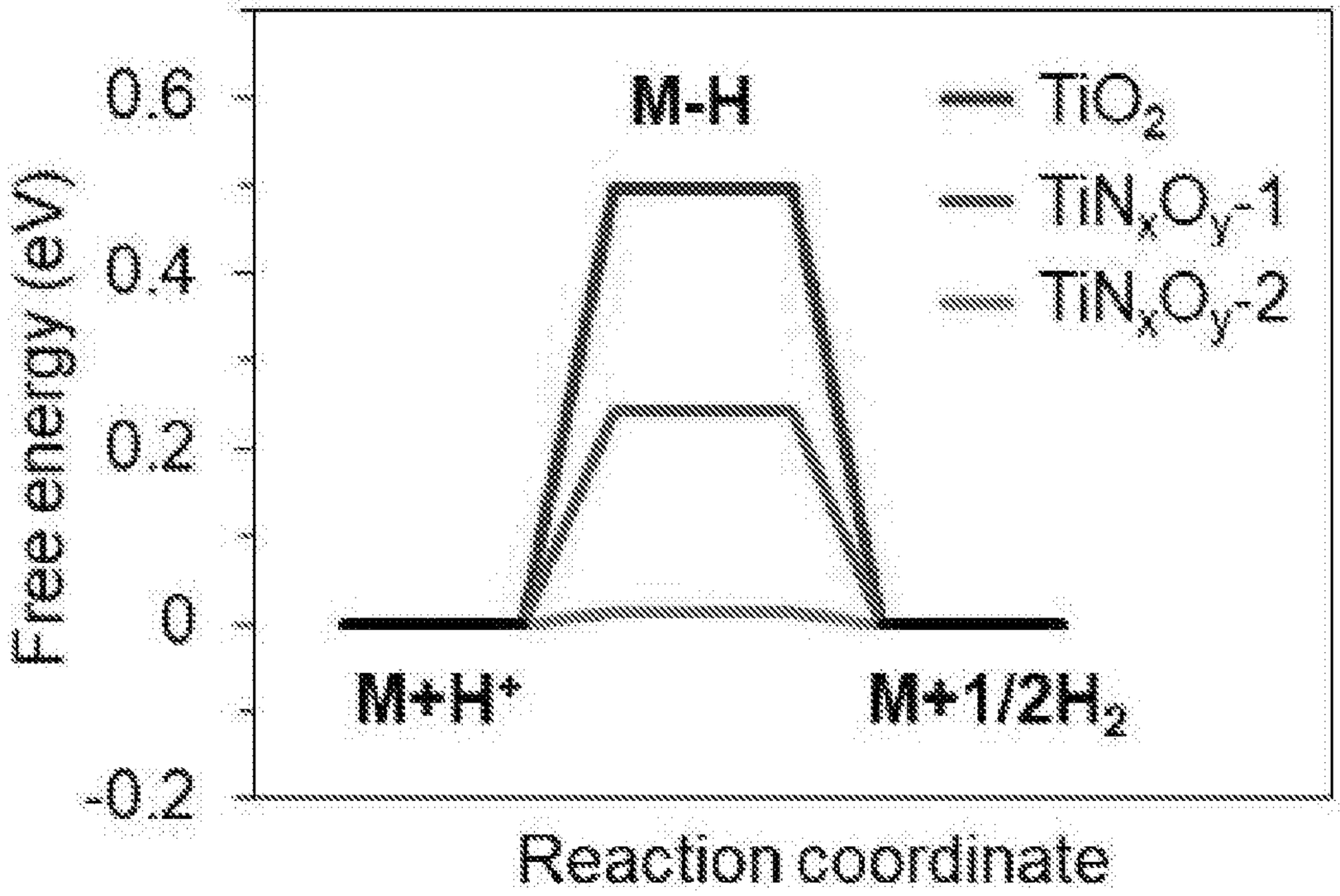


FIG. 30B

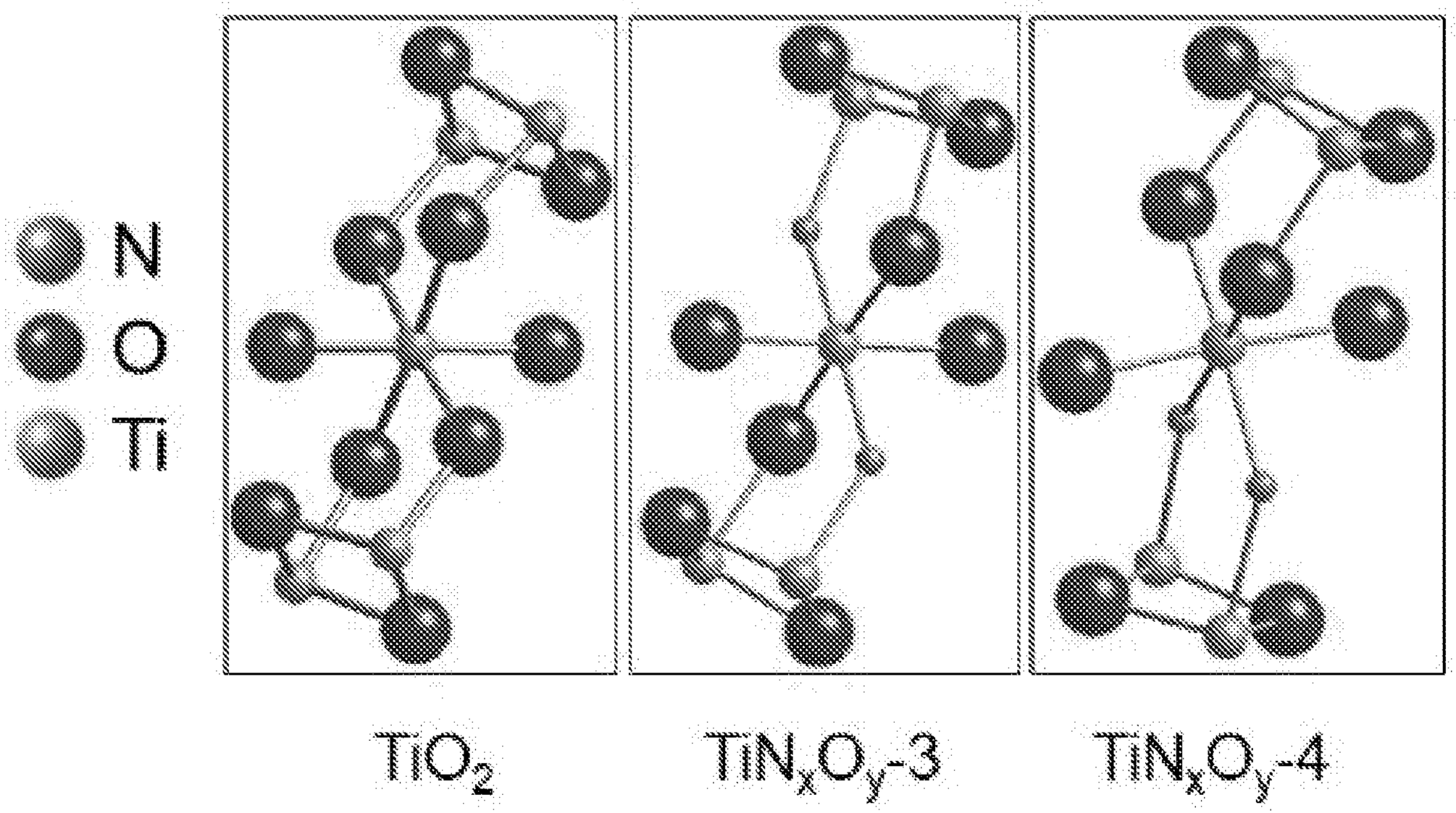


FIG. 31A

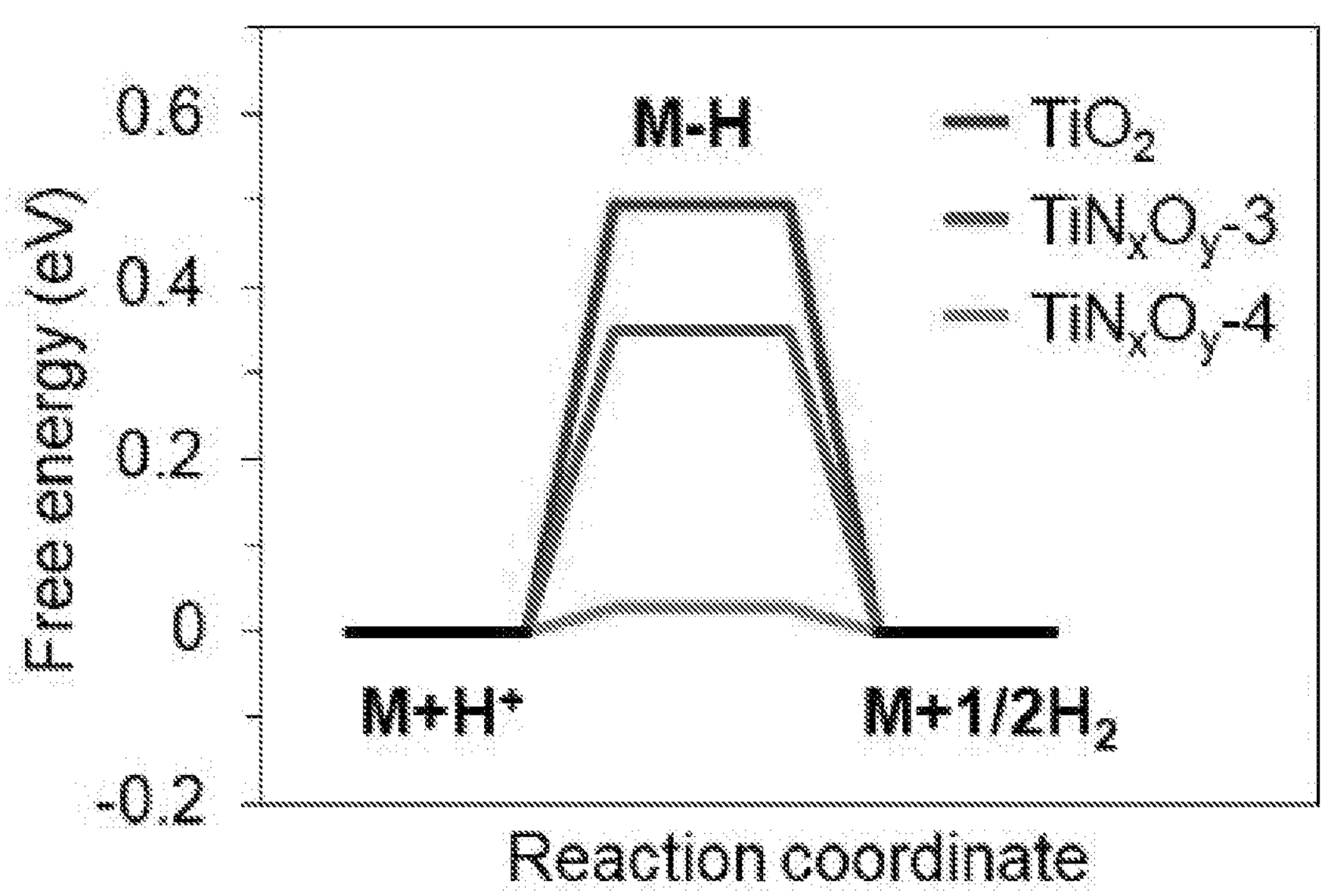


FIG. 31B

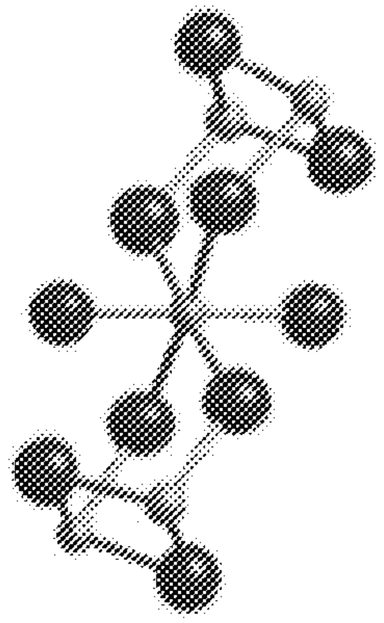
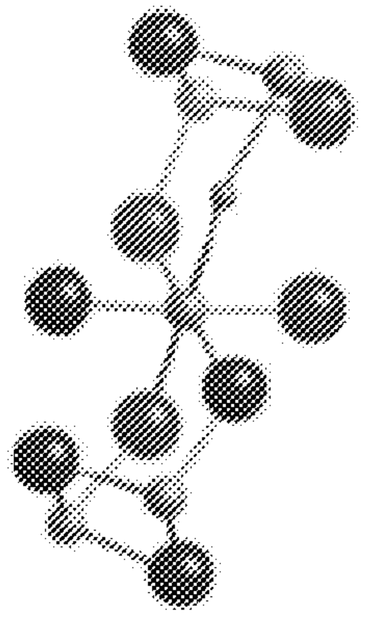
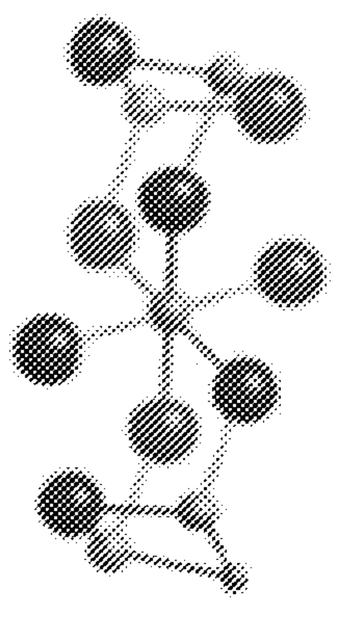
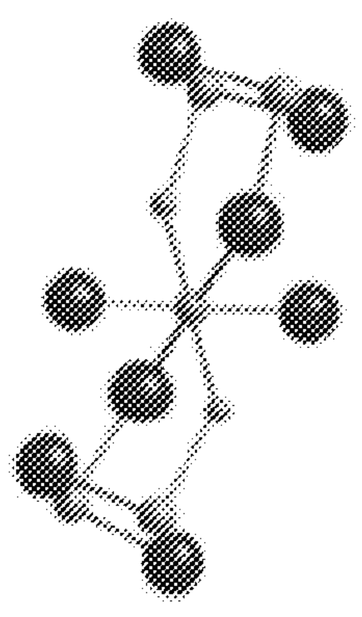
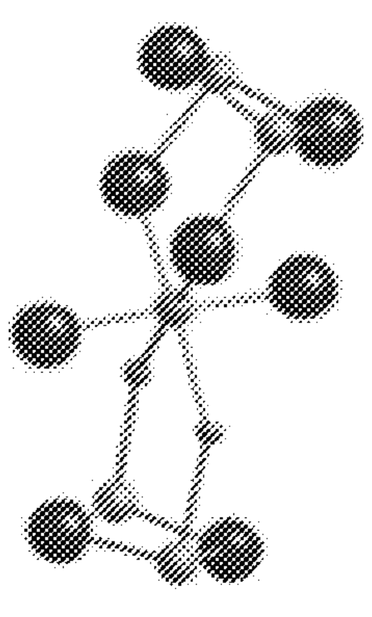
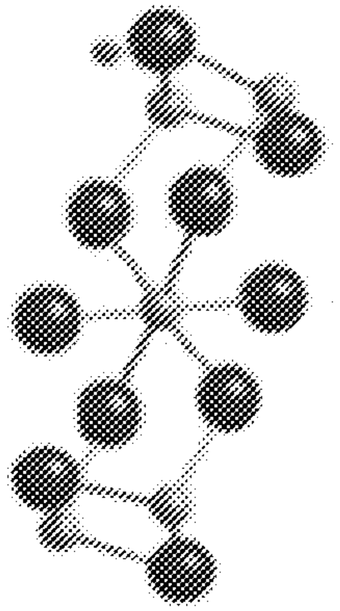
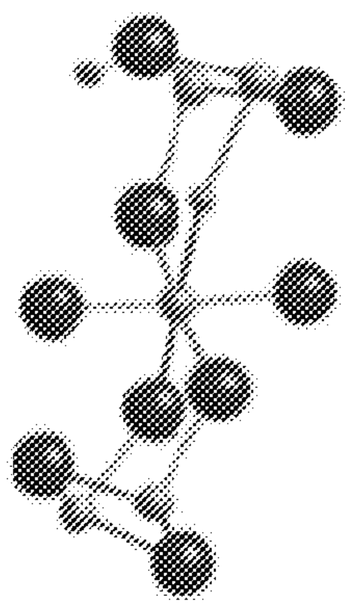
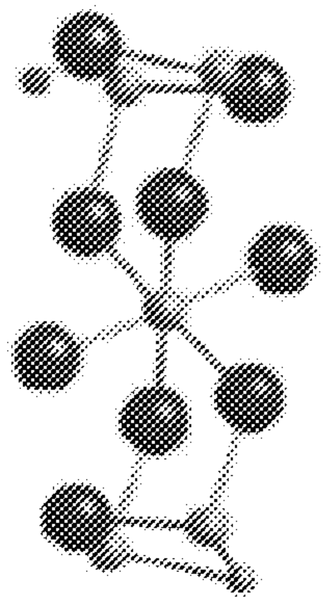
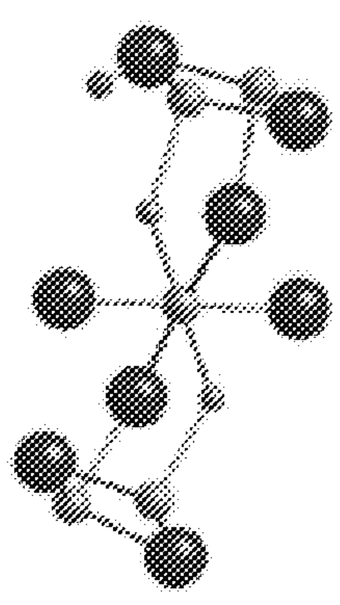
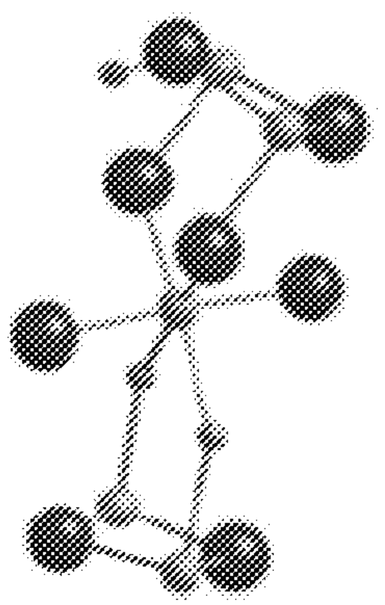
M	TiO_2	TiN_xO_y-1	TiN_xO_y-2	TiN_xO_y-3	TiN_xO_y-4
E_M	 -12.282 eV	 -14.865 eV	 -14.378 eV	 -18.086 eV	 -18.058 eV
E_{M-H}	 -13.547 eV	 -16.382 eV	 -16.125 eV	 -19.498 eV	 -19.792 eV
ΔE_H	0.255 eV	0.003 eV	-0.227 eV	0.108 eV	-0.214 eV
ΔG_H^*	0.495 eV	0.243 eV	0.013 eV	0.348 eV	0.026 eV

FIG. 32

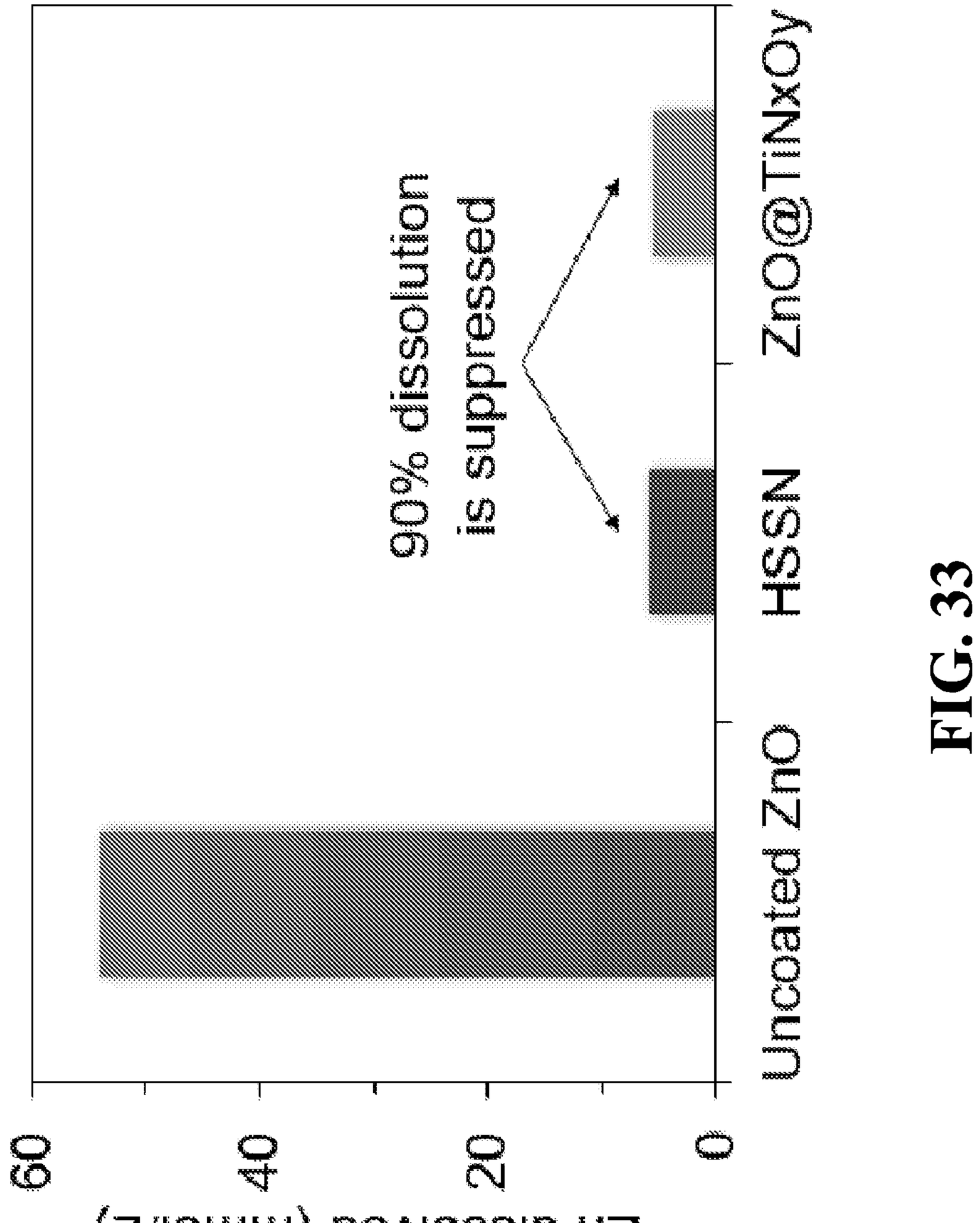

Zn dissolved (mmol/L)
0
2
4
6
Uncoated ZnO
HSSN ZnO@TiNxOy
90% dissolution
is suppressed

FIG. 33

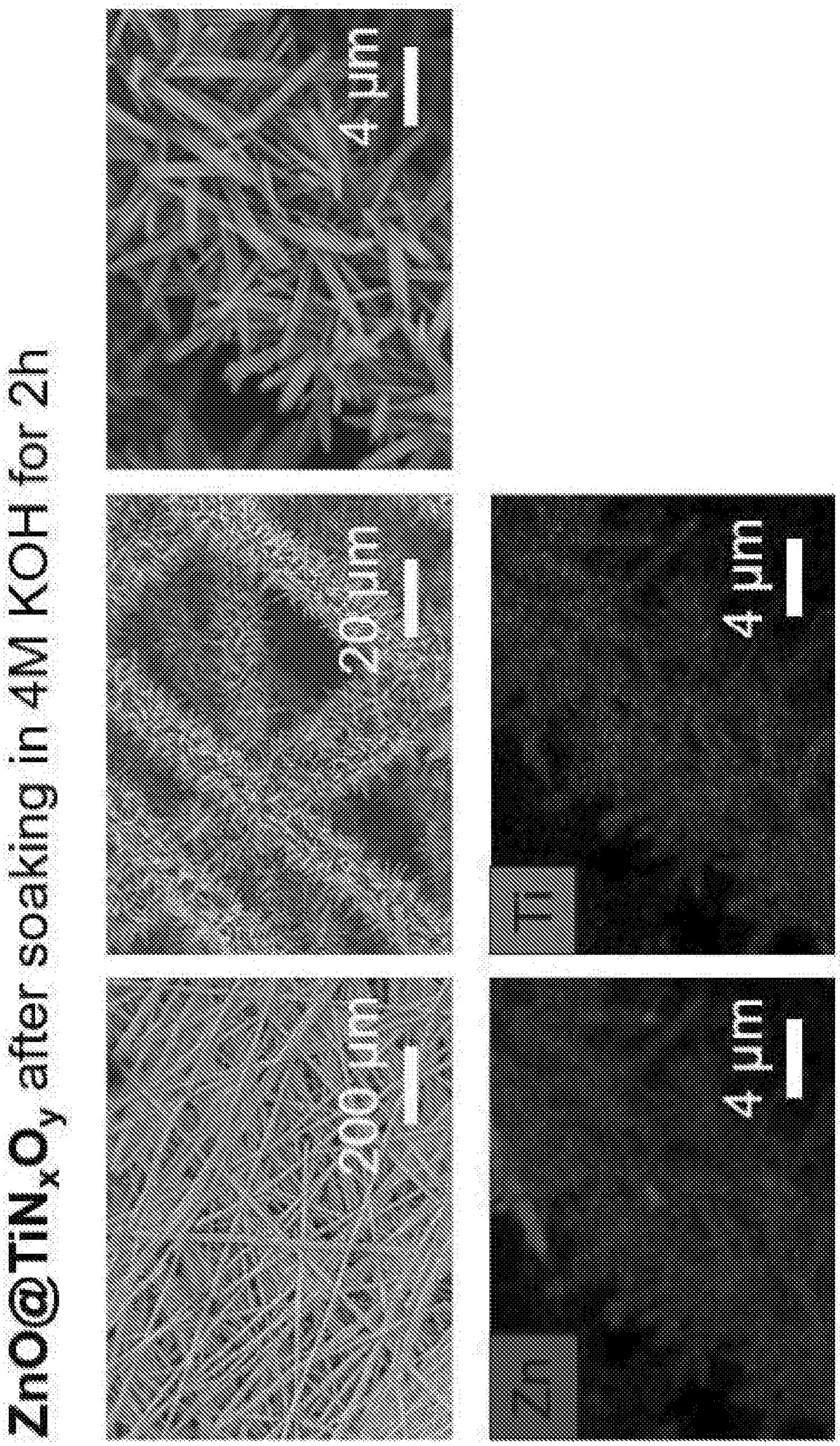

ZnO@TiN$_x$O$_y$ after soaking in 4M KOH for 2h
4 μm
20 μm
20μm
4 μm
20μm
4 μm

FIG. 34

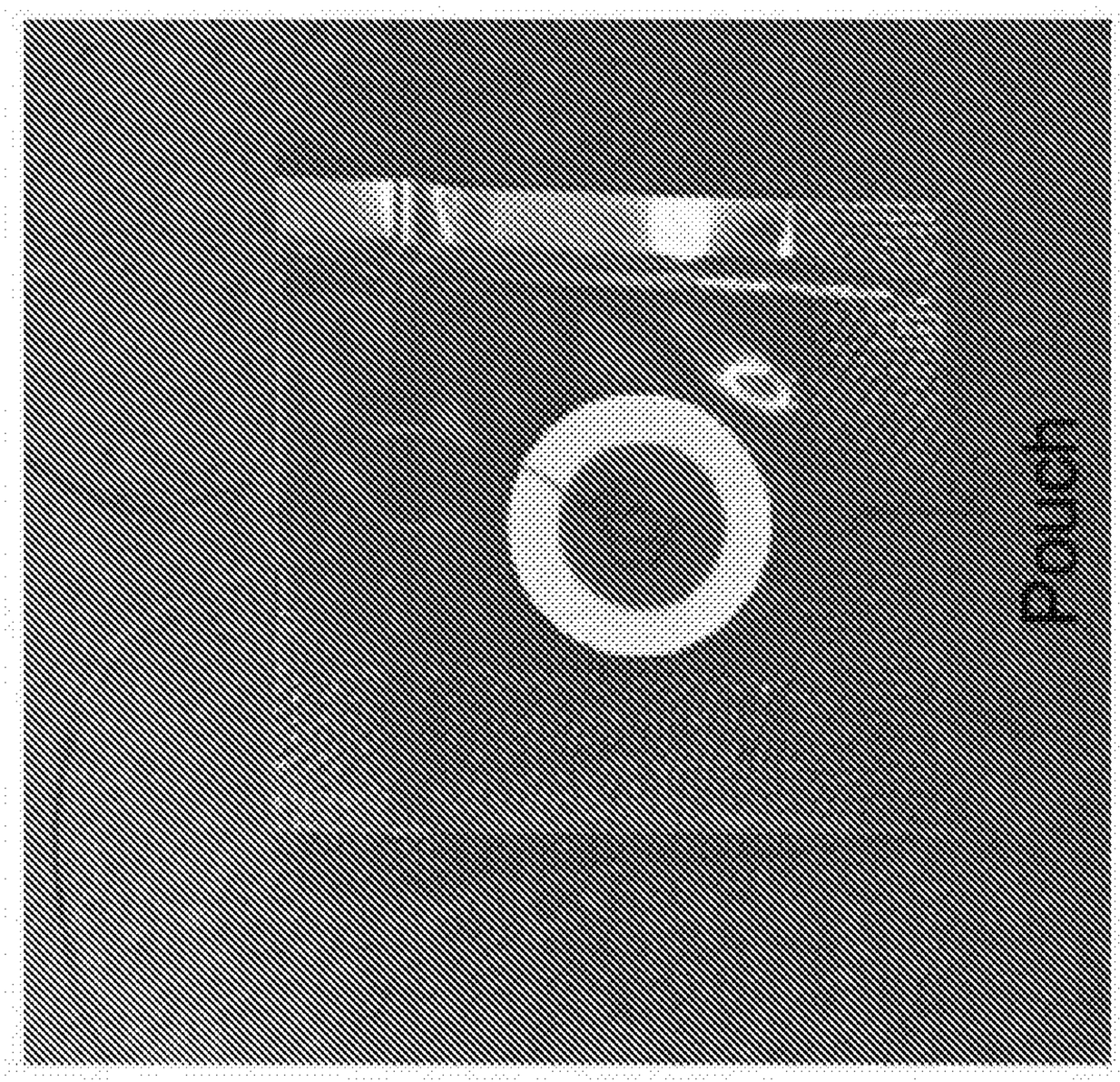


FIG. 35B

FIG. 35A

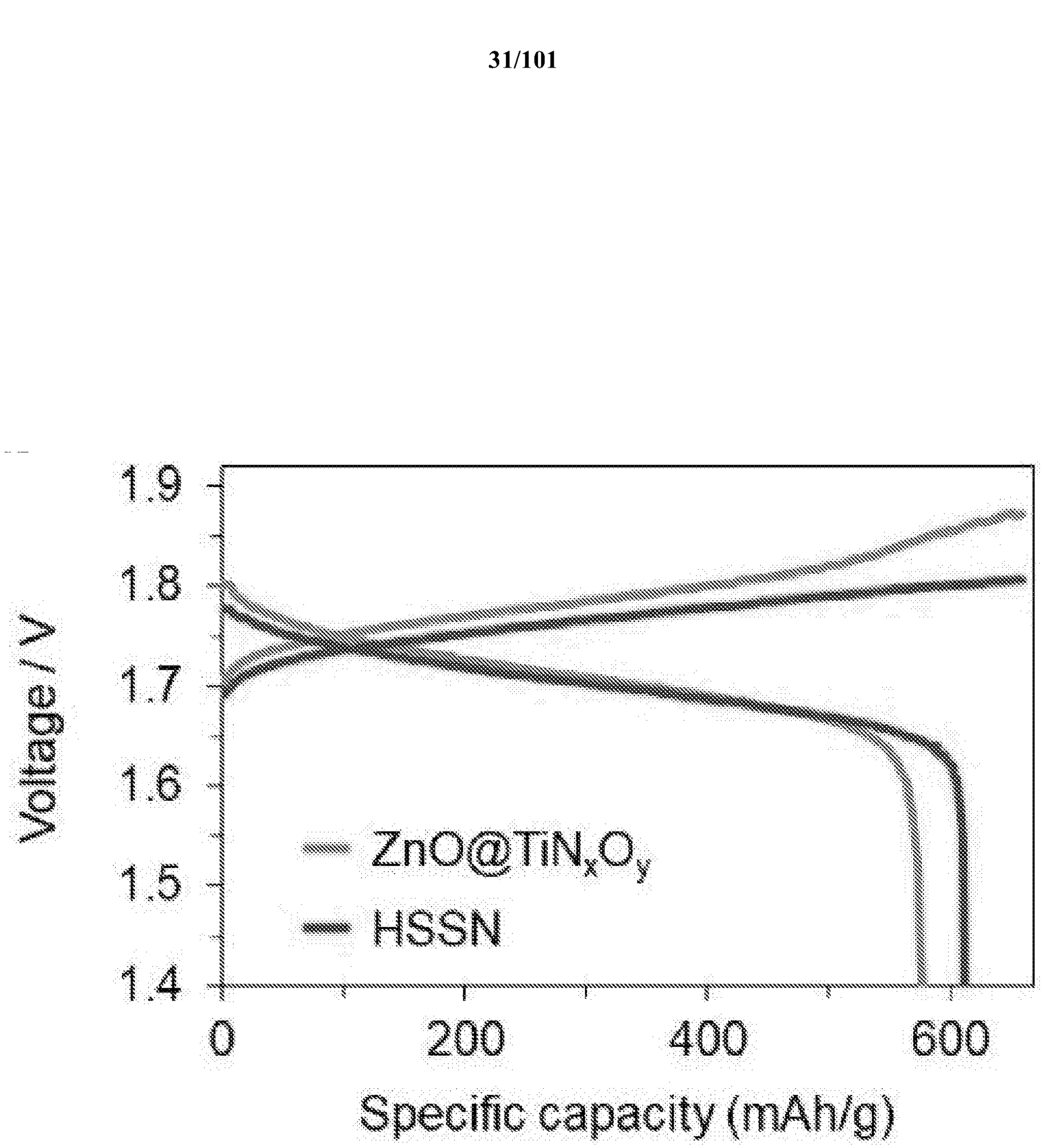

Voltage / V
1.9
1.8
1.7
1.6
1.5
1.4
0
200
400
600
Specific capacity (mAh/g)
ZnO@TiNxOy
HSSN

FIG. 36

FIG. 37A

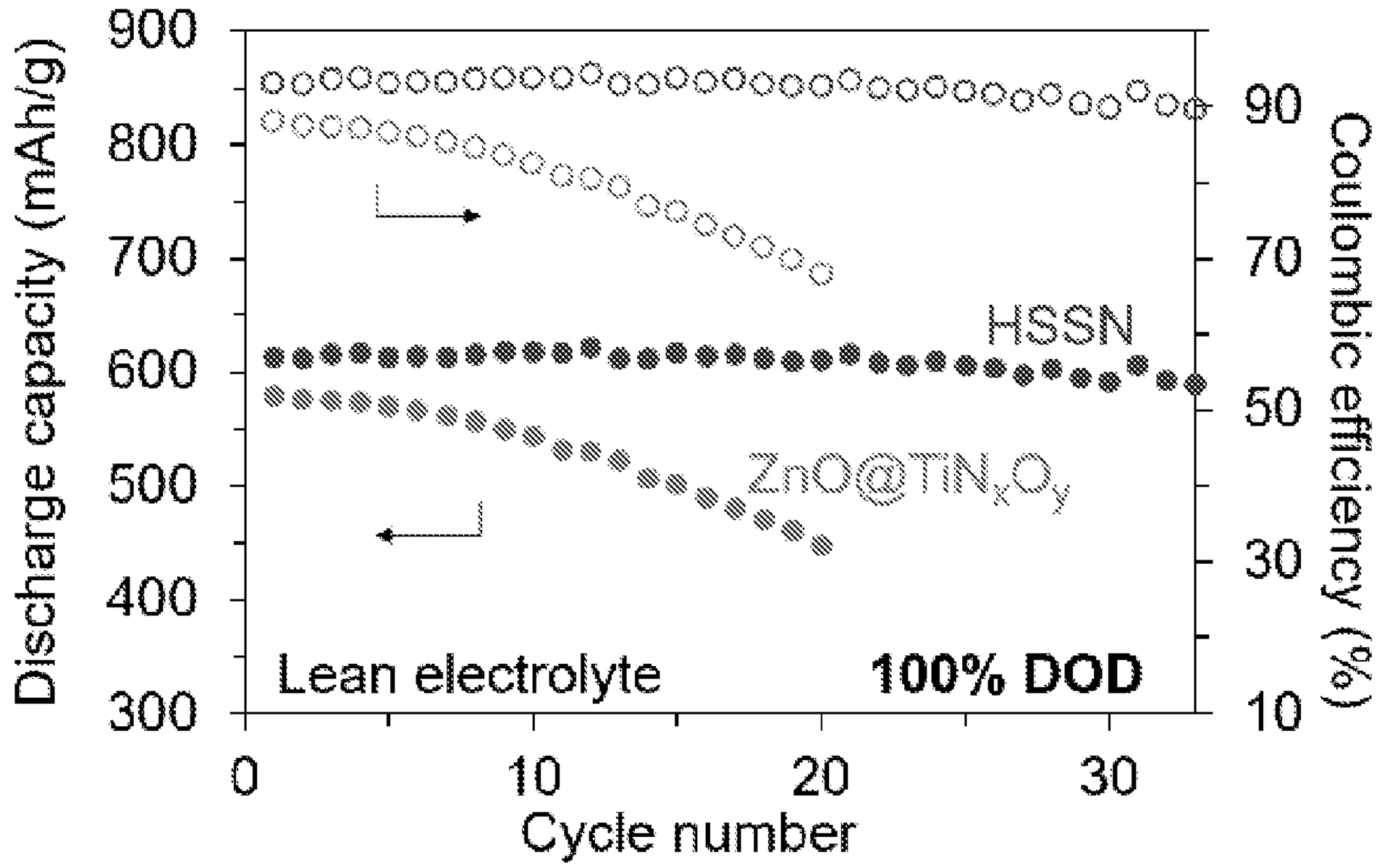
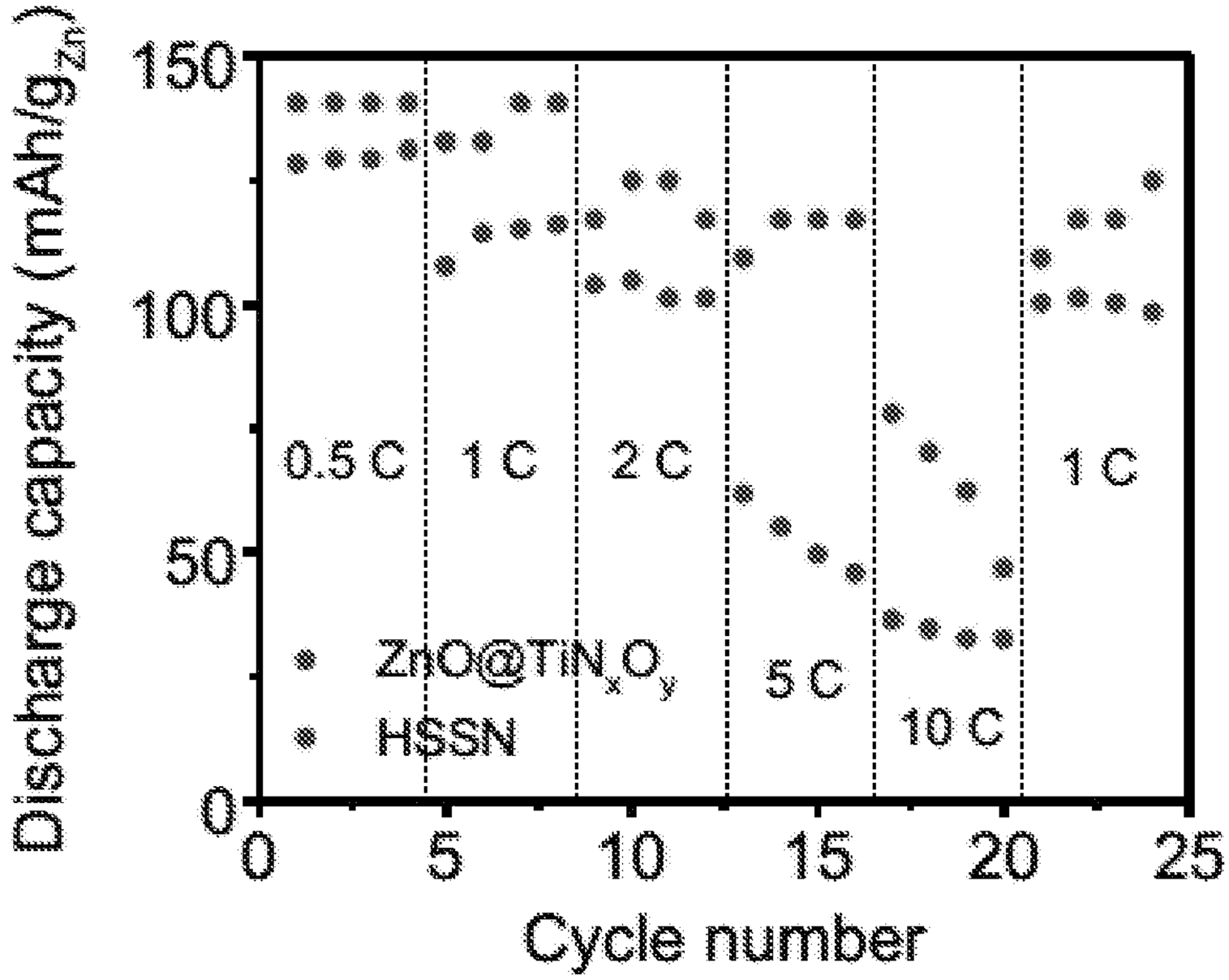


FIG. 37B



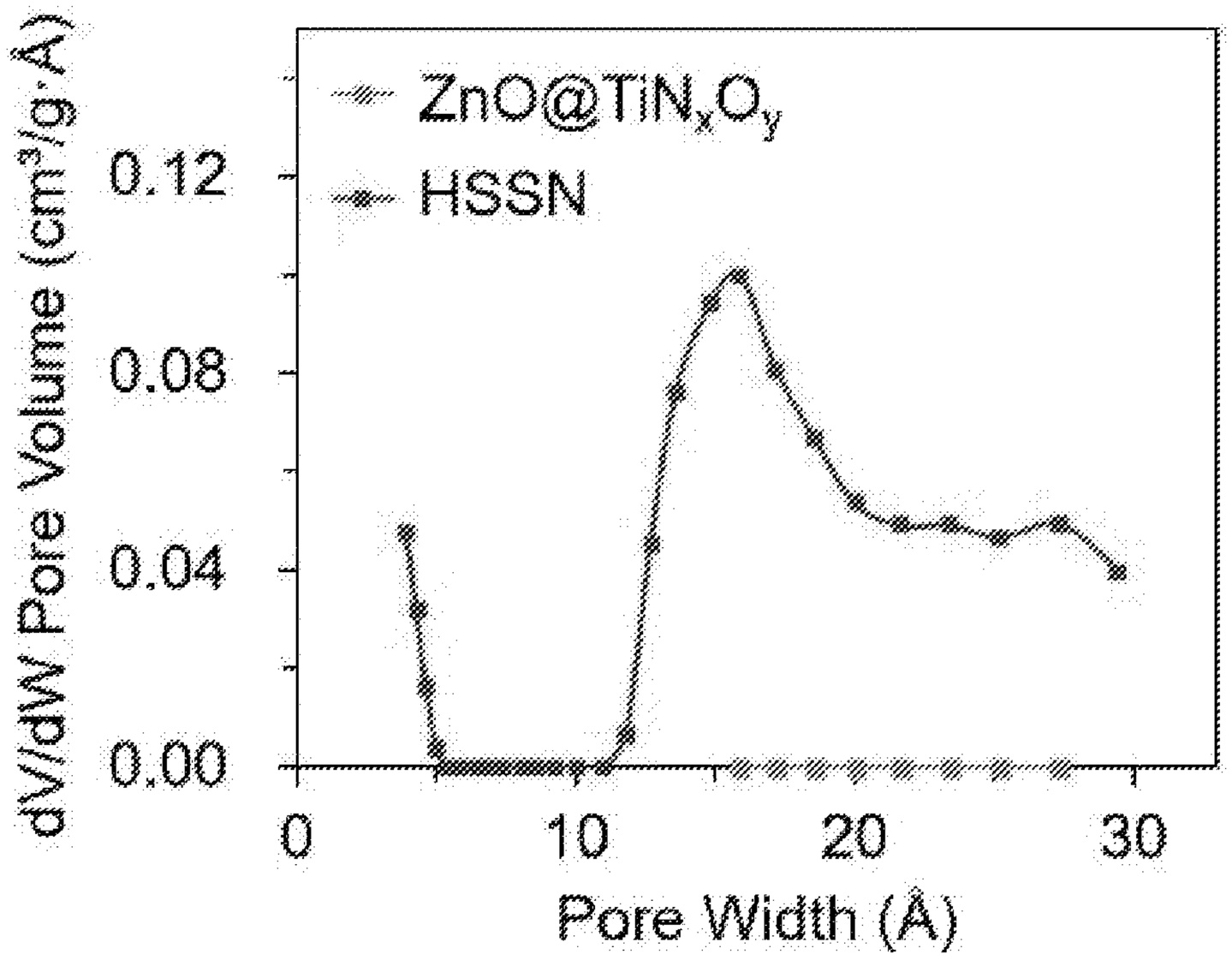


FIG. 38A

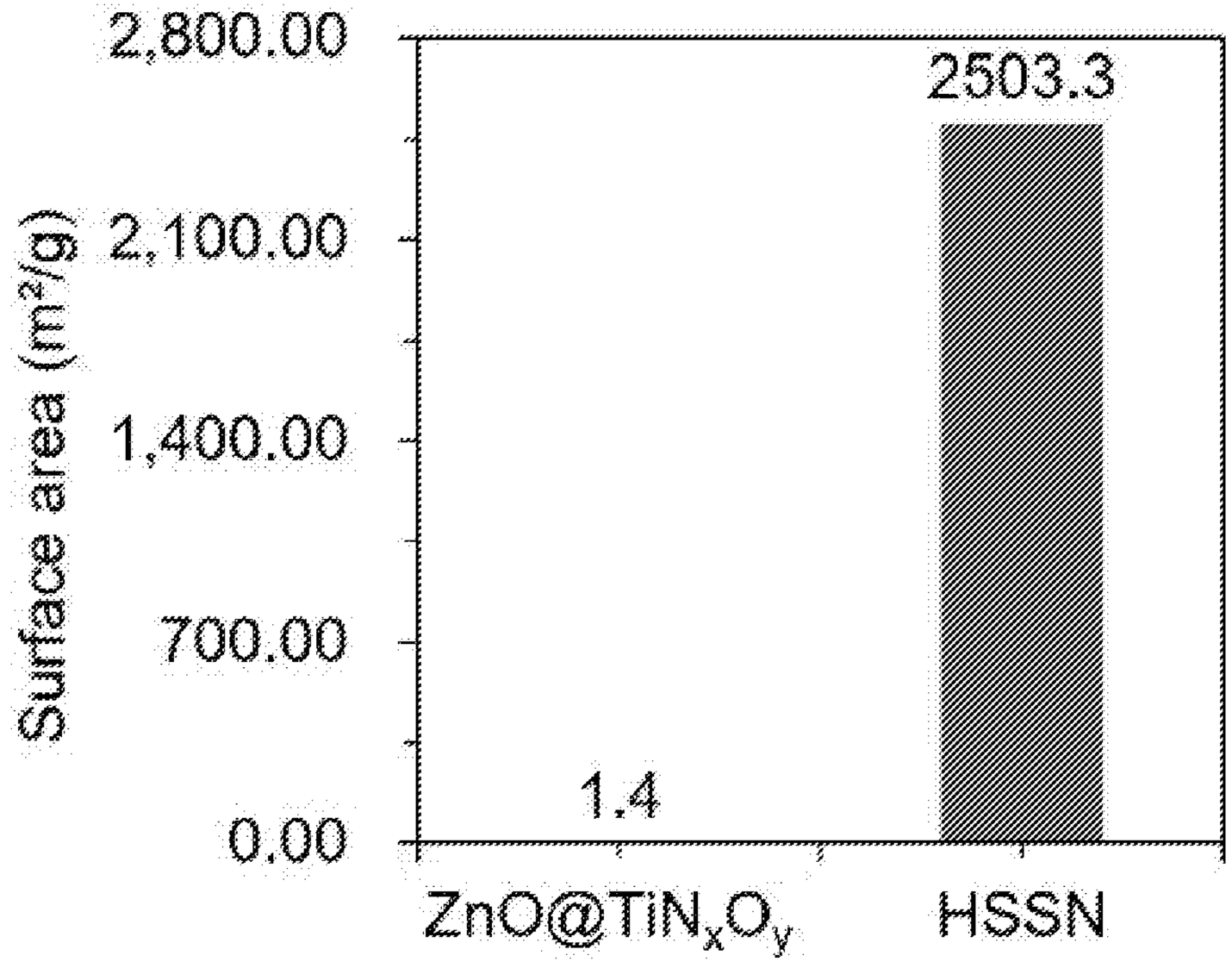


FIG. 38B

Anode material	Coulombic efficiency (%)
$Ca(OH)_2$-coated ZnO	29.10
$Sn_6O_4(OH)_4$-coated ZnO	37.50
ZnO nanoplate	69.15
Ag-modified ZnO	71.43
ZnAlSb-LDH	78.10
ZnO/SnO_2	84.62
ZnO@RGO	85.00
ZnO microspheres	86.63
ZnO@Ag@Polypyrrole	89.00
LDOs	89.42
Ag/ZnO	89.67
IZO	91.04
SnO_2@ZnO	91.19
Ag-LDH	93.19
The Present HSSN Anode	**93.50**

FIG. 39

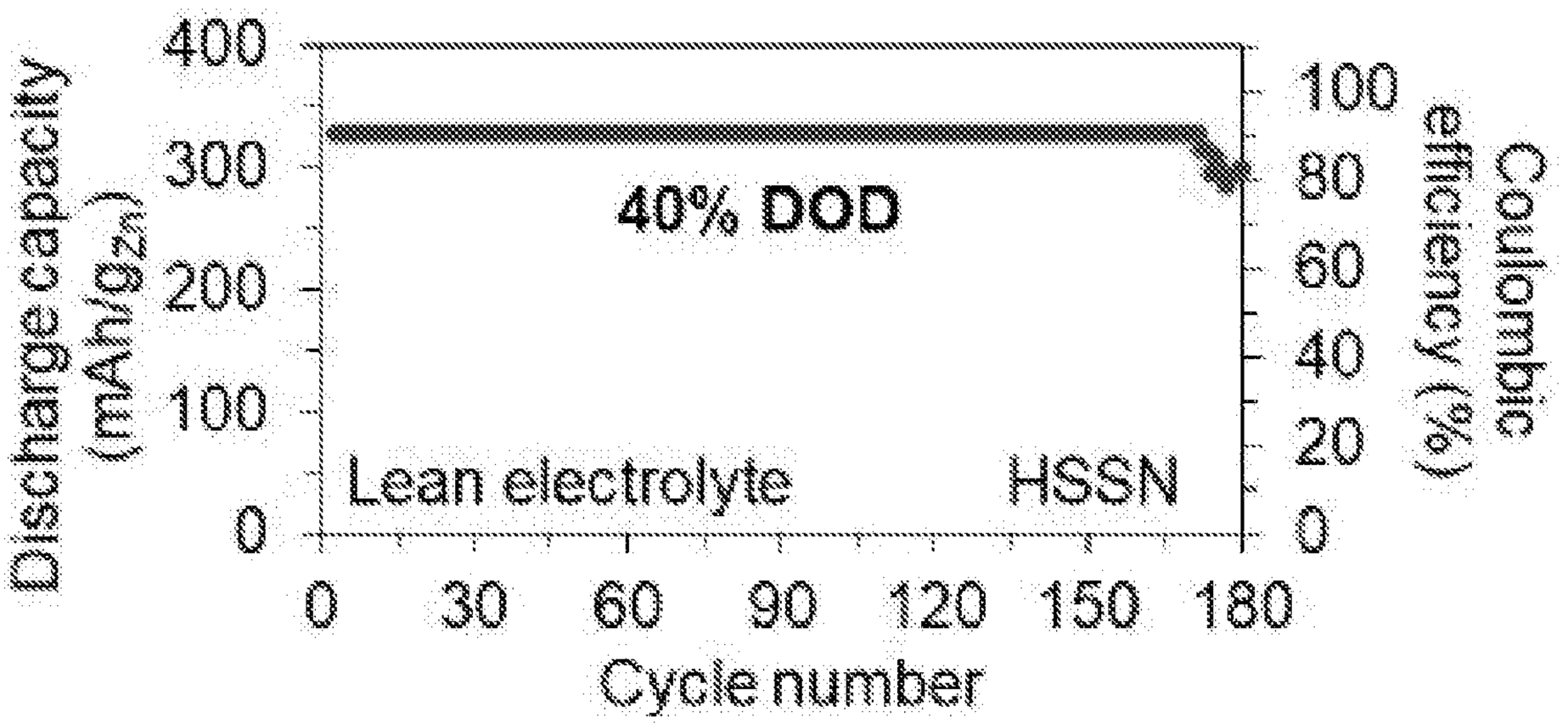

Discharge capacity (mAh/gZn)
400
300
200
100
0
40% DOD
Lean electrolyte
HSSN
Coulombic efficiency (%)
100
80
60
40
20
0
0
30
60
90
120
150
180
Cycle number

FIG. 40

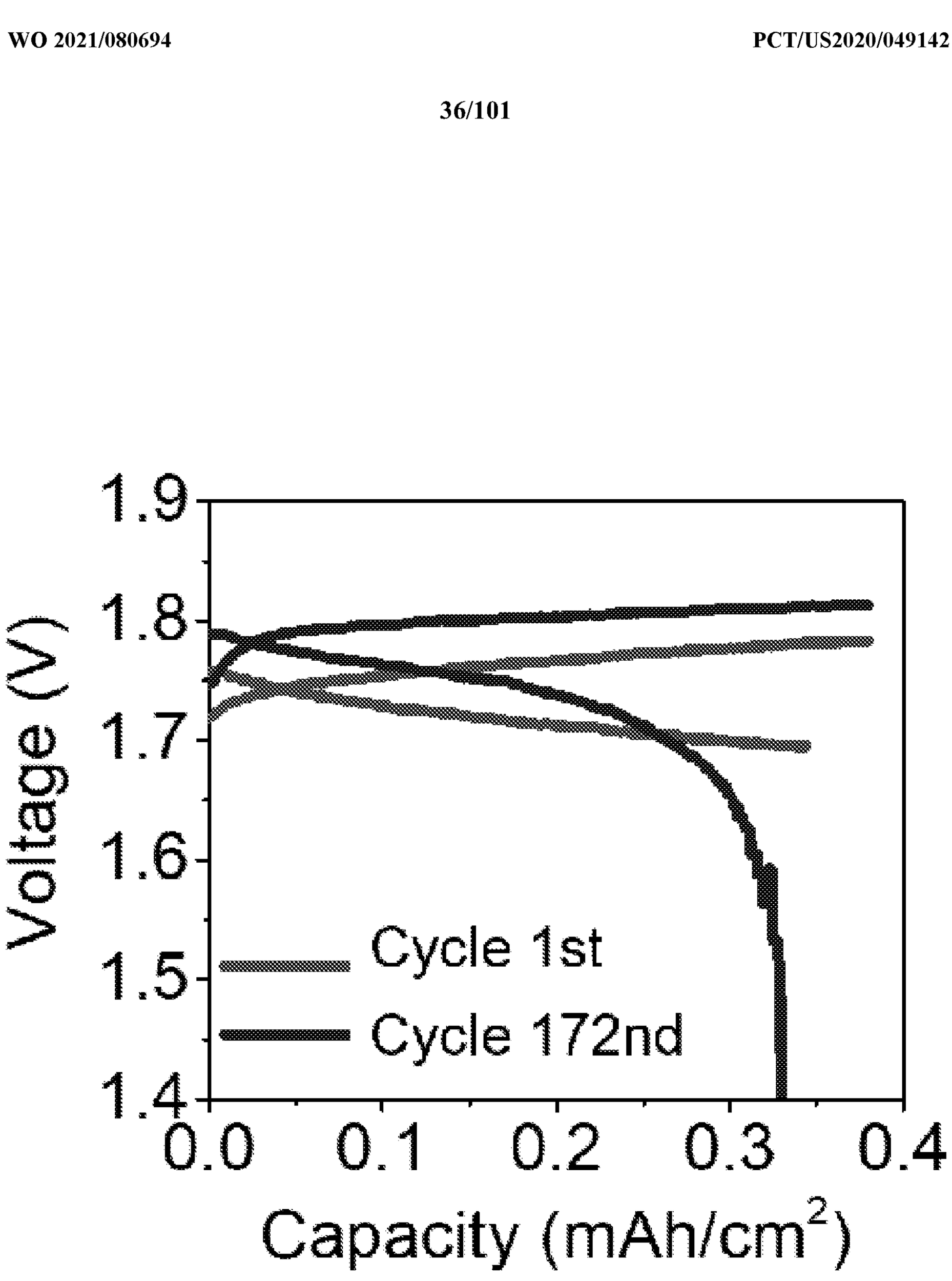

1.9
1.8
1.7
1.6
1.5
1.4
Voltage (V)
Cycle 1st
Cycle 172nd
0.0
0.1
0.2
0.3
0.4
Capacity (mAh/cm^2)

FIG. 41

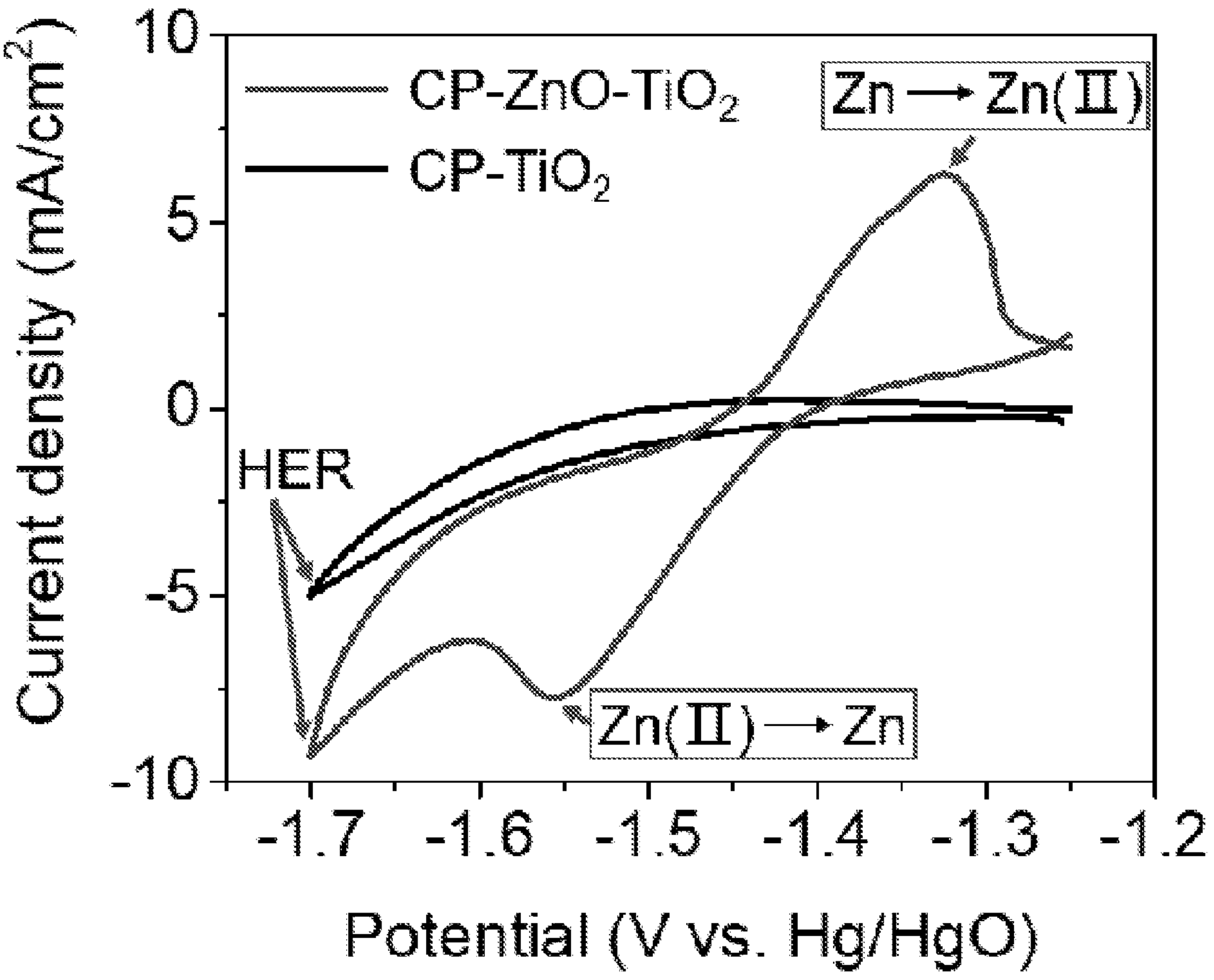
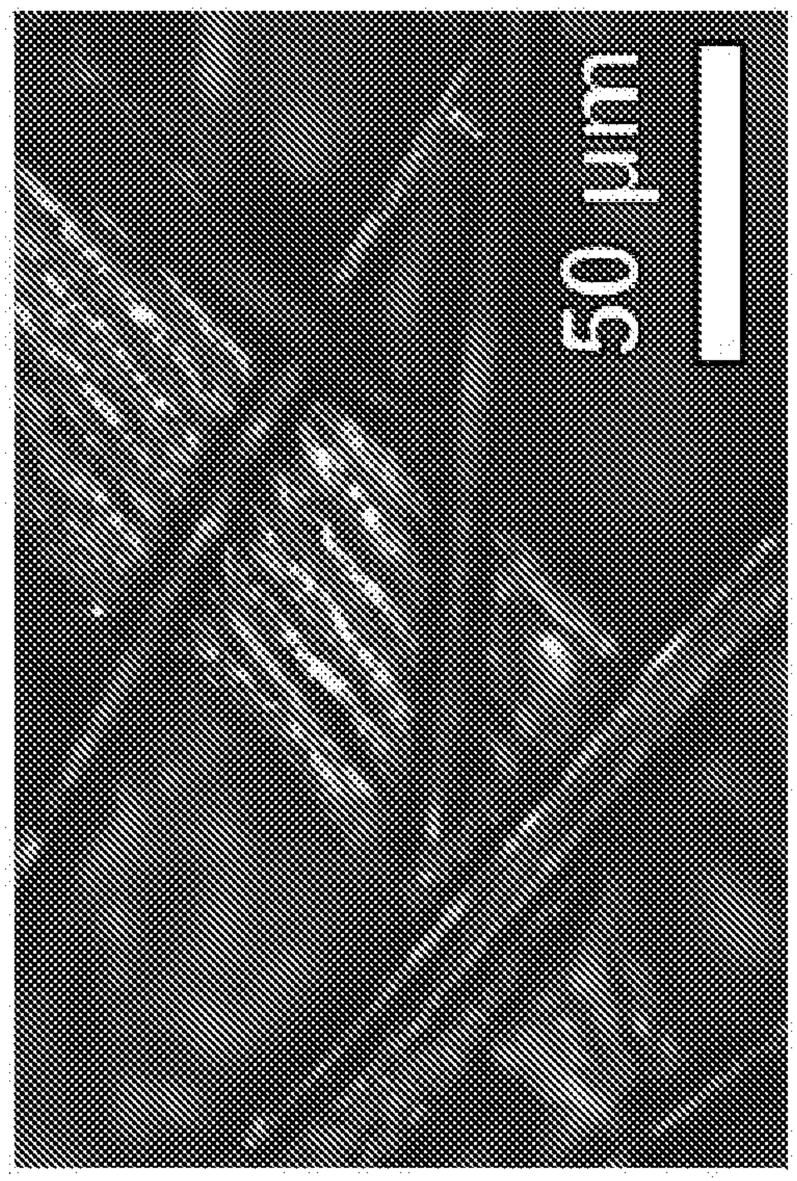

CP-ZnO-TiO2
CP-TiO2
Zn → Zn(II)
Zn(II) → Zn
HER
Current density (mA/cm2)
Potential (V vs. Hg/HgO)
10
5
0
-5
-10
-1.7
-1.6
-1.5
-1.4
-1.3
-1.2

FIG. 42



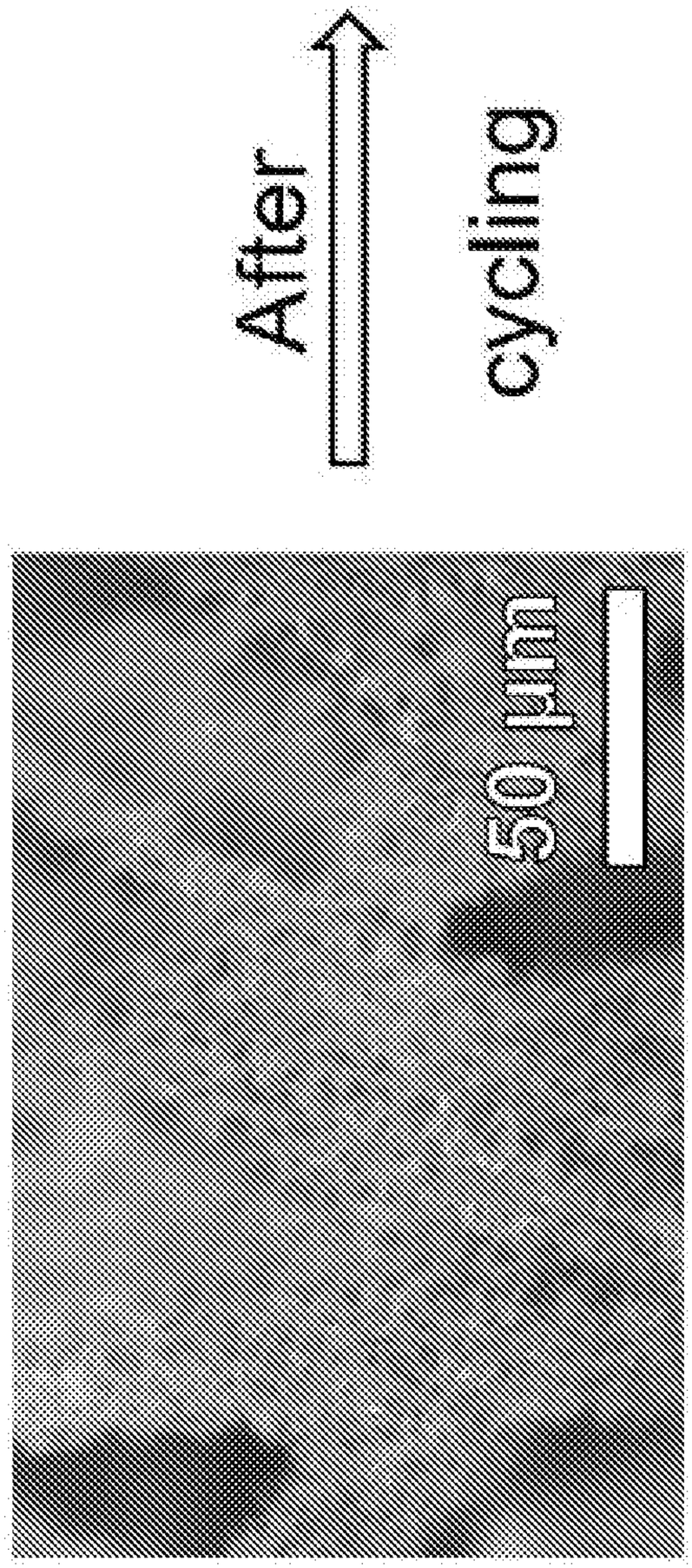


FIG. 43

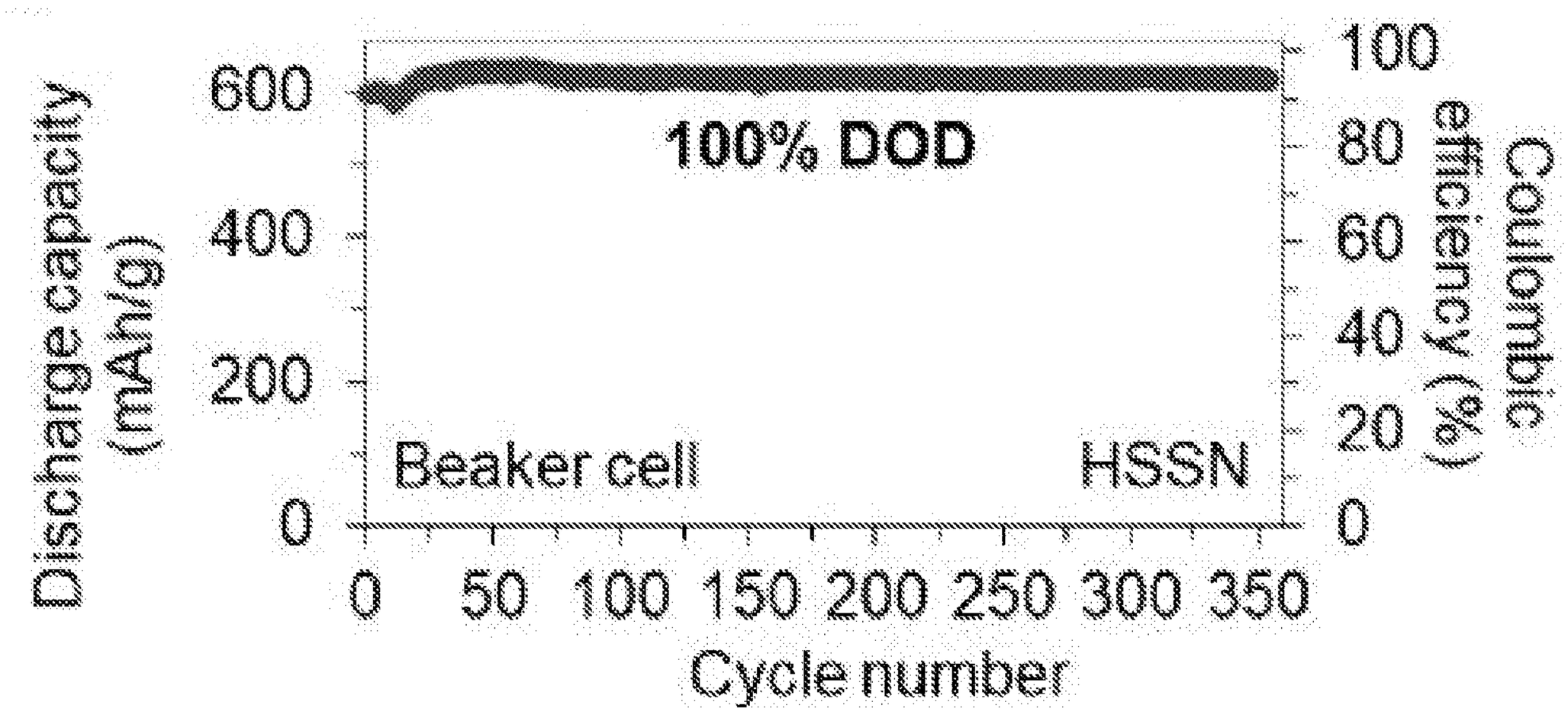

100% DOD
Beaker cell
HSSN
Discharge capacity (mAh/g)
Coulombic efficiency (%)
Cycle number
0
200
400
600
0
20
40
60
80
100
0
50
100
150
200
250
300
350

FIG. 44

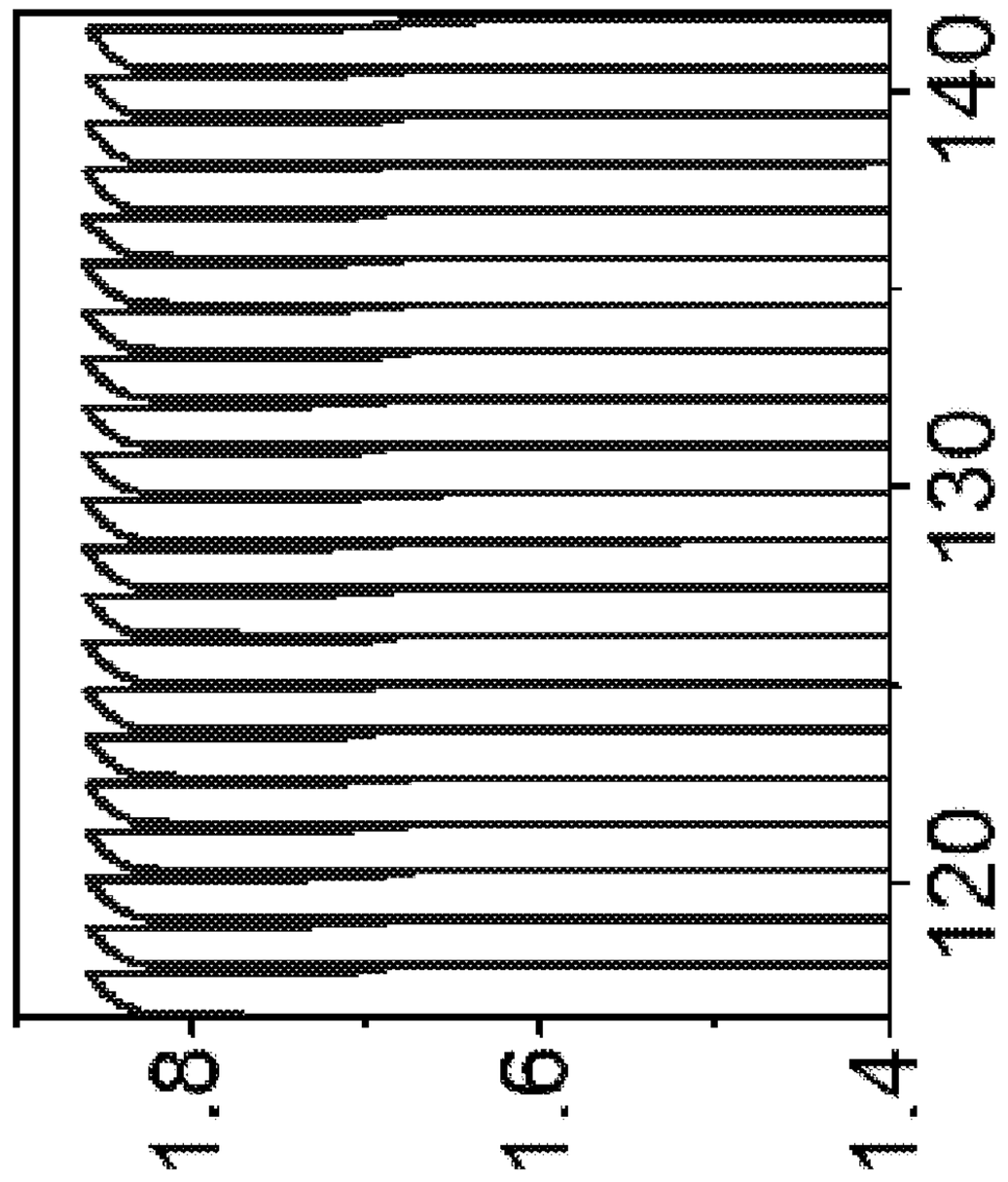


FIG. 45A

FIG. 45B

Anode No.	Anode material	E/DC ratio (mL/mAh)	Coulombic efficiency (%)
0	Zn sponge	0.0062	~100
1	Backside-plating zinc	34.09	92.0
2	ZnO@C	0.29	58.8
3	ZnO@TiN_xO_y	0.47	81.6
4	Zn-pome	0.27	55.5
5	ZnO lasagna	0.32	47.9
6	ZnO nanoparticle	0.06	67.1
7	ZnO particle	0.05	72.7
8	ZnO nanorod	0.05	79.3
9	Calcium zincate	0.10	77.5
10	Zn@Bi_2O_3-CaO-ZnO glass	8.00	83.3
11	IHCP-ZnO/C	0.10	60.8
12	Commercial ZnO	0.58	85.5
13	TRIEN-ZnO	0.59	84.5
14	EN-ZnO	0.58	86.5
15	DIEN-ZnO	0.53	93.7
16	Cr_xZnO	0.41	82.0
17	$Ni_xZn_{(1-x)}O$	0.34	98.0
18	Microcrystalline ZnO	0.38	87.0
19	$Fe_{0.01}ZnO$	0.72	92.0
20	ZnO-LiOH	0.36	93.0
21	$Mg_xZn_{1-x}O$	0.58	85.5
22	**The Present HSSN Anode**	0.14	93.8

FIG. 46

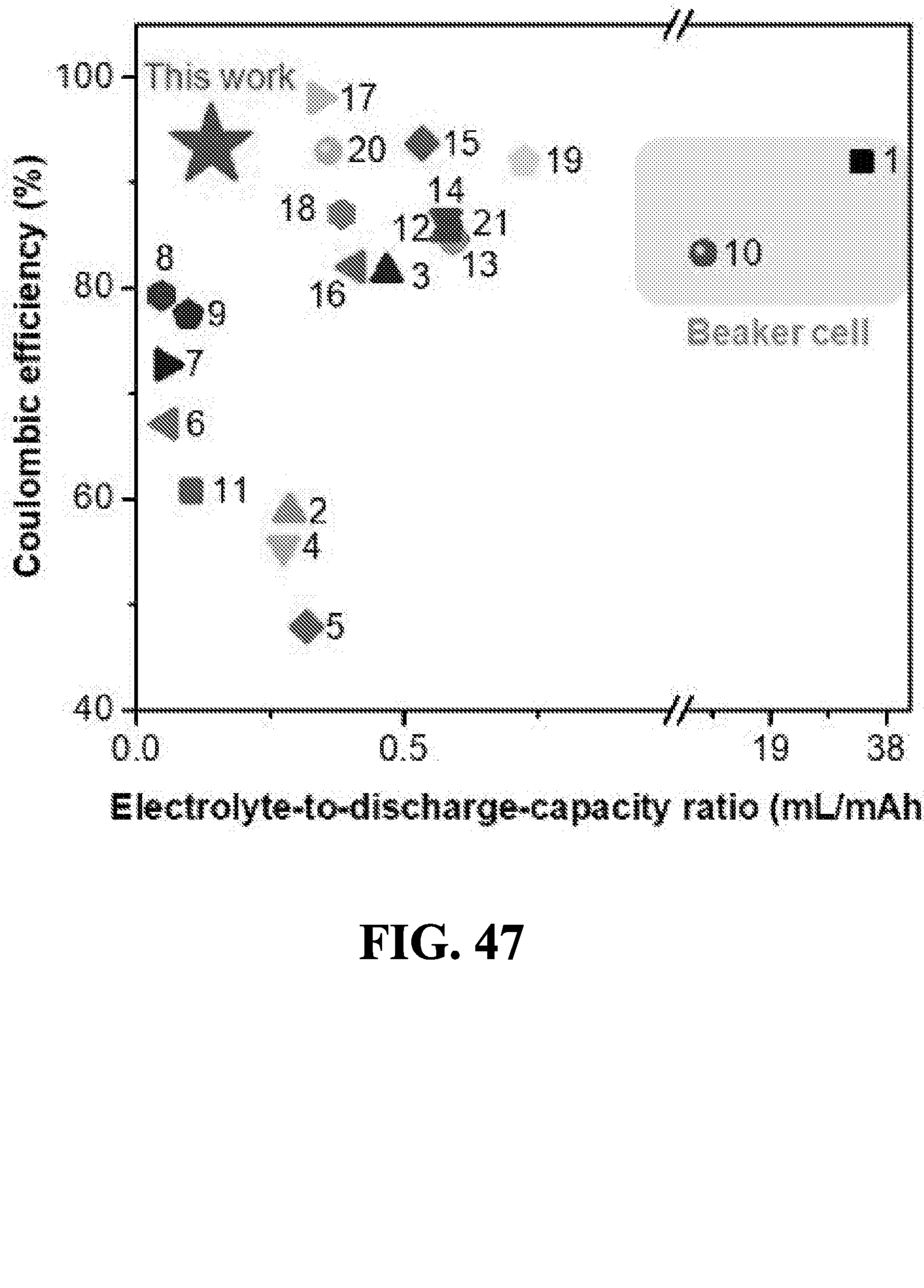

This work
17
20
15
19
14
18
12
21
13
3
16
8
9
7
6
11
2
4
5
1
10
Beaker cell
100
80
60
40
0.0
0.5
19
38
Coulombic efficiency (%)
Electrolyte-to-discharge-capacity ratio (mL/mAh)

FIG. 47

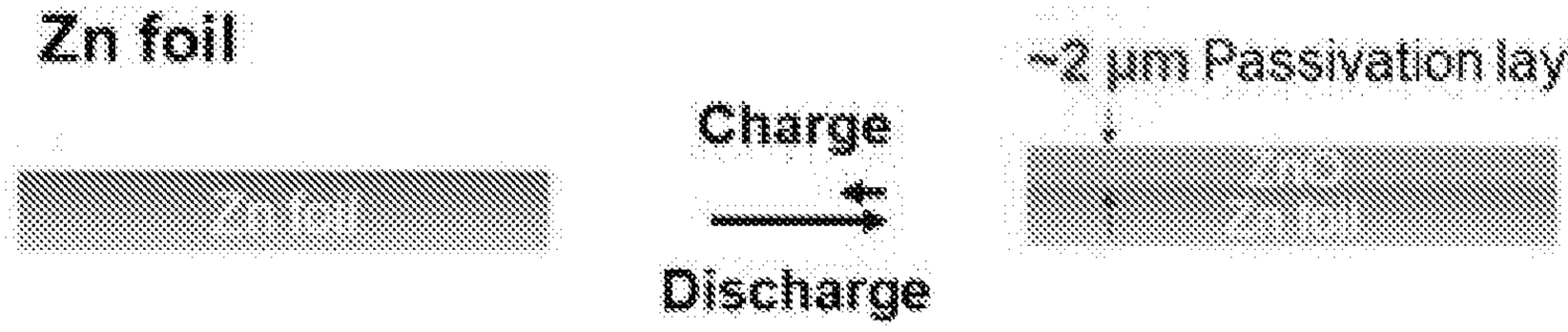

Zn foil
~2 μm Passivation layer
Zn foil
Charge
Discharge

FIG. 48

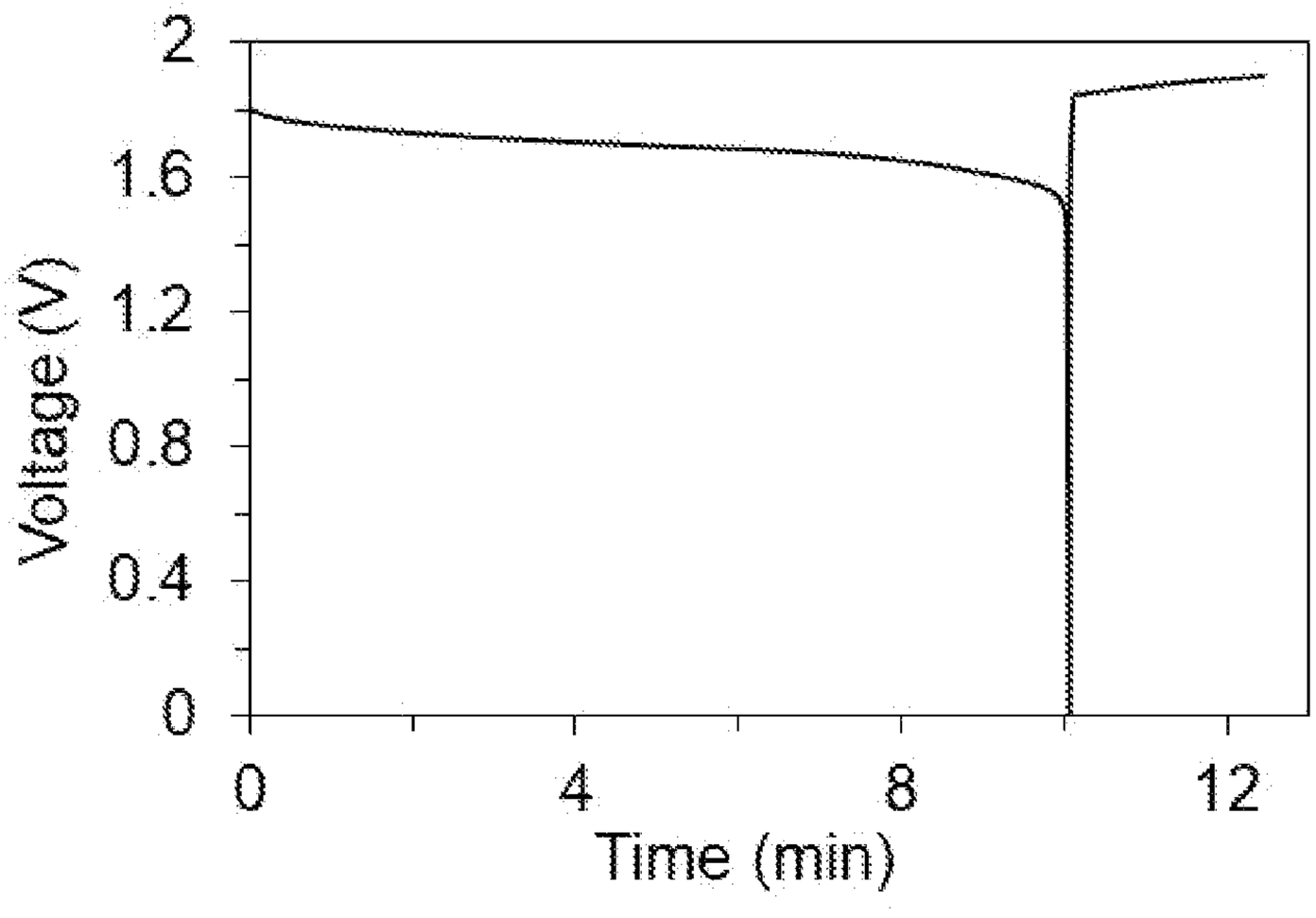

2
1.6
1.2
0.8
0.4
0
Voltage (V)
0
4
8
12
Time (min)

FIG. 49

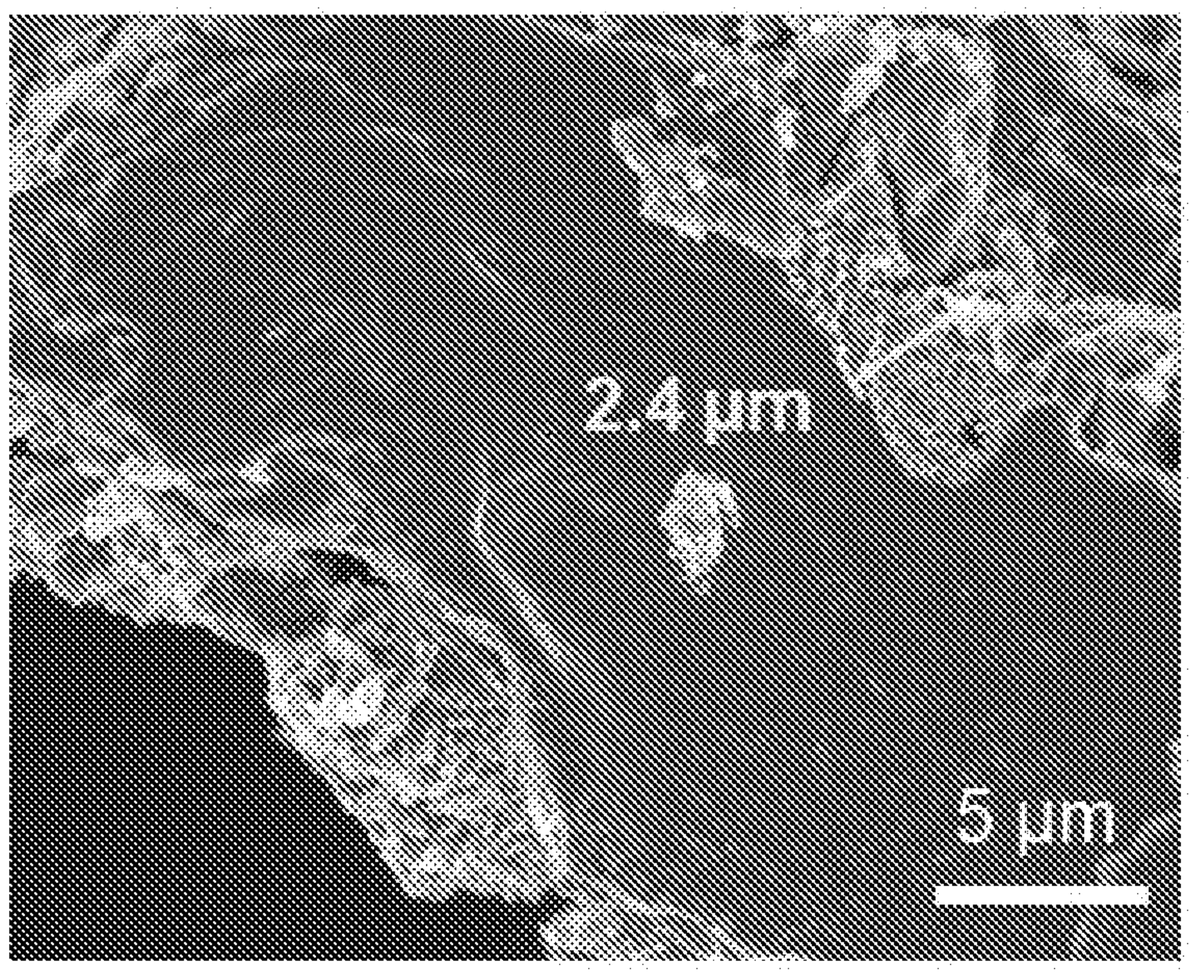

2.4 µm
5 µm

FIG. 50

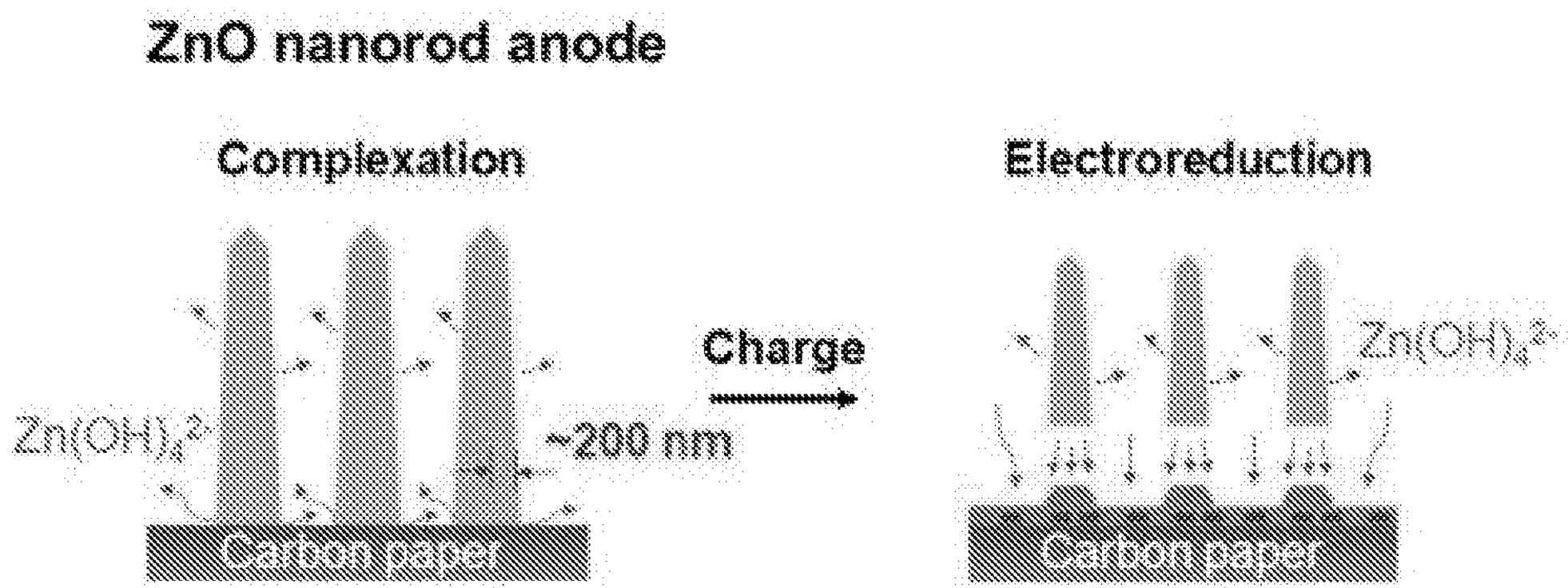

ZnO nanorod anode
Complexation
Electroreduction
Charge
$Zn(OH)_4^{2-}$
~200 nm
Carbon paper
$Zn(OH)_4^{2-}$
Carbon paper

FIG. 51

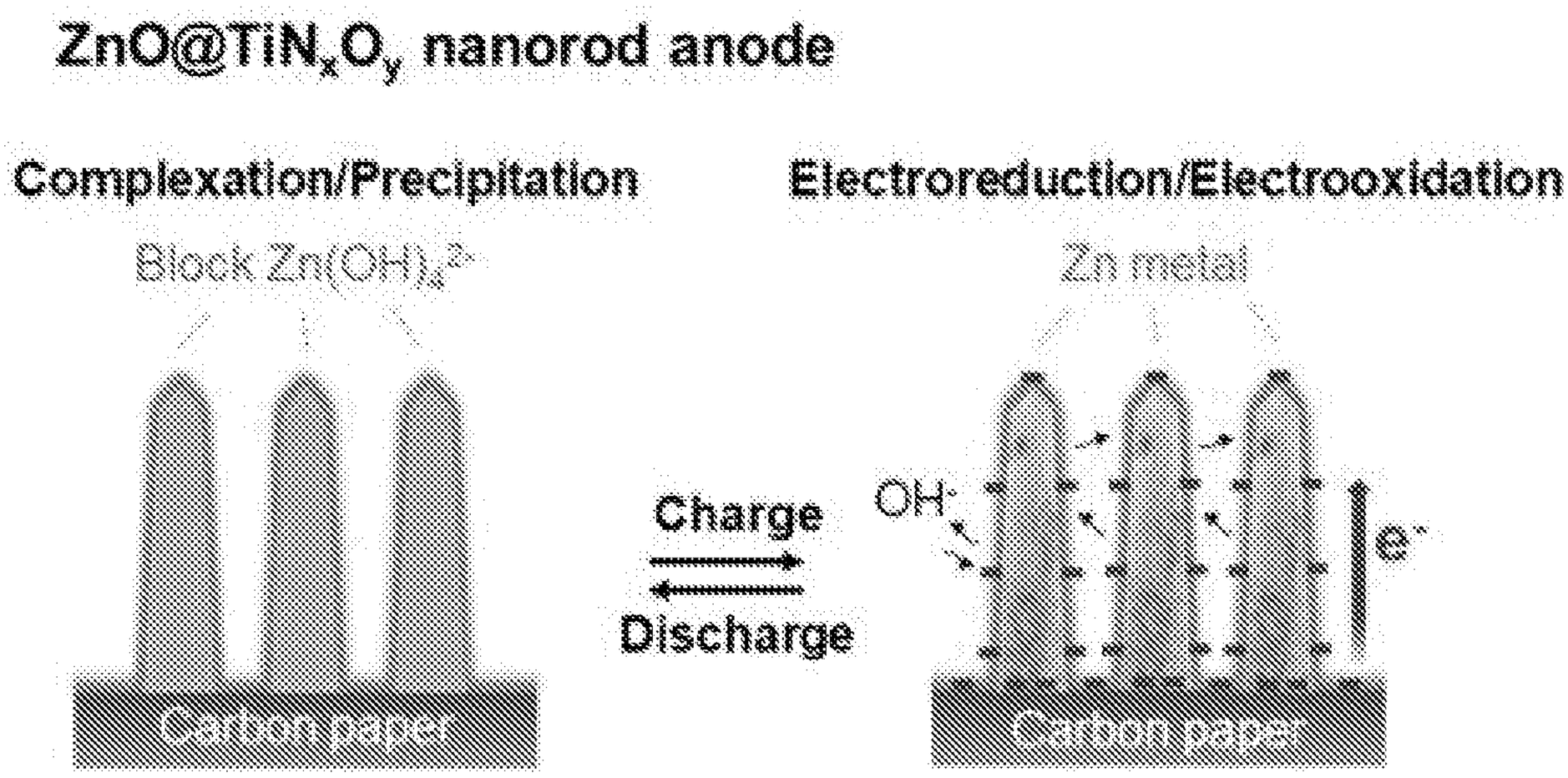

ZnO@TiN$_x$O$_y$ nanorod anode
Complexation/Precipitation
Electroreduction/Electrooxidation
Block Zn(OH)$_4^{2-}$
Zn metal
Charge
Discharge
OH$^-$
e$^-$
Carbon paper
Carbon paper

FIG. 52

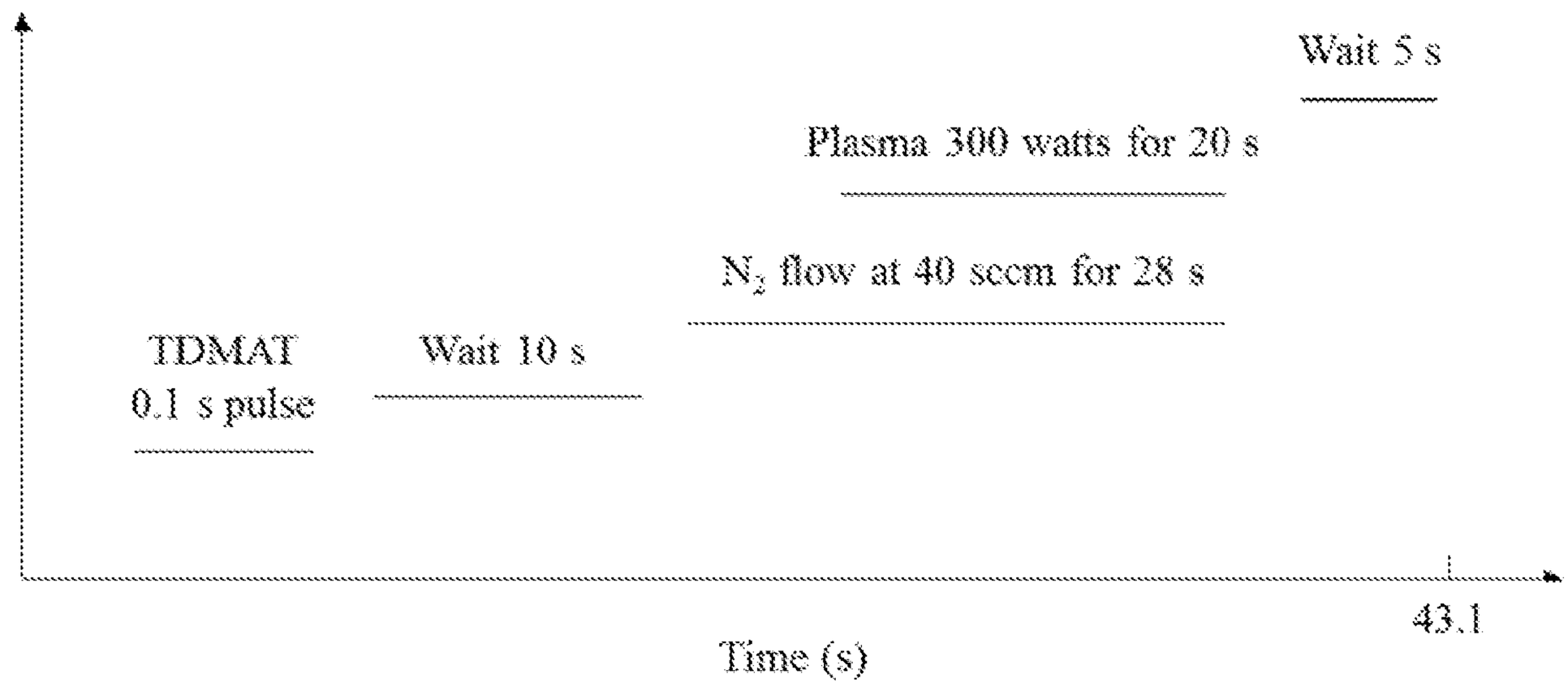

Wait 5 s
Plasma 300 watts for 20 s
N$_2$ flow at 40 sccm for 28 s
TDMAT
0.1 s pulse
Wait 10 s
43.1
Time (s)

FIG. 53

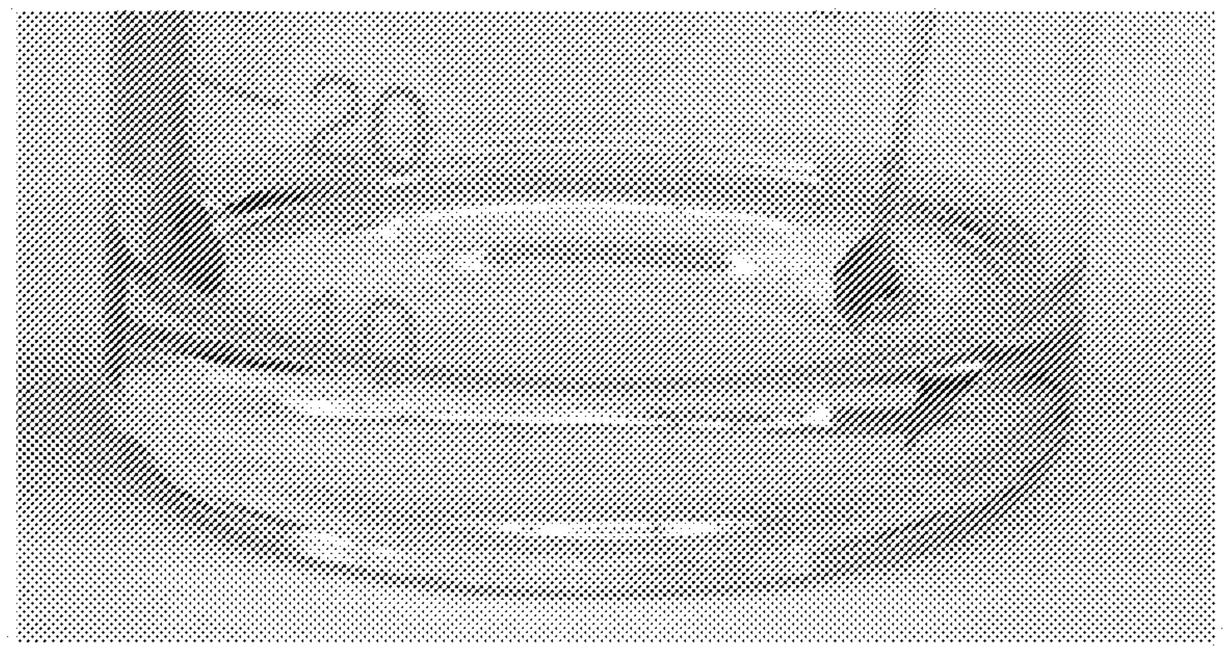


FIG. 54A



FIG. 54B

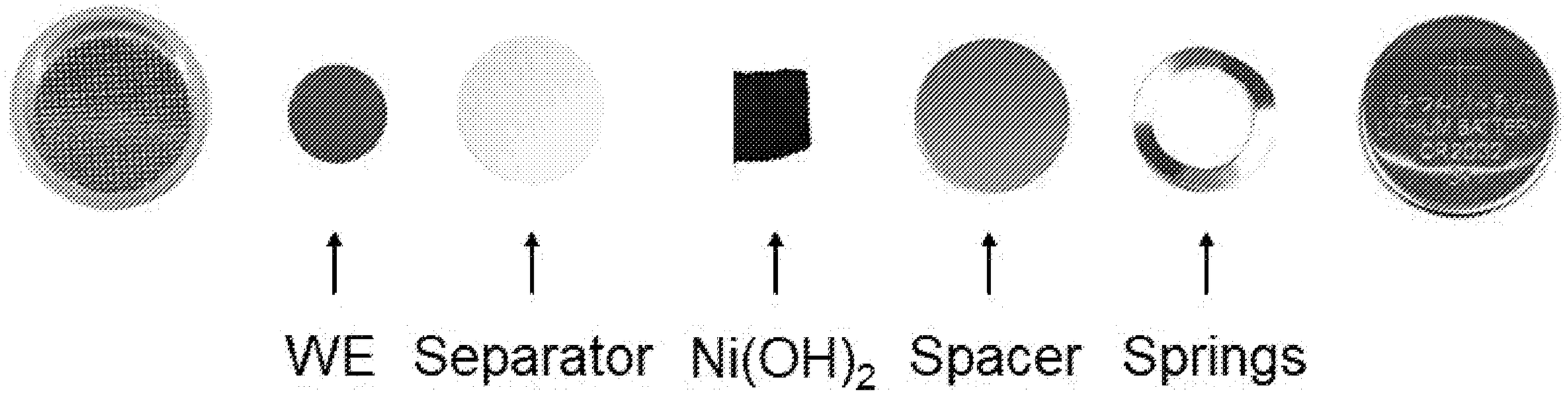


FIG. 54C

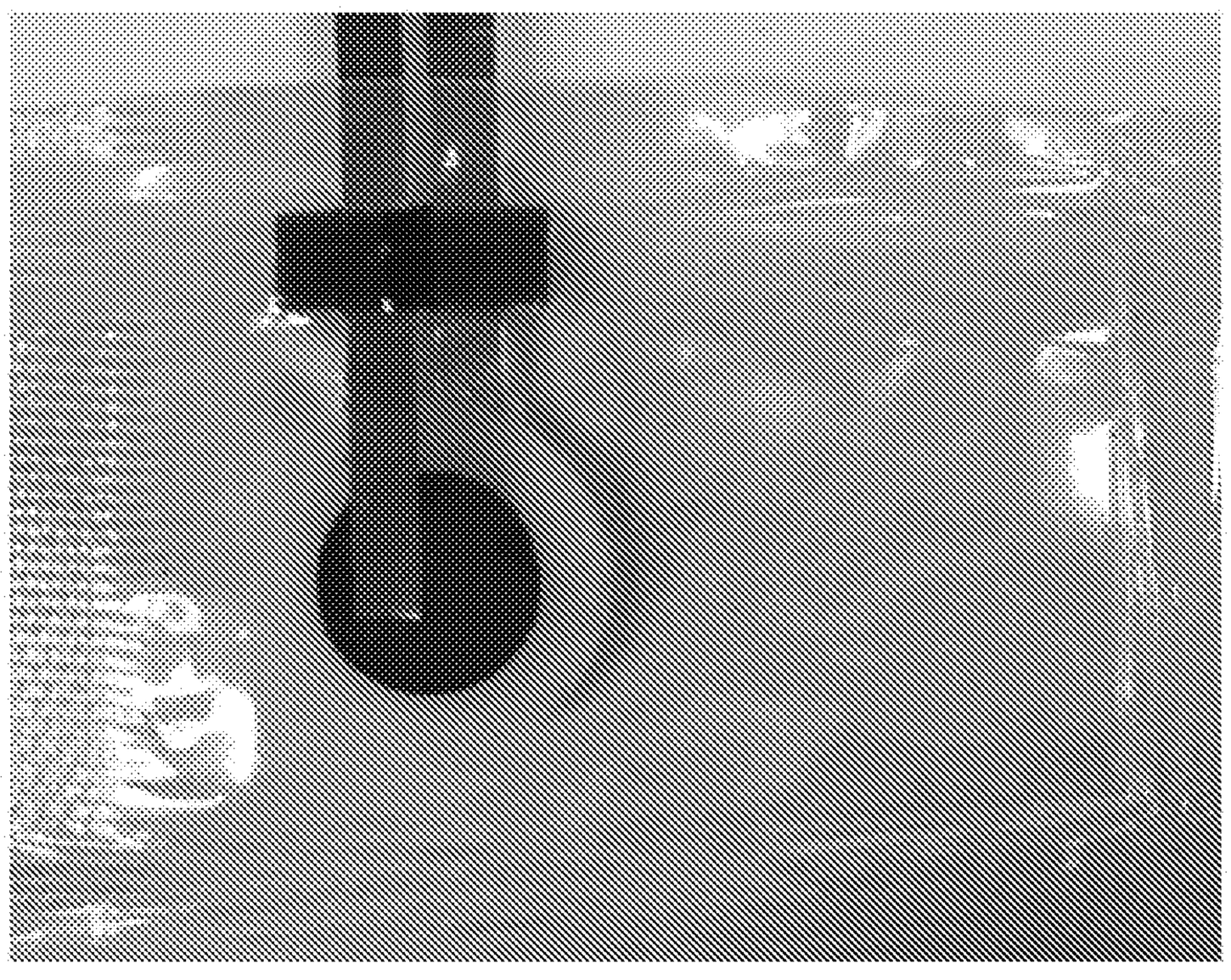


FIG. 55

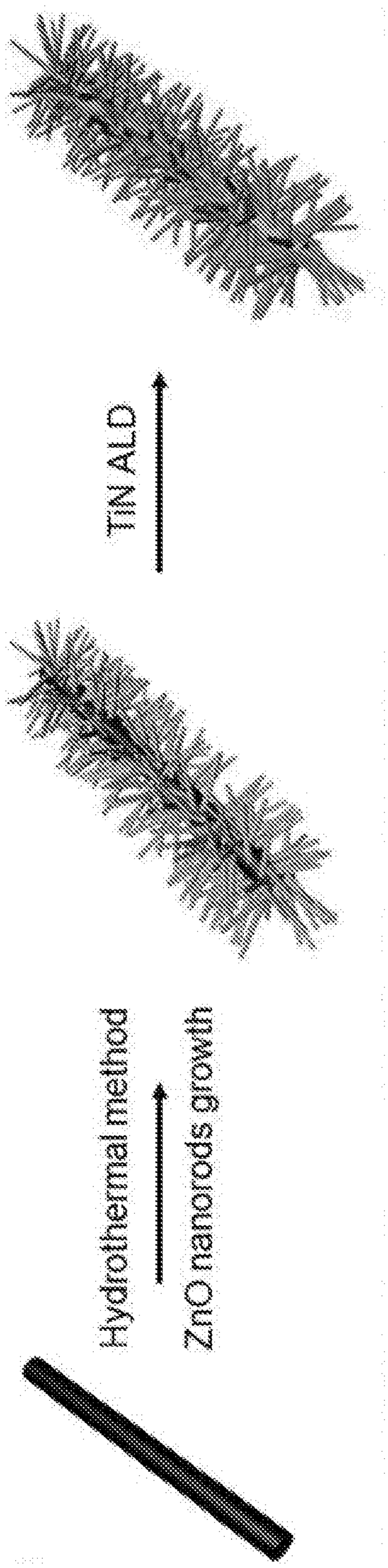


FIG. 56

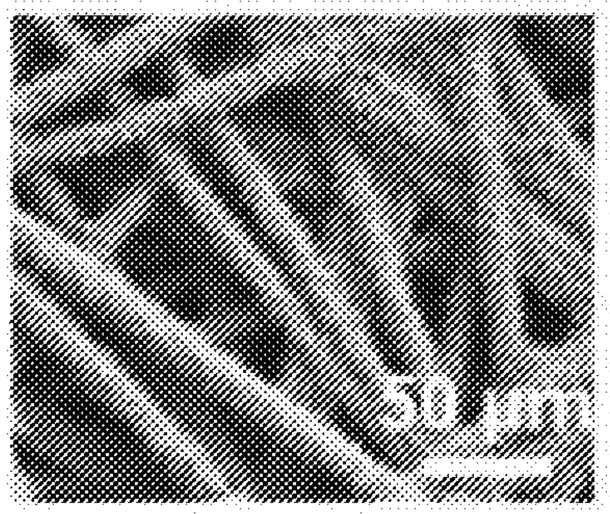


FIG. 57

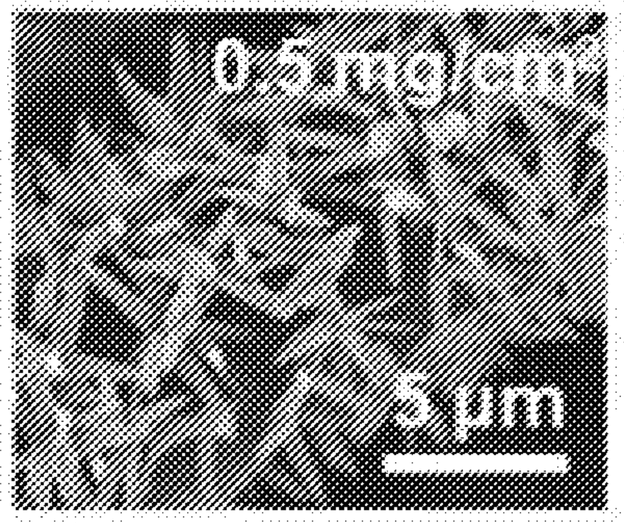


FIG. 58A

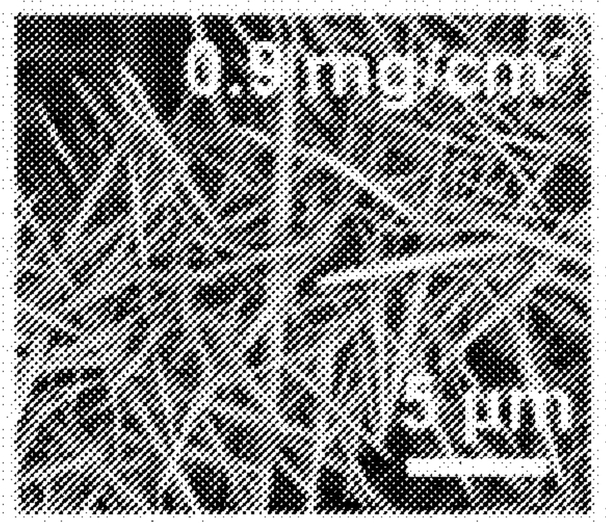


FIG. 58B

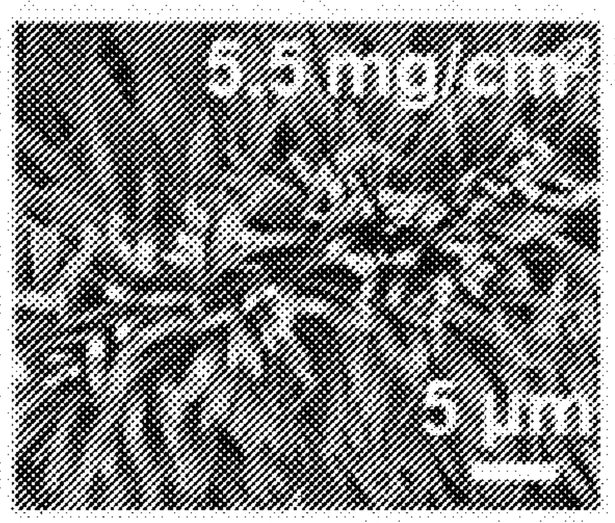


FIG. 58C

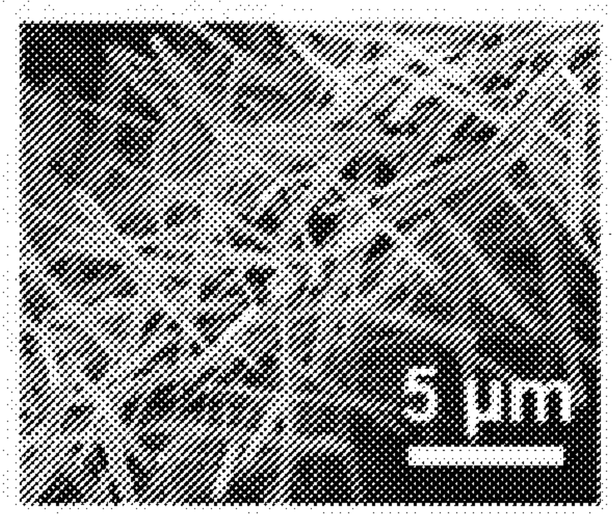


FIG. 59

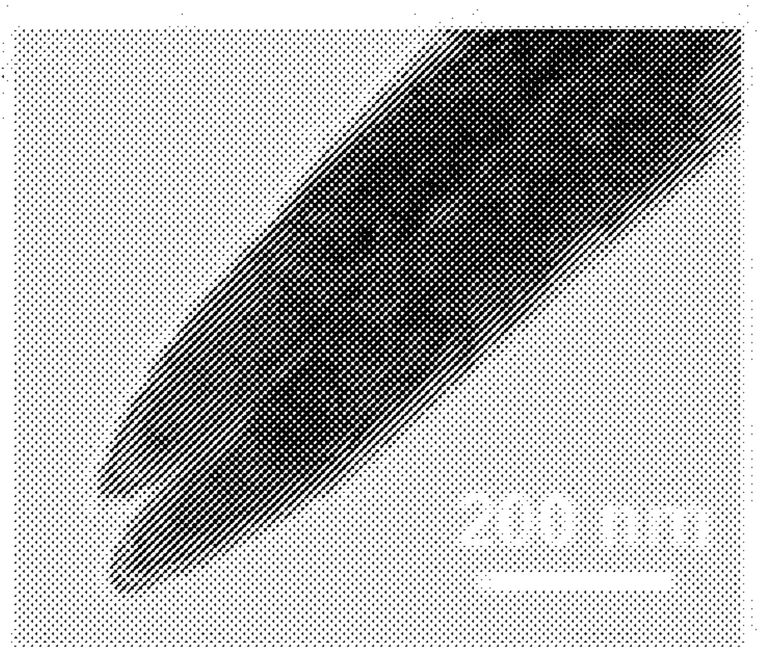


FIG. 60

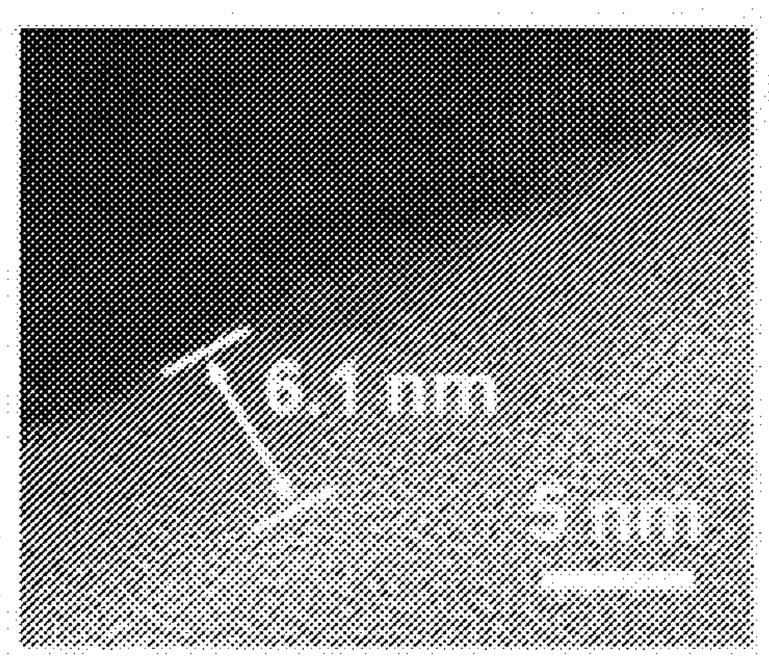


FIG. 61

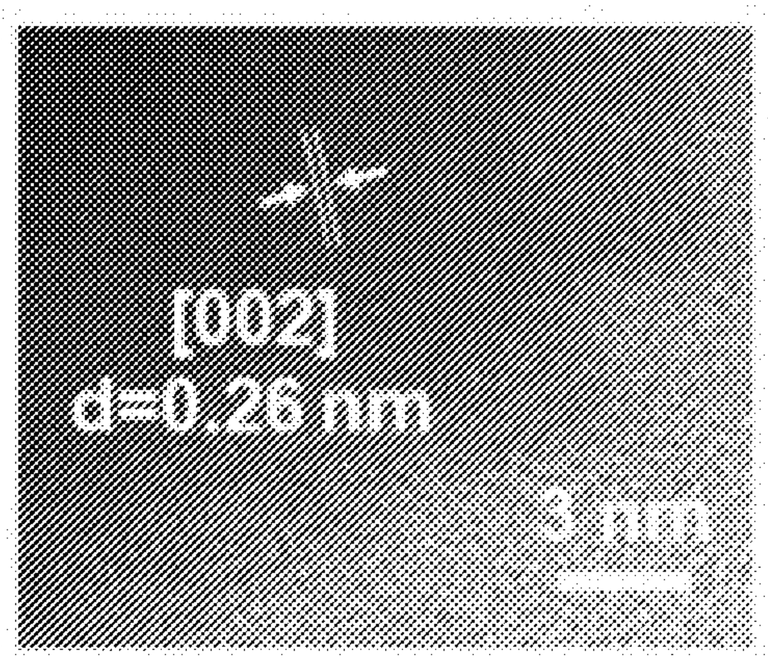


FIG. 62

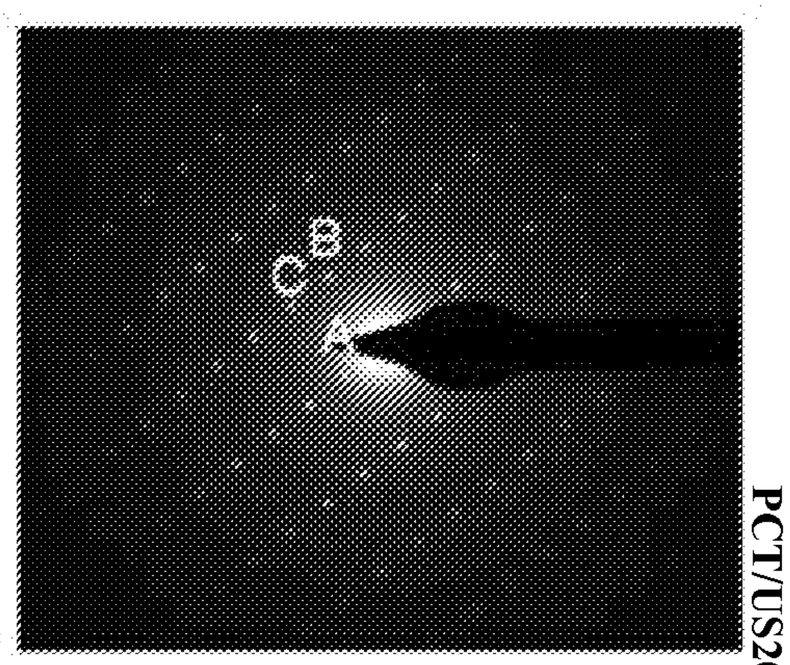


FIG. 63

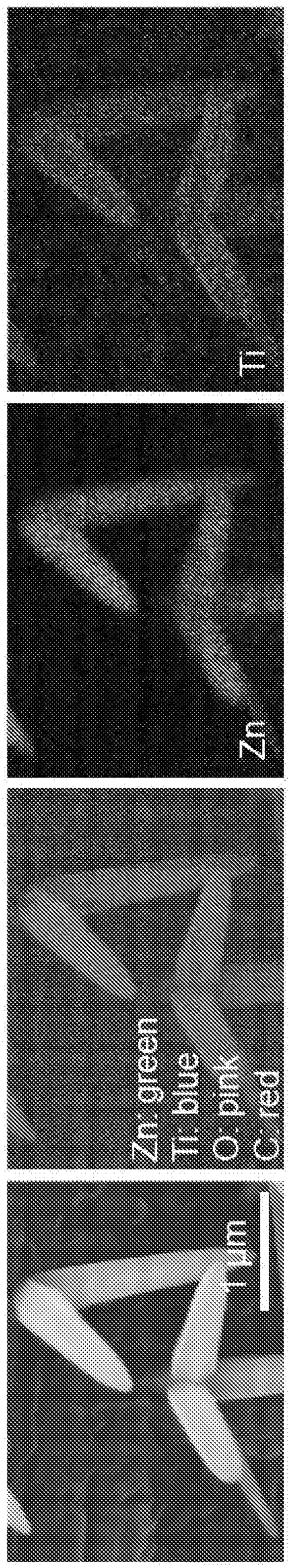


FIG. 64

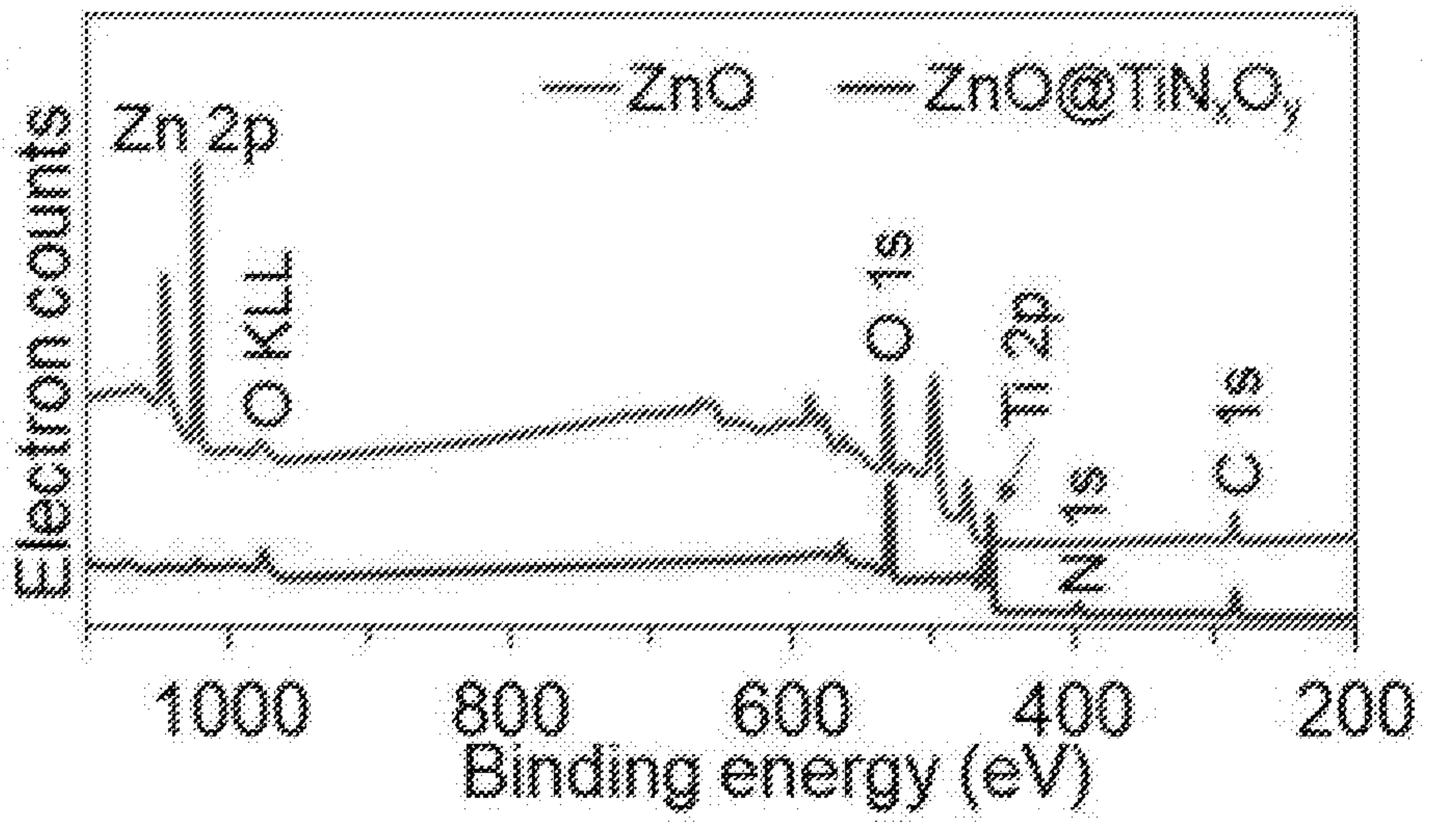


FIG. 65

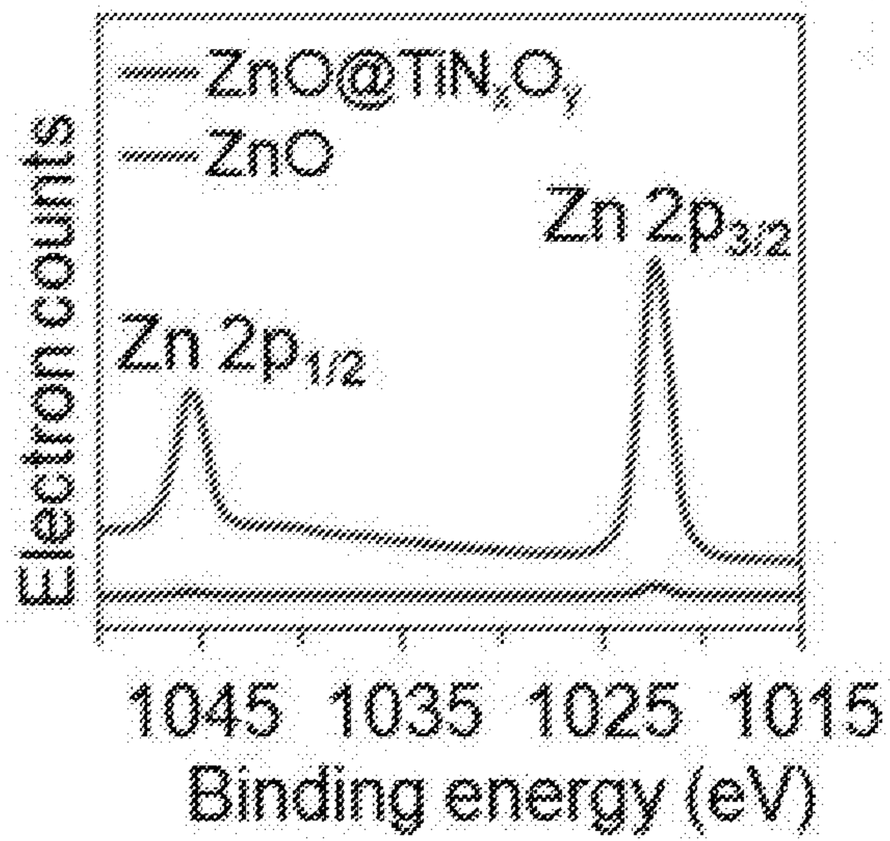


FIG. 66

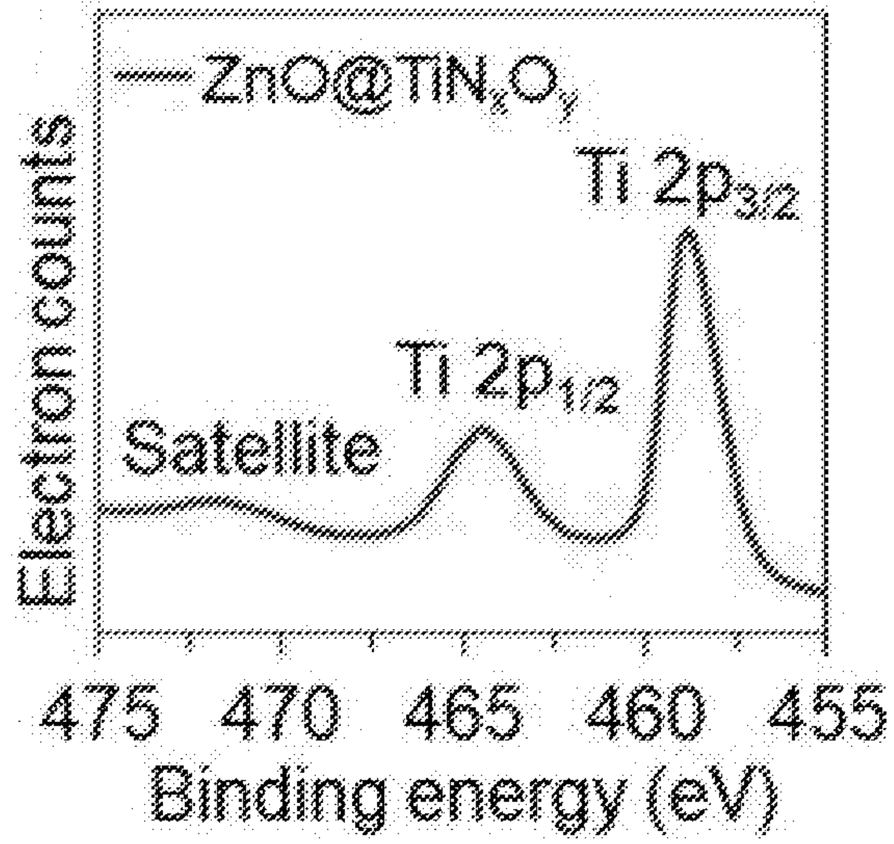


FIG. 67

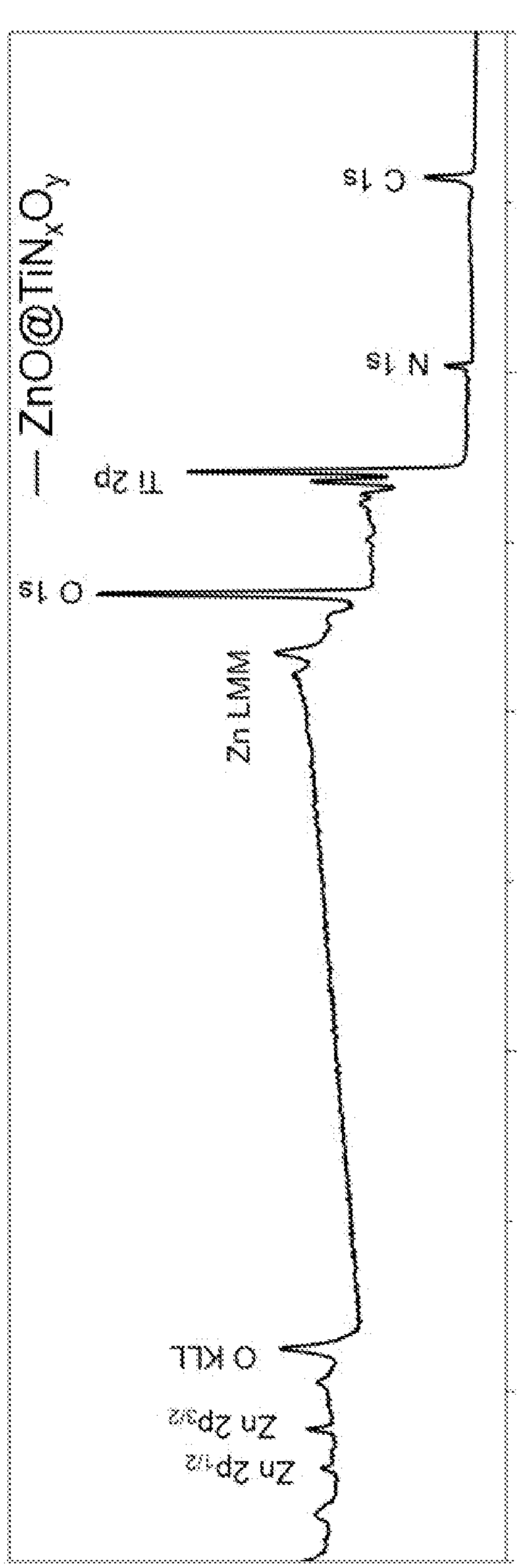

— ZnO@TiNxOy
O 1s
Ti 2p
C 1s
N 1s
Zn LMM
O KLL
Zn 2p1/2
Zn 2p3/2
Electron counts
Binding energy (eV)

FIG. 68

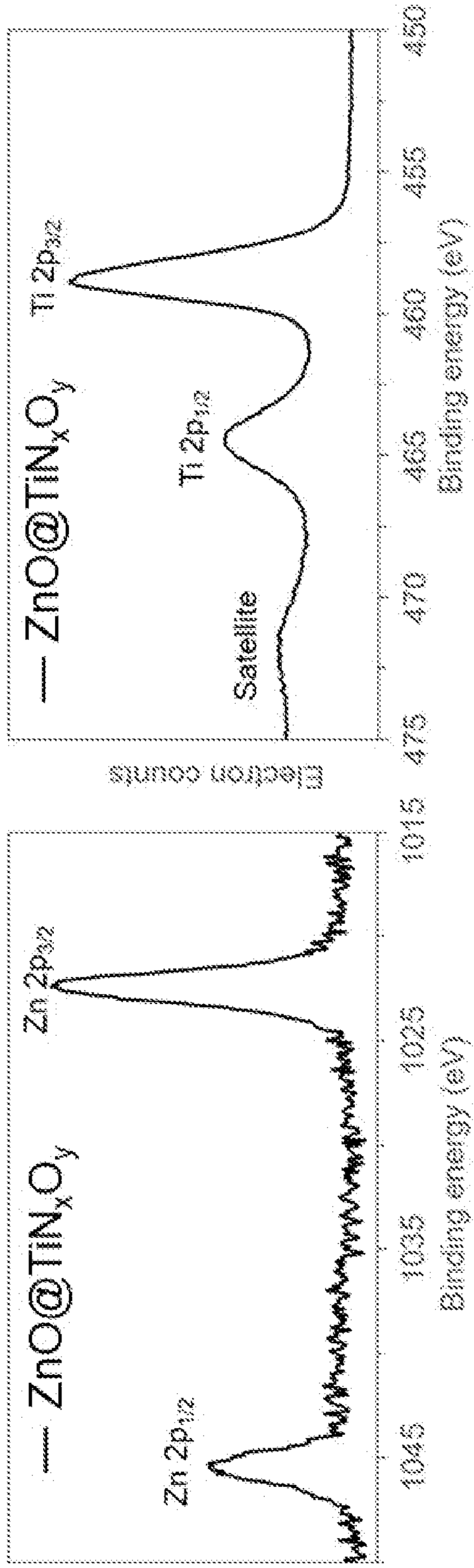

— ZnO@TiNxOy
Ti 2p3/2
Ti 2p1/2
Satellite
Zn 2p3/2
Zn 2p1/2
Electron counts
Binding energy (eV)

FIG. 69

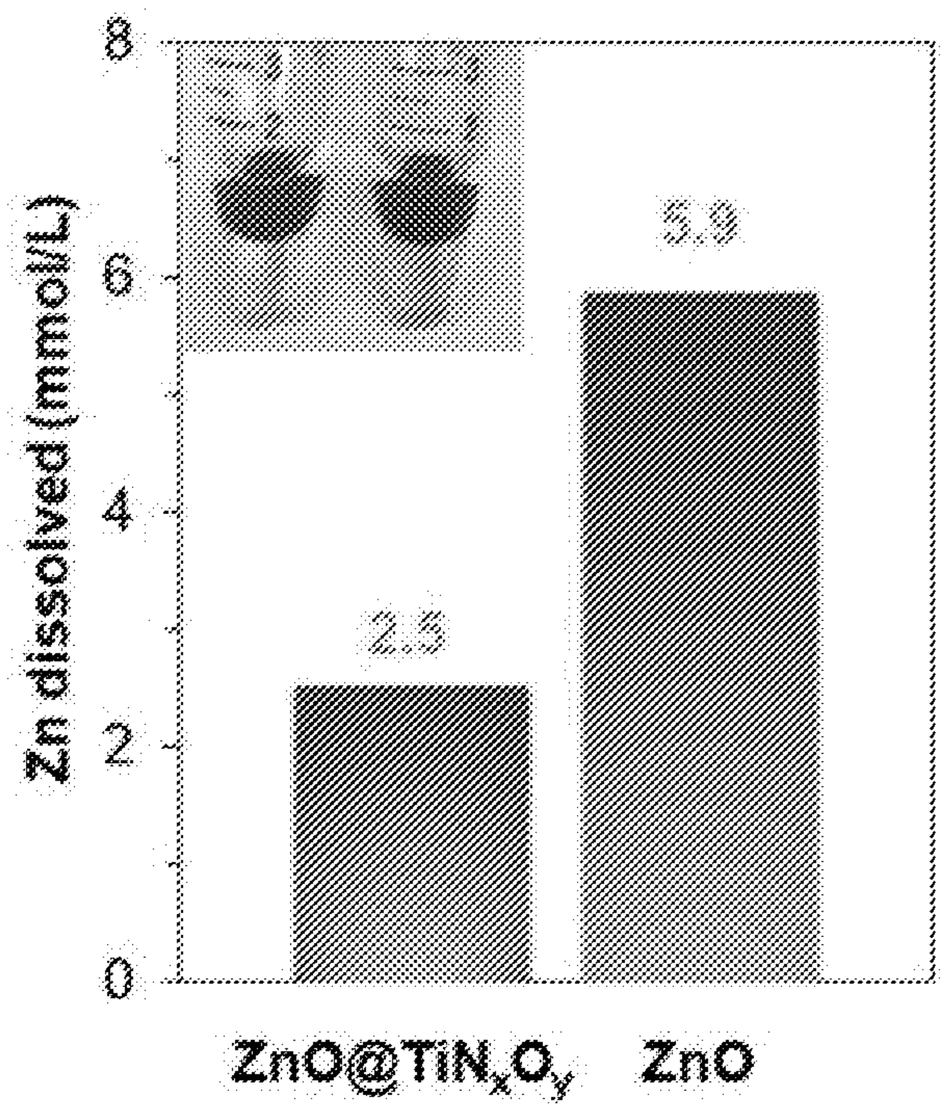


FIG. 70

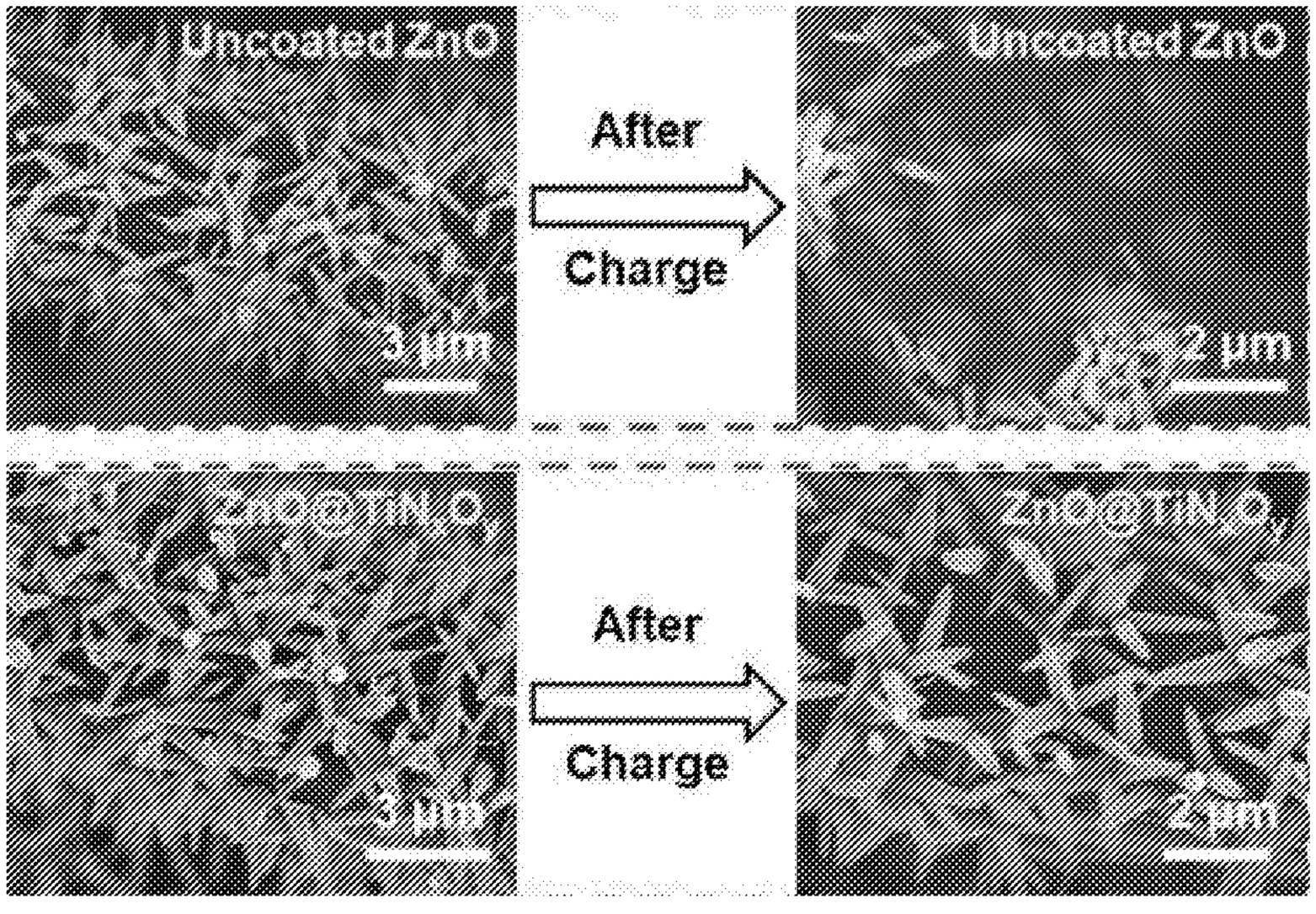


FIG. 71

FIG. 72

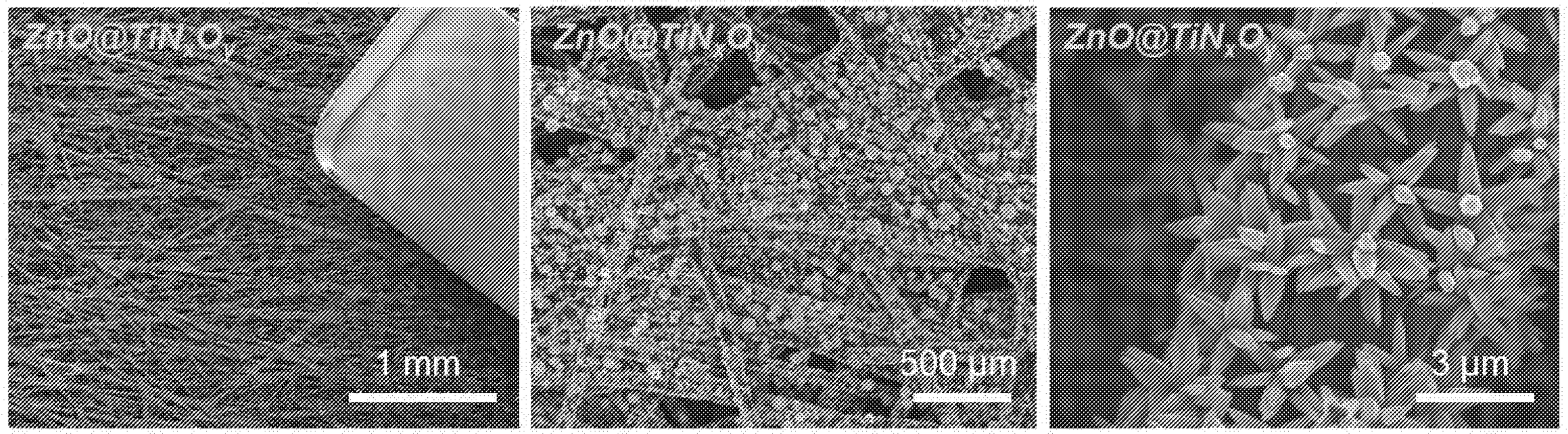


FIG. 73

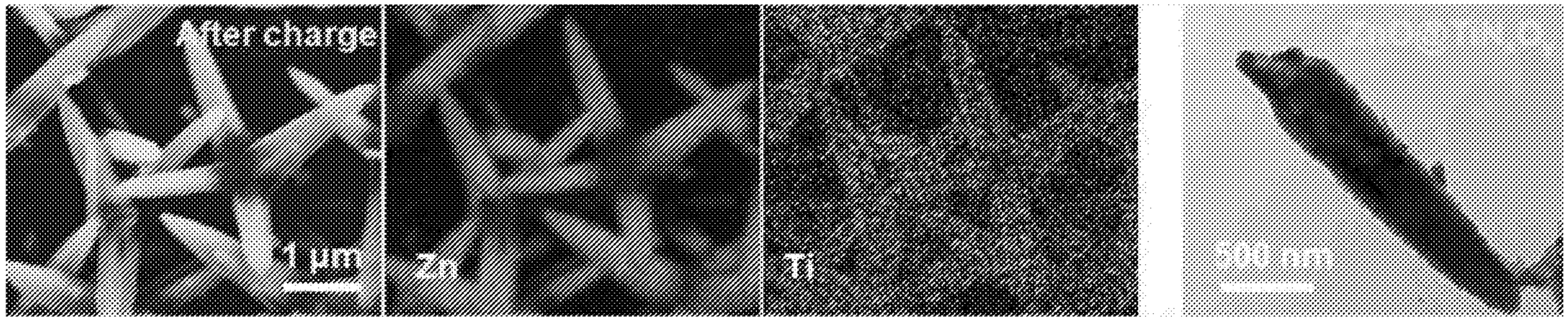


FIG. 74

FIG. 75

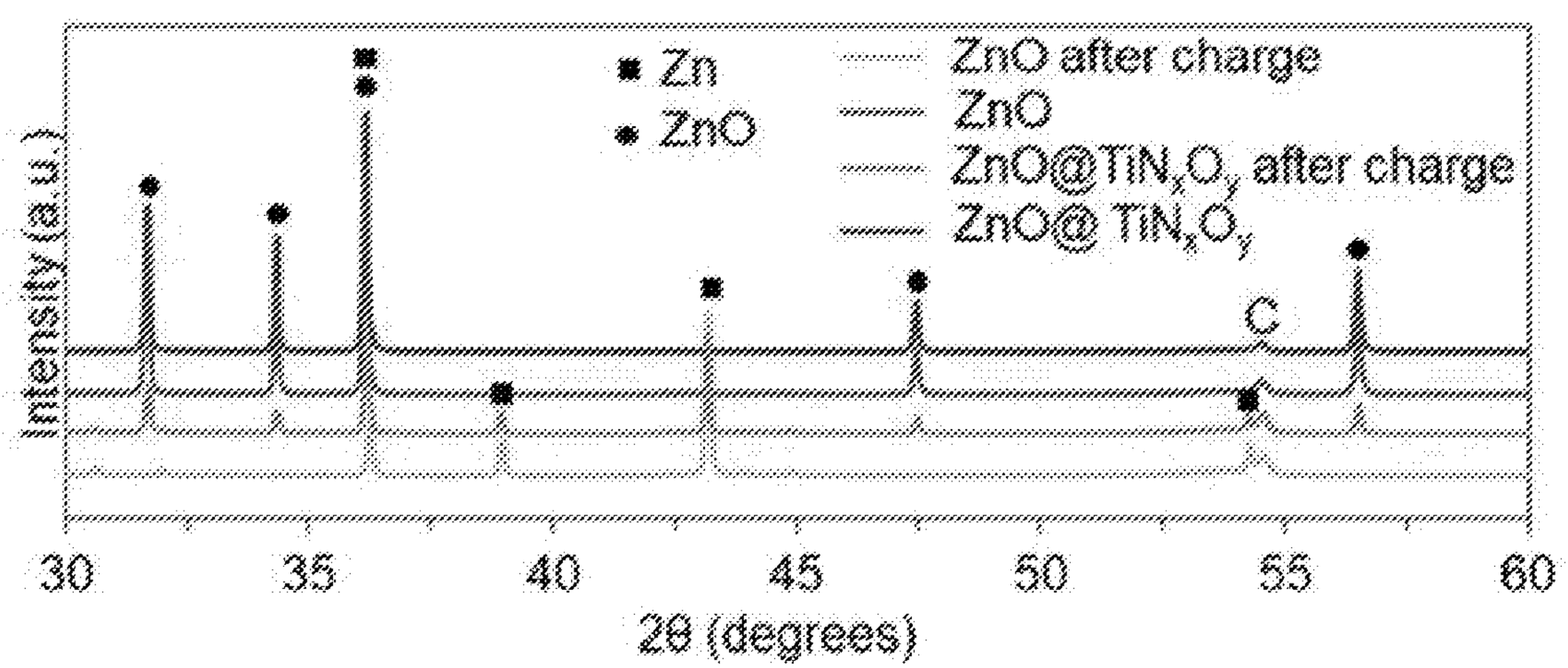


FIG. 76

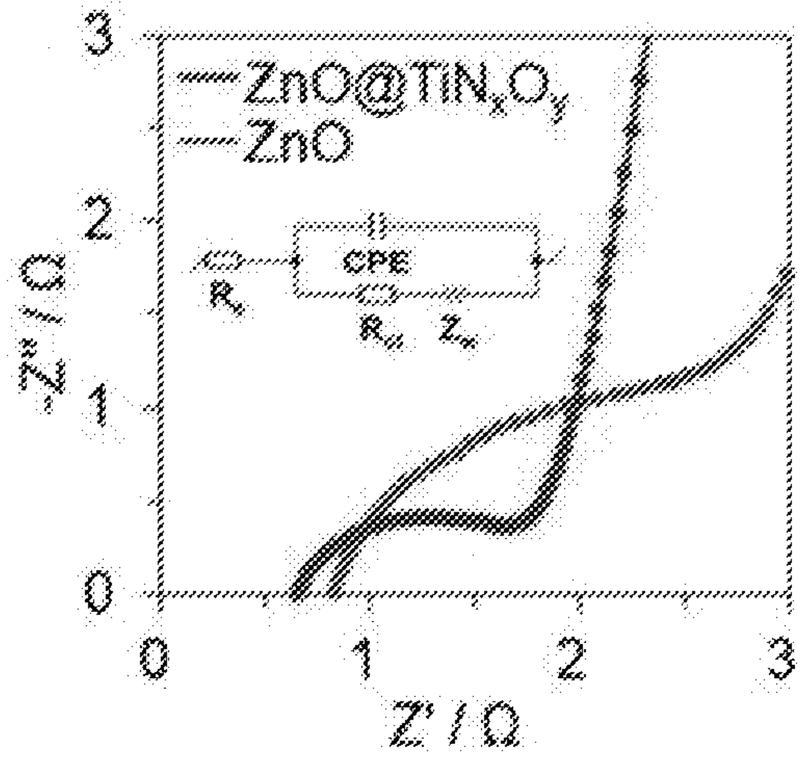


FIG. 77

FIG. 78

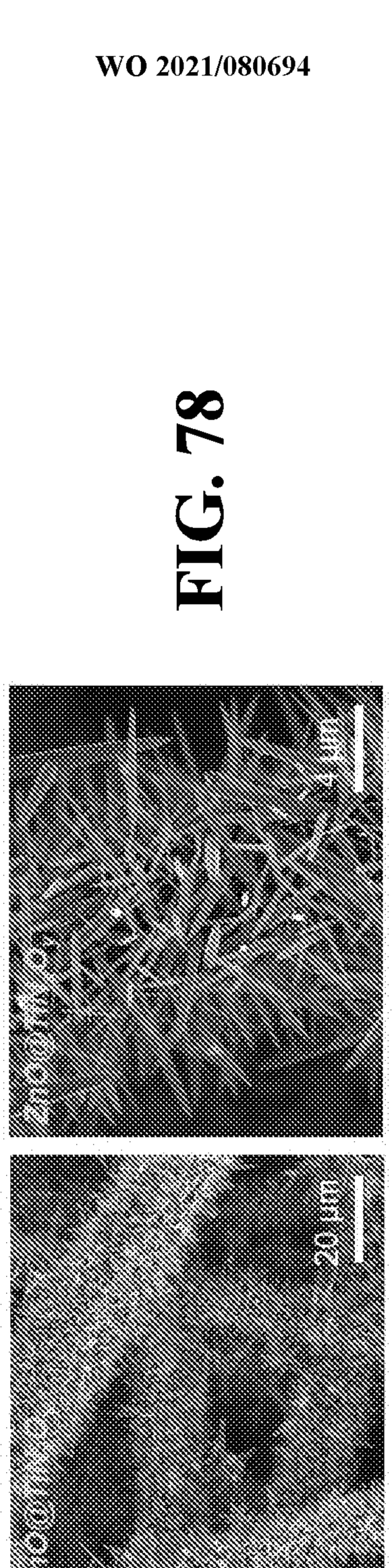


FIG. 79

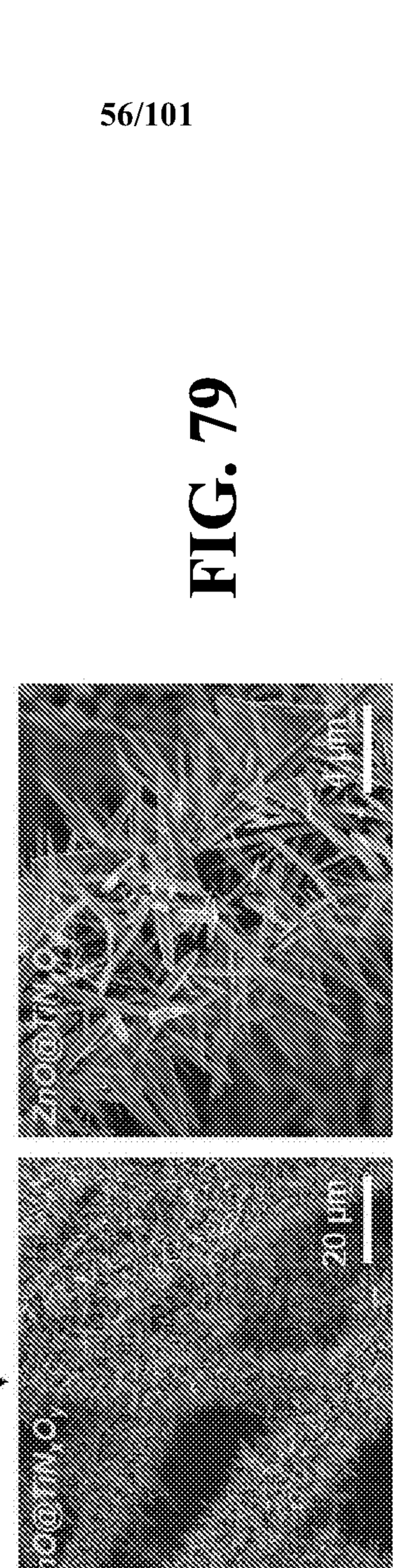
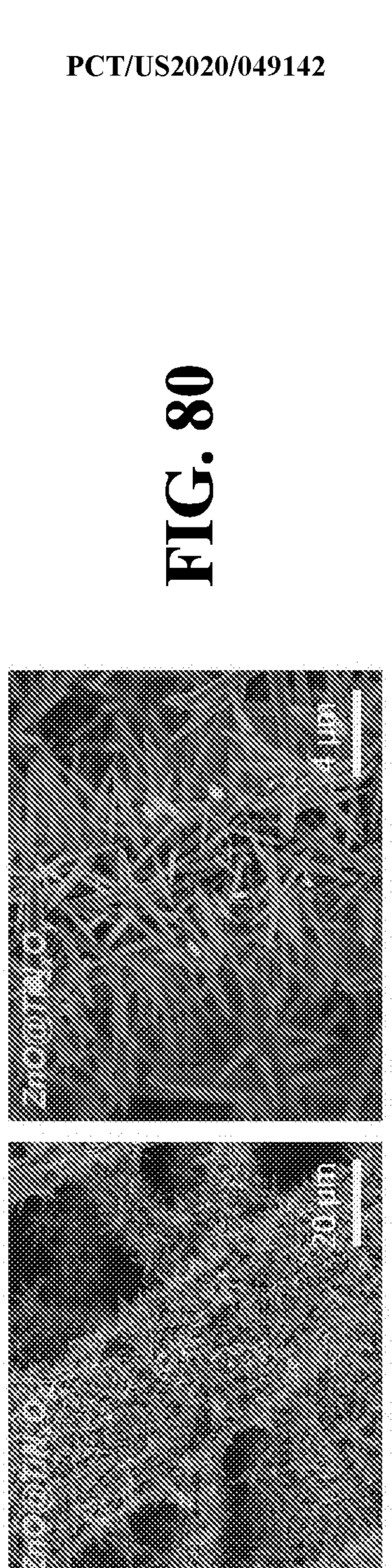
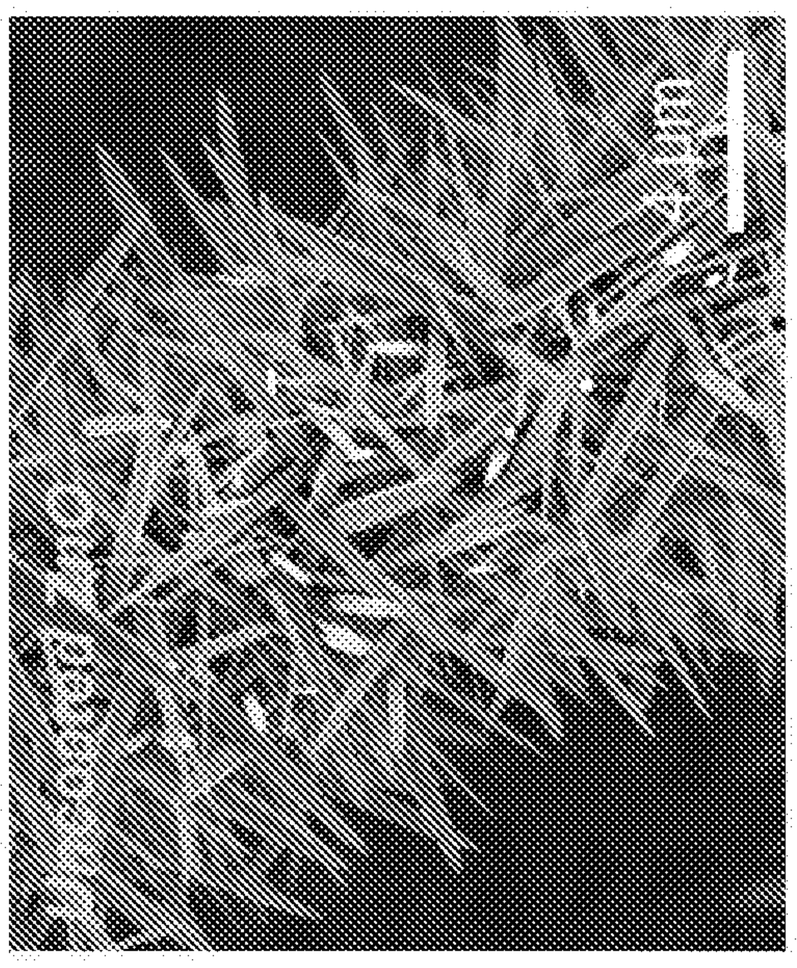
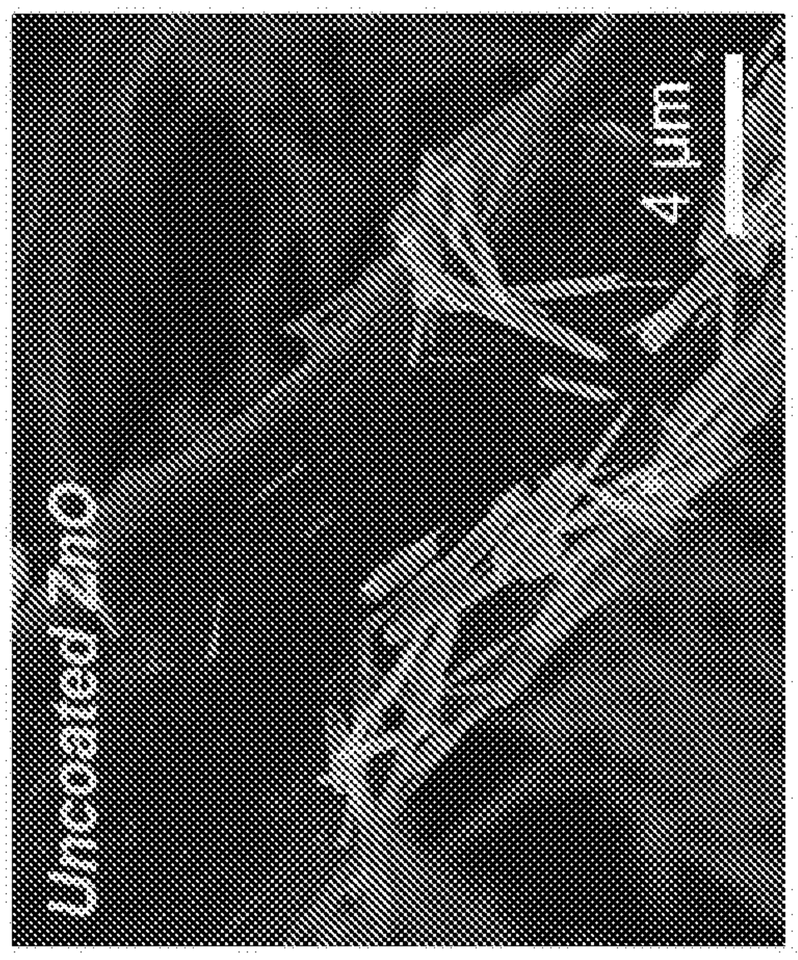
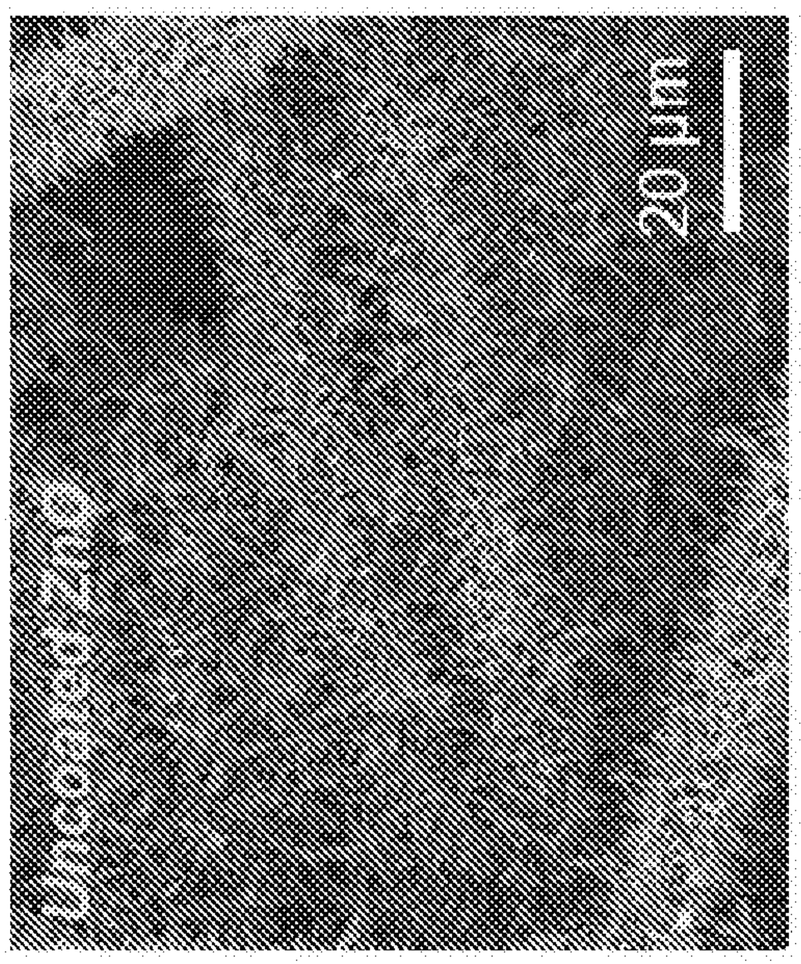


FIG. 80









Charge

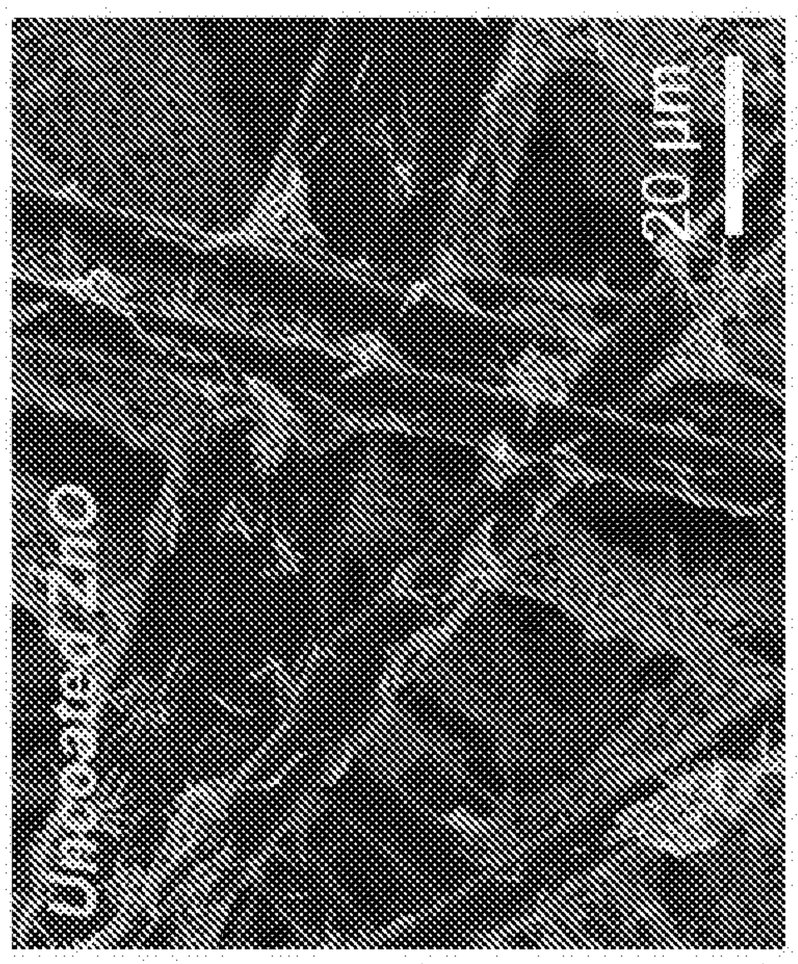
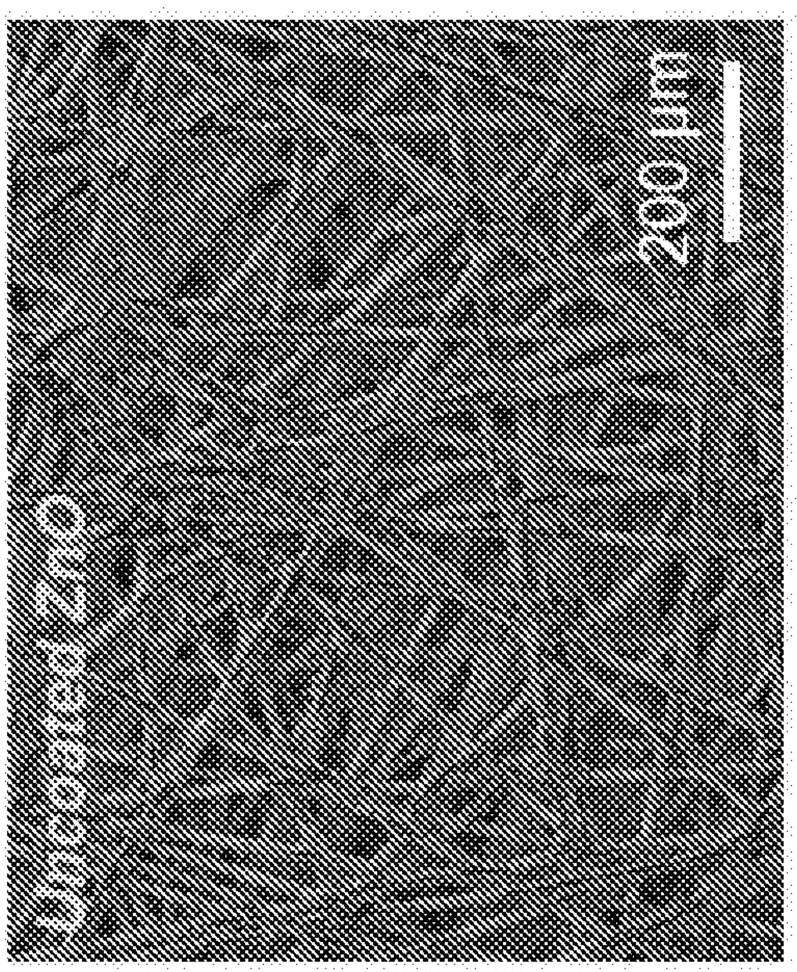


FIG. 81



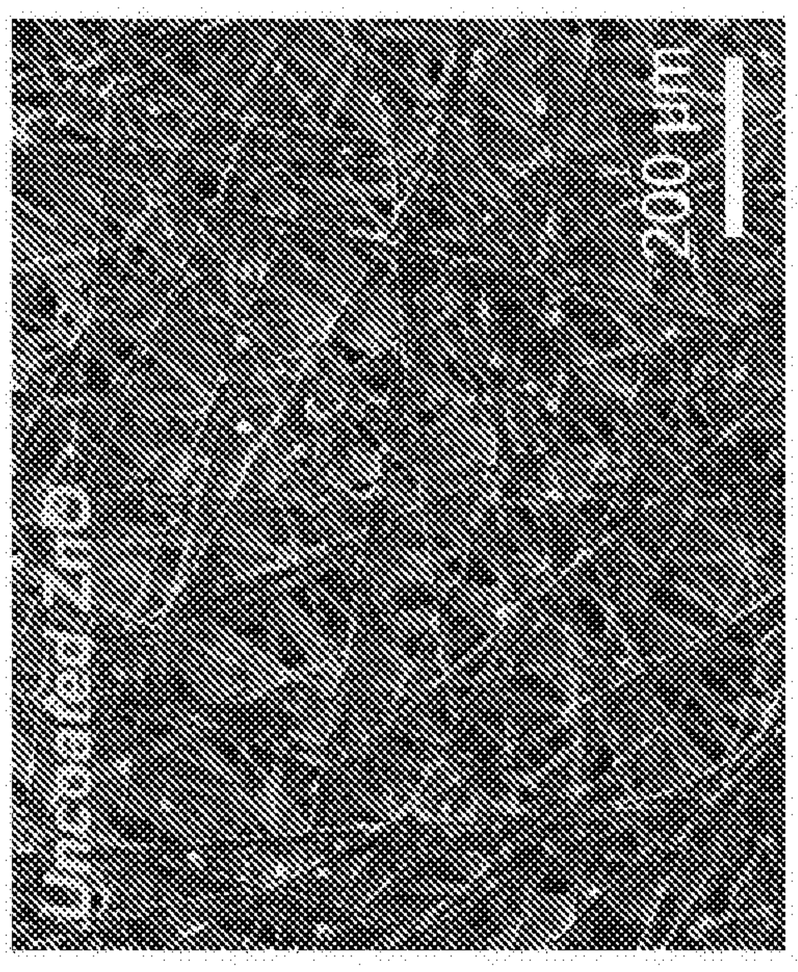


FIG. 82

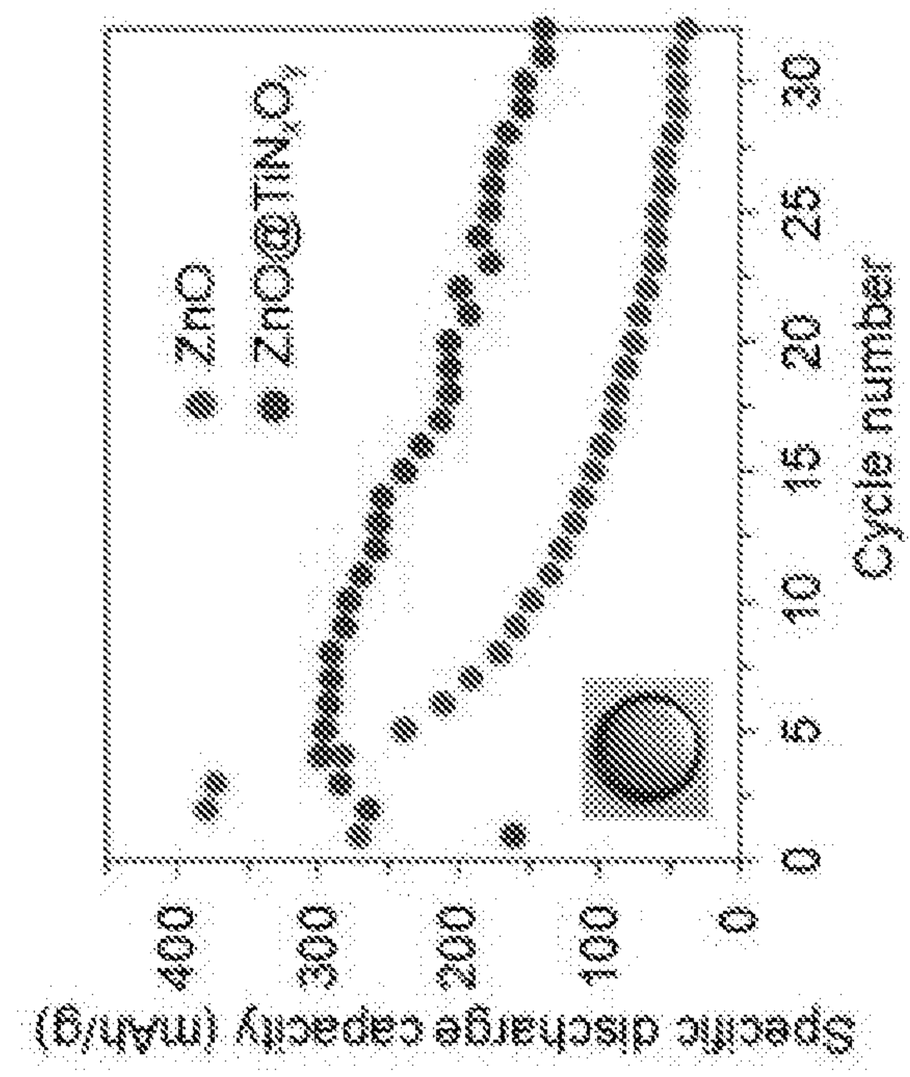


FIG. 85

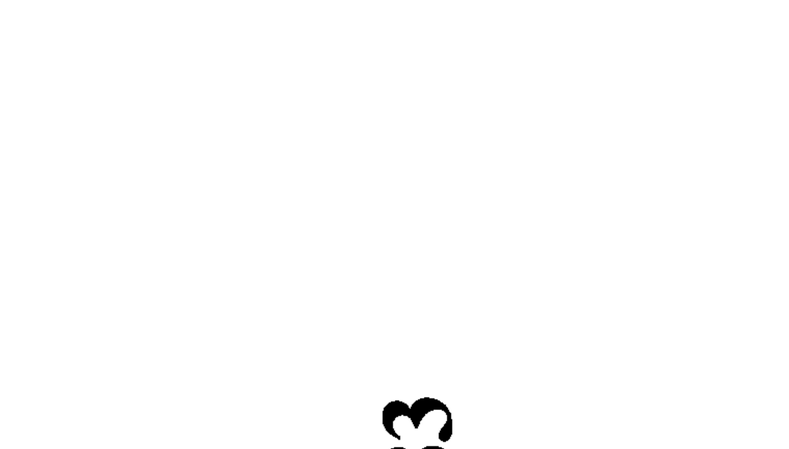


FIG. 83

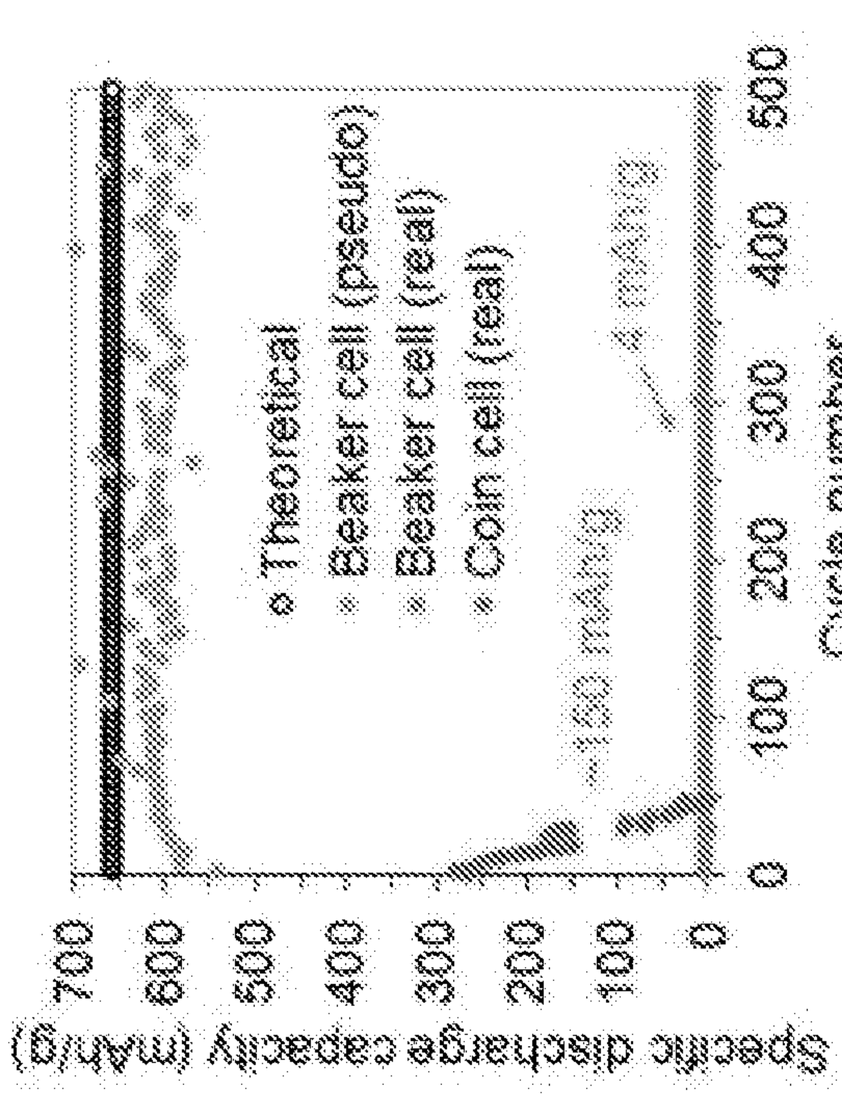
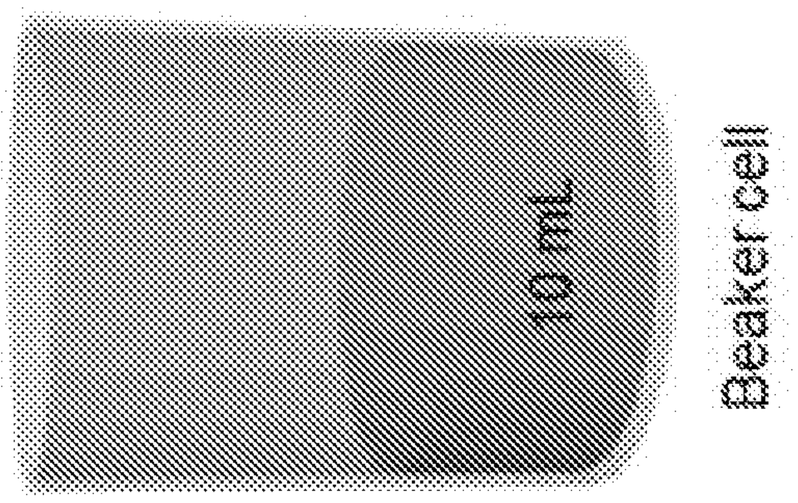


FIG. 84



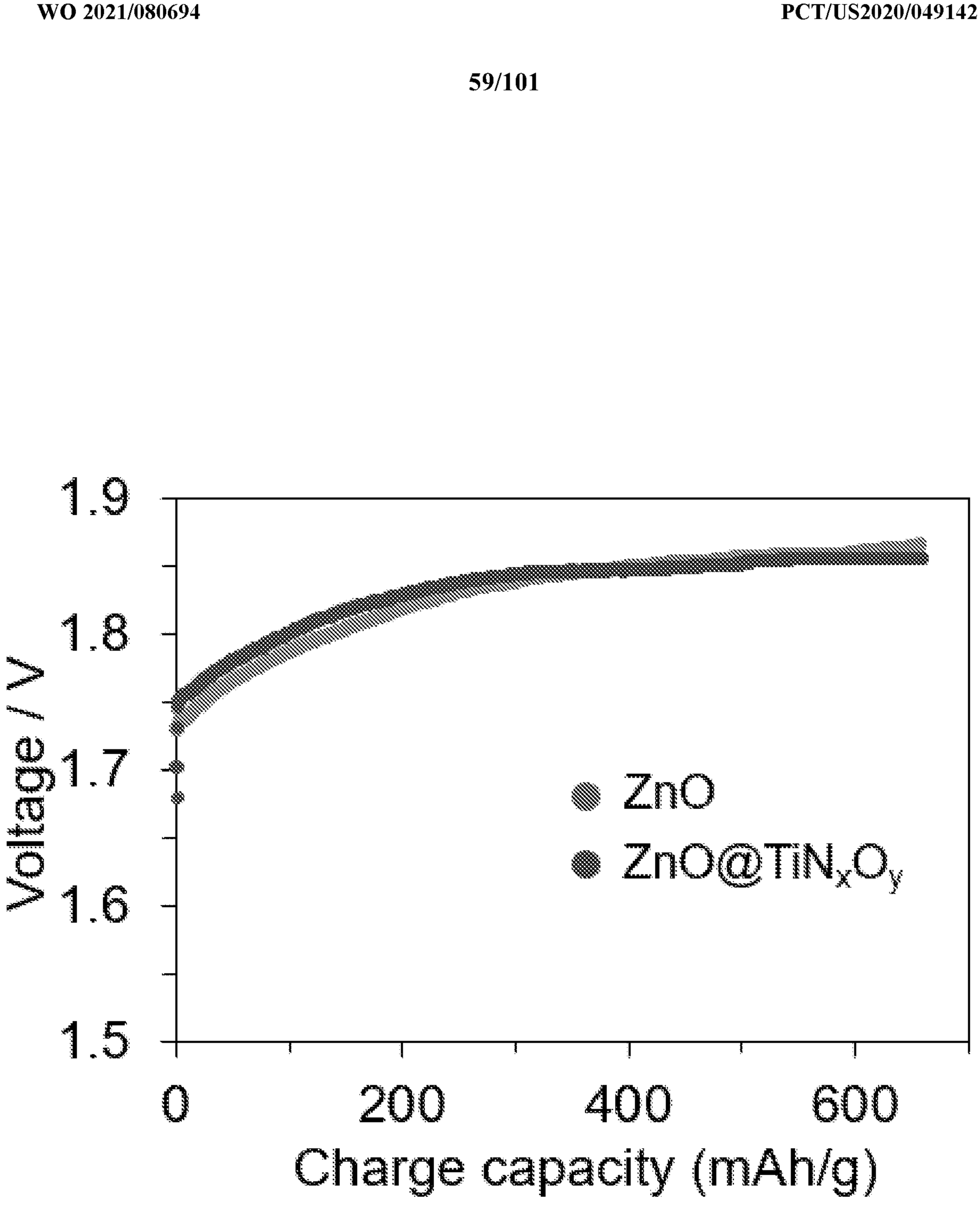

1.9
1.8
1.7
1.6
1.5
Voltage / V
0
200
400
600
Charge capacity (mAh/g)
ZnO
ZnO@TiNxOy

FIG. 86

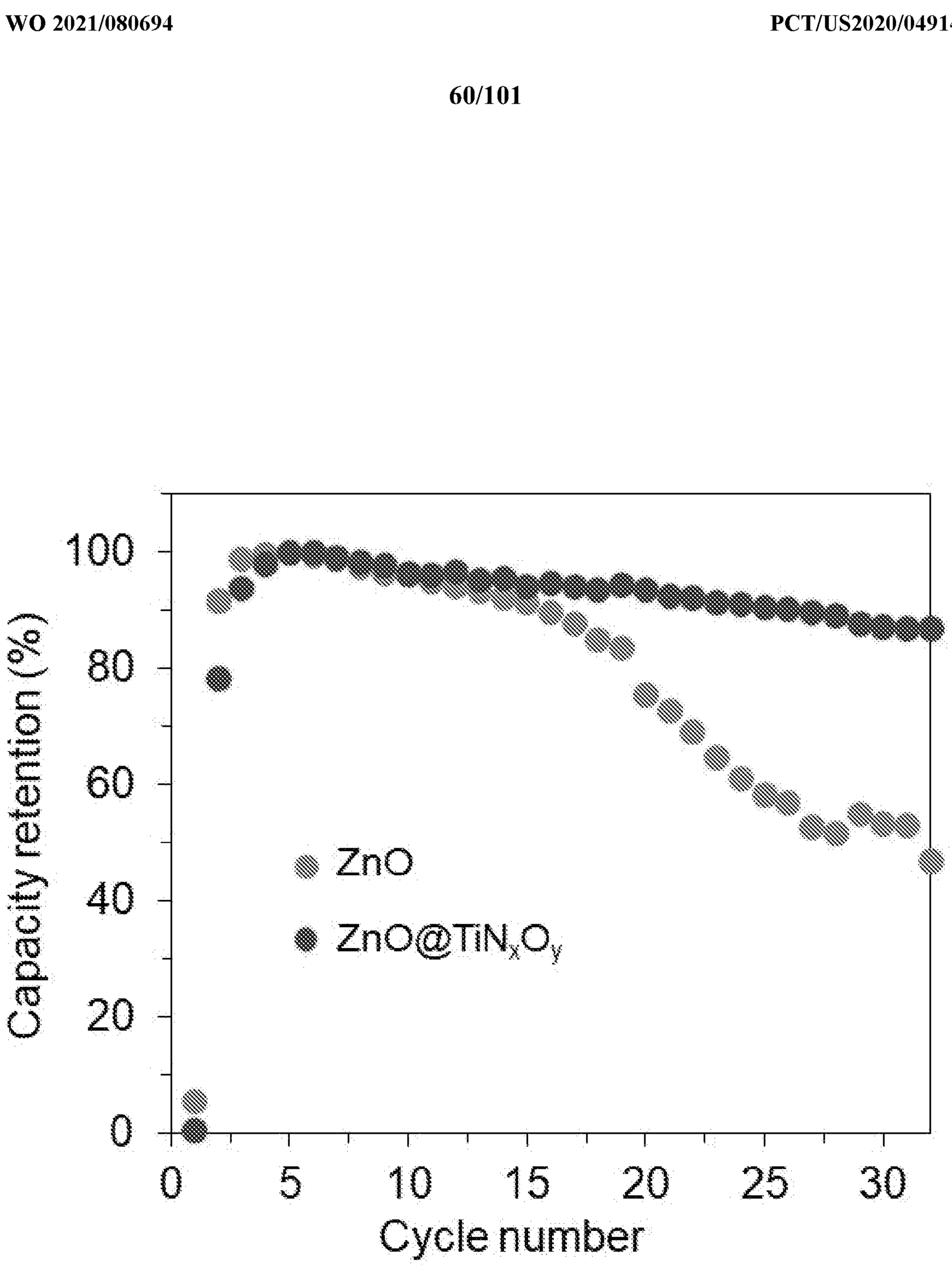

Capacity retention (%)
100
80
60
40
20
0
ZnO
ZnO@TiN$_x$O$_y$
0
5
10
15
20
25
30
Cycle number

FIG. 87

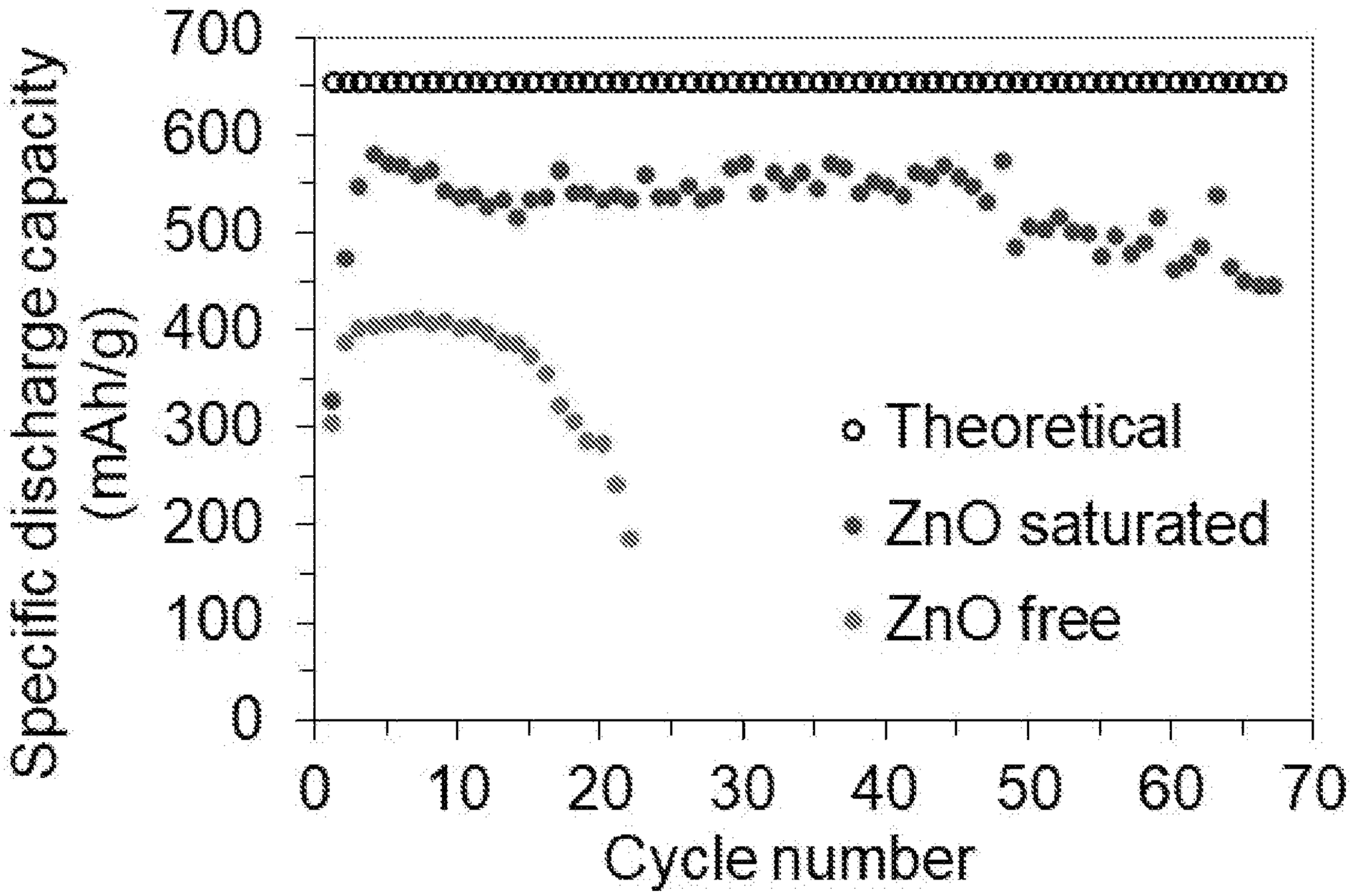

Specific discharge capacity (mAh/g)
700
600
500
400
300
200
100
0
0
10
20
30
40
50
60
70
Cycle number
Theoretical
ZnO saturated
ZnO free

FIG. 88

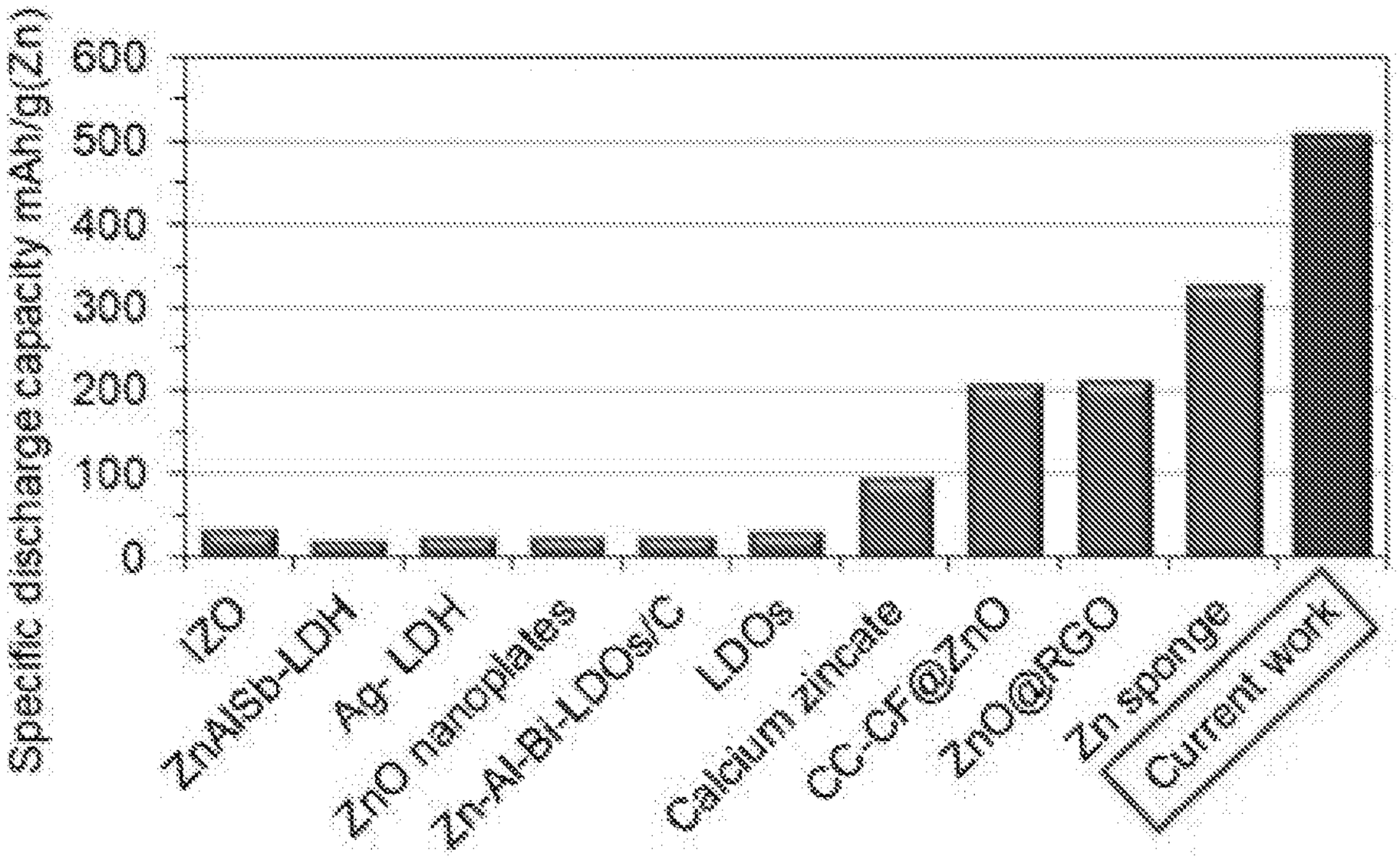

Specific discharge capacity mAh/g(Zn)
600
500
400
300
200
100
0
IZO
ZnAlSb-LDH
Ag- LDH
ZnO nanoplates
Zn-Al-Bi-LDOs/C
LDOs
Calcium zincate
CC-CF@ZnO
ZnO@RGO
Zn sponge
Current work

FIG. 89

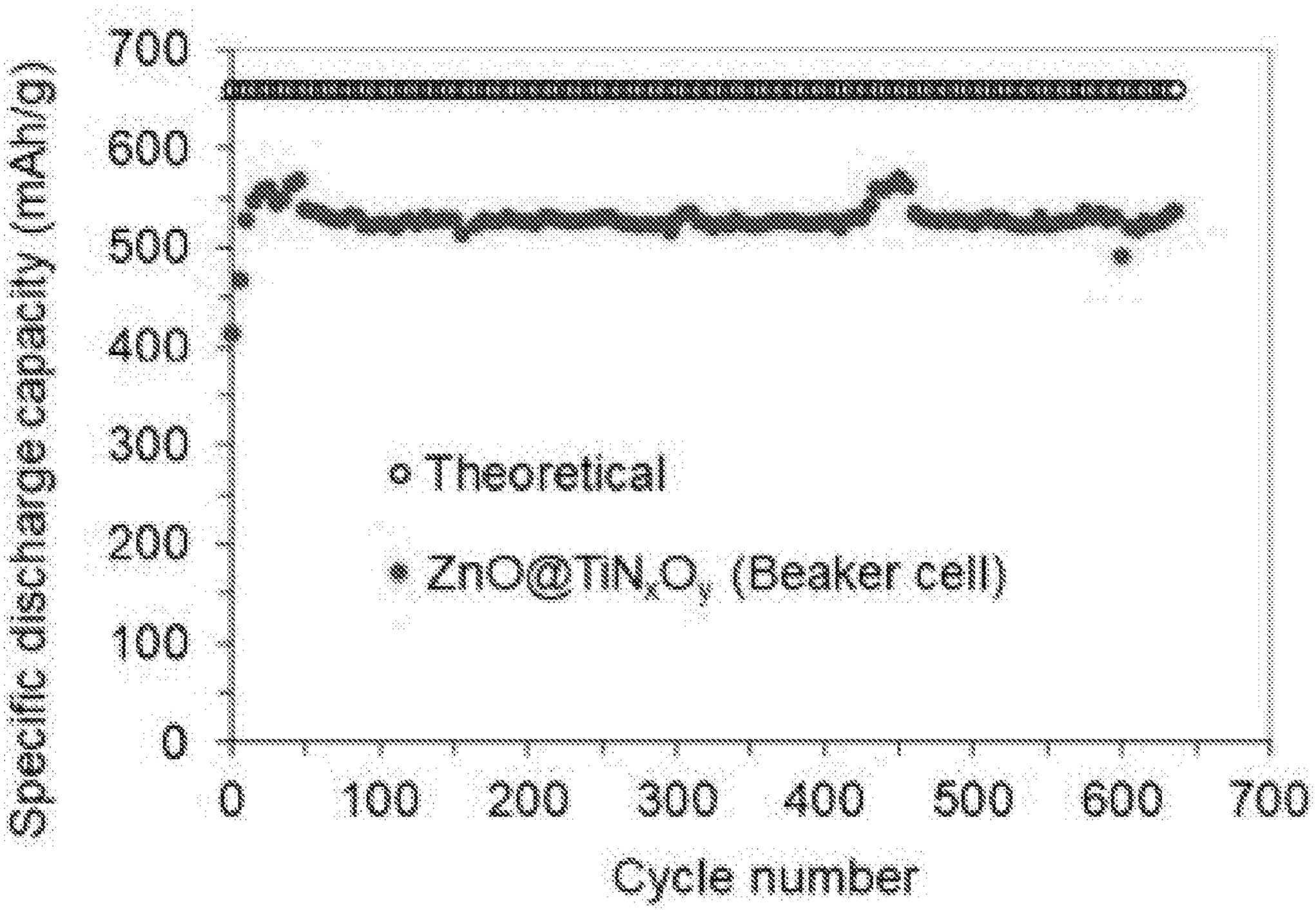

Specific discharge capacity (mAh/g)
700
600
500
400
300
200
100
0
0
100
200
300
400
500
600
700
Cycle number
Theoretical
ZnO@TiNxOy (Beaker cell)

FIG. 90

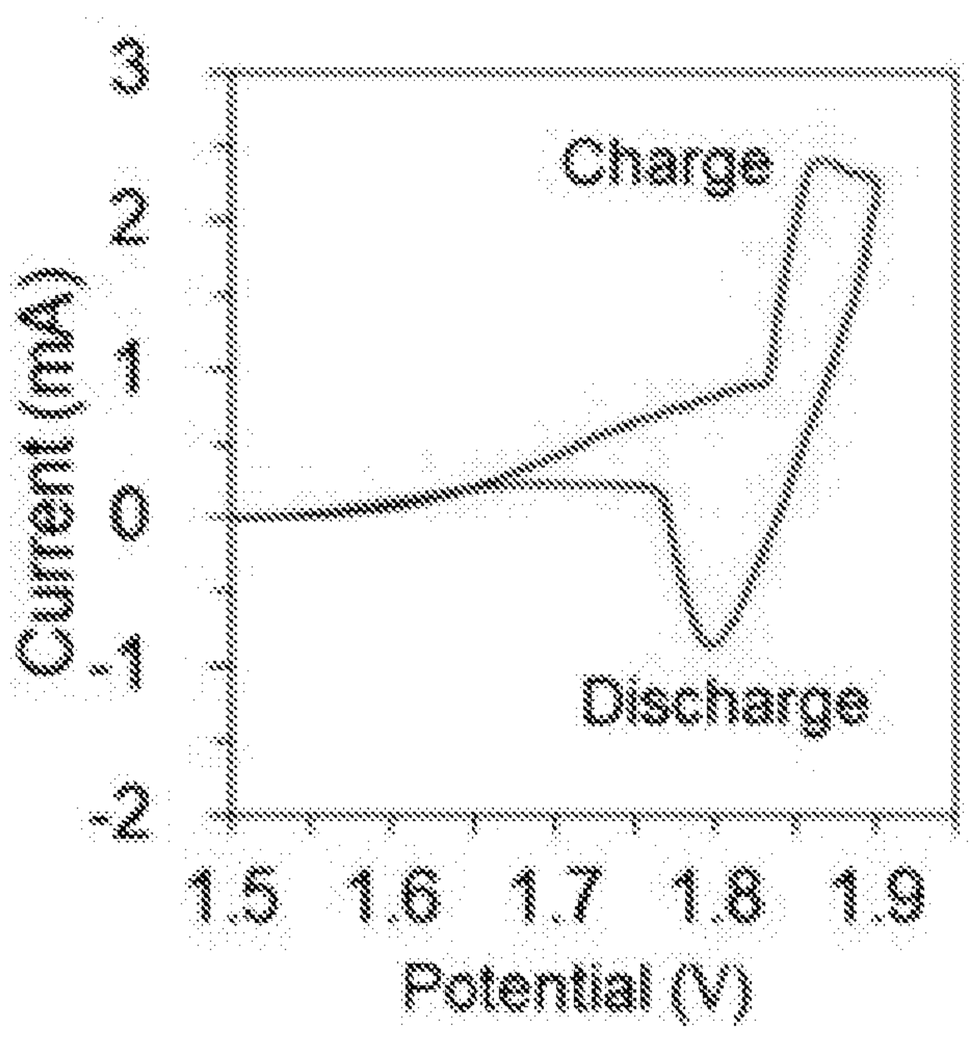


FIG. 91

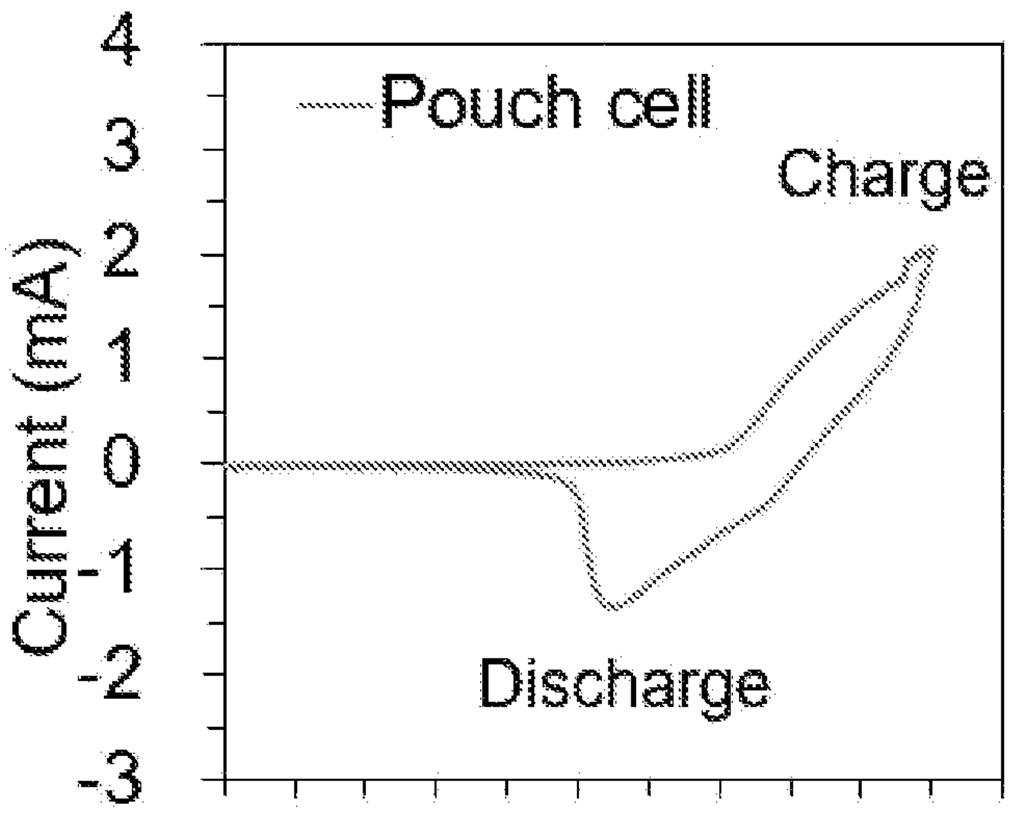


FIG. 92

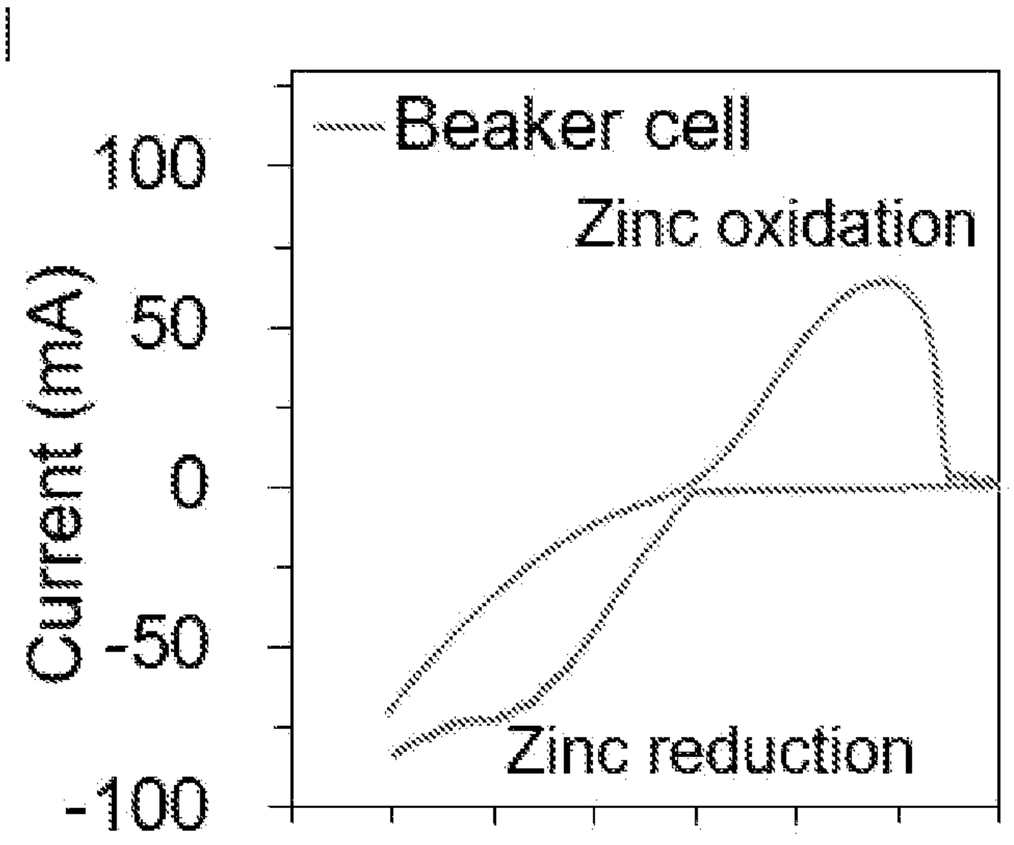


FIG. 93

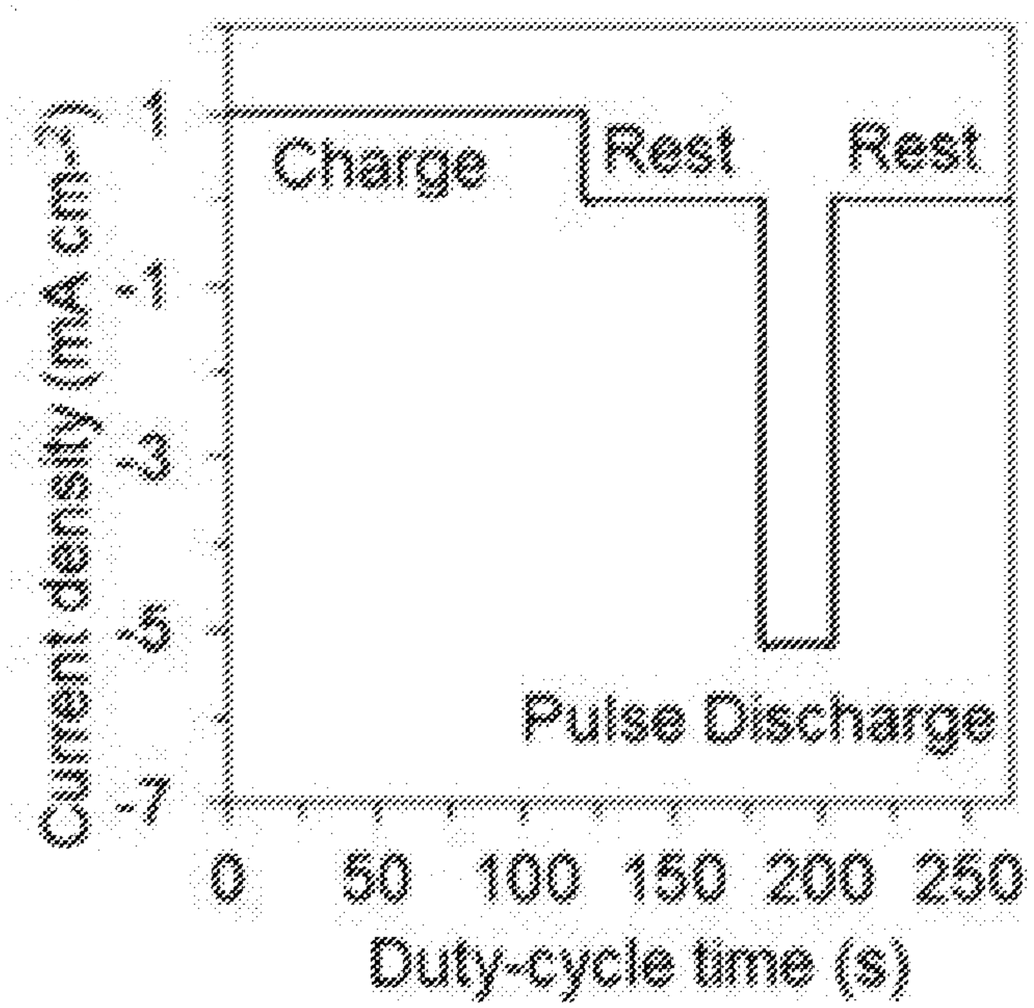

Charge
Rest
Rest
Pulse Discharge
Current density (mA cm-2)
1
-1
-3
-5
-7
0
50
100
150
200
250
Duty-cycle time (s)

FIG. 94

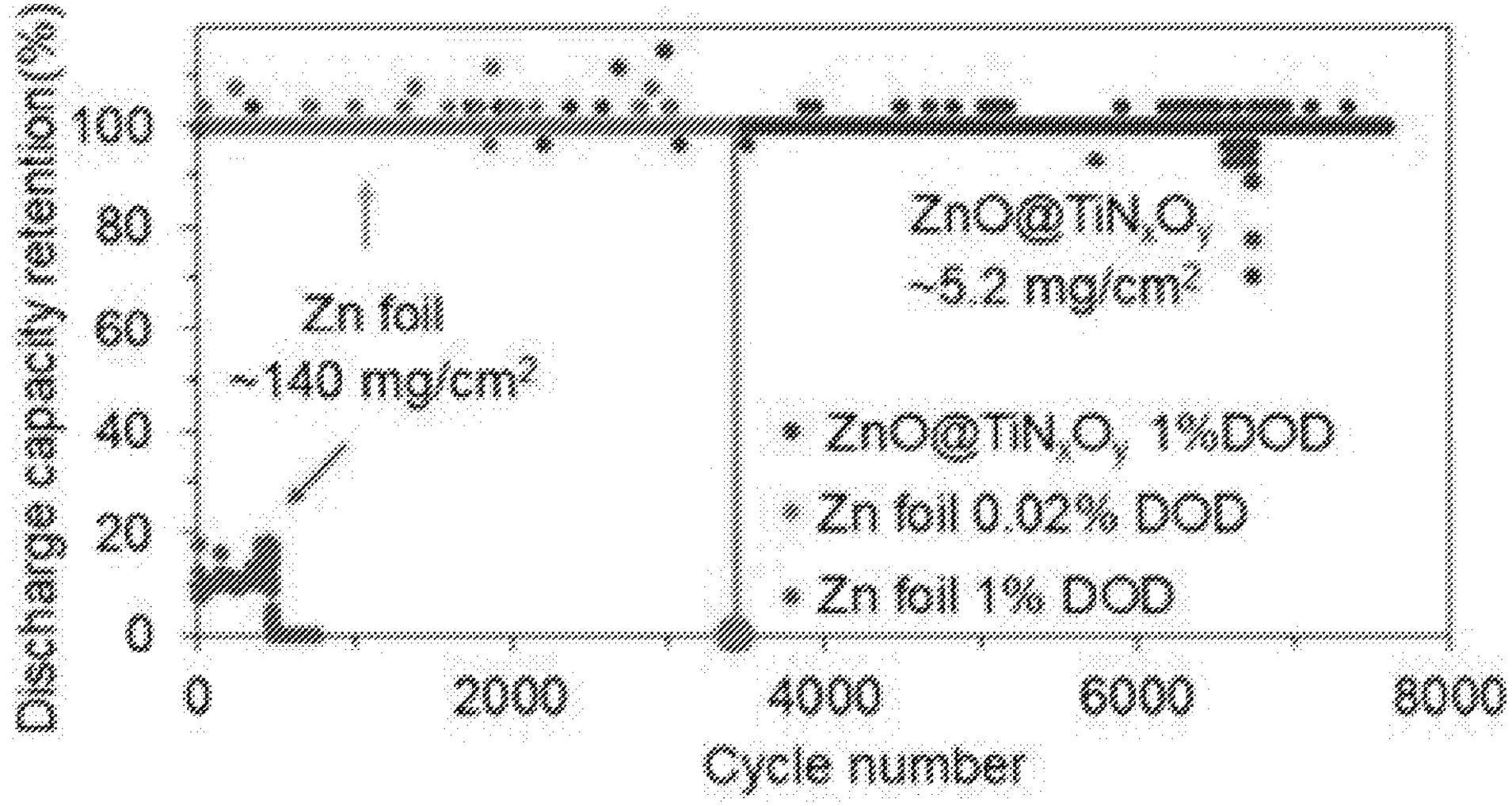

Zn foil
~140 mg/cm2
ZnO@TiNxOy
~5.2 mg/cm2
• ZnO@TiNxOy 1%DOD
• Zn foil 0.02% DOD
• Zn foil 1% DOD
Discharge capacity retention (%)
100
80
60
40
20
0
0
2000
4000
6000
8000
Cycle number

FIG. 95

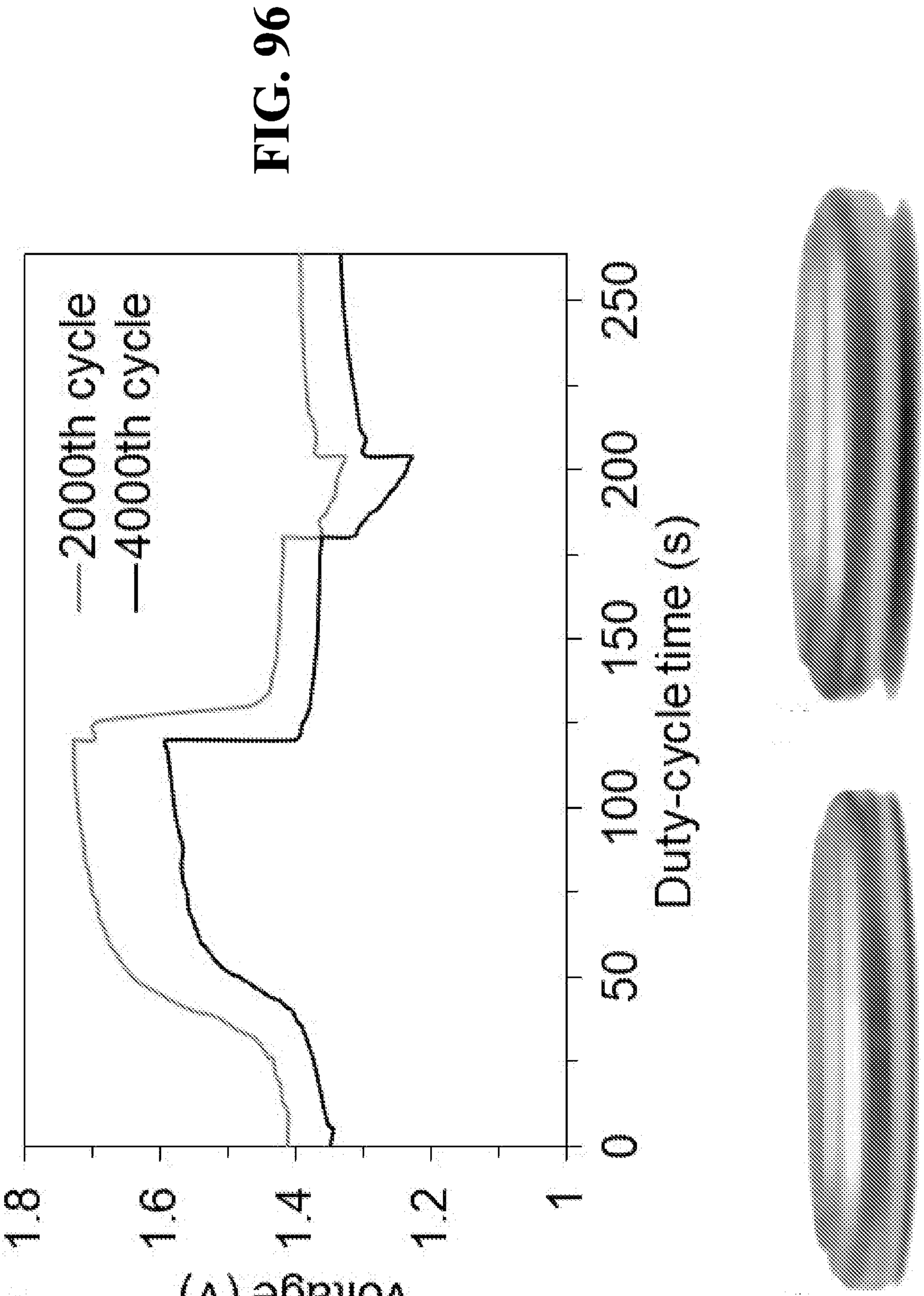


FIG. 96

FIG. 98

FIG. 97

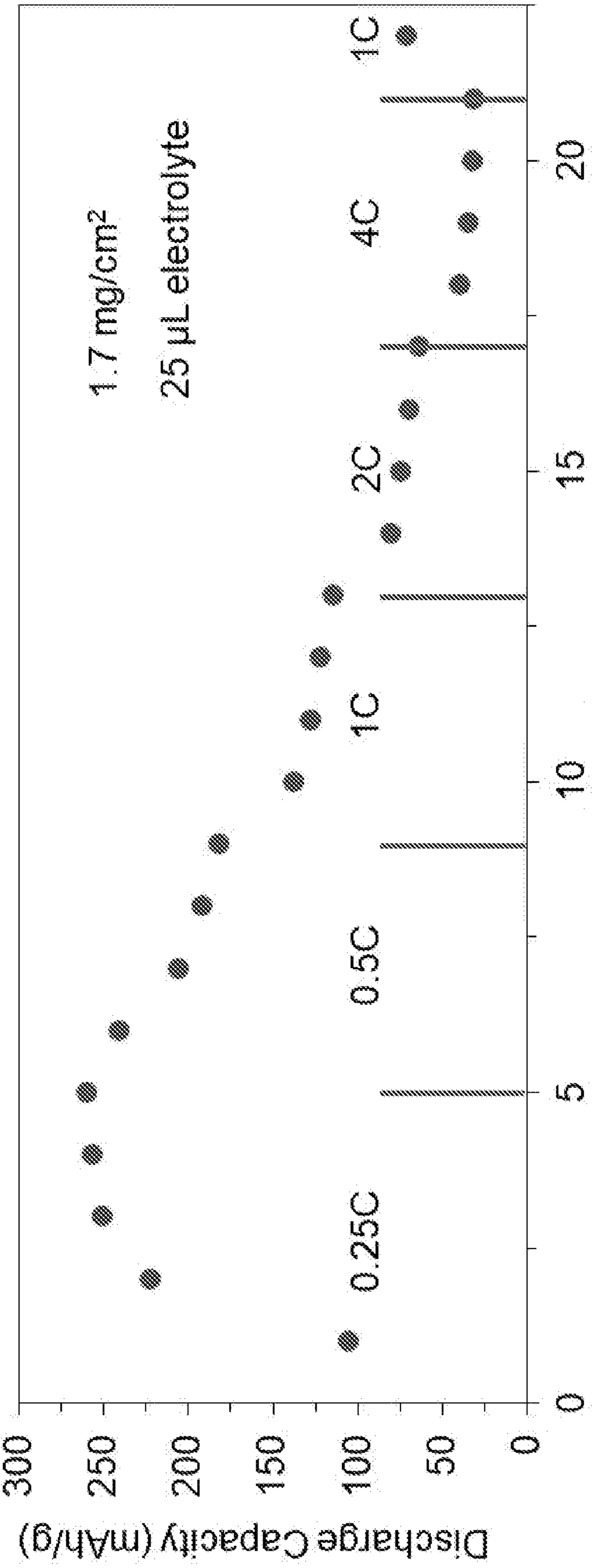

1.7 mg/cm2
25 µL electrolyte
0.25C
0.5C
1C
2C
4C
1C
0
5
10
15
20
Cycle number
Discharge Capacity (mAh/g)
0
50
100
150
200
250
300

FIG. 99

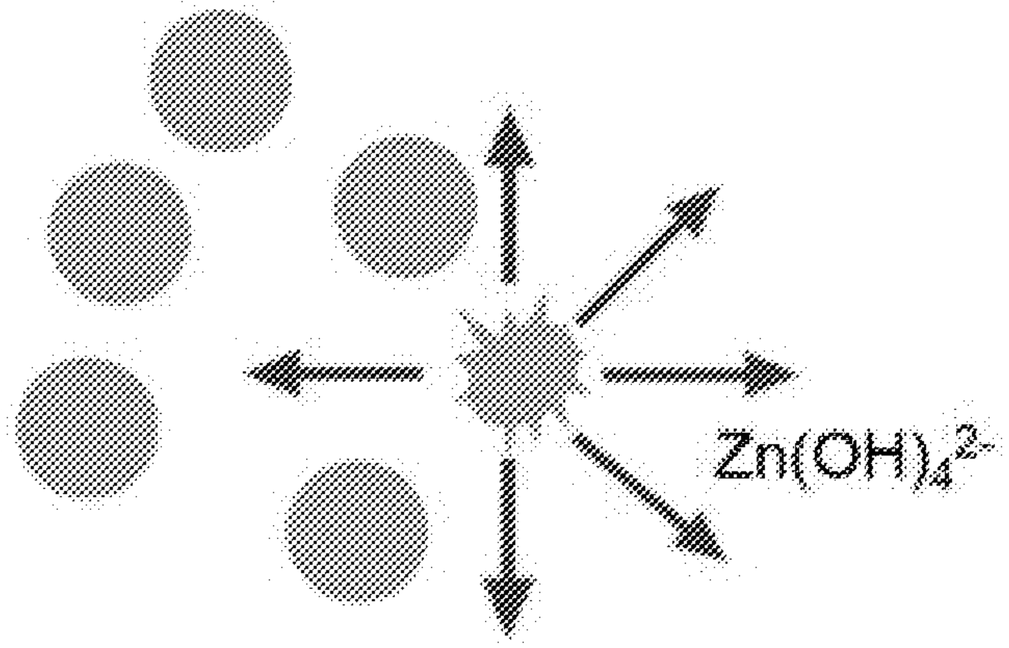


FIG. 100A

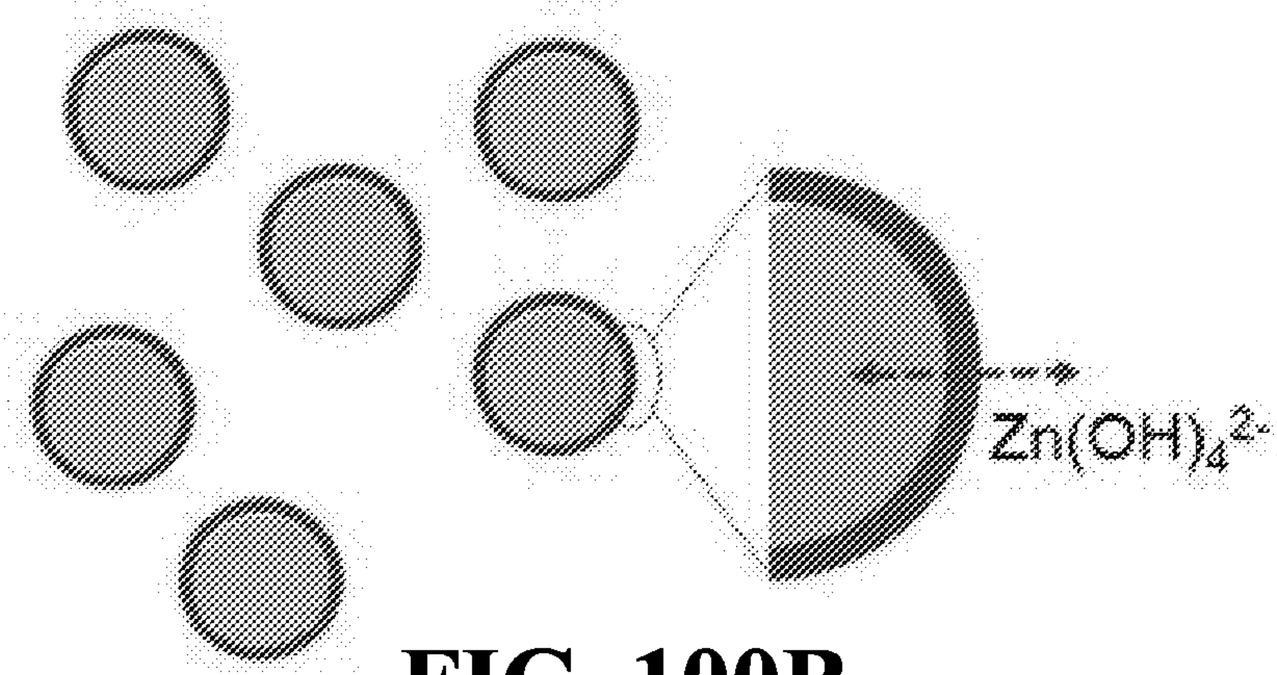


FIG. 100B

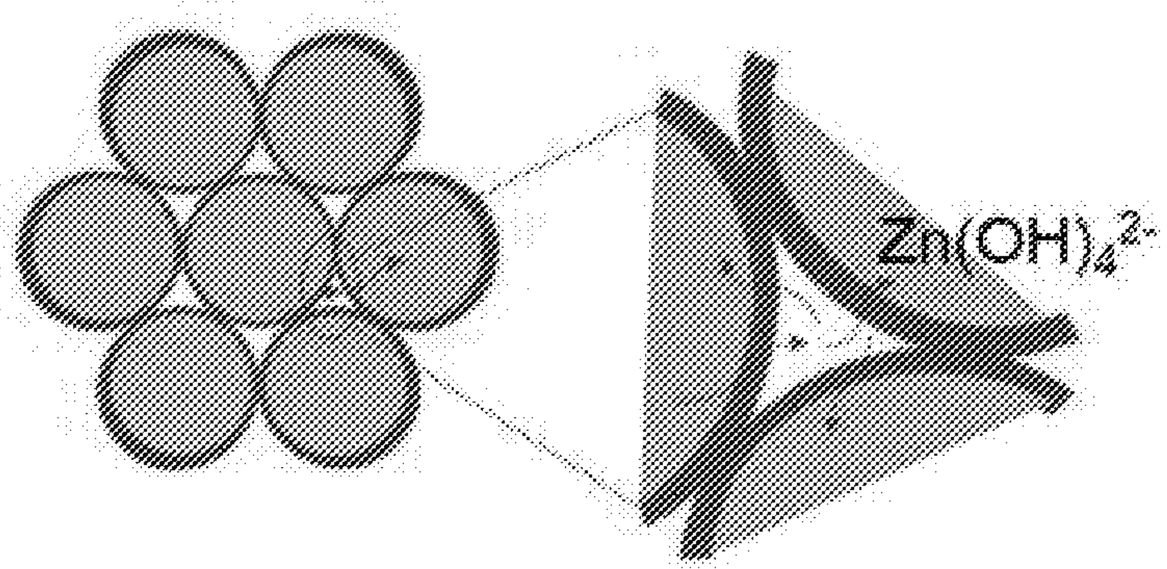


FIG. 100C

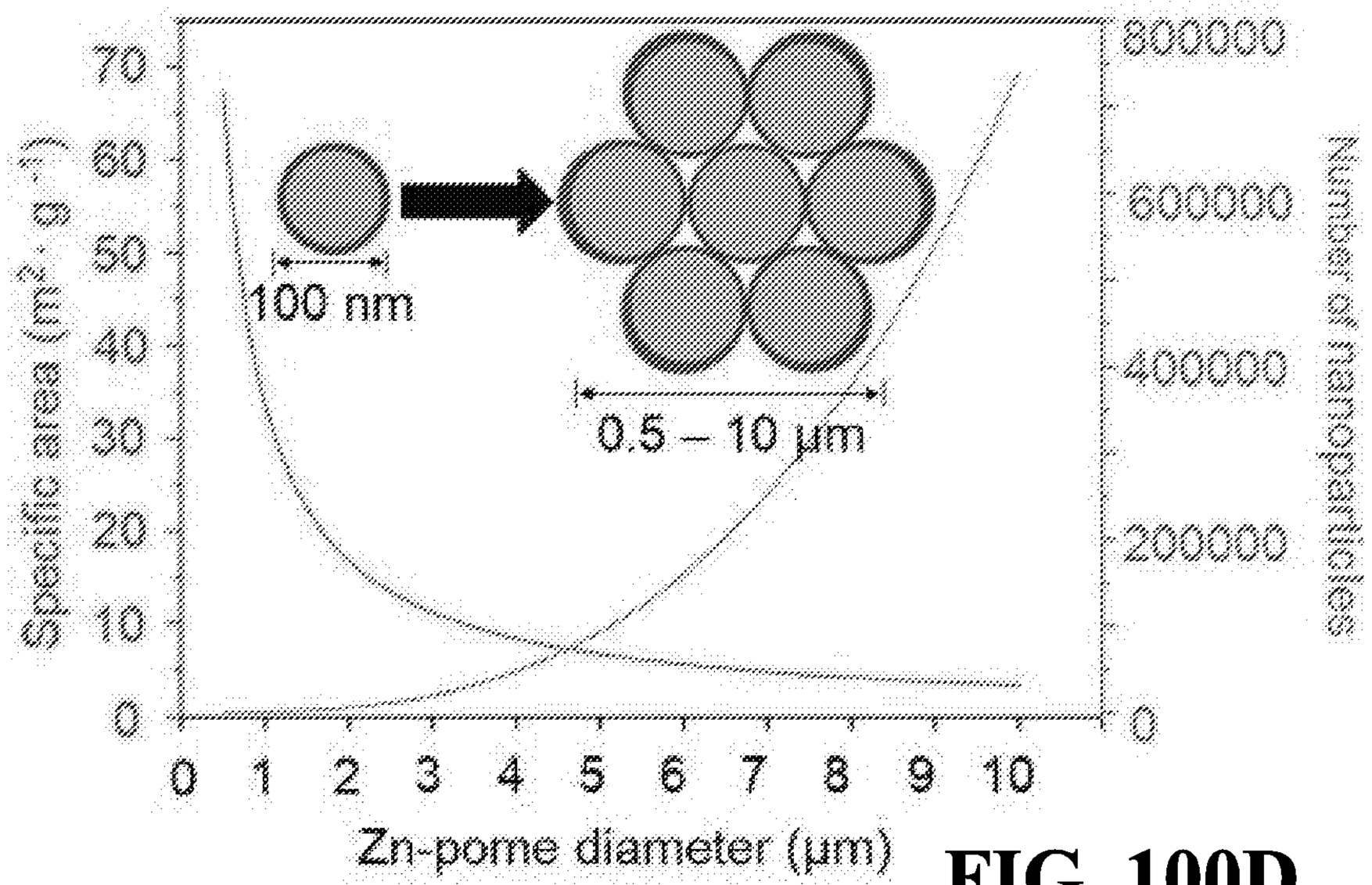


FIG. 100D

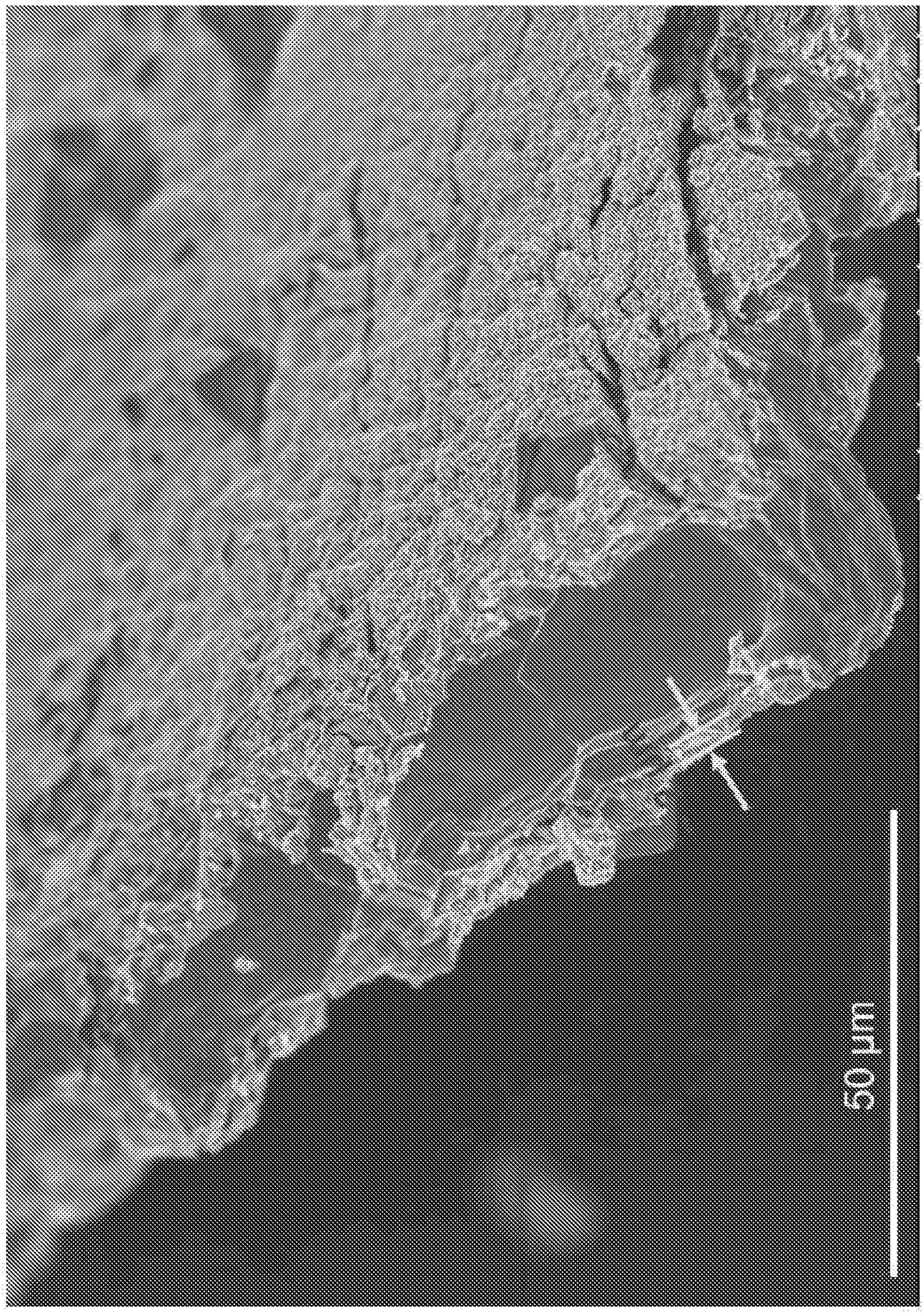


FIG. 101

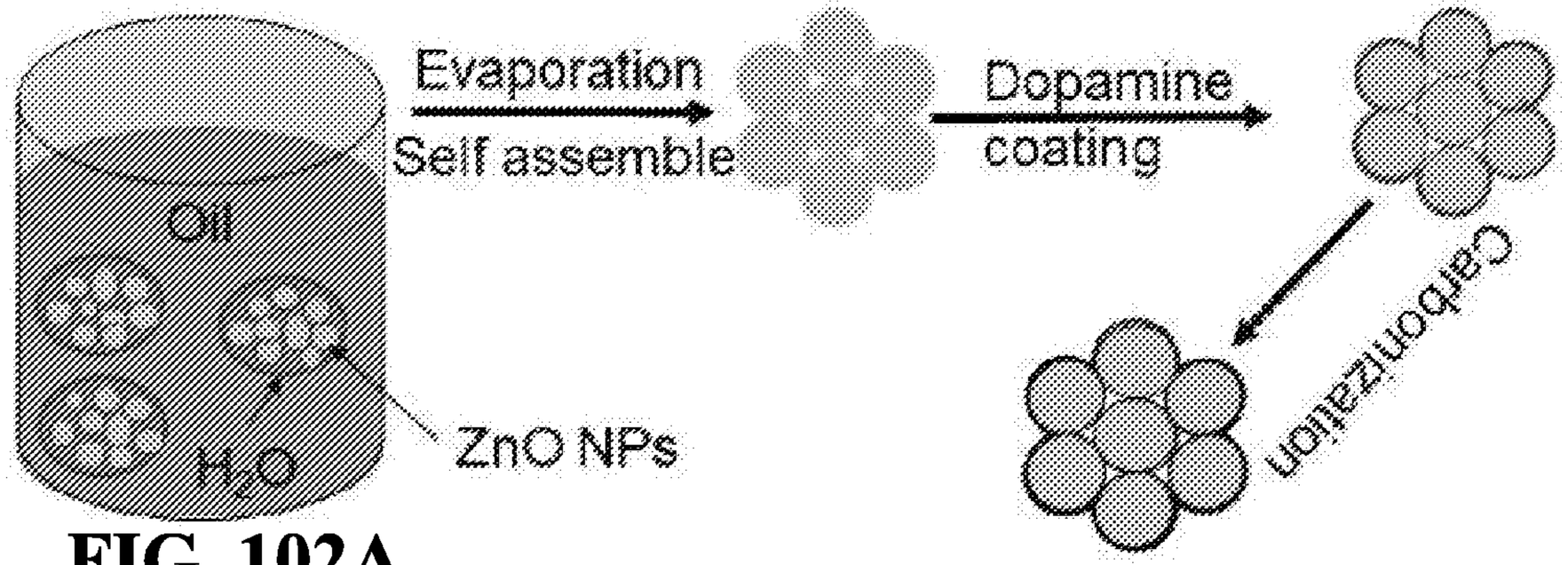


FIG. 102A

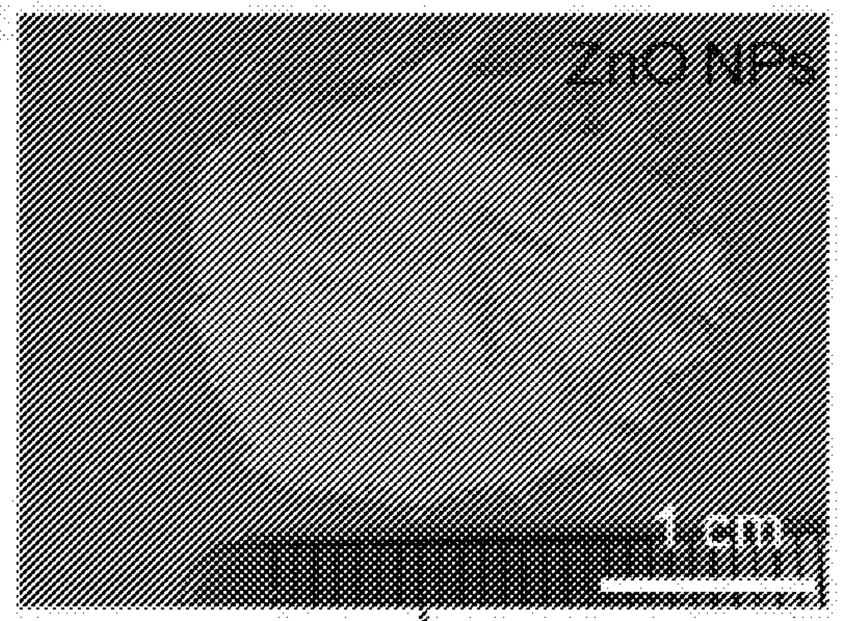


FIG. 102B

Self assemble

FIG. 102D

FIG. 102E

FIG. 102C

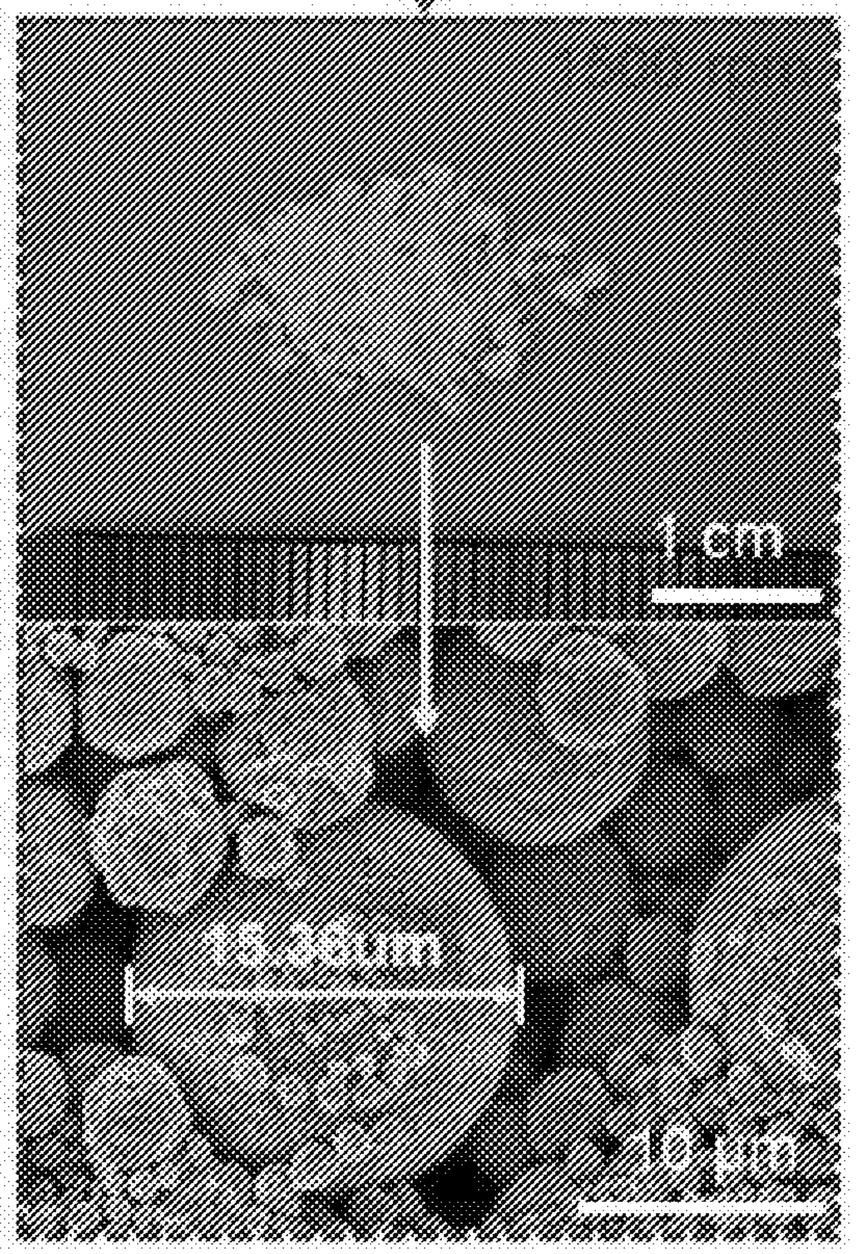


FIG. 102F

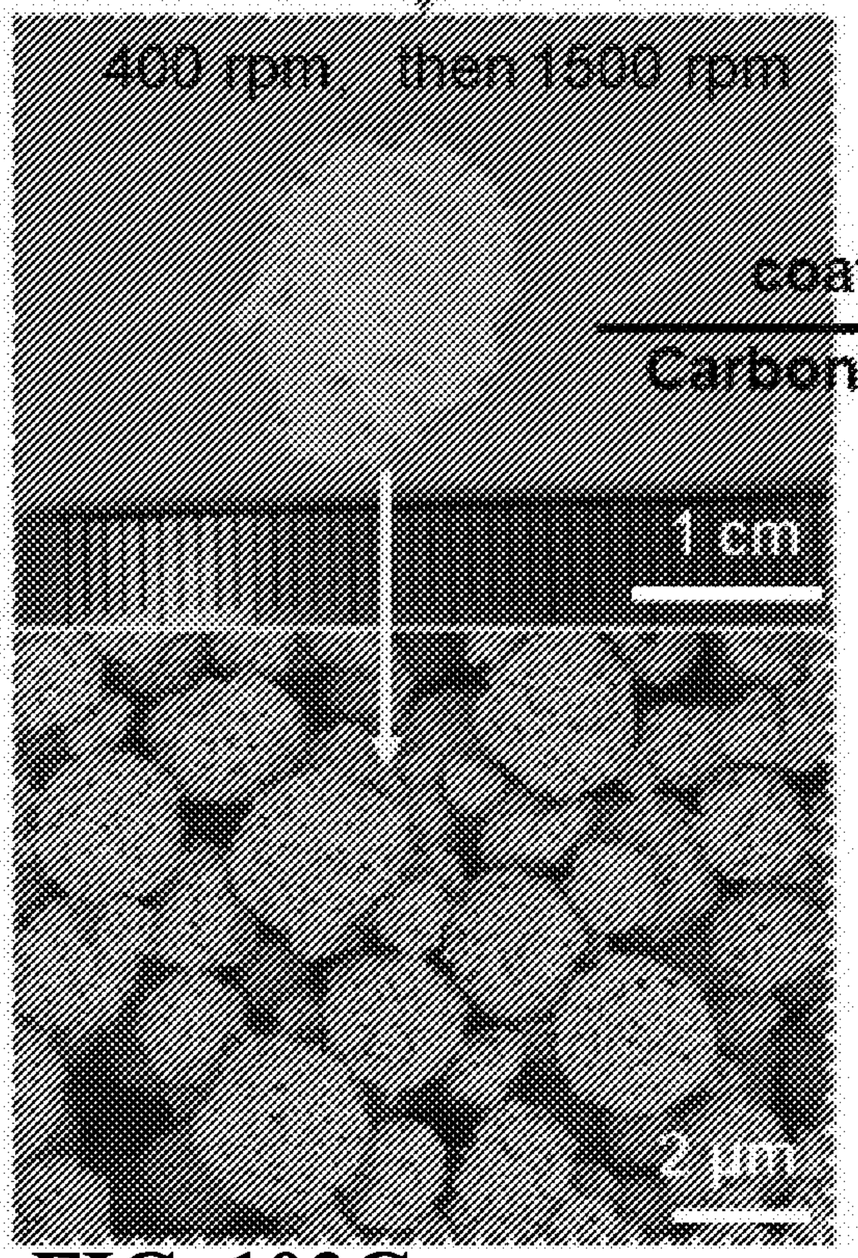


FIG. 102G

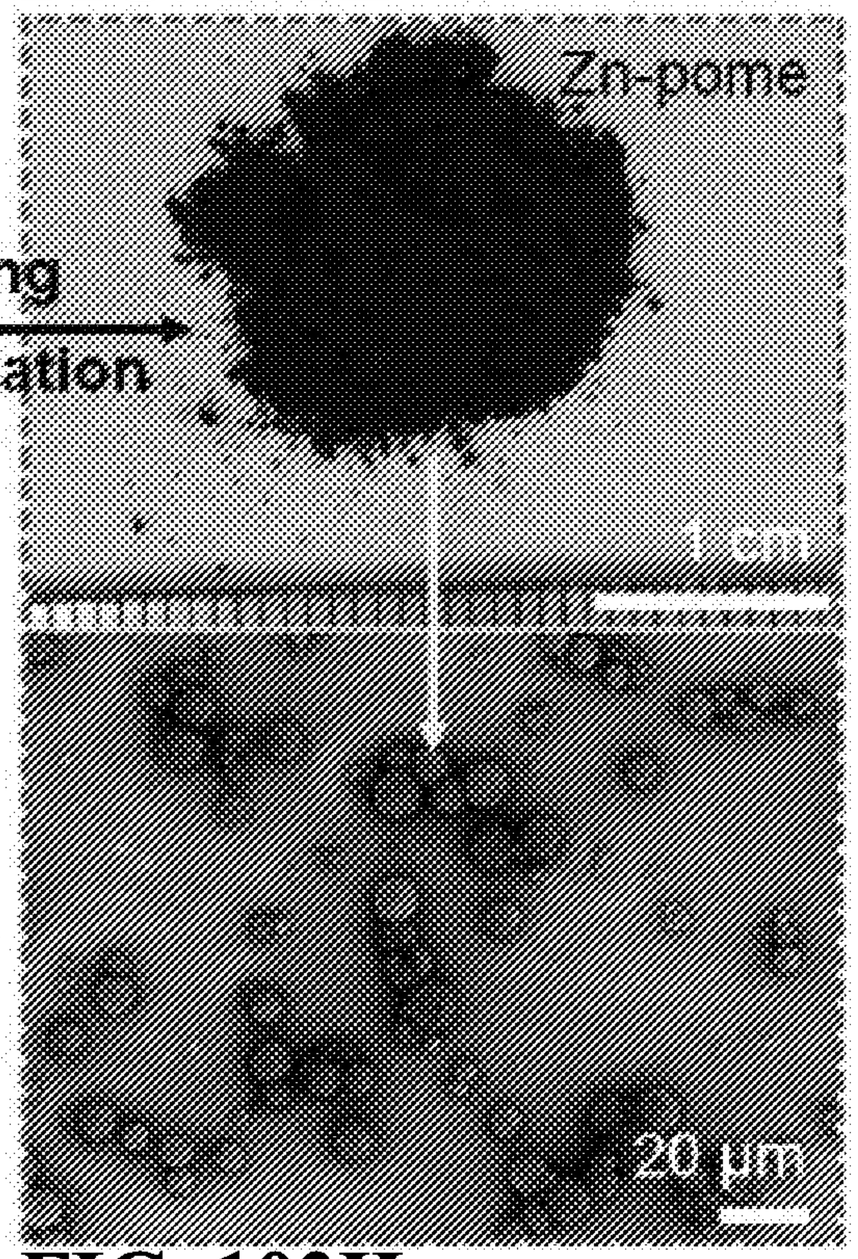


FIG. 102H

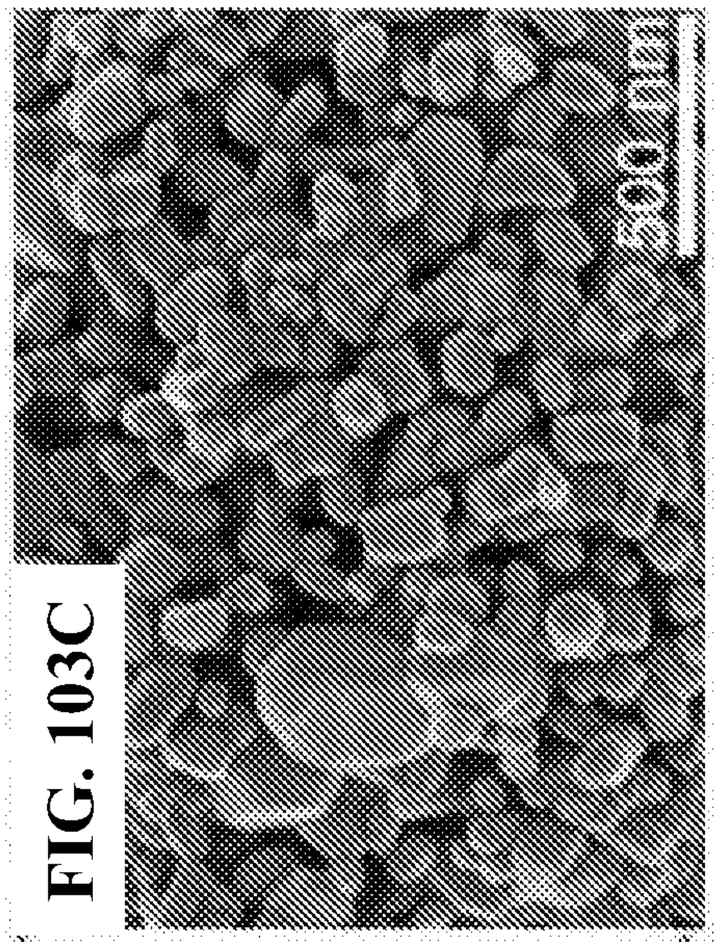


FIG. 103C

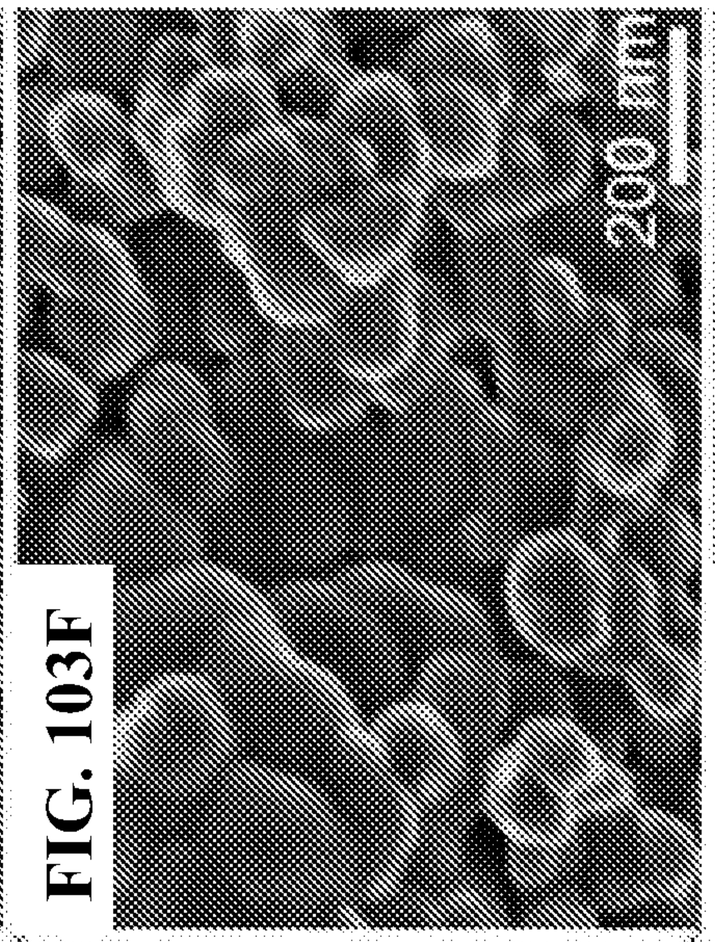


FIG. 103F

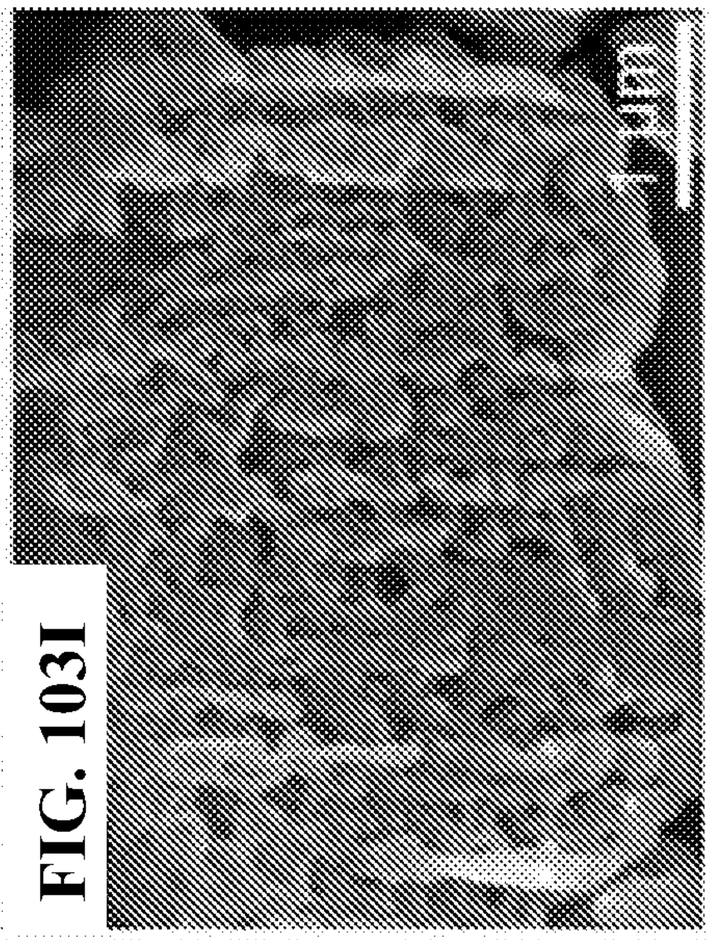


FIG. 103I

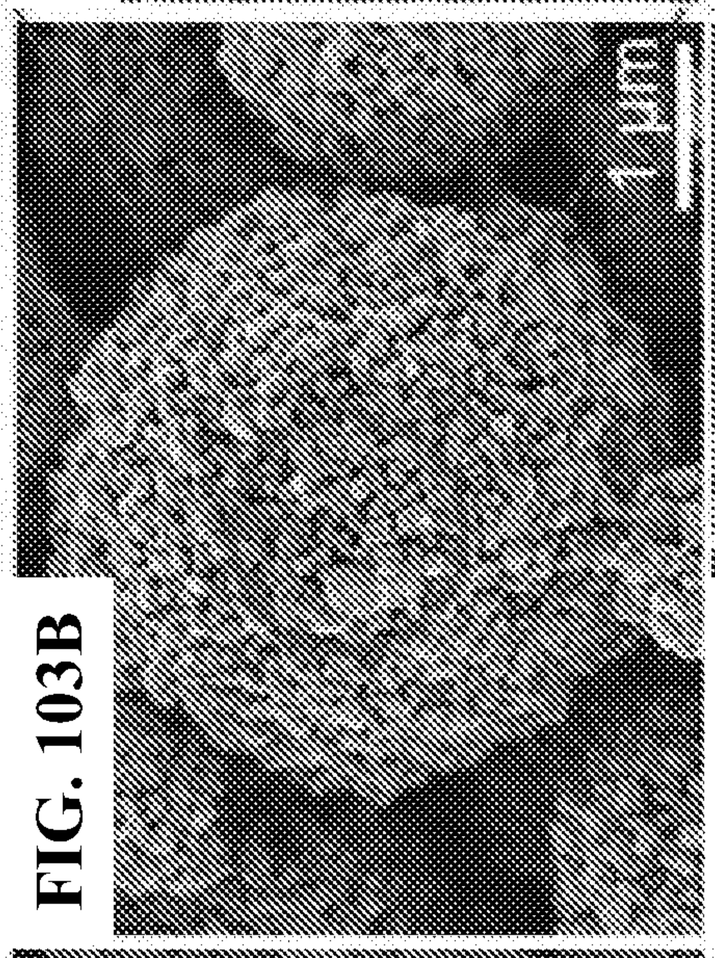


FIG. 103B

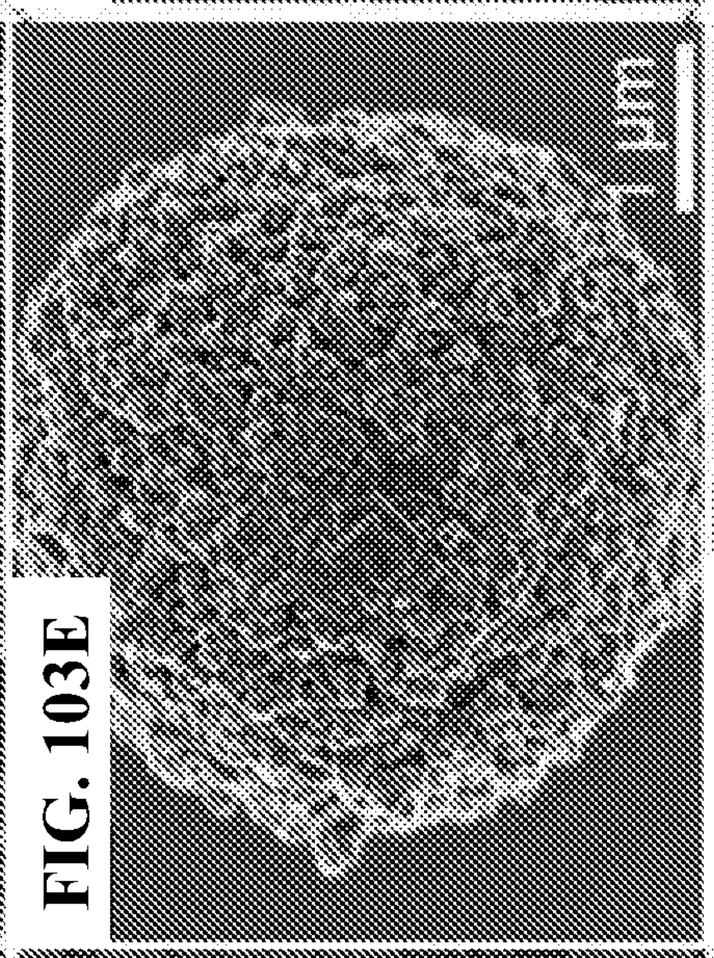


FIG. 103E

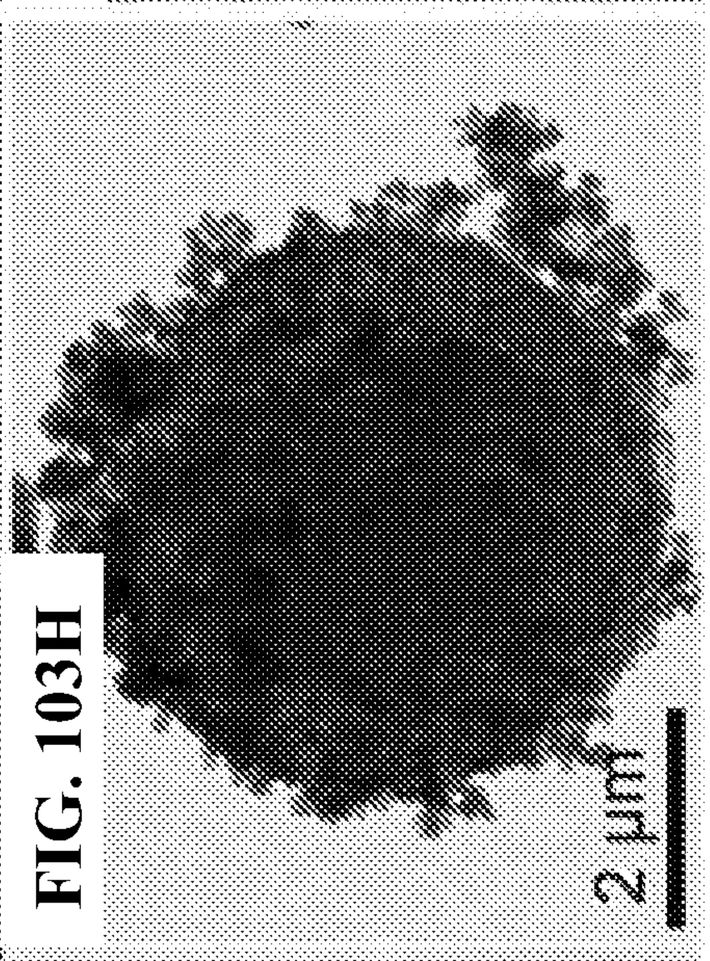


FIG. 103H

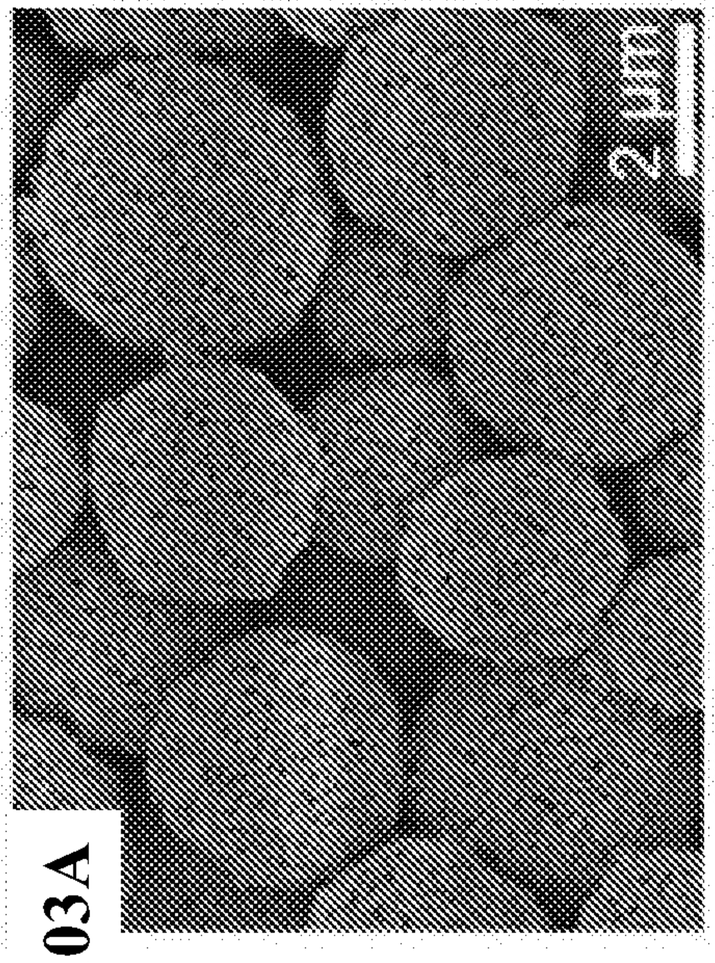


FIG. 103A

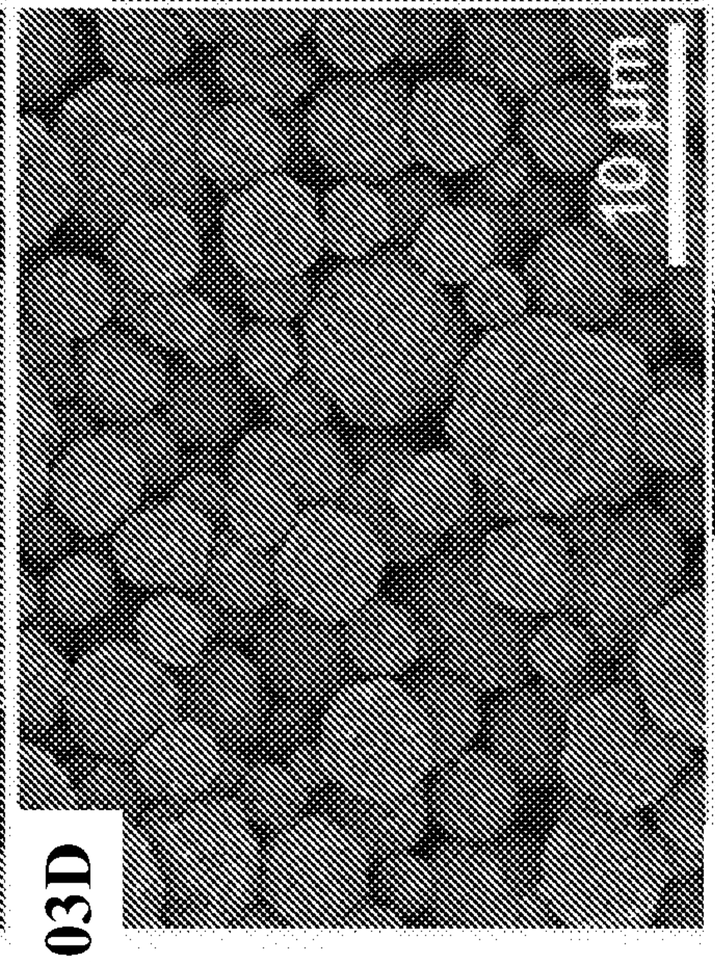


FIG. 103D

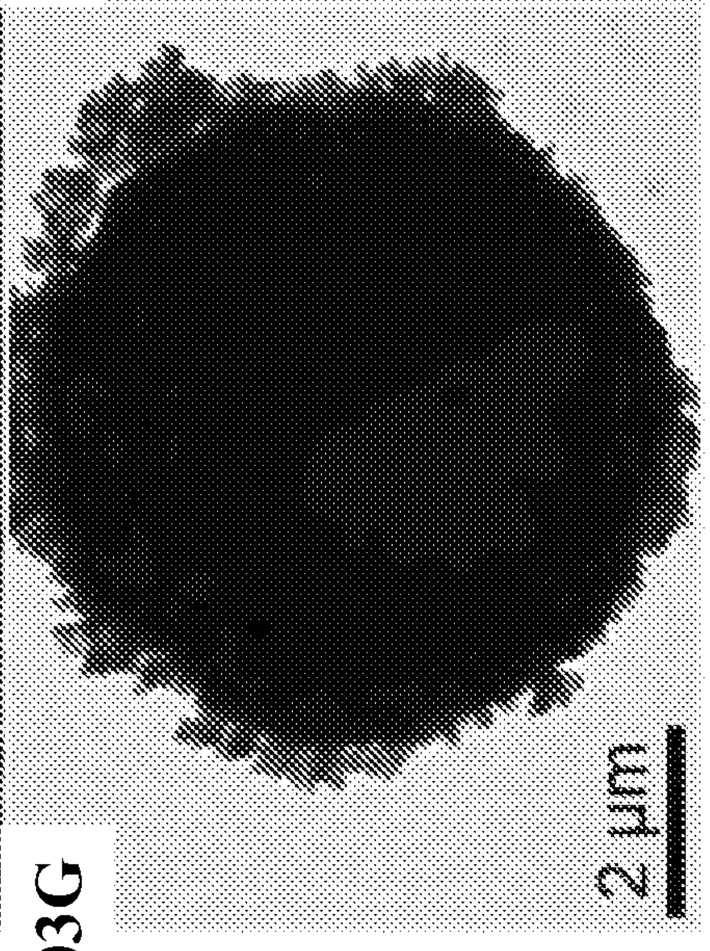


FIG. 103G

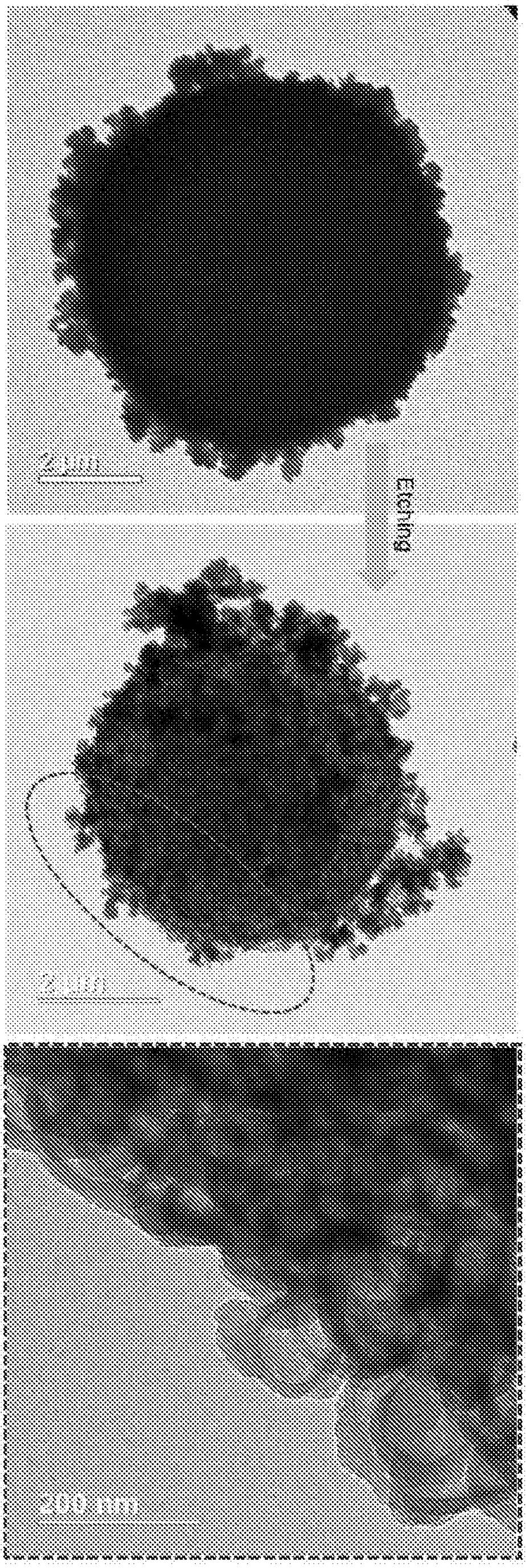


FIG. 104A

FIG. 104C

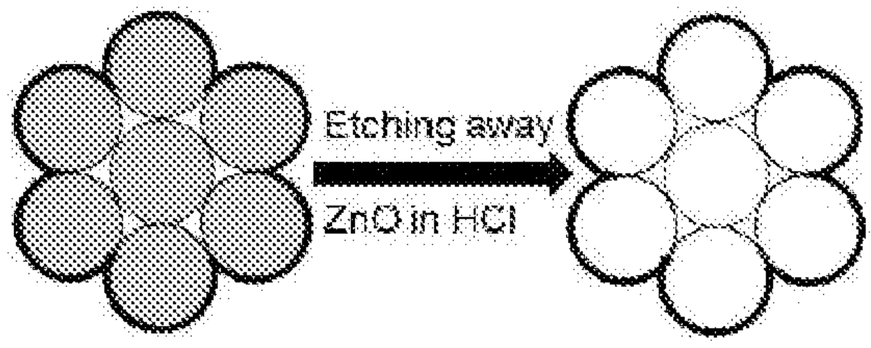


FIG. 104B

FIG. 104D

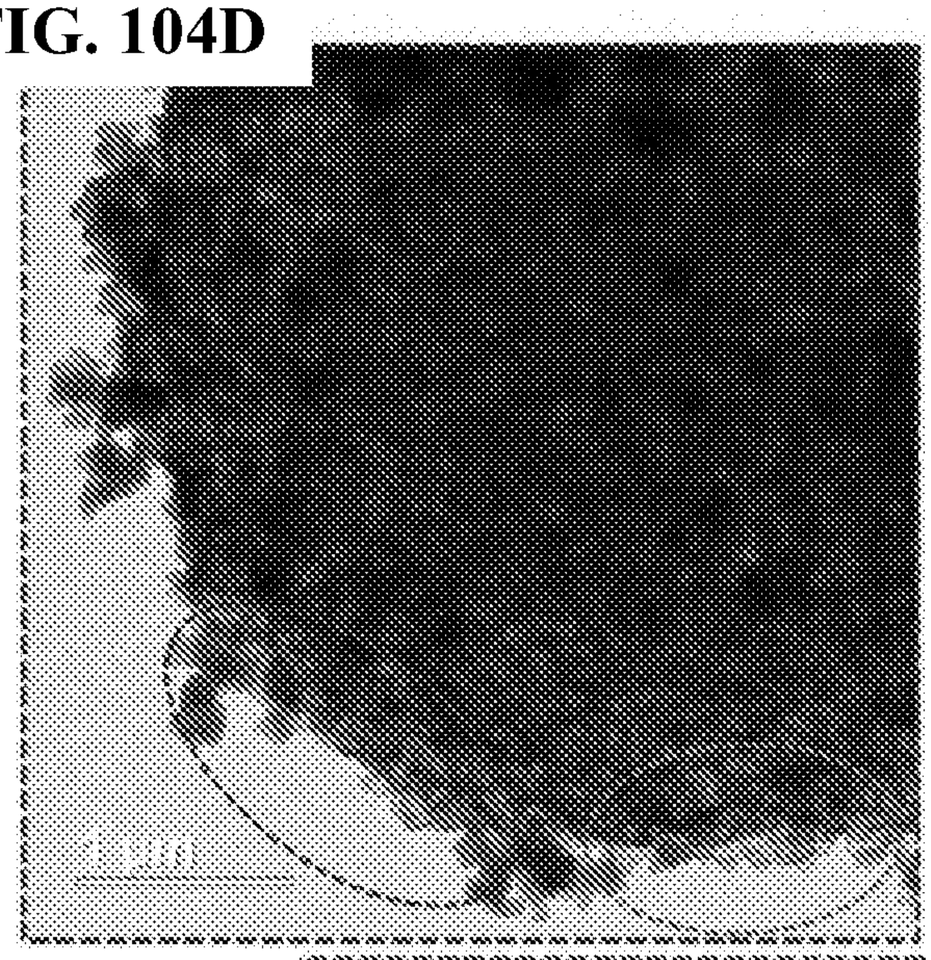
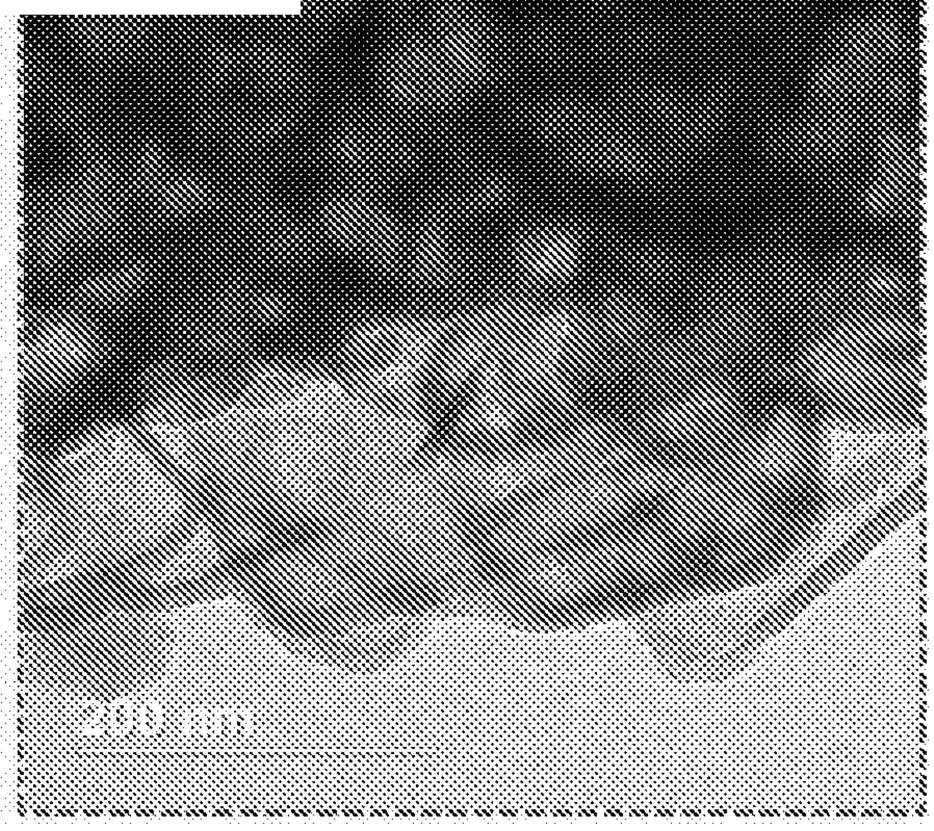


FIG. 104F

FIG. 104E



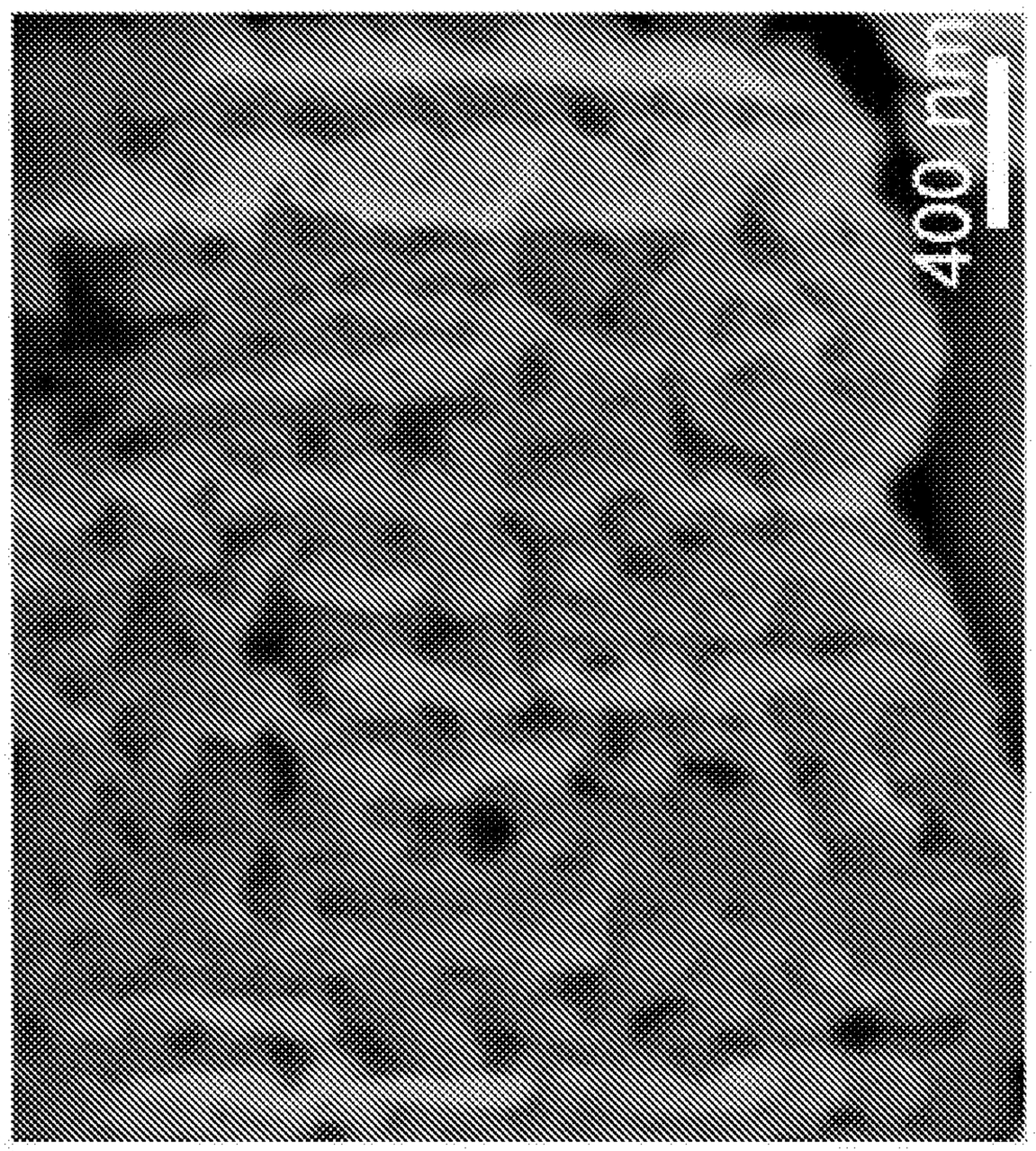


FIG. 106

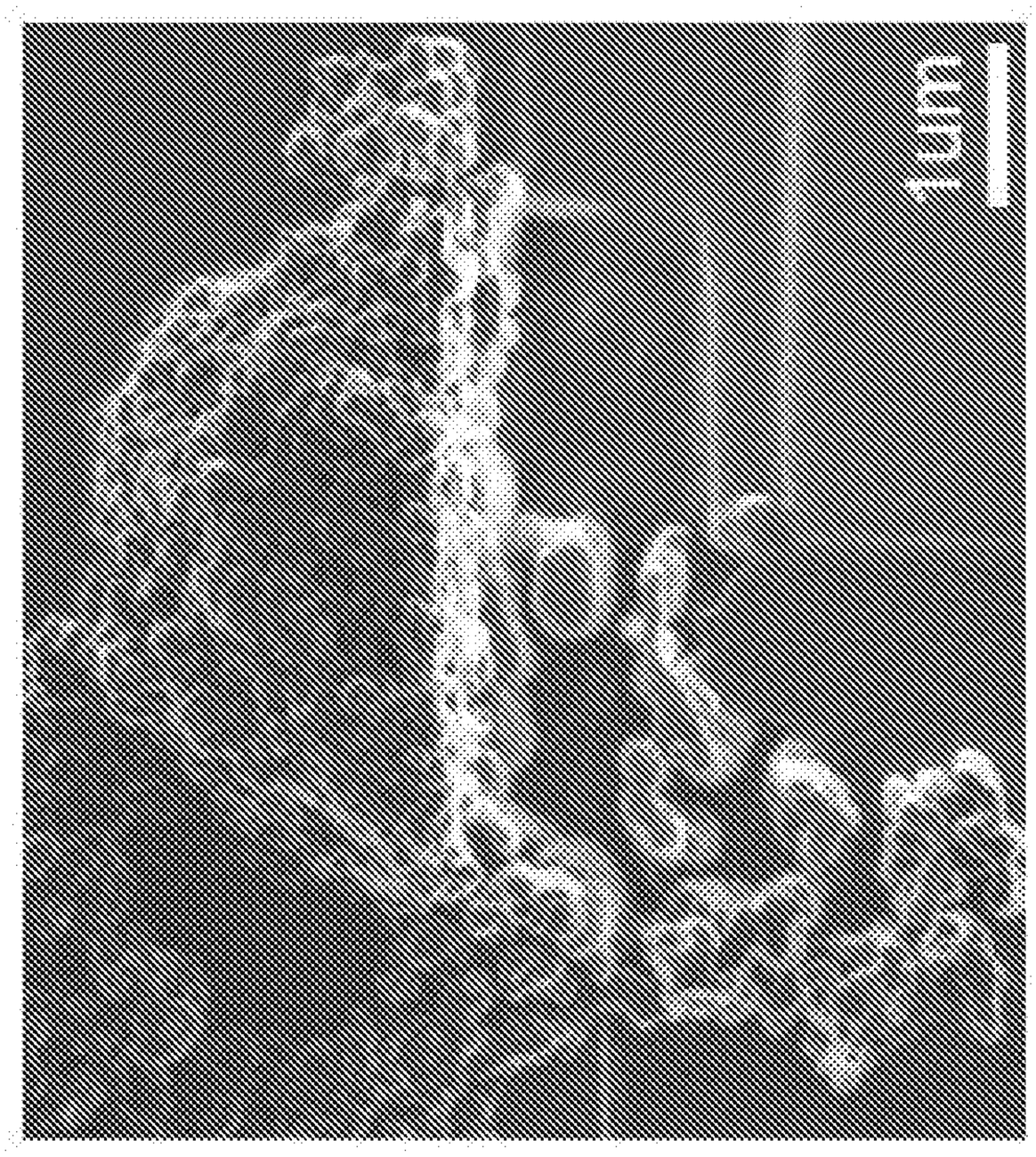


FIG. 105

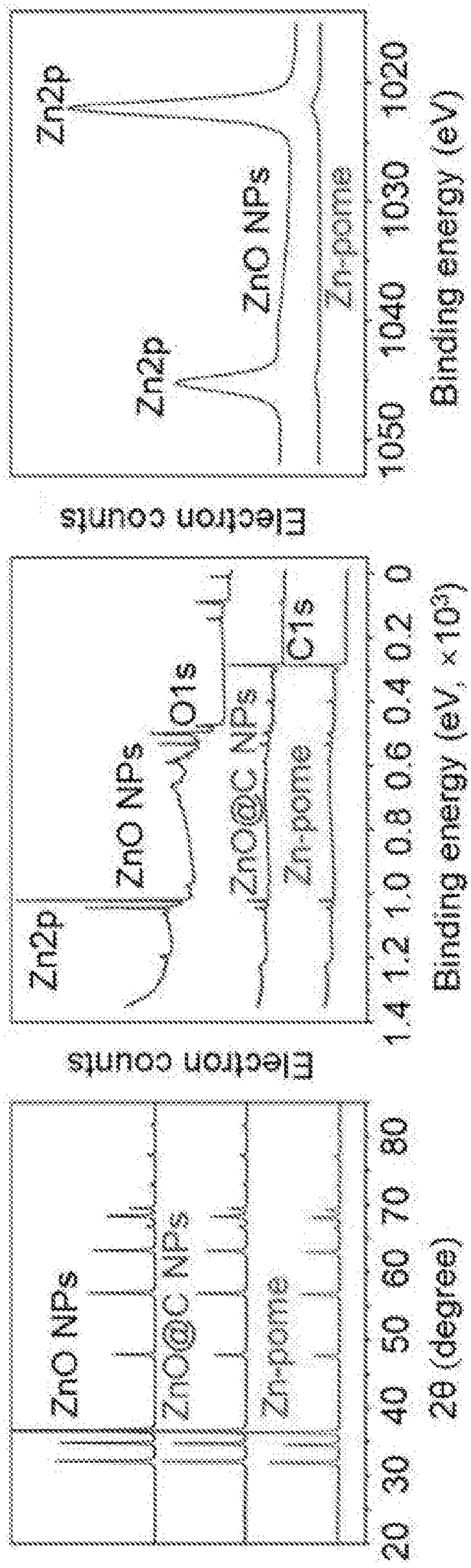


FIG. 107C

FIG. 107B

FIG. 107A

FIG. 107D

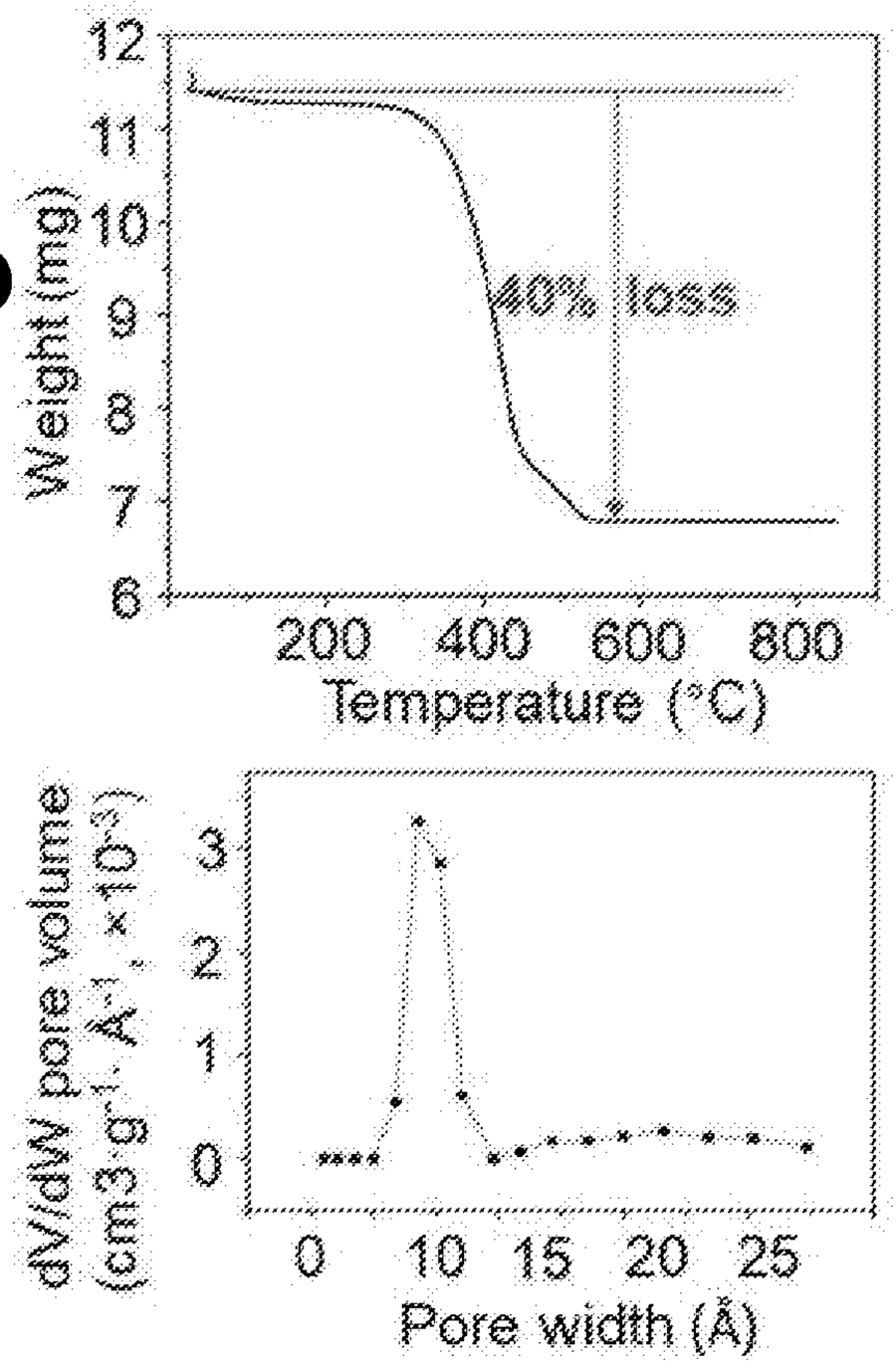


FIG. 107E

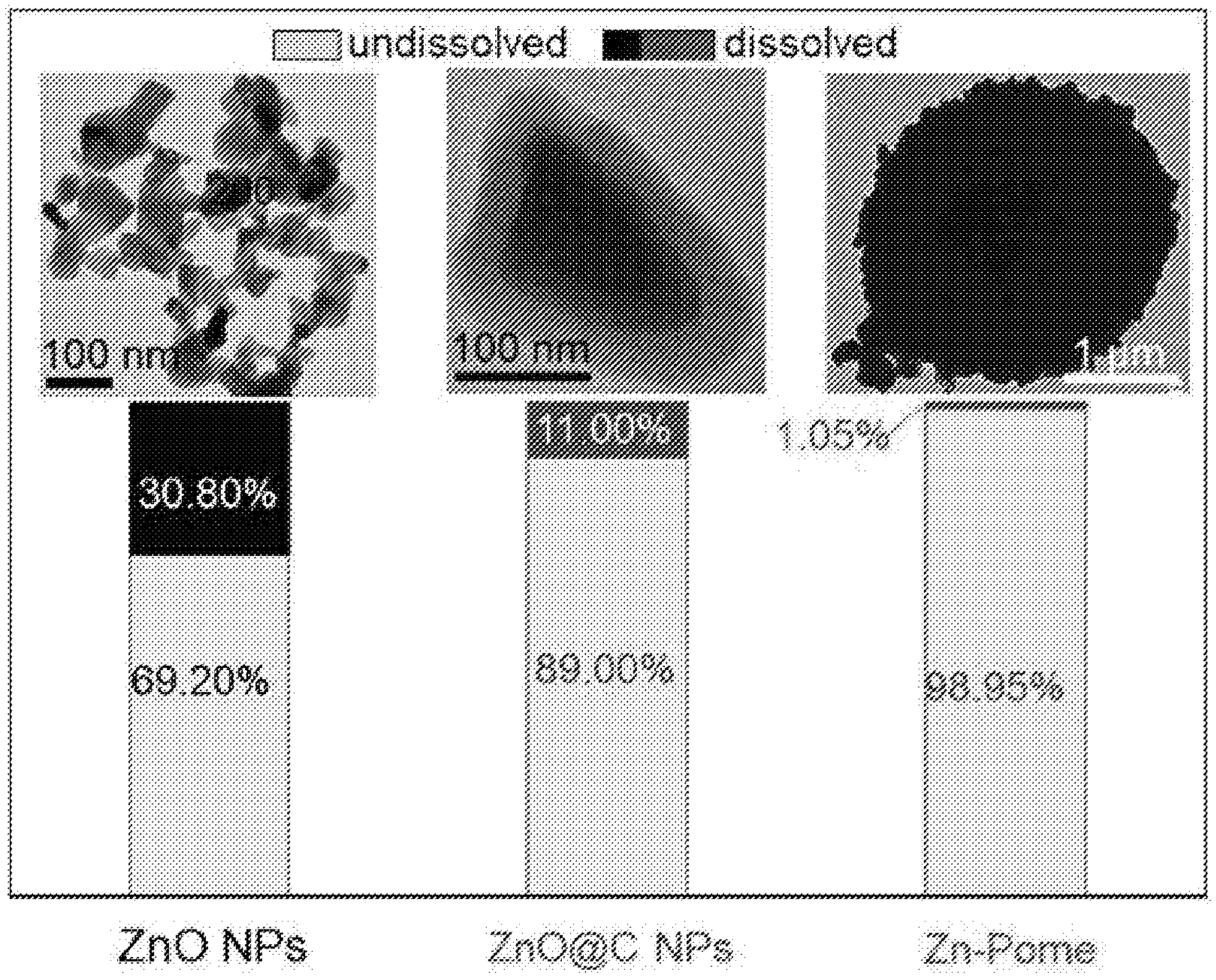
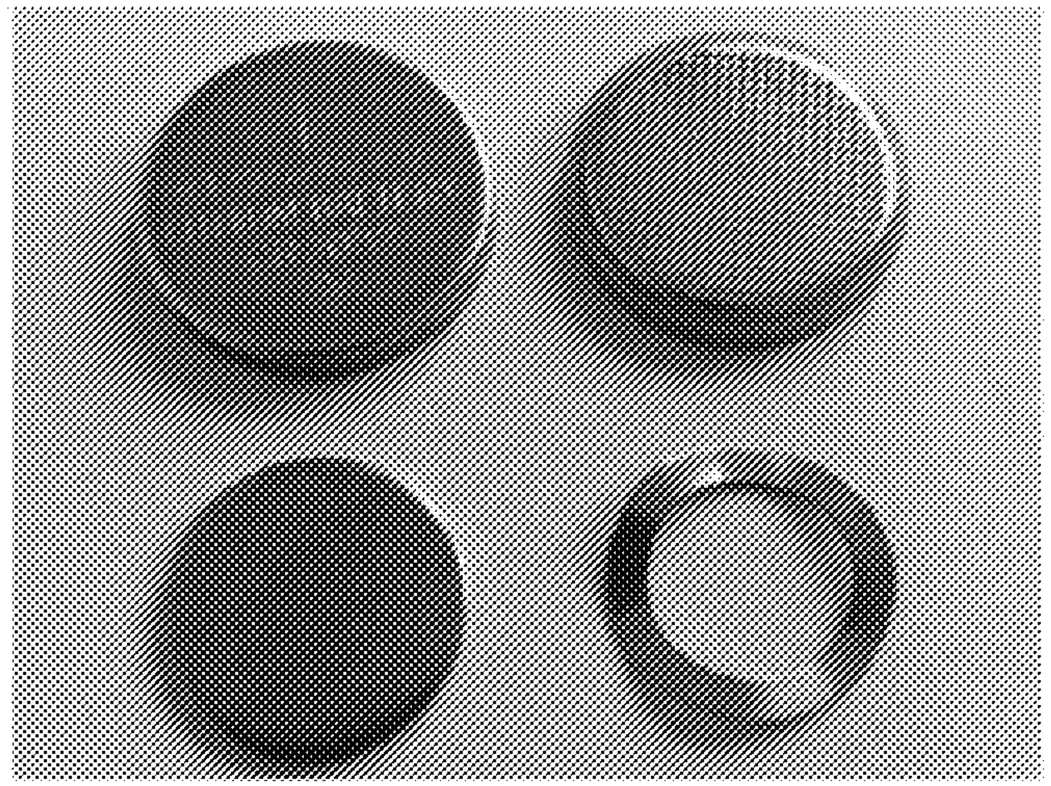


FIG. 107F



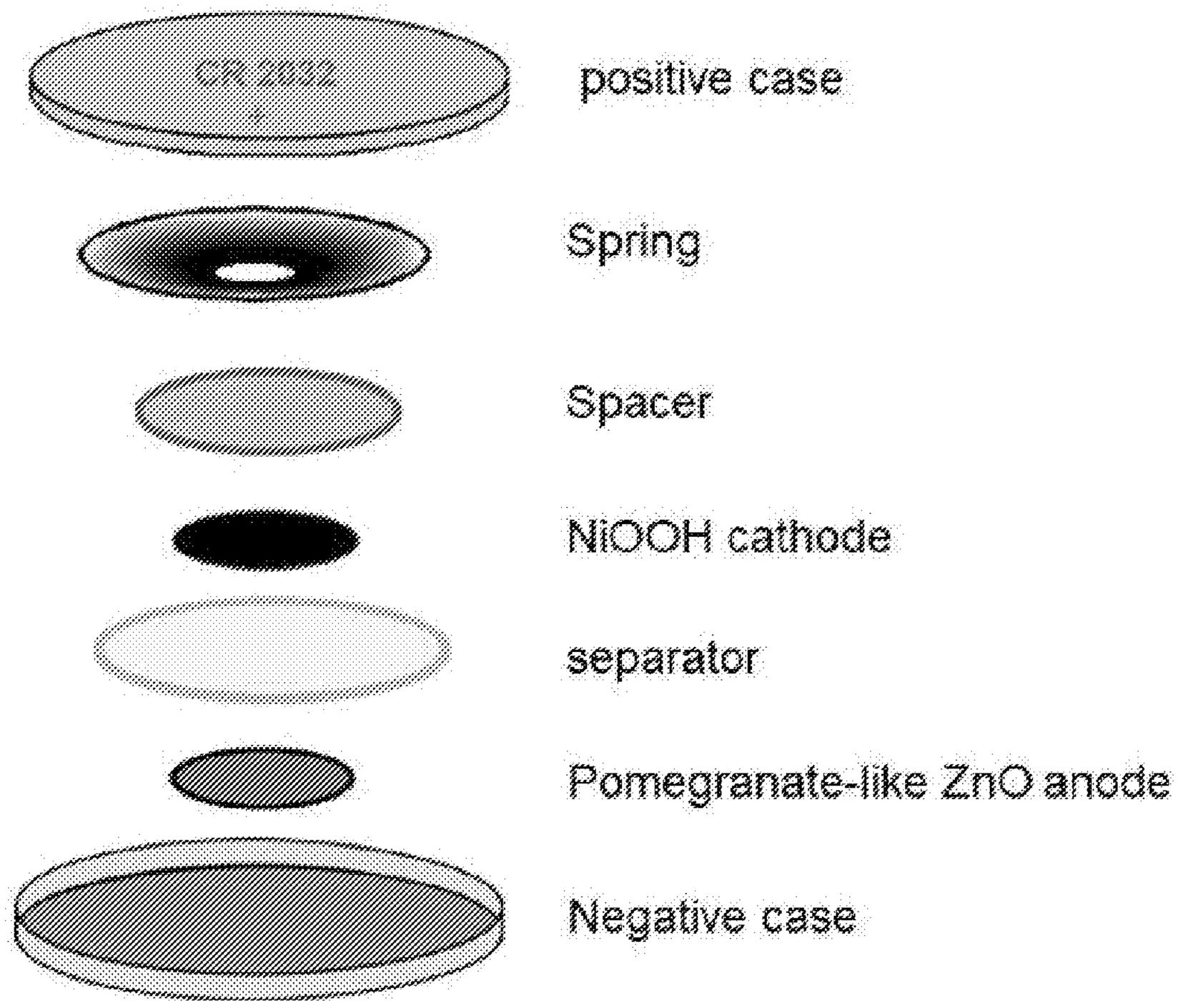

CR 2032
positive case
Spring
Spacer
NiOOH cathode
separator
Pomegranate-like ZnO anode
Negative case

FIG. 108

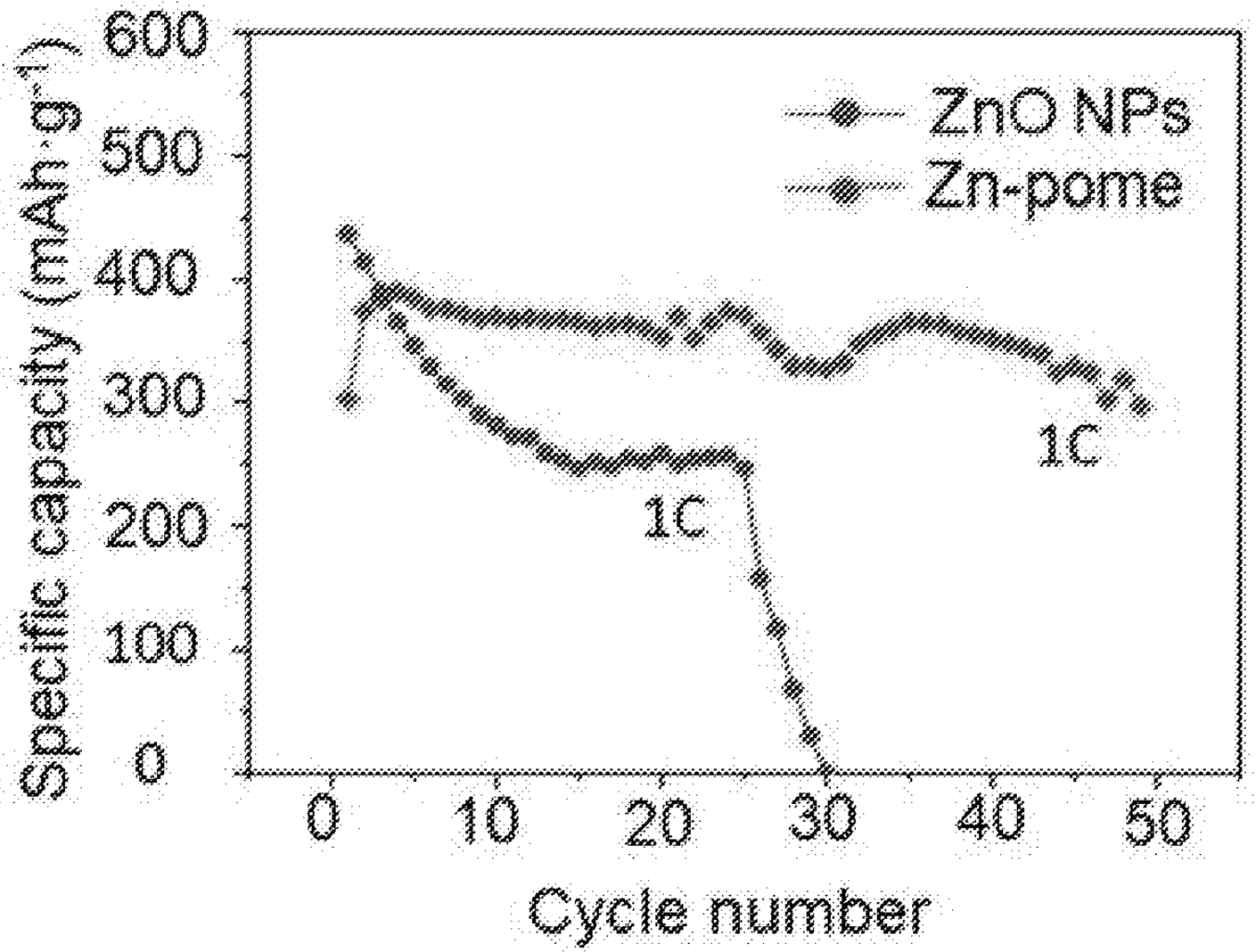


FIG. 109A

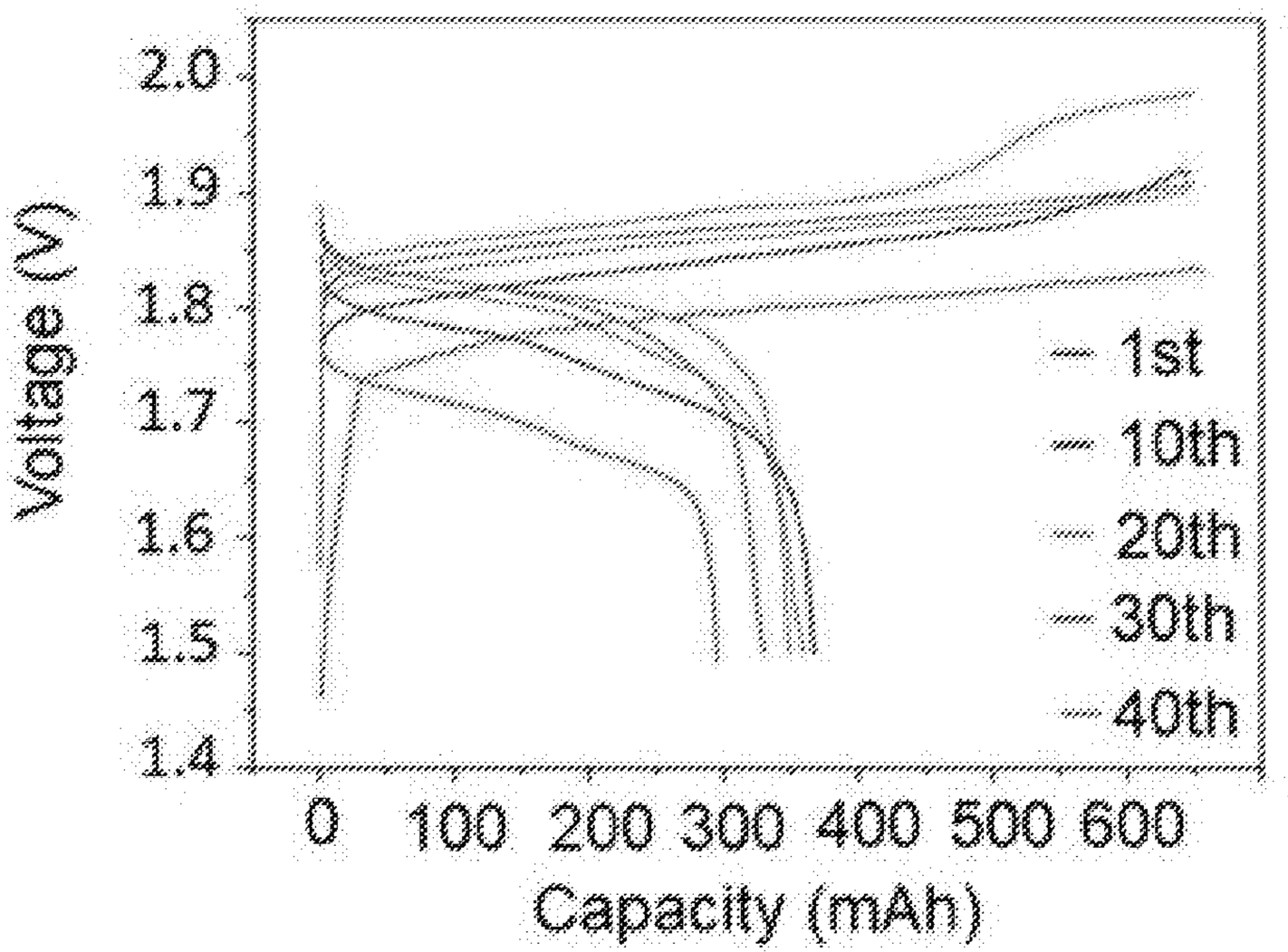


FIG. 109B

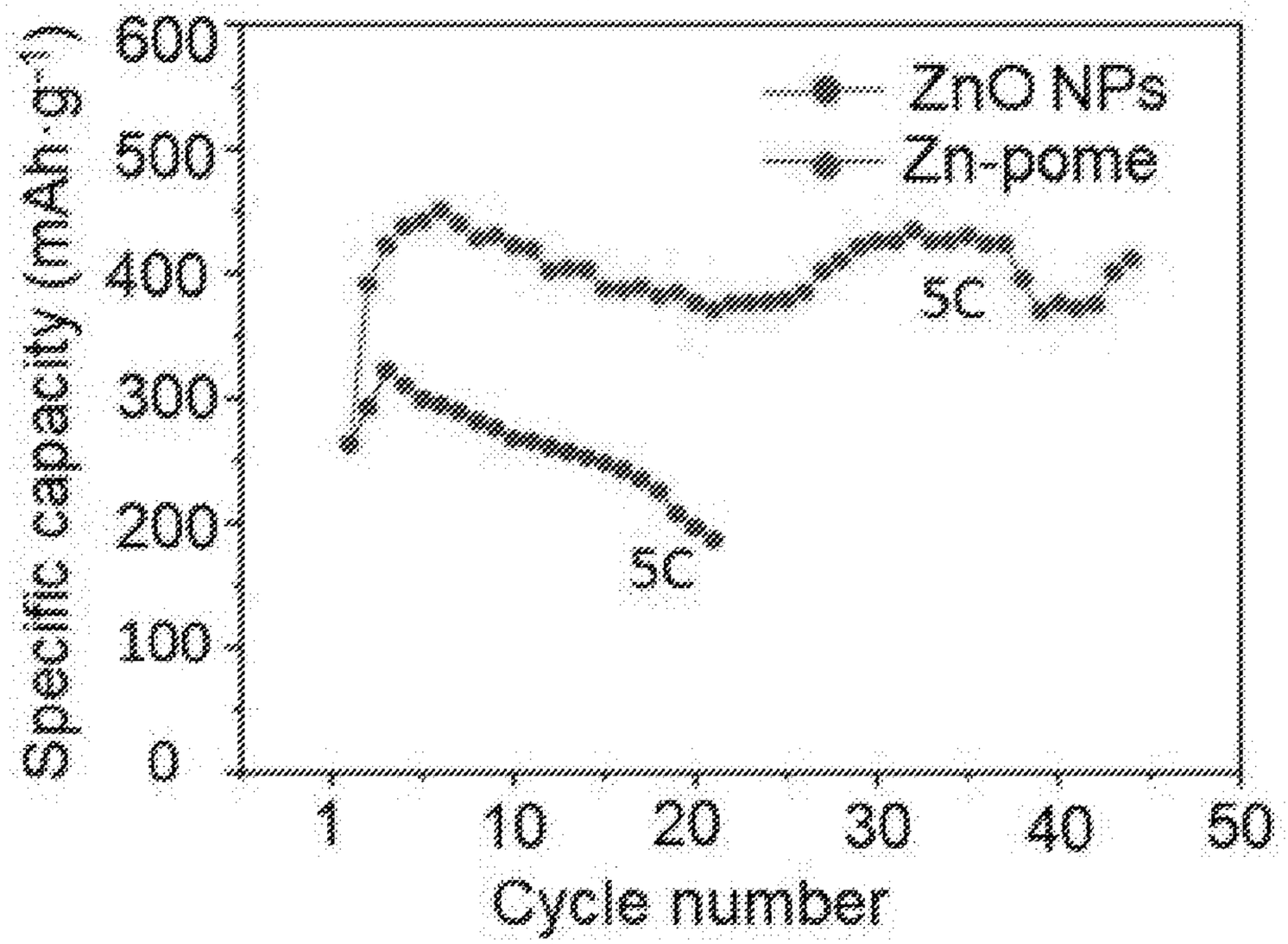


FIG. 109C

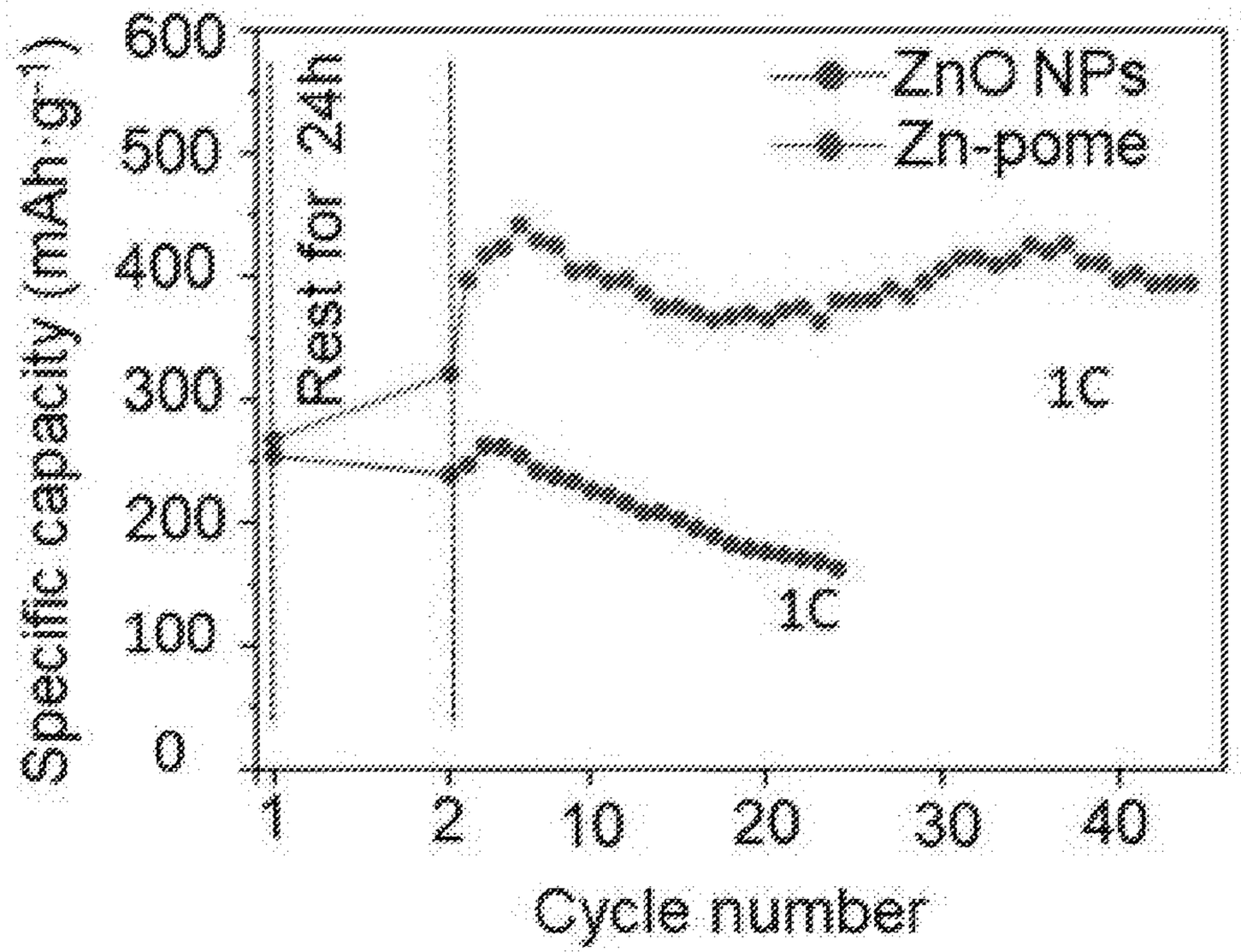


FIG. 109D

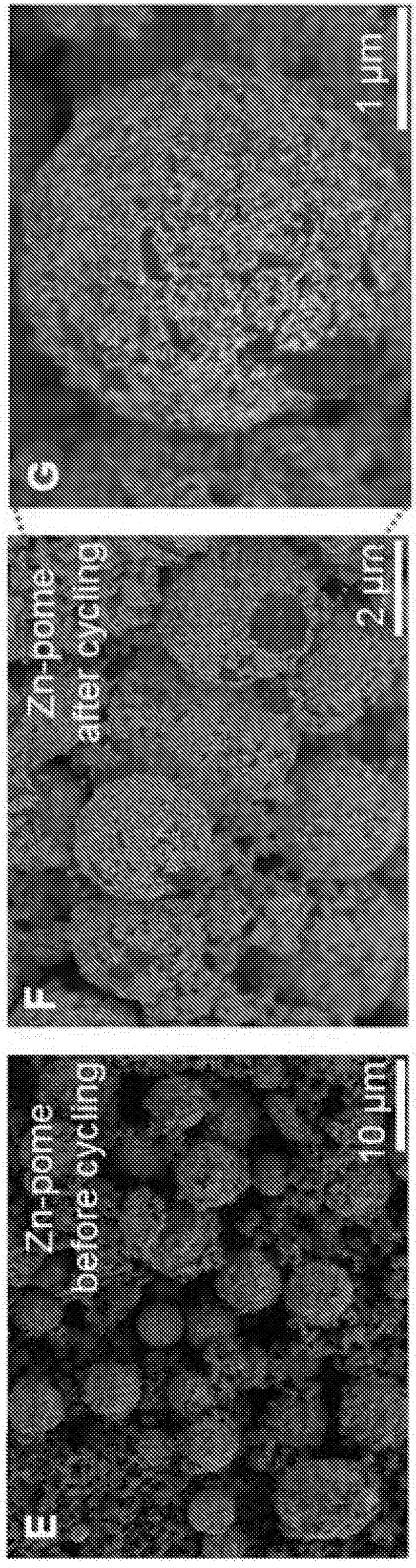


FIG. 109G

FIG. 109F

FIG. 109E

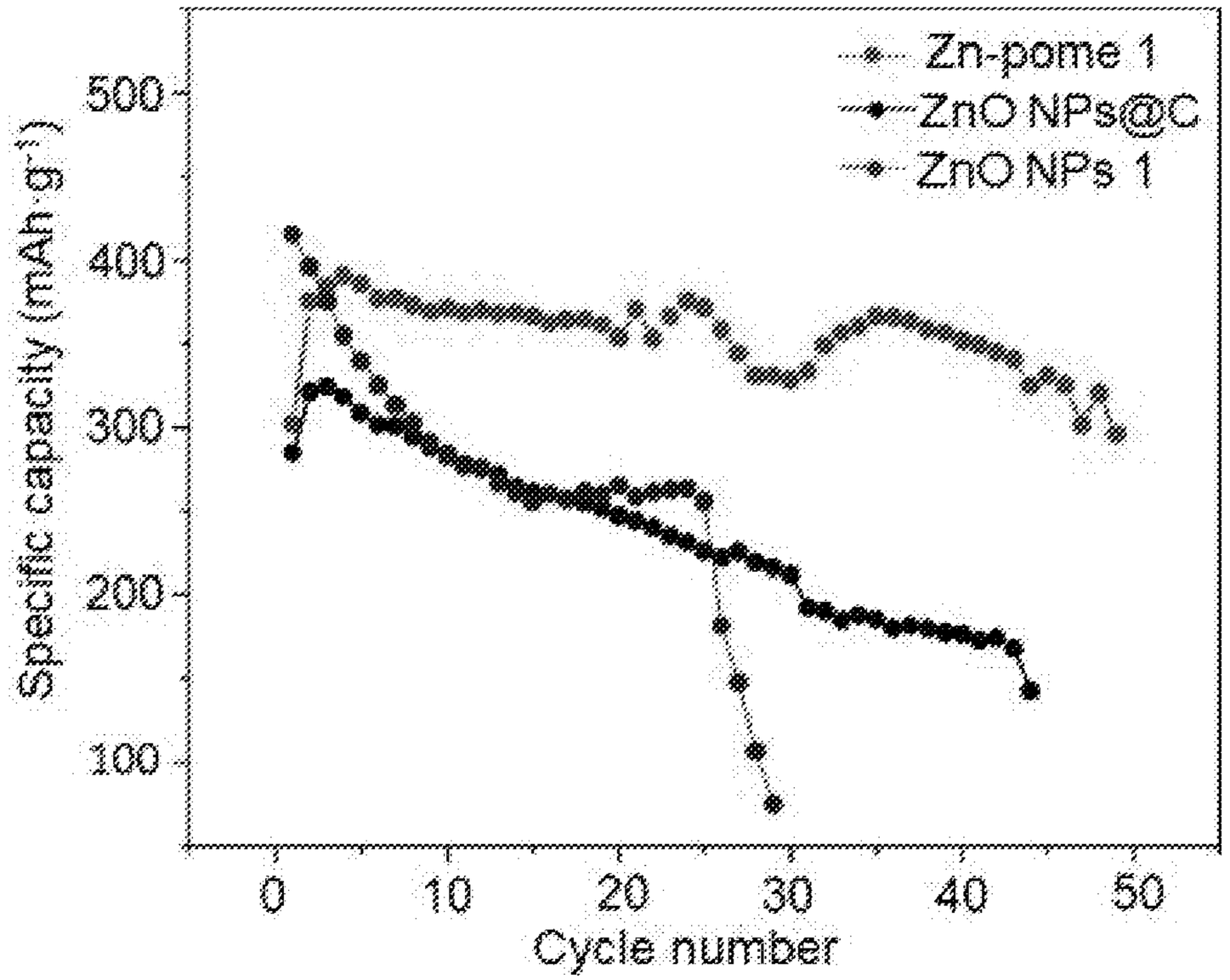


FIG. 110A

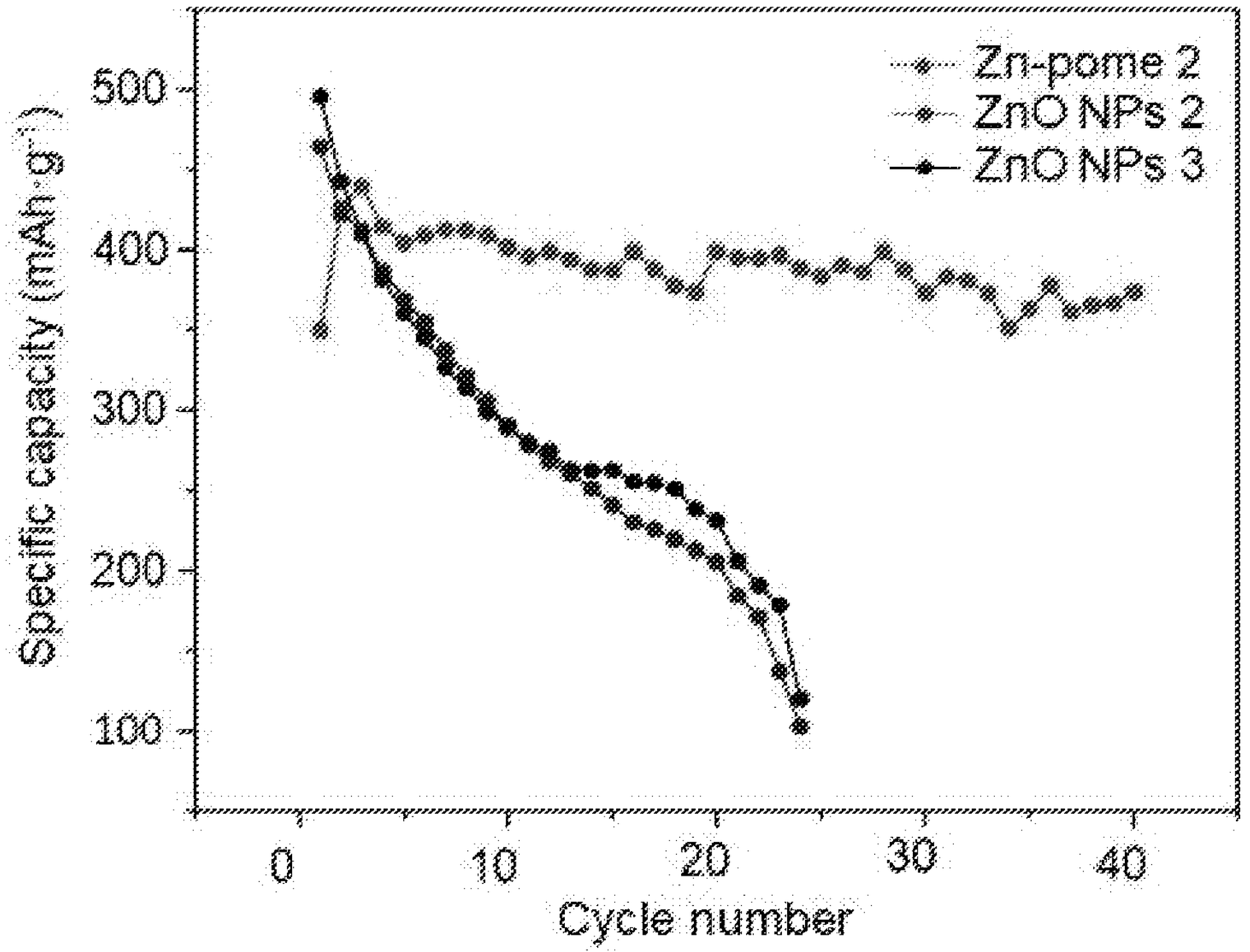


FIG. 110B

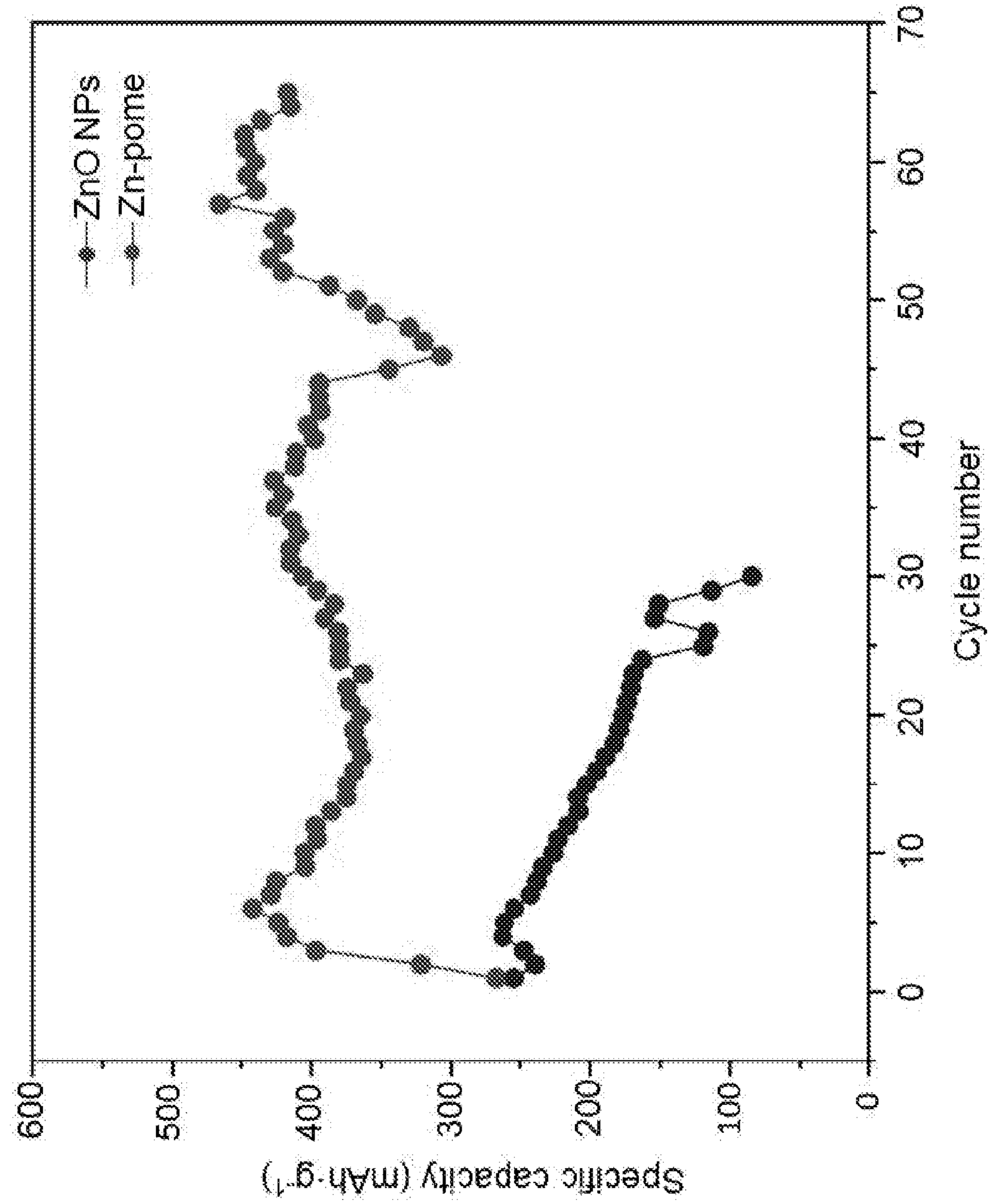

ZnO NPs
Zn-pome
Specific capacity (mAh·g⁻¹)
Cycle number
0
100
200
300
400
500
600
0
10
20
30
40
50
60
70

FIG. 111

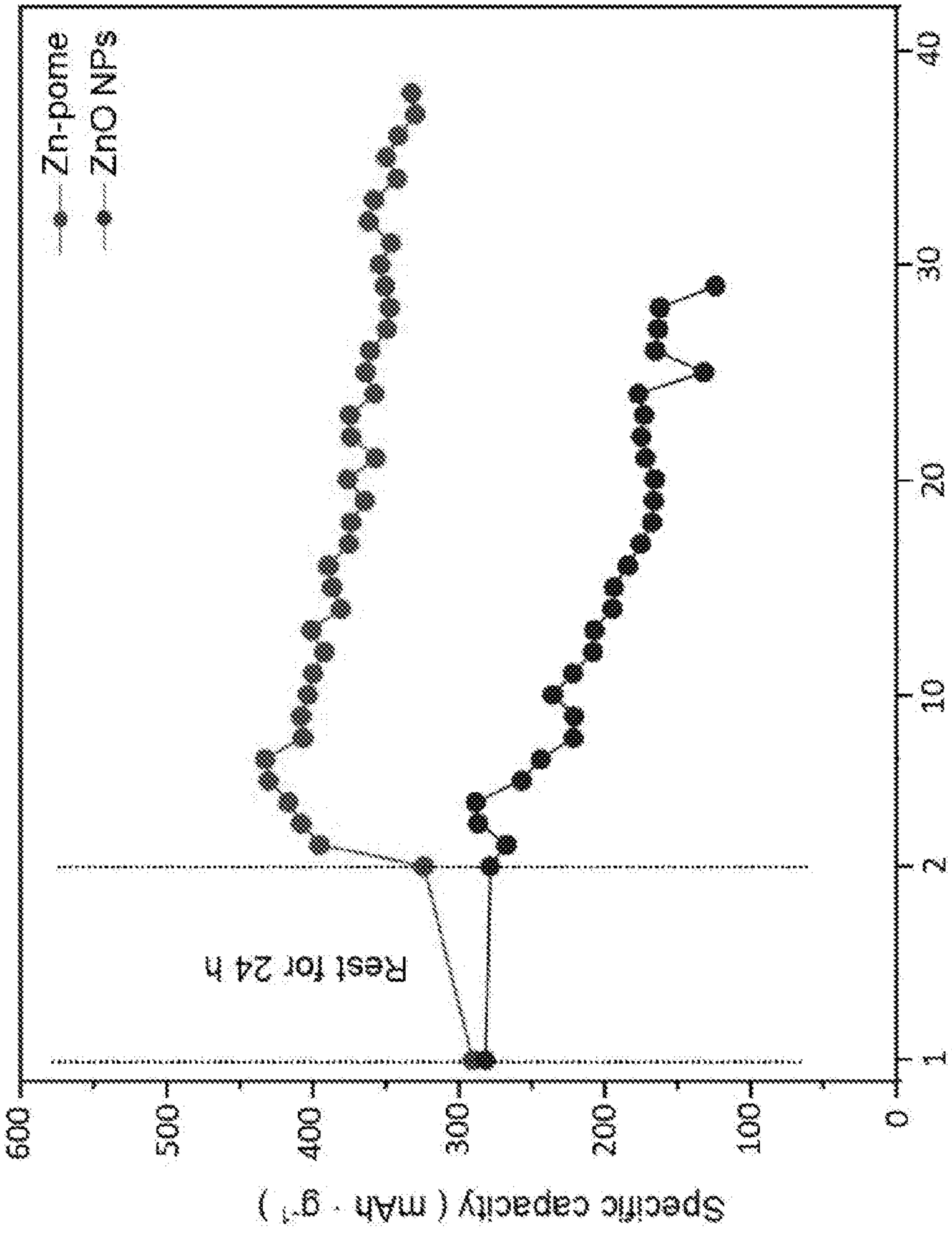

Zn-pome
ZnO NPs
Rest for 24 h
Specific capacity (mAh · g⁻¹)
Cycle number
600
500
400
300
200
100
0
1
2
10
20
30
40

FIG. 112

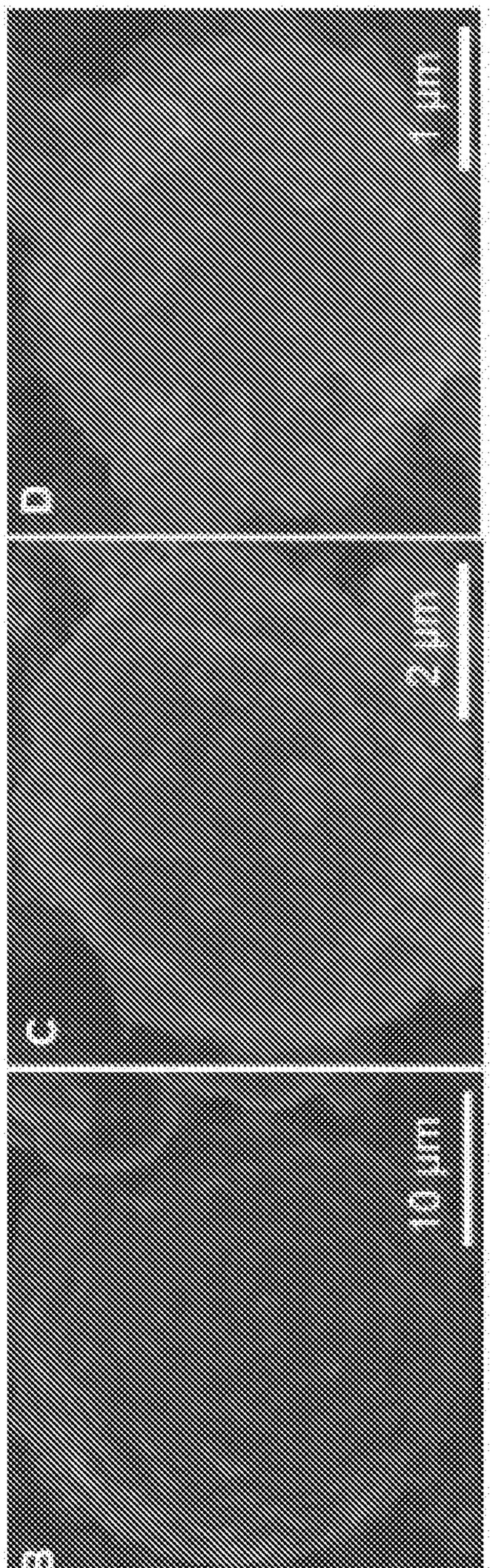


FIG. 113A

FIG. 113B

FIG. 113C

FIG. 113D

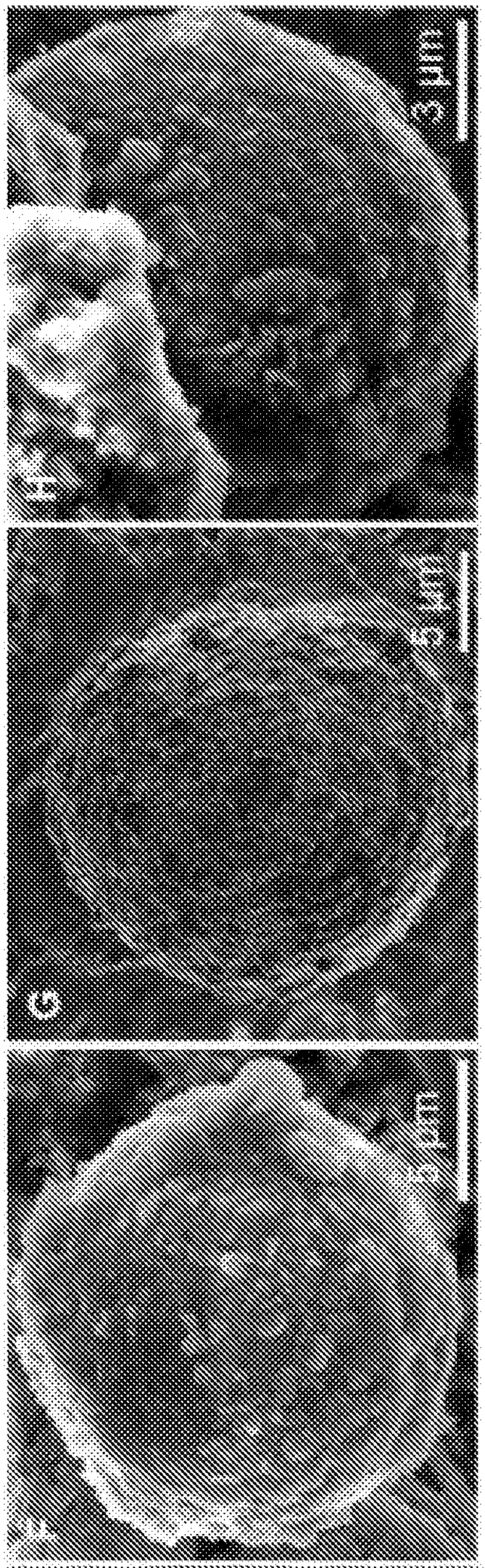


FIG. 113H

FIG. 113G

FIG. 113F

FIG. 113E

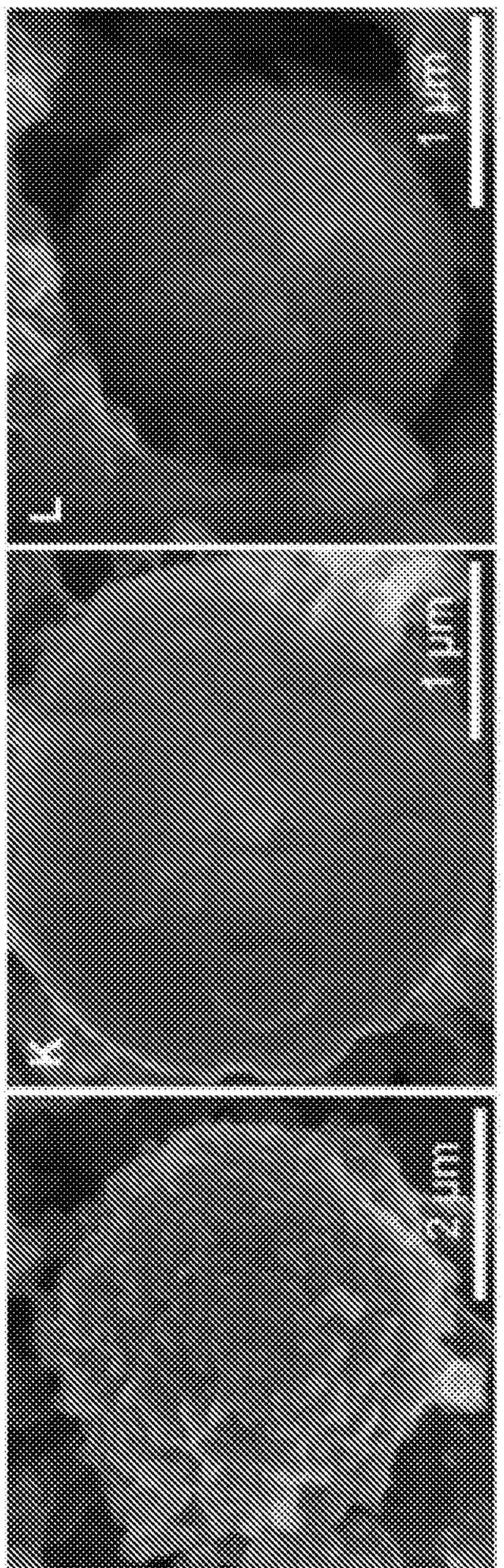


FIG. 113L

FIG. 113K

FIG. 113J

FIG. 113I

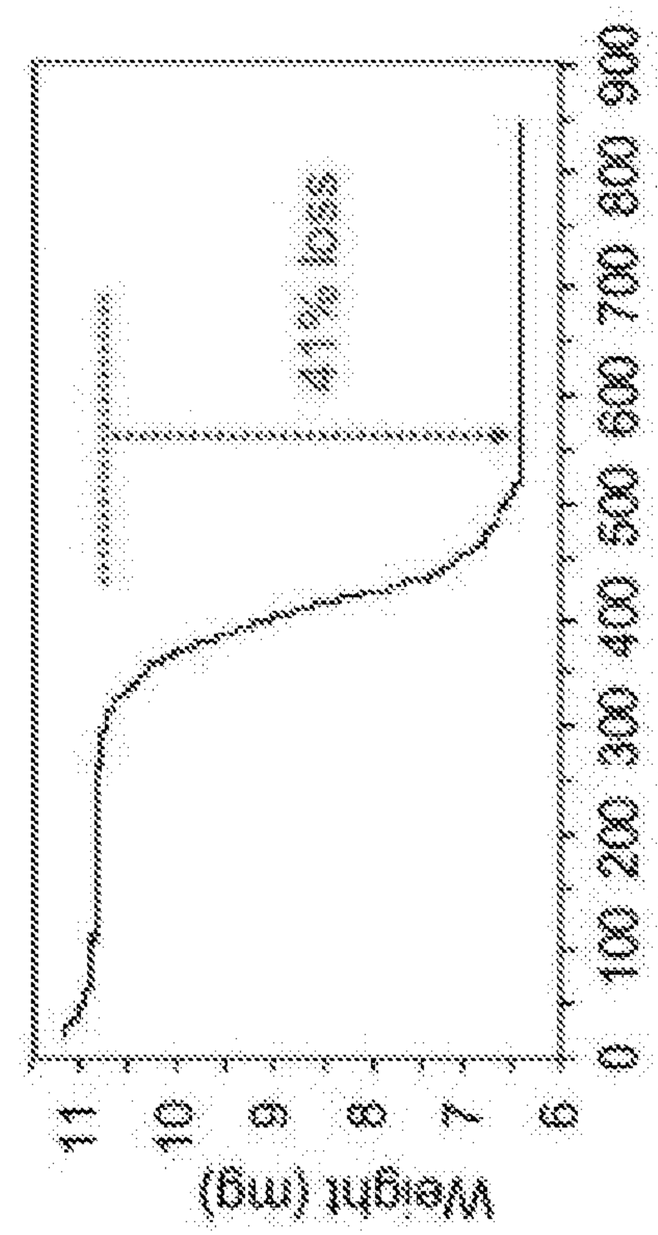


FIG. 114C

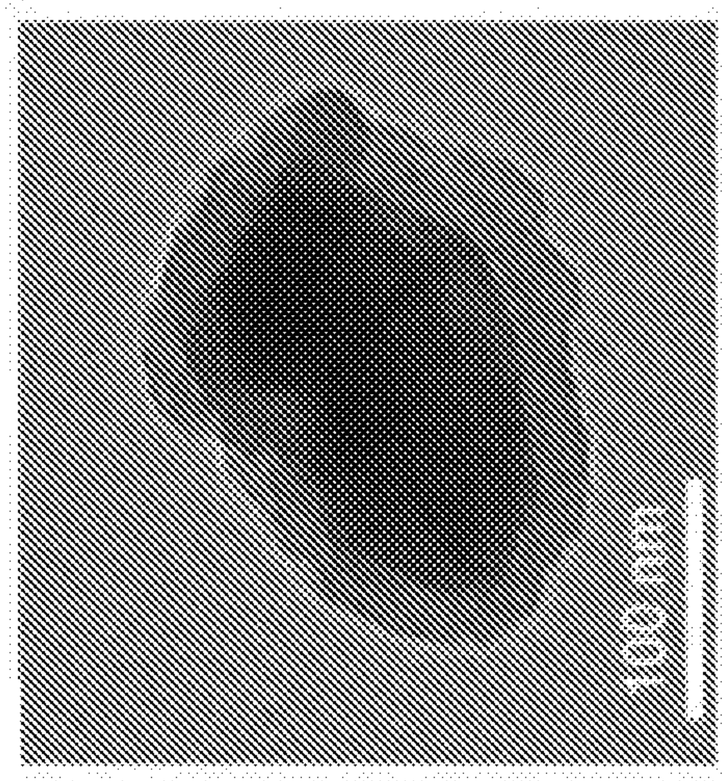


FIG. 114B

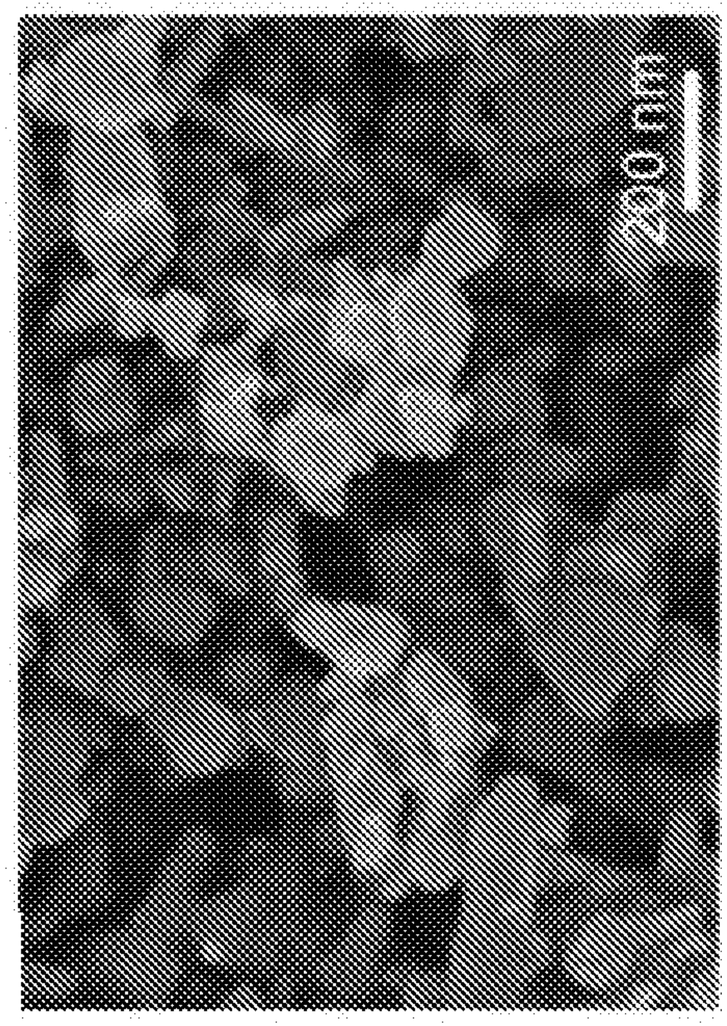


FIG. 114A

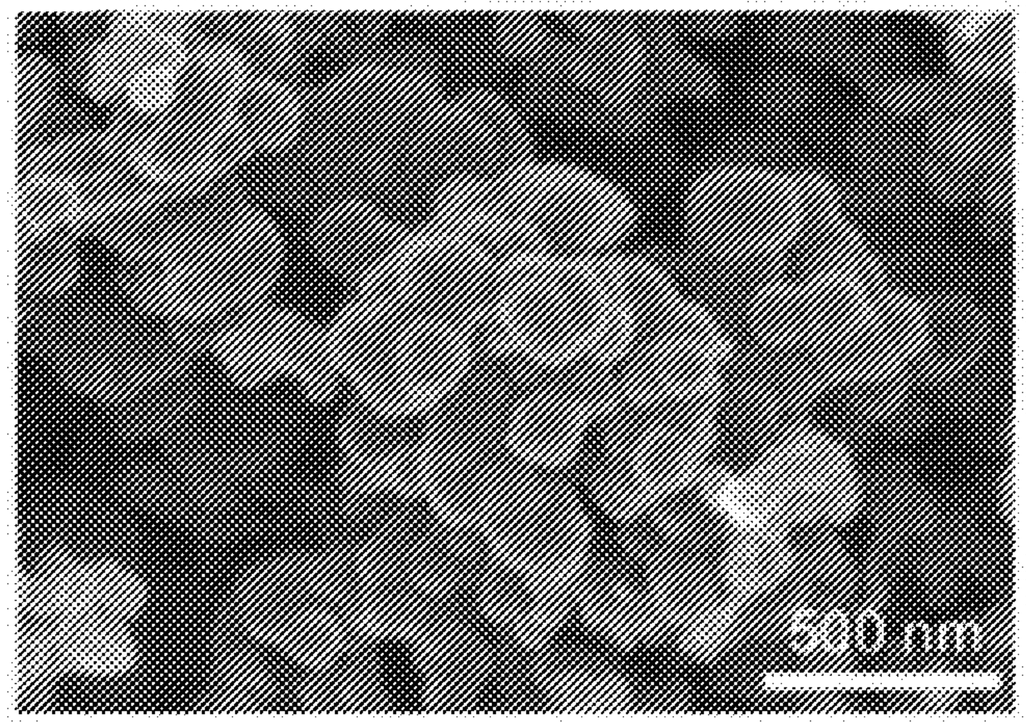


FIG. 114D

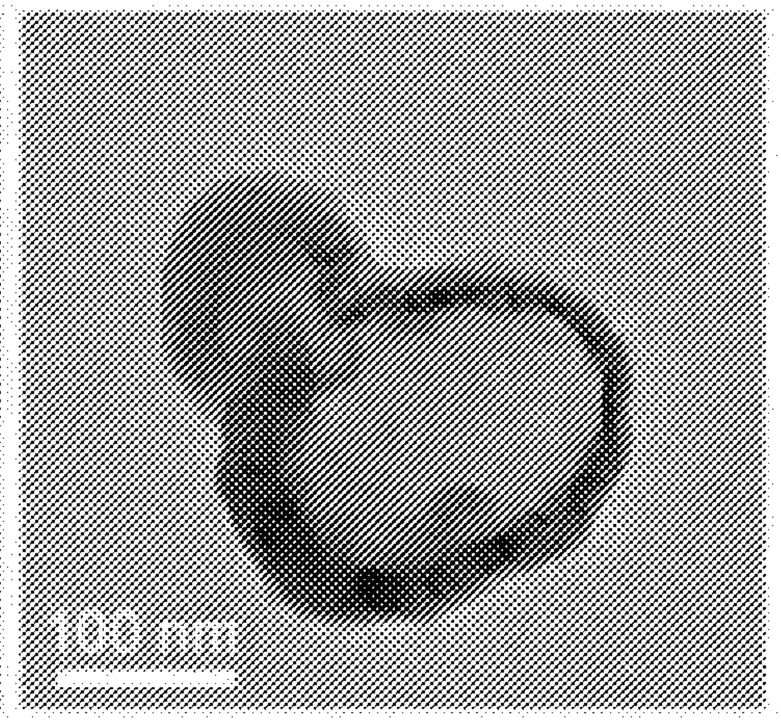


FIG. 114E

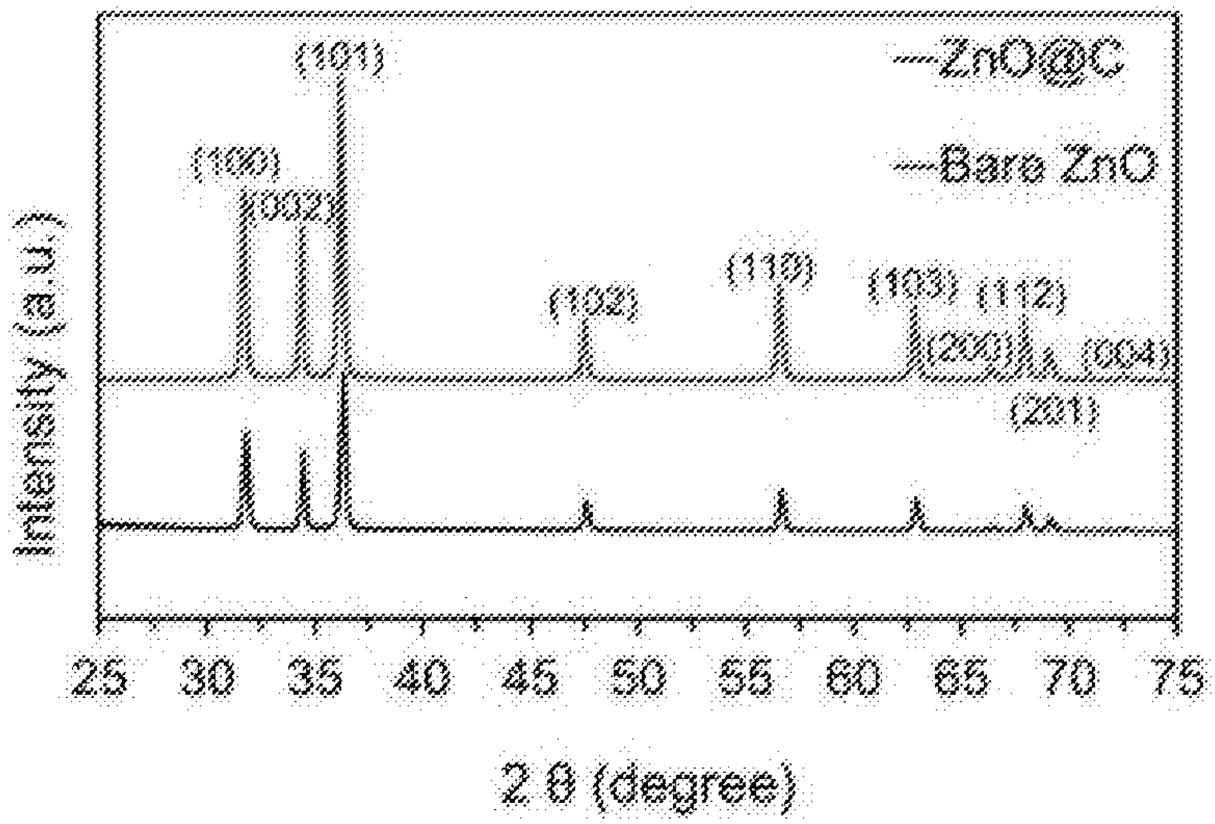


FIG. 114F

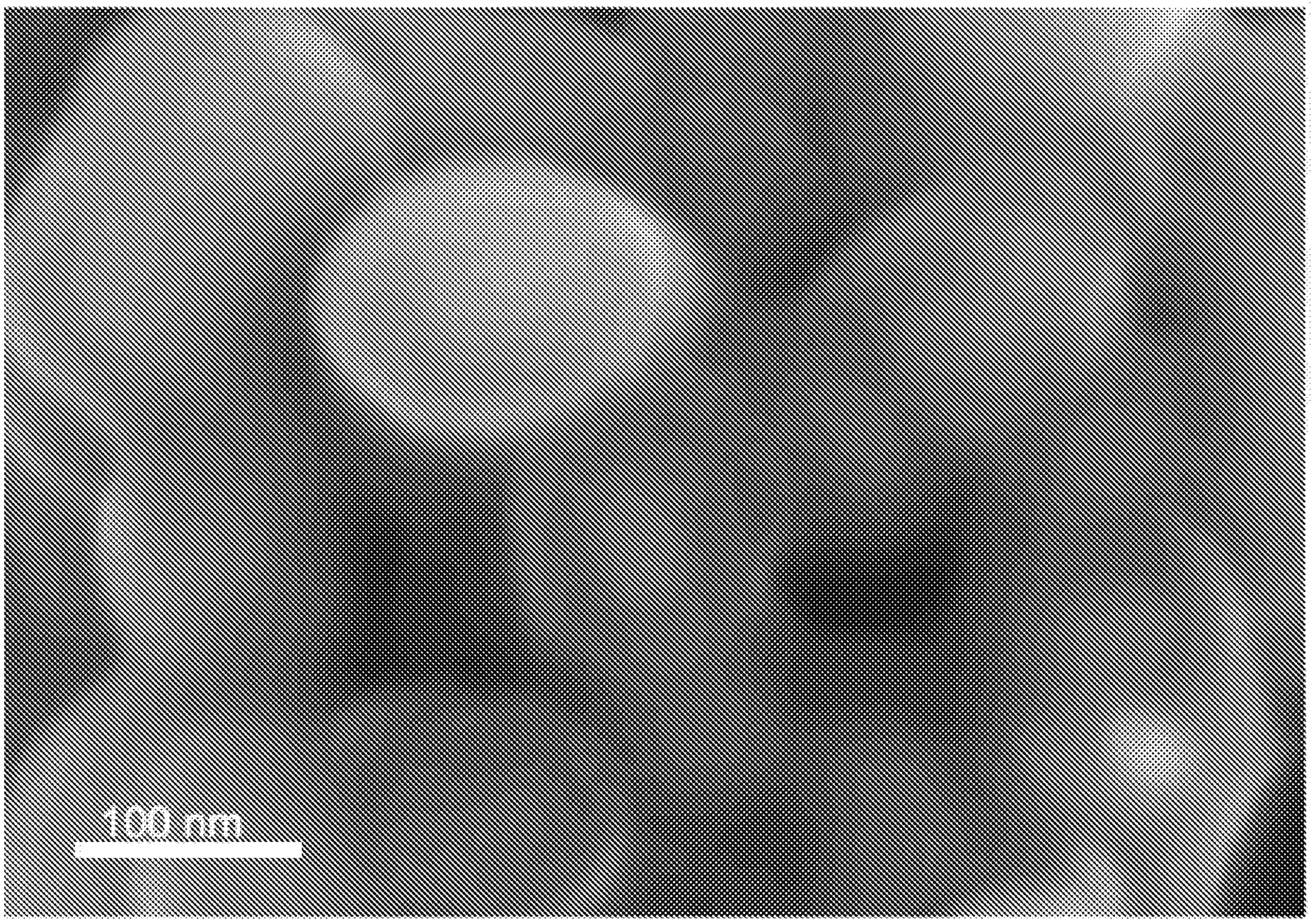


FIG. 115

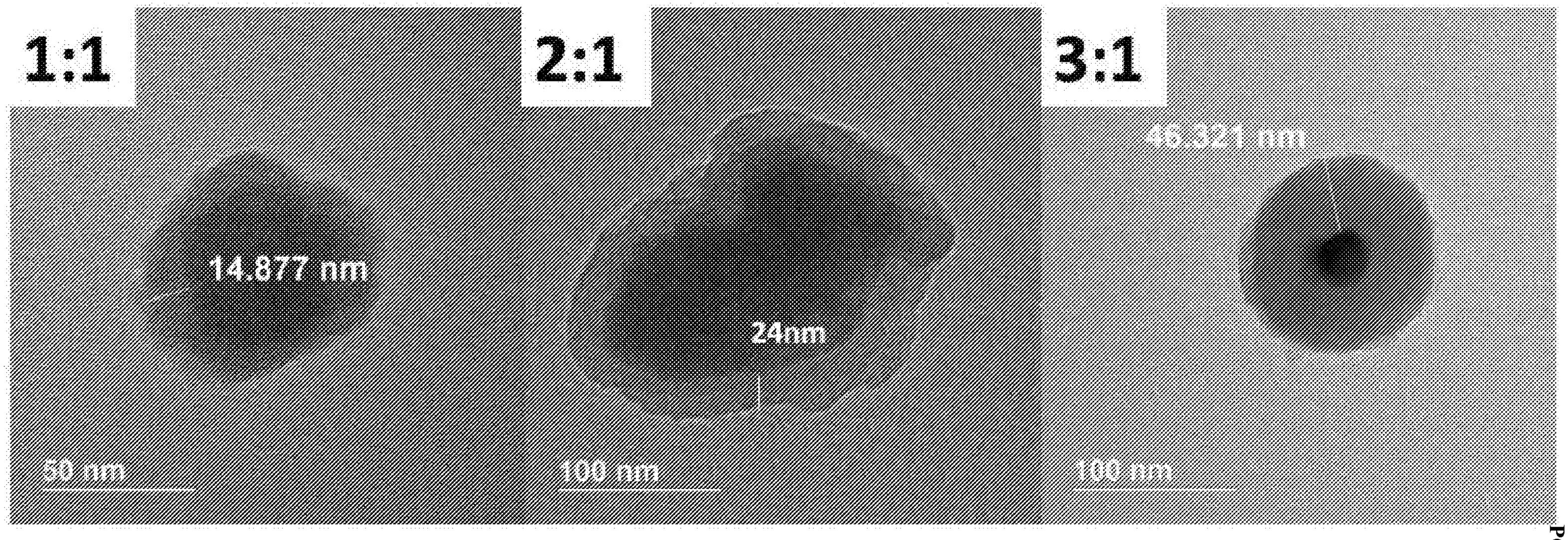


FIG. 116

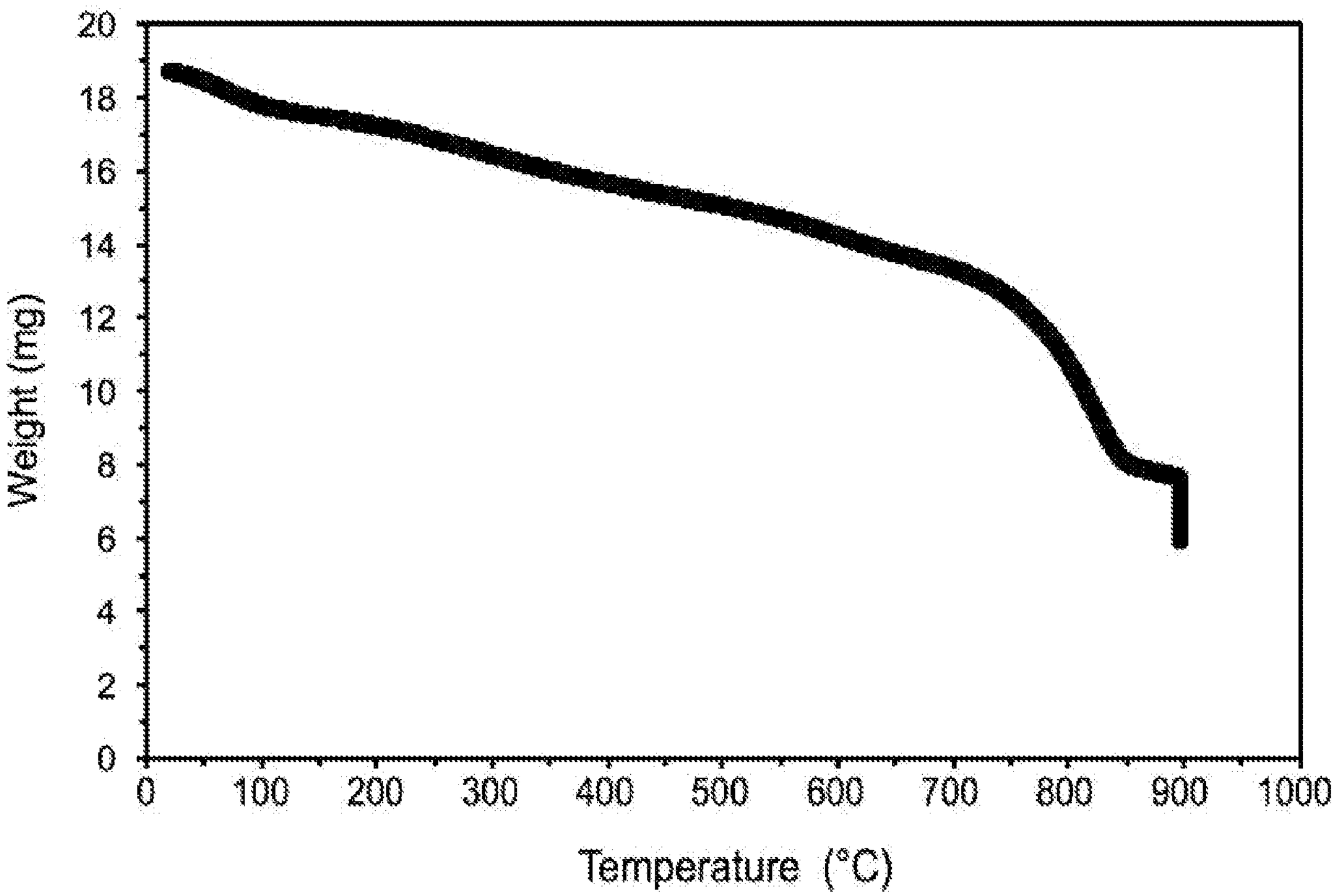

Weight (mg)
20
18
16
14
12
10
8
6
4
2
0
0
100
200
300
400
500
600
700
800
900
1000
Temperature (°C)

FIG. 117

FIG. 118A

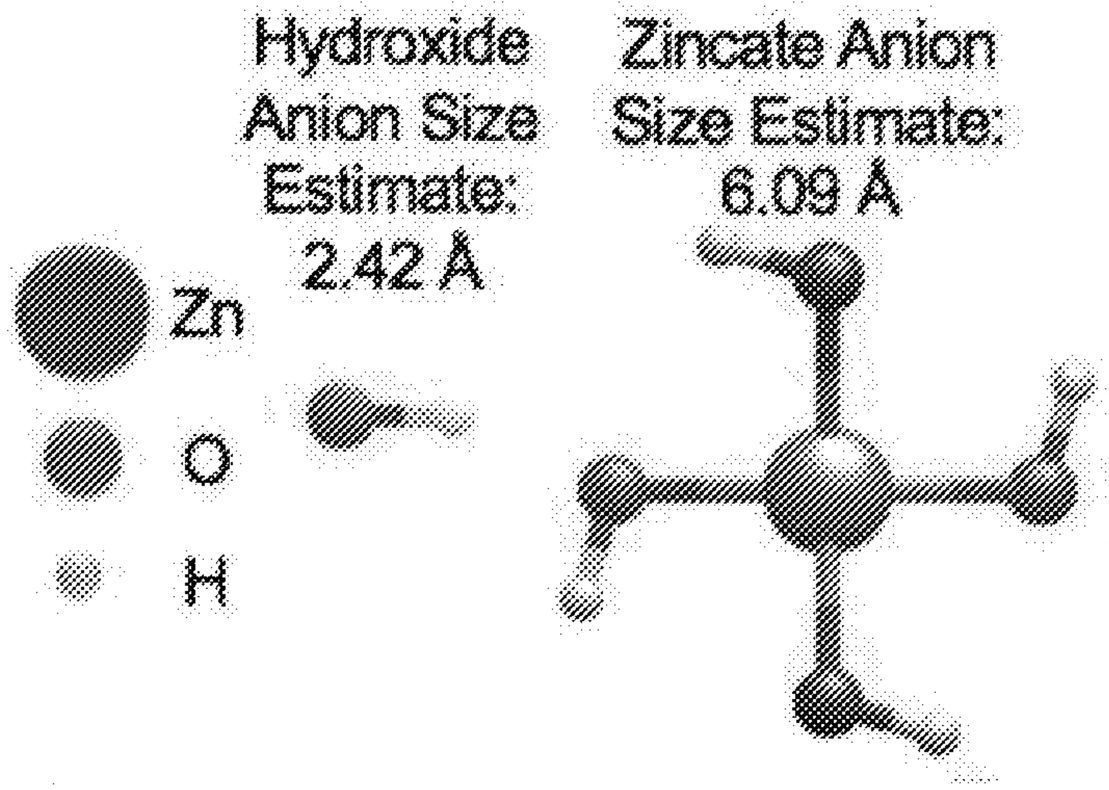


FIG. 118B

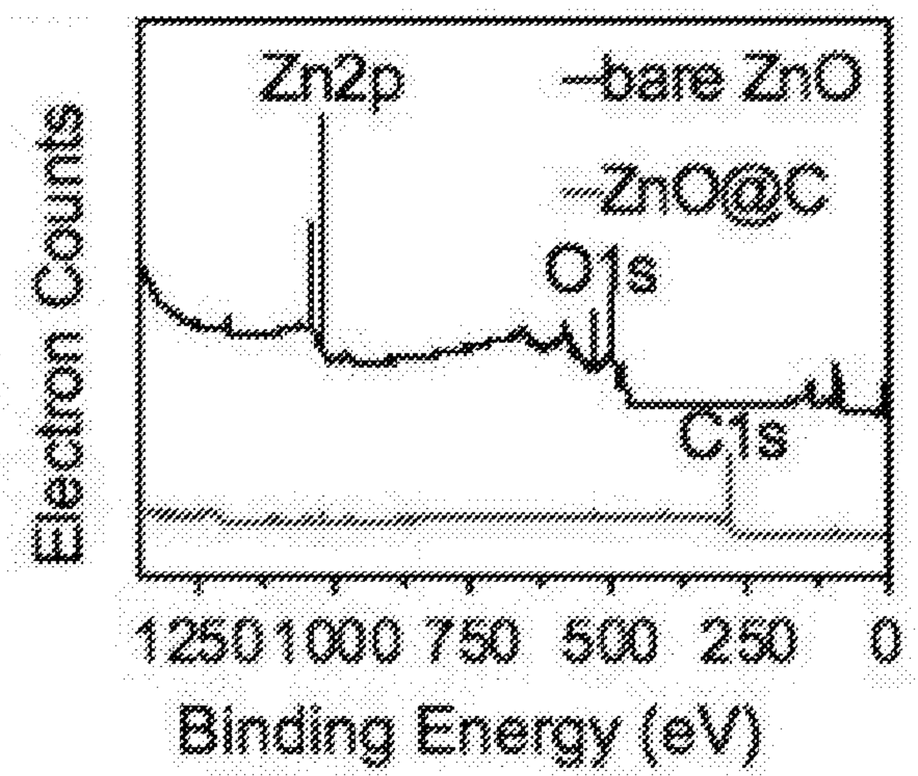
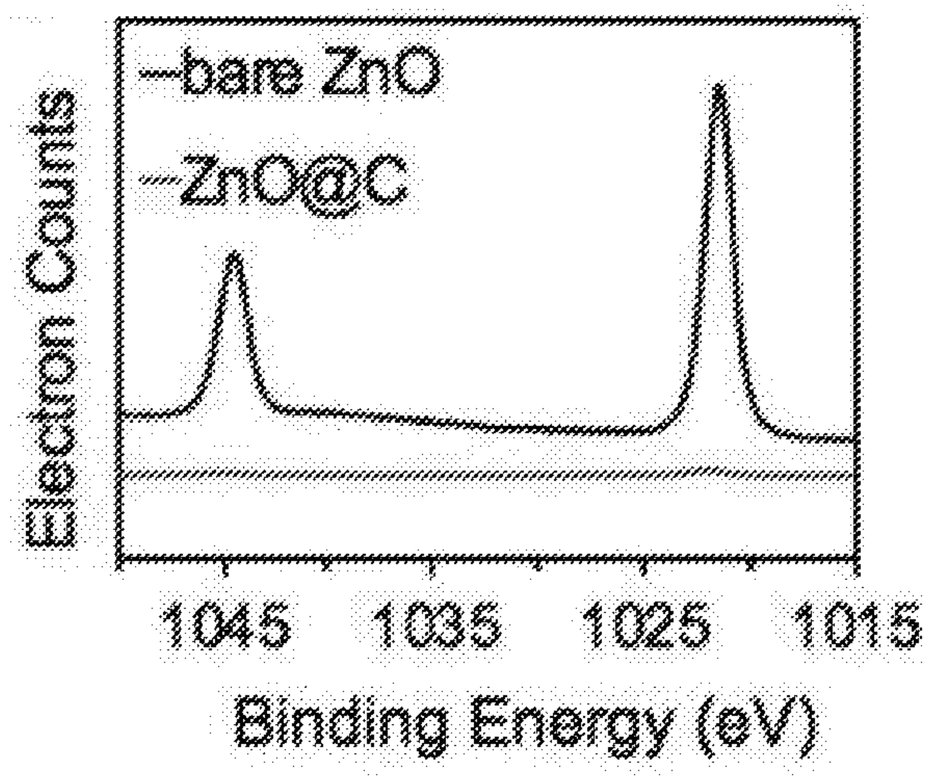


FIG. 118C



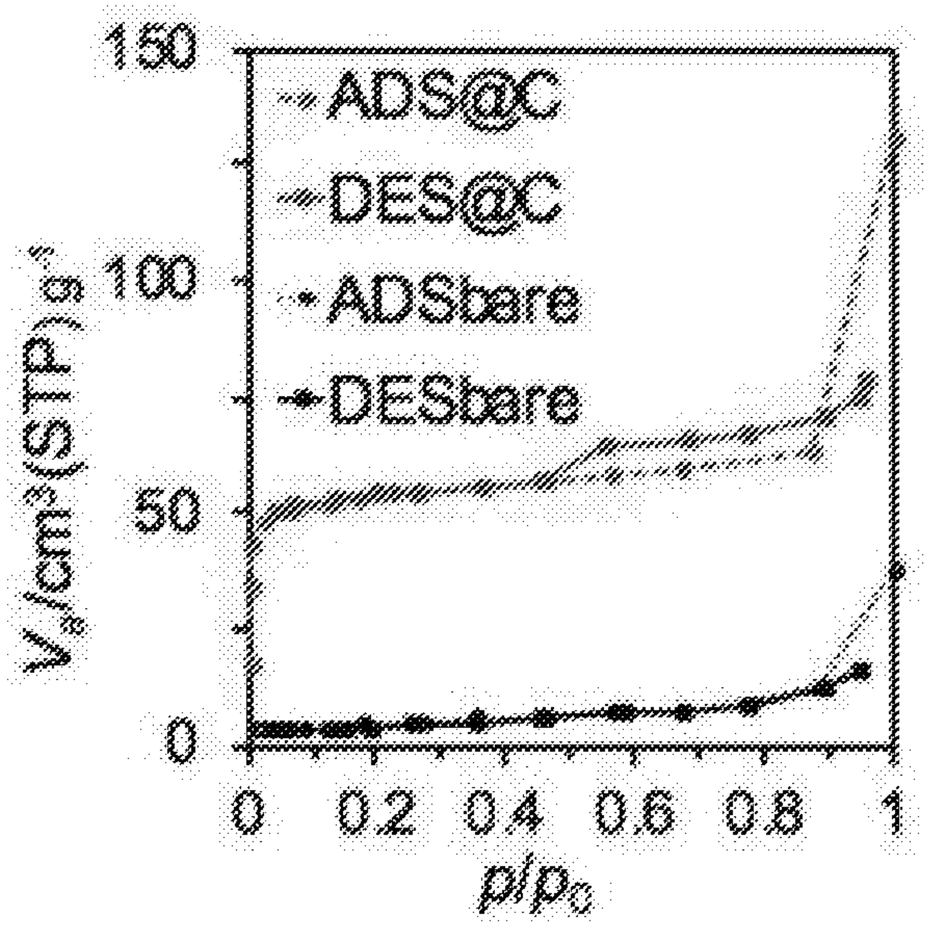


FIG. 118D

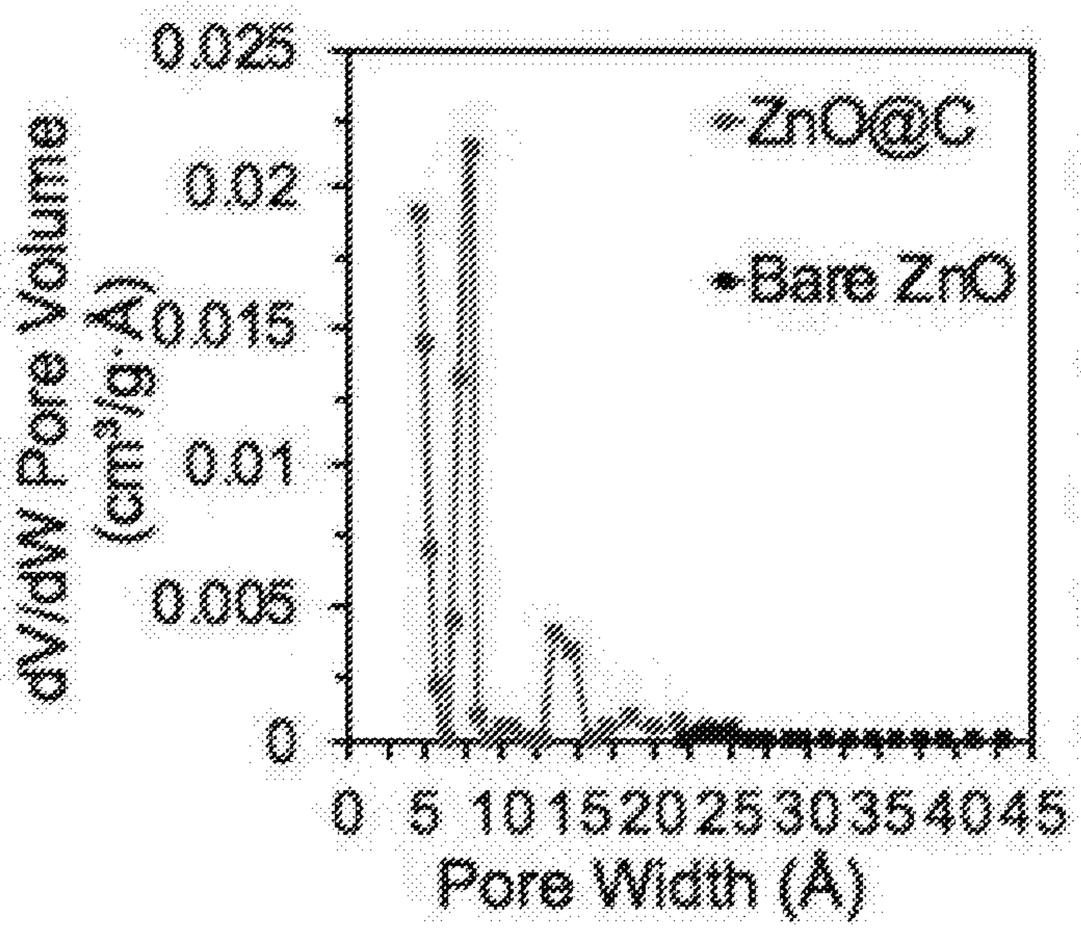


FIG. 118E

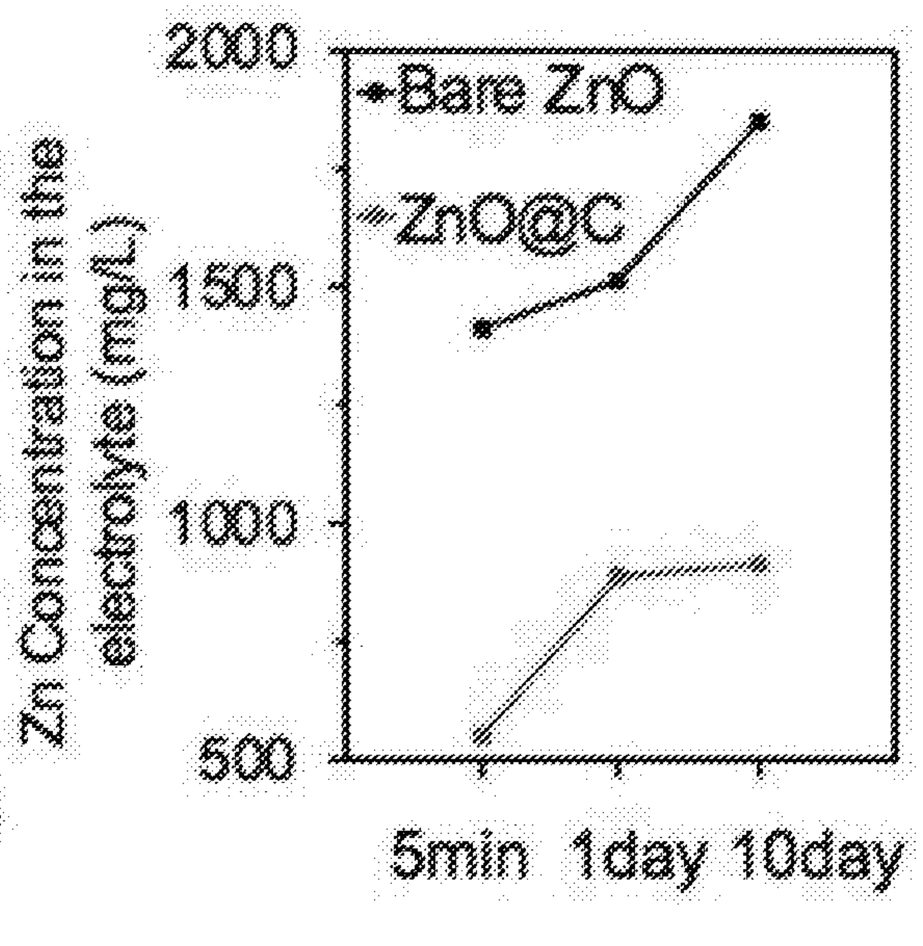


FIG. 118F

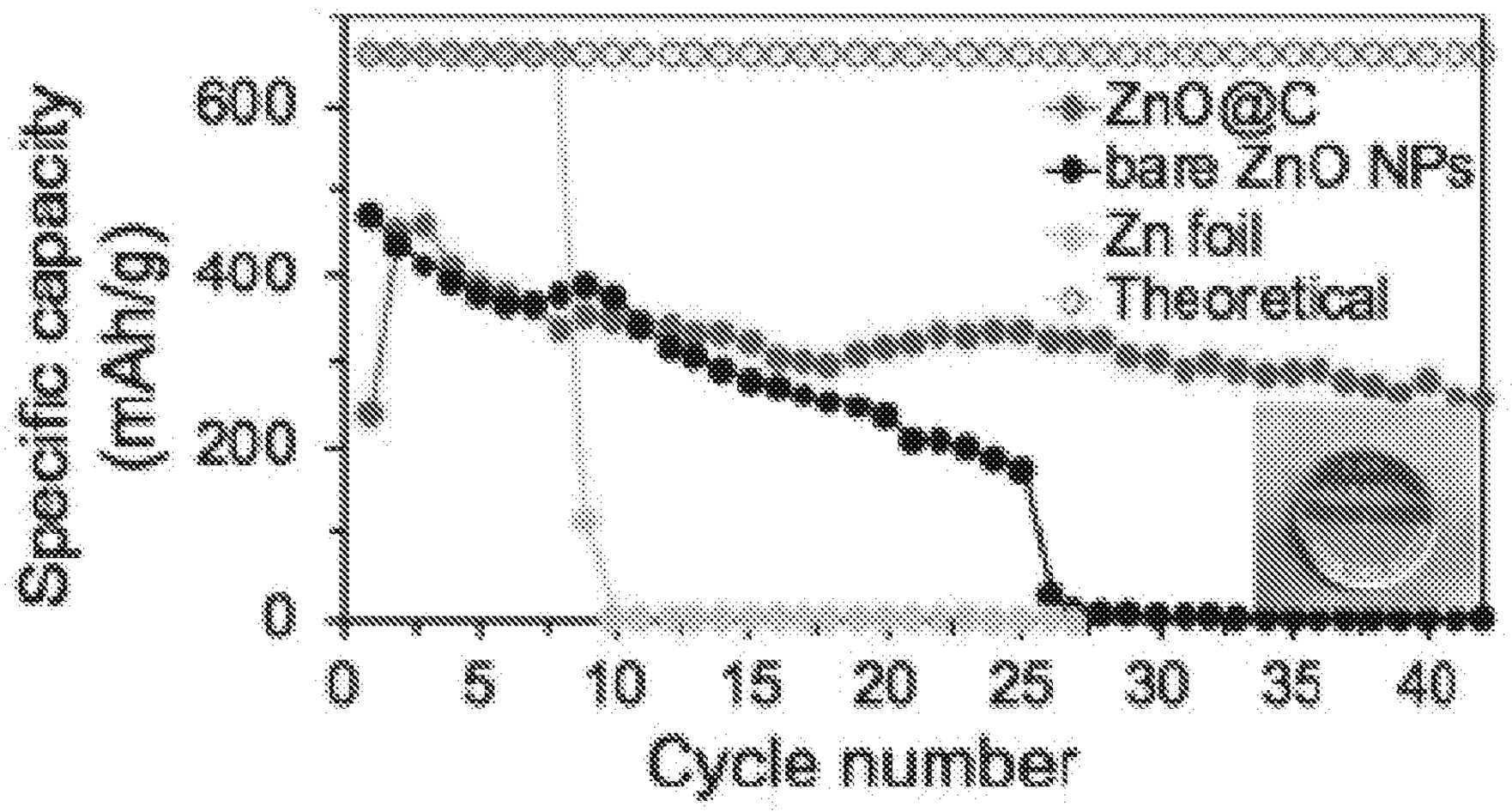

ZnO@C
bare ZnO NPs
Zn foil
Theoretical
Specific capacity (mAh/g)
600
400
200
0
0
5
10
15
20
25
30
35
40
Cycle number

FIG. 119

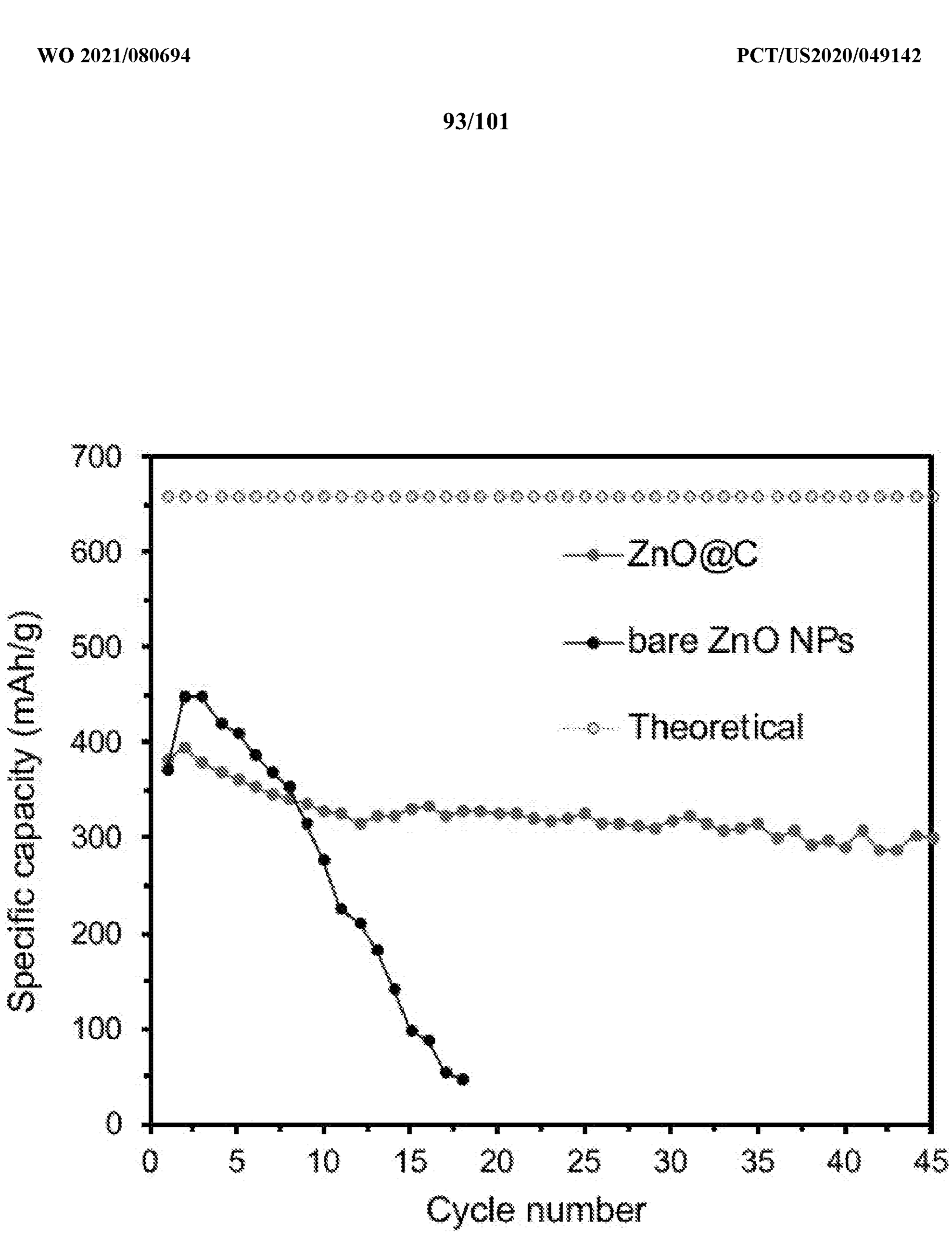

700
600
500
400
300
200
100
0
Specific capacity (mAh/g)
0
5
10
15
20
25
30
35
40
45
Cycle number
ZnO@C
bare ZnO NPs
Theoretical

FIG. 120

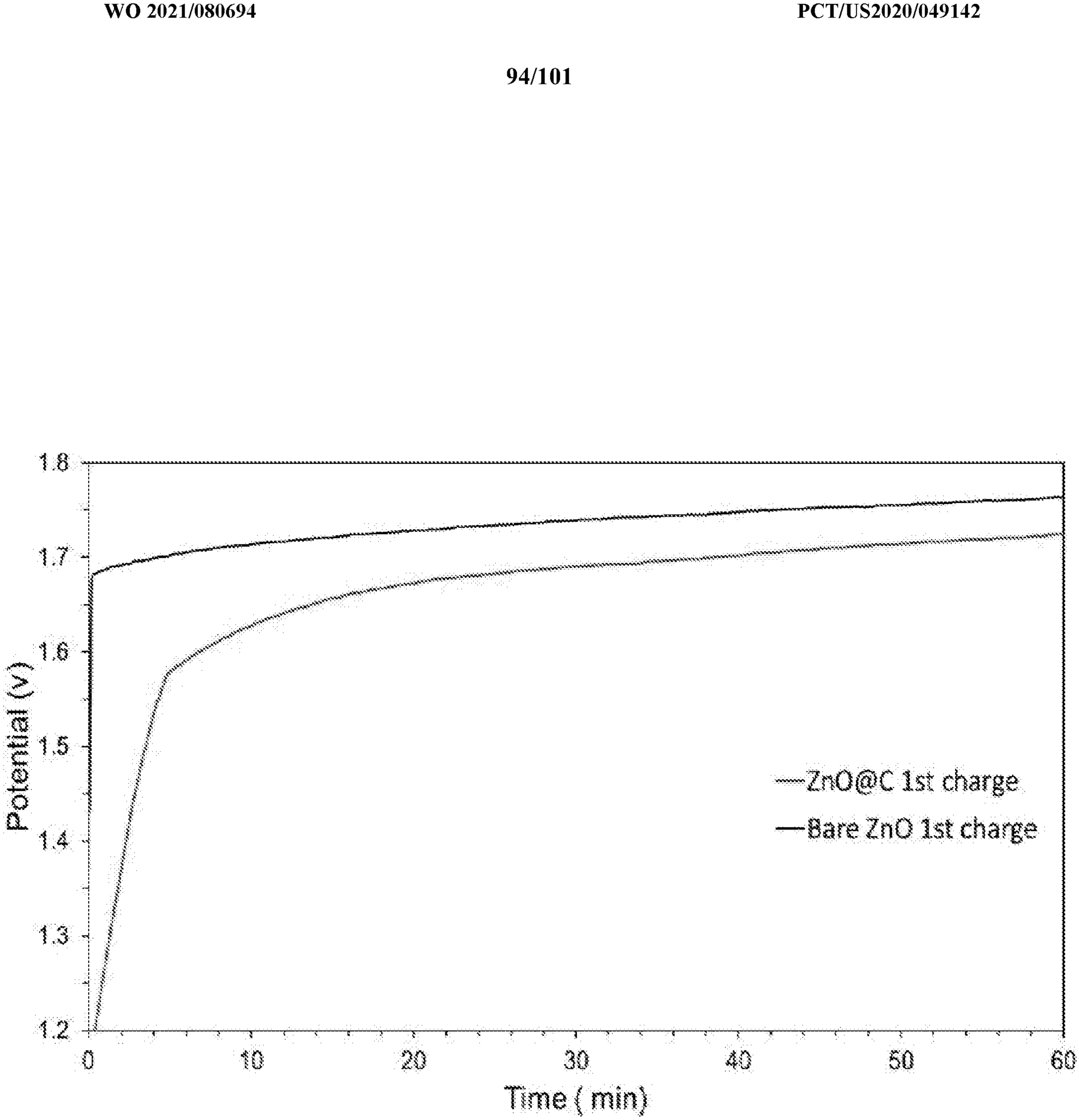

1.8
1.7
1.6
1.5
1.4
1.3
1.2
Potential (V)
0
10
20
30
40
50
60
Time (min)
—ZnO@C 1st charge
—Bare ZnO 1st charge

FIG. 121

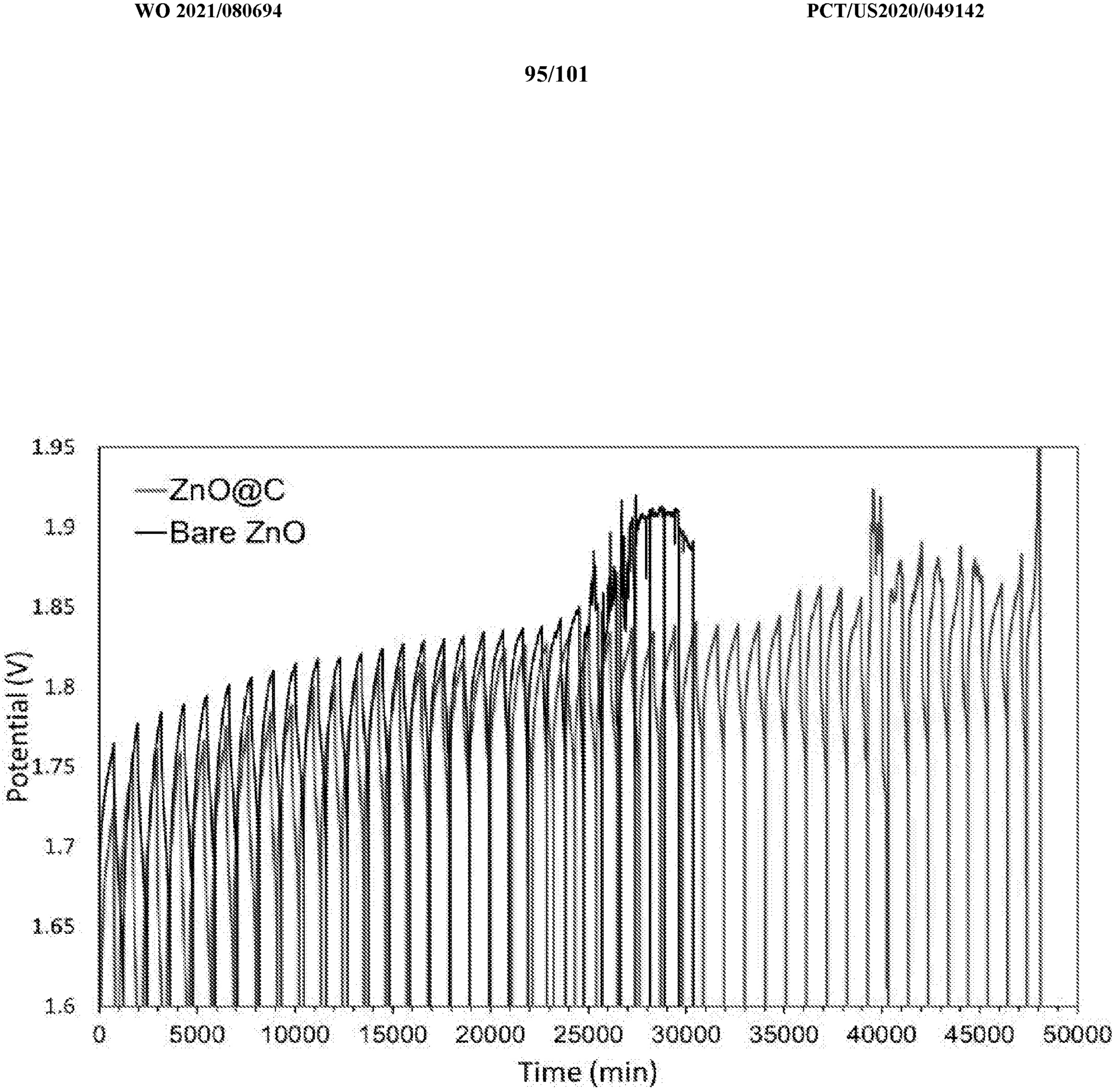

ZnO@C
Bare ZnO
Potential (V)
1.95
1.9
1.85
1.8
1.75
1.7
1.65
1.6
0
5000
10000
15000
20000
25000
30000
35000
40000
45000
50000
Time (min)

FIG. 122

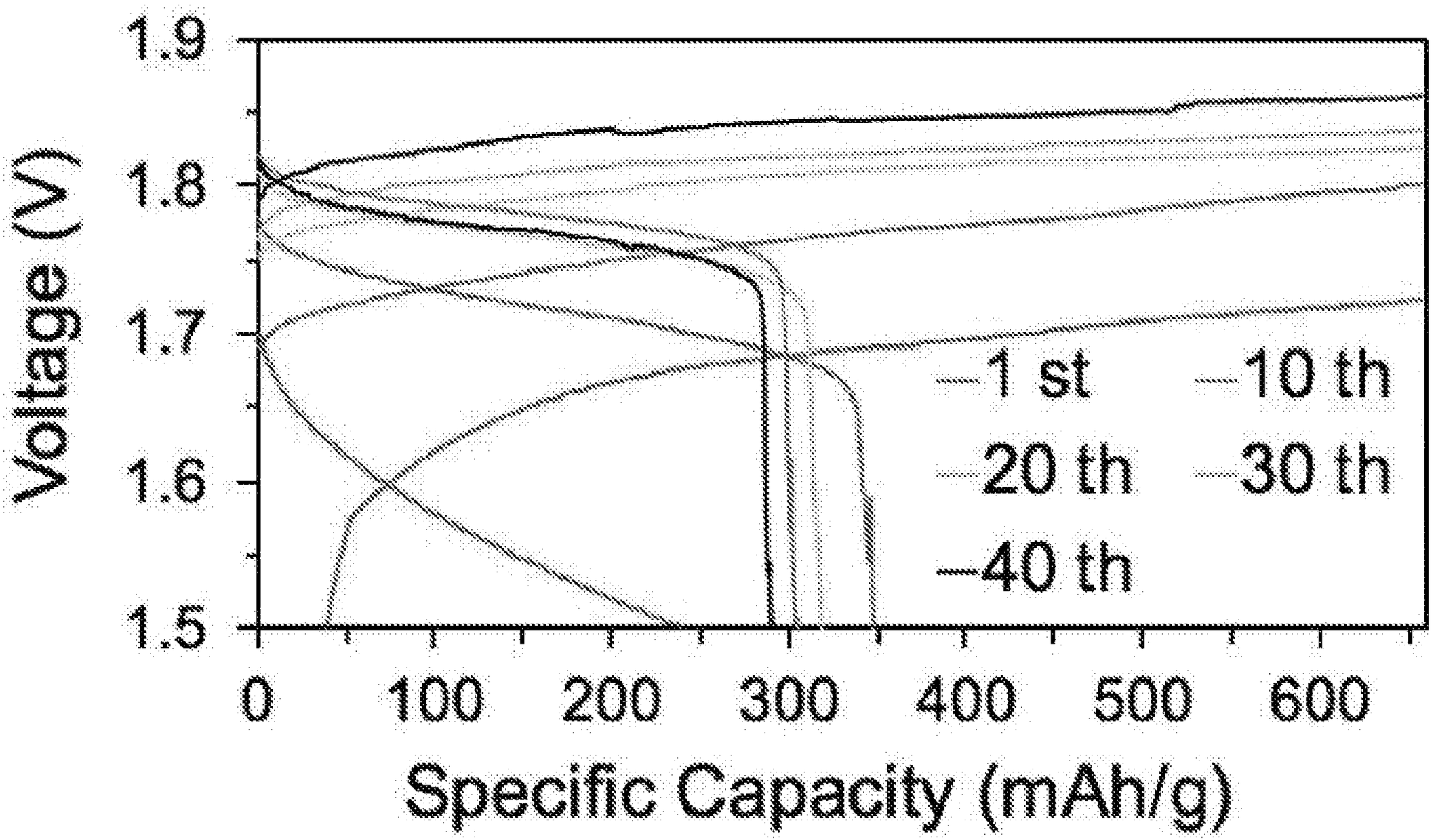

1.9
1.8
1.7
1.6
1.5
Voltage (V)
0
100
200
300
400
500
600
Specific Capacity (mAh/g)
1 st
10 th
20 th
30 th
40 th

FIG. 123

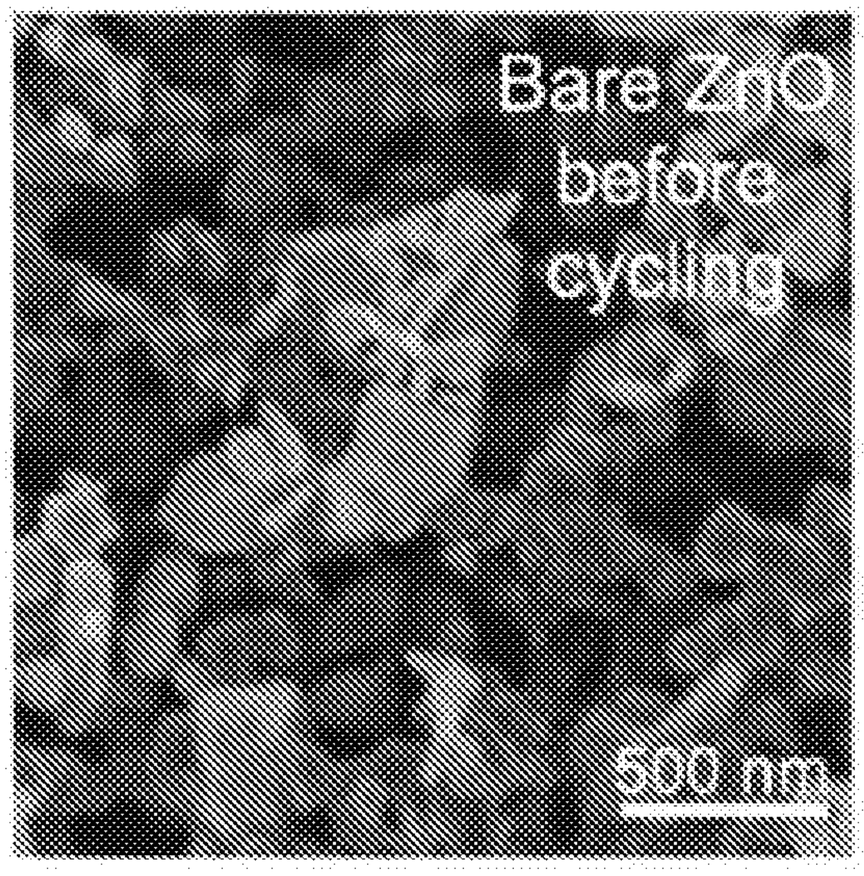


FIG. 124A

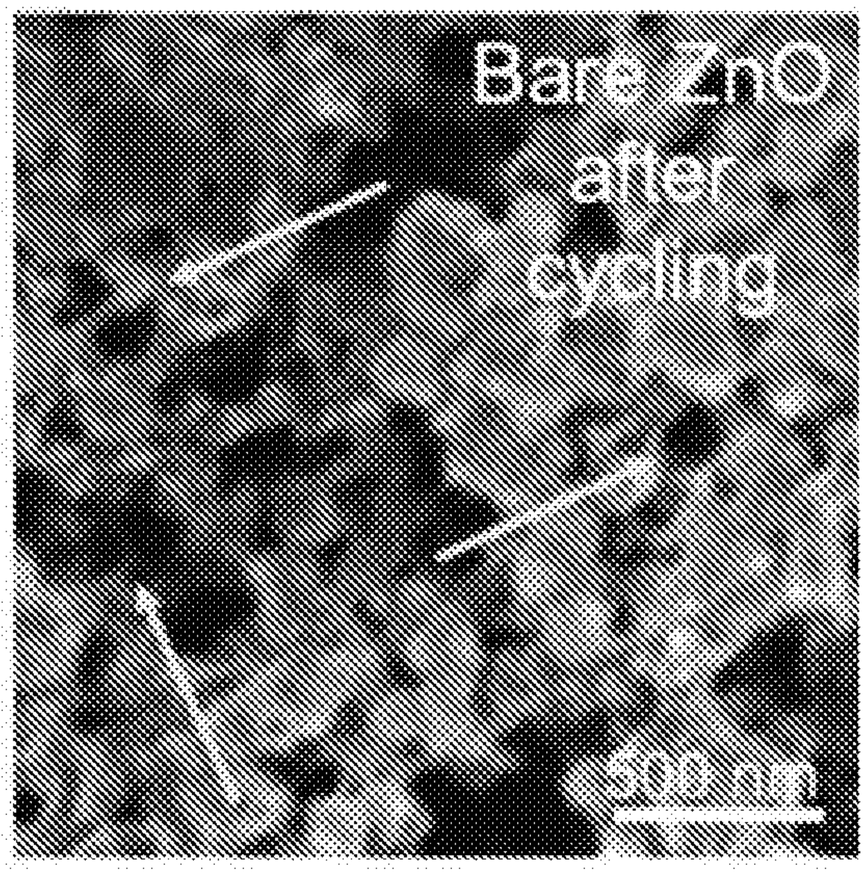


FIG. 124B

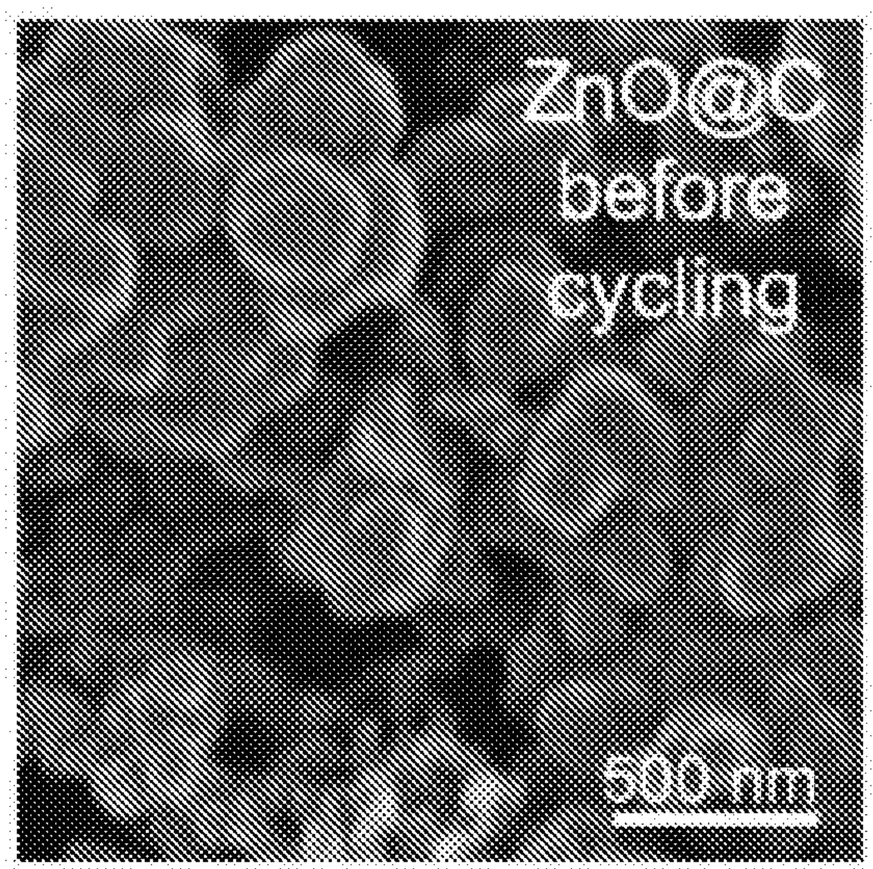


FIG. 124C

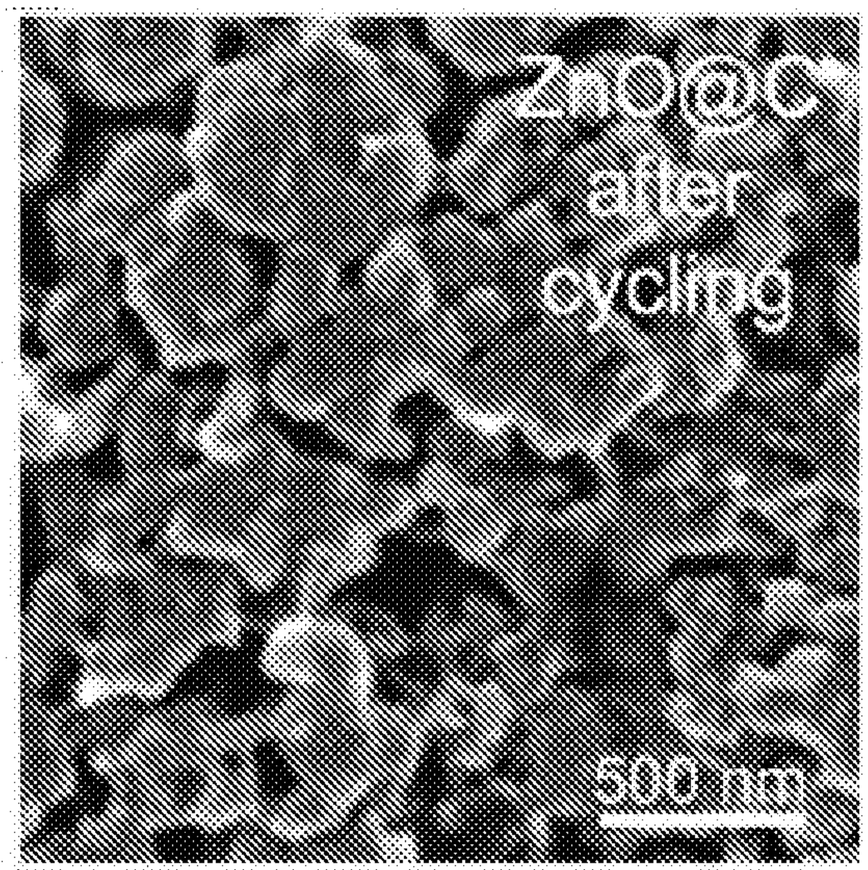


FIG. 124D

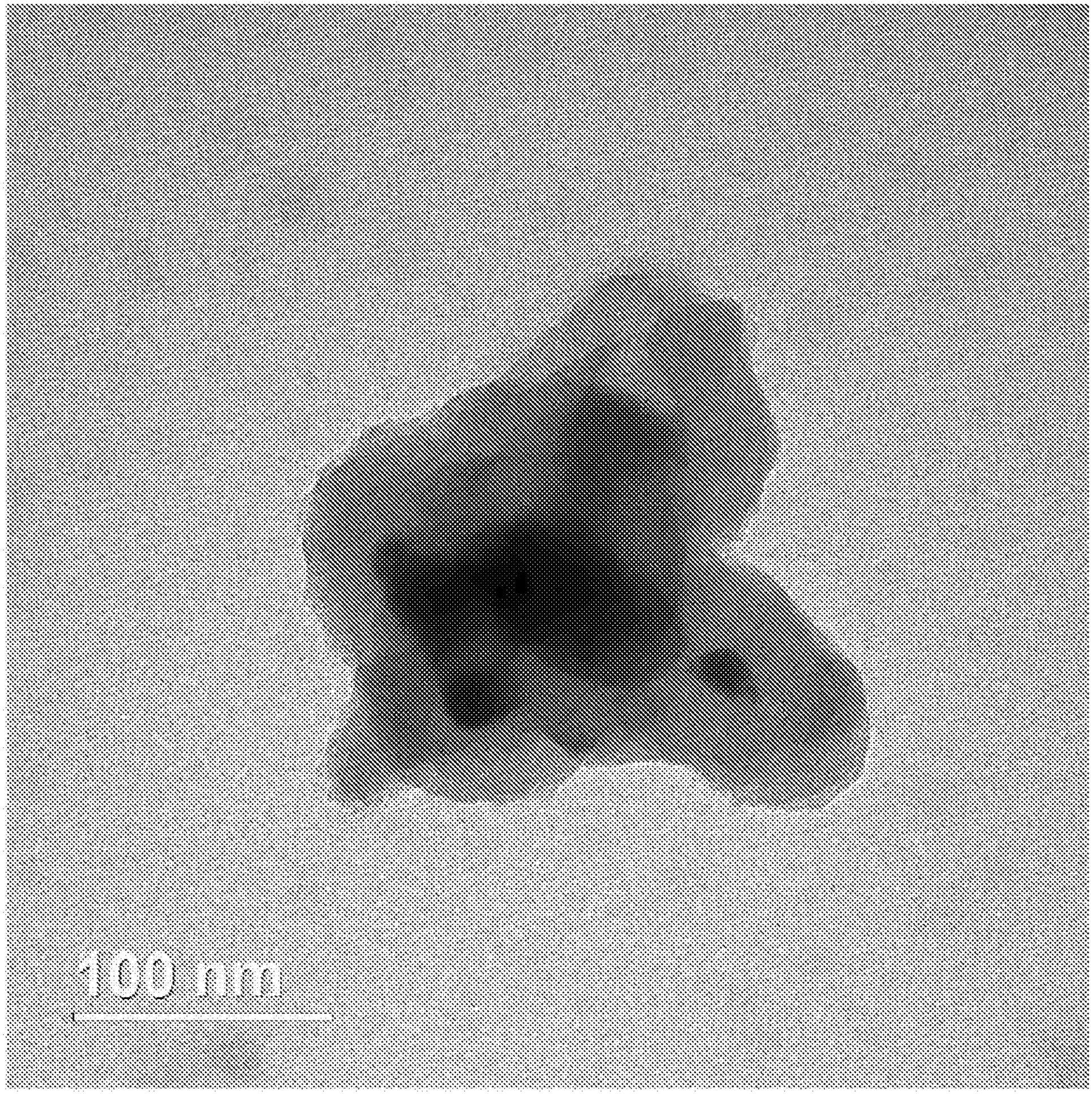


FIG. 125

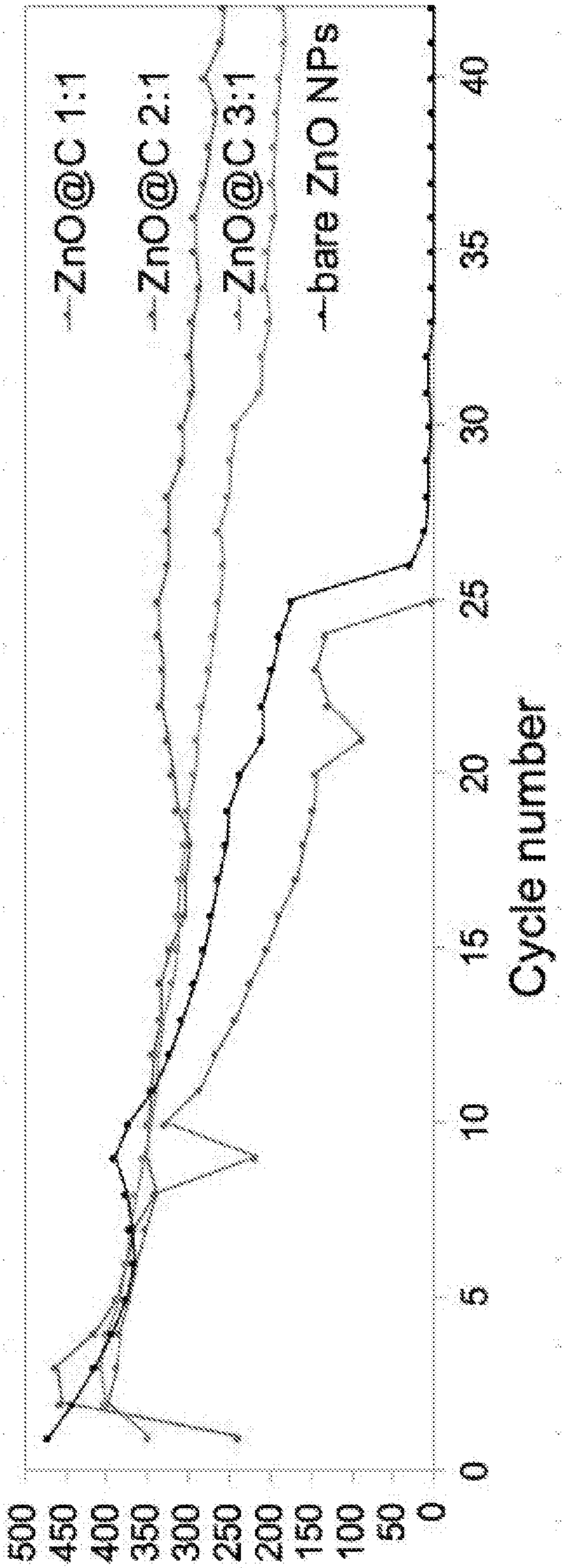

ZnO@C 1:1
ZnO@C 2:1
ZnO@C 3:1
bare ZnO NPs
Cycle number
Specific capacity
(mAh/g)
0
5
10
15
20
25
30
35
40
0
50
100
150
200
250
300
350
400
450
500

FIG. 126

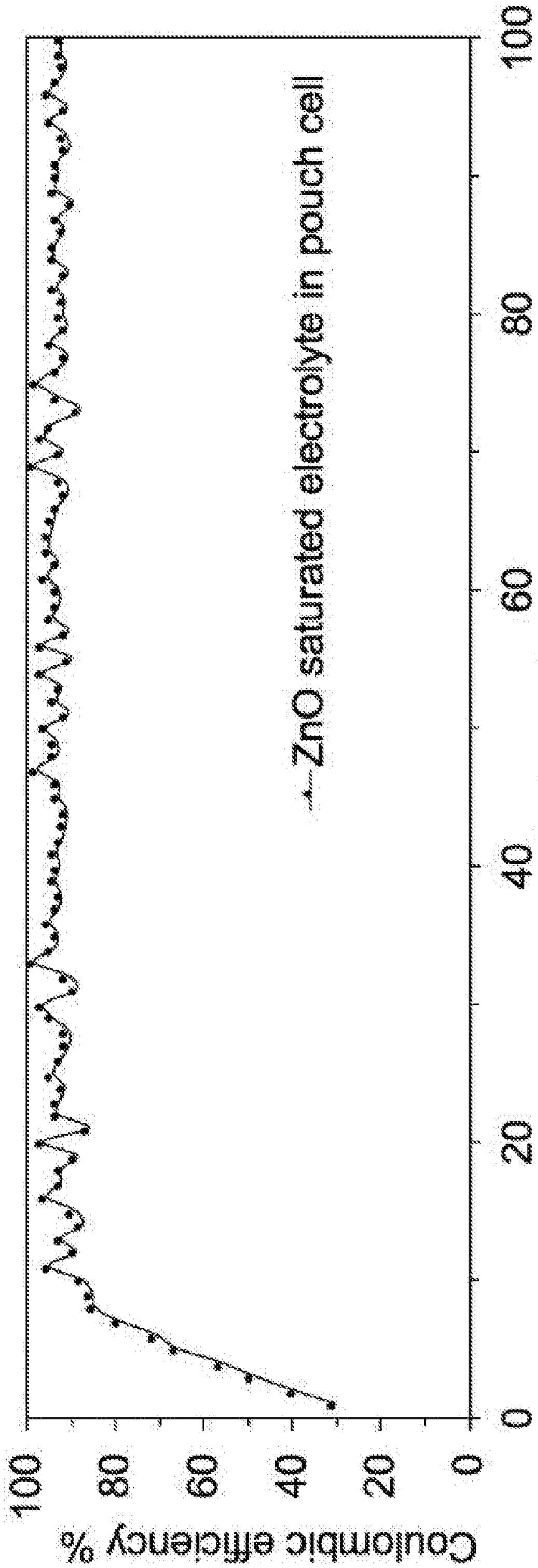

100
80
60
40
20
0
Cycle number
Zn-MnO2 saturated electrolyte in pouch cell
Coulombic efficiency %
100
80
60
40
20
0

FIG. 127

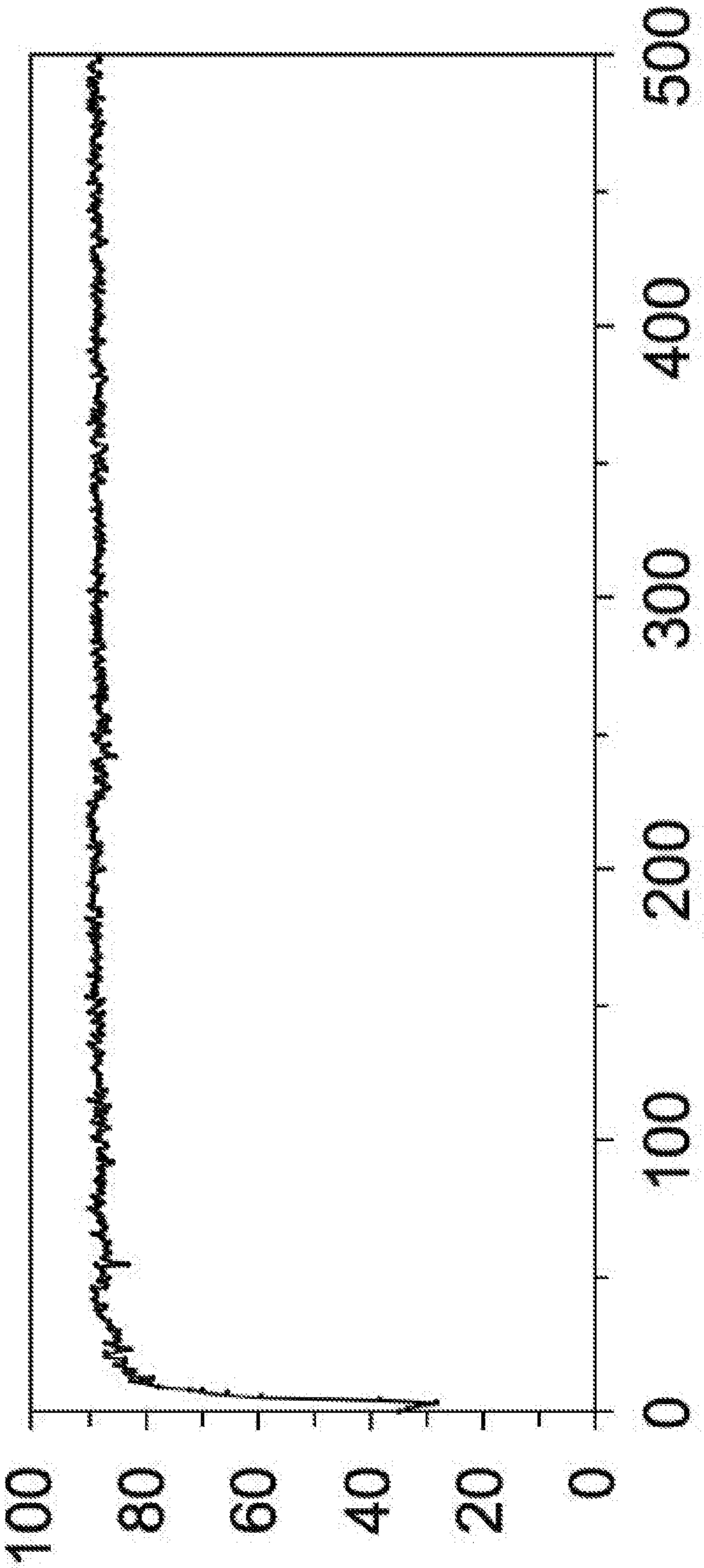

Coulombic efficiency %
100
80
60
40
20
0
0
100
200
300
400
500
Cycle number

FIG. 128